Electronic and vibrational properties of diamondoid derivatives, graphite, and carbon nanotubes

vorgelegt von
Master of Science (M.Sc.)
Christoph Tyborski
geb. in Berlin

von der Fakultät II - Mathematik und Naturwissenschaften
der Technischen Universität Berlin
zur Erlangung des akademischen Grades

Doktor der Naturwissenschaften
- Dr. rer. nat. -

genehmigte Dissertation

Promotionsausschuss:

Vorsitzender: Prof. Dr. Michael Lehmann
Gutachter: Prof. Dr. Axel Hoffmann
Gutachter: Prof. Dr. Ralph Krupke
Gutachterin: Prof. Dr. Janina Maultzsch

Tag der wissenschaftlichen Aussprache: 12. Oktober 2018

Berlin 2018

Zusammenfassung

In dieser Arbeit werden vibronische und elektronische Eigenschaften von Diamantoiden, Graphen, mehrlagigem Graphen, Graphit und Kohlenstoffnanoröhren untersucht. Alle Untersuchungen basieren auf optischen Spektroskopiemethoden, wie Raman-Spektroskopie, Photolumineszens-Spektroskopie, Photolumineszens-Anregungsspektroskopie und Absorptionsspektroskopie, deren Ergebnisse mit computergestützten Rechnungen verglichen werden. Obwohl die untersuchten Materialsysteme schon einige Zeit bekannt sind, gibt es besonders im tiefen UV Bereich noch offene Fragen bezüglich deren optischer Eigenschaften. Es wird gezeigt, dass sowohl die Struktur der Kohlenstoffallotrope, als auch die Hybridisierung des enthaltenden Kohlenstoffs, die optischen Eigenschaften im UV Bereich bestimmen.

Im ersten Teil geht es um Diamantoide und deren Derivate. Große Fortschritte im Verständnis ihrer chemischen Reaktivität führten zu verschiedensten Funktionalisierungen von den ansonsten weitestgehend inerten Diamantoiden. Gezielte Funktionalisierungen bieten die Möglichkeit strukturbezogene Eigenschaften zu ändern. Beispielsweise hängen optische Übergangsenergien stark von der Art einer funktionellen Gruppe ab, sodass diese an mögliche Anwendungen angepasst werden kann.
Wir untersuchen im Besonderen Diamantoidoligomere, die aus verschiedenen Monomeren mittels einer Kohlenstoffeinfachbindung oder -doppelbindung verbunden sind. Die Funktionalisierung mit sp^2 Defekten, führt zu einer Verkleinerung optischer Übergangsenergien von $\sim 6.5\,\mathrm{eV}$ für unfunktionalisierte Diamantoide, auf $\sim 4.7\,\mathrm{eV}$ für deren Derivate. Weiterhin zeigen wir, dass deren vibronische Eigenschaften denen von unfunktionalisierten Diamantoiden ähneln, strukturbezogene Änderungen aber zum Auftreten neuer Schwingungsmoden führen. Beispielhaft seien Dimer-Atmungsmoden, sowie hochlokalisierte C-H Streckschwingungen erwähnt. Diamantoide bilden van-der-Waals Kristalle, die besonders hohe Bindungsenergien aufweisen. Deren periodische Anordnung führt zu einer Ausprägung von kollektiven Eigenschaften wie einer vibronischen oder elektronischen Bandstruktur. Mit resonanten Raman und Absorptionsmessungen zeigen wir, dass in Diamantoid van-der-Waals Kristallen, die optischen Übergänge um ca. $1\,\mathrm{eV}$ kleiner sind als in vergleichbaren, isolierten Molekülen.

Im zweiten Teil diskutieren wir doppeltresonante Raman Streuprozesse in Graphit, Graphen und Kohlenstoffnanoröhren (KN) im tiefen UV Bereich. Obwohl das Konzept der doppeltresonanten Ramanstreuung bereits vor mehr als 10 Jahren eingeführt wurde, ist es bis heute nicht bekannt, wie sich die Streuprozesse bei sehr hohen Anregungsenergien bis in den UV Bereich ändern. Wir werden sehen, dass die Intensitäten für die gut verstandenen, doppeltresonanten Moden, wie die D, $2D$ oder iTOLA (transversal op-

tisch + longitudinal akustisch) bei Anregungsenergien zwischen 4.69 eV und 5.46 eV stark zurückgehen. Anstelle dessen finden wir asymmetrische Ramanmoden, die wir der vibronischen Zustandsdichte in zweiter Ordnung zuordnen. Die gemessenen Moden können den zweifach entarteten LO/TO Phonon am Γ Punkt, den LA/LO und TO Phononen am M Punkt, sowie dem Maximum des LO Phononenzweiges zugeordnet werden. Mit computergestützten Rechnungen zeigen und erklären wir den Streumechanismus, der zu den neuen Moden führt. Anregungen nahe der M Punkt Energie von $\sim 4.7\,\mathrm{eV}$ führen zur Aktivierung von doppeltresonanten Ramanmoden mit den kürzestmöglichen resonanten Phonon Wellenvektoren. Eine prominente, dadurch entstehende Ramanmode, ist die $2D$ Mode, die durch die sehr kurzen involvierten Phonon Wellenvektoren bei sehr hohen Energien von ca. $3050\,\mathrm{cm}^{-1}$ zu finden ist. Weiterhin untersuchen wir die vibronische Zustandsdichte in zweiter Ordnung von mehrlagigem Graphen. Wir können zeigen, dass die Energien von den jeweils zweifach entarteten LO/TO Phononenzweigen am Γ Punkt und die Maxima der LO Phononenzweige nur sehr wenig von der Lagenanzahl abhängen.

Im letzten Teil analysieren wir intensitätsschwache Ramanmoden von Kohlenstoffnanoröhren. Wir konzentrieren uns dabei auf die Moden bei ca. $1950\,\mathrm{cm}^{-1}$ und $2450\,\mathrm{cm}^{-1}$ in einer Ensembleprobe. Beide Moden sind über einen großen Anregungsbereich von 1.71 eV-2.73 eV dispersiv und zeigen jeweils verschiedene, ausgeprägte Bereiche. Mit Hilfe von DFT (Dichtefunktionaltheorie) Rechnungen, ordnen wir deren Dispersionen einem Ensemble Effekt zu. Abhängig von der Anregungsenergie, sind verschiedene KN in Resonanz, deren charakteristische vibronische Eigenschaften dann in Spektrum zu finden sind. Besonders im Anregungsbereich zwischen 2.1 eV-2.5 eV, sind einerseits metallische, aber andererseits auch halbleitende KN zu finden. Aufgrund ihrer unterschiedlichen elektronischen Struktur, haben beide Arten verschiedene Durchmesser für gleiche optische Übergangsenergien. Dies führt zu starken Unterschieden in ihren vibronischen Eigenschaften, wodurch sich beide Spezies im Ramanspektrum gut unterscheiden lassen.
Mit Hilfe von DFT und NOTB (non-orthogonal tight-binding) Rechnungen, können wir die $\sim 2450\,\mathrm{cm}^{-1}$ Mode zu einem doppeltresonanten iTOLA Prozess in der Nähe des K Punktes zuordnen. Im Gegensatz dazu, ist die Mode bei $1950\,\mathrm{cm}^{-1}$ in den DFT Rechnungen eine doppeltresonante LOLA Kombinationsmode aus der Nähe des Γ Punktes. Für die Zuordnung wurden die Dispersionen und Intensitäten aller $6 \times 6 = 36$ Kombinationsmoden im Ausgangsmaterial Graphen verglichen. Im NOTB Ansatz jedoch, ist die $\sim 1950\,\mathrm{cm}^{-1}$ Mode eine doppeltresonante TOZO (ZO: optische Schwingung nicht in der Ebene von Graphen) Mode in der Nähe des K Punktes. Wir glauben, dass im DFT Ansatz eine mögliche Beteiligung von ZO Phononen an Streuprozessen zu wenig berücksichtigt wird. Dieser nutzt die Elektron-Phonon Kopplungselemente des Ausgansmaterials Graphen, wo der ZO Phononenzweig Raman-inaktiv ist. Deshalb ordnen wir die Mode bei ca. $1950\,\mathrm{cm}^{-1}$ eher einer TOZO Kombination zu.
Wir zeigen einen erweiterten "Kataura plot", dh. eine Übersicht von optischen Übergangsenergien abhängig von dem Durchmesser einer KN. Die Erweiterung bezieht sich auf Energien im tiefen UV Bereich bis hin zu den höchstmöglichen optischen $\pi \rightarrow \pi^*$ Übergängen in Kohlenstoffnanoröhren. Einerseits bestimmen der "Quantum confinement"-, aber auch der "Trigonal warping"-Effekt die Übergangsenergien im tiefen UV Bereich. Andererseits können wir mit Hilfe von berechneten optischen Matrixelementen zeigen, dass es

verbotene Übergänge für Anregungen höher als die M Punkt Energie ($\sim$ 4.7 eV) gibt. Dies trifft für keinen Übergang unterhalb der M Punkt Energie zu. Am Ende zeigen wir eine Möglichkeit, wie mit Hilfe von KN und UV Licht, Siderit aus Eisen und Kohlenstoff erzeugt werden kann. Alle Untersuchungen basieren auf der Analyse einer charakteristischen Siderit Ramanmode, die systematisch mit der Variation von verschiedenen Parametern wie verschiedenen Reaktionsgasen, verschiedenen Anregungsenergien und verschiedenen Belichtungszeiten durchgeführt wird.

Abstract

In this work, we present an analysis of vibrational and electronic properties of diamondoids, graphene, multilayer graphene, graphite, and carbon nanotubes. The realized studies are based on optical spectroscopy, such as Raman spectroscopy, photo luminescence, photo luminescence excitation, and absorption spectroscopy, but also on in-depth model calculations. Although the analyzed material systems have been partly known for many decades now, fundamental optical properties, especially in the deep-UV, have not been explored yet. We will see that both, structural characteristics of carbon allotropes, and the hybridization of carbon have a large impact on the measured optical responses. All findings are discussed with a deep analysis of supportive DFT (density functional theory) computations, revealing new insights into the manifold properties of carbon allotropes.

The first part focuses on diamondoids and diamondoid derivatives which form a new class of highly interesting materials. Recent developments in the functionalization of the widely inert diamondoids possibly opened a new path of carbon to find its way in applications. The functionalization-caused altering of their electronic and vibrational properties is, therefore, more and more of scientific interest. We focus our analysis on diamondoid oligomers, that are diamondoid moieties connected by carbon-carbon single and carbon-carbon double bonds. We will see that the introduction of sp^2 defects leads to a downshift of optical transition energies from $\sim 6.5\,\mathrm{eV}$ for pristine diamondoids, to $\sim 4.7\,\mathrm{eV}$ for their derivatives. We will further see that their vibrational properties can be classified by the characteristic vibrations from carbon and hydrogen atoms, also know from unfunctionalized diamondoids. However, structure-imposed vibrations, such as dimer-breathing modes (DBM) or localized vibrational modes are reported that are unique for diamondoid oligomers. Diamondoids tend to form stable van-der-Waals crystals with exceptionally high binding energies. The ordered structures lead to a self-altering of optical transition energies. With resonant Raman and absorption measurements, we find that optical transition energies in van-der-Waals crystals of two different diamondoid derivatives are $\sim 1\,\mathrm{eV}$ than in isolated molecules.

The second part discusses double-resonant Raman processes in graphite, graphene, and carbon nanotubes in the deep-UV range. Although the concept of double-resonant Raman scattering was introduced more than a decade ago, it is today still unclear how the scattering mechanism changes for very high excitation energies. We will see that for excitation energies between 4.69 and 5.46 eV, the intensities of the well-known double-resonant modes such as the D, $2D$ mode, or the iTOLA mode (in-plane transverse optical, longitudinal acoustic) in graphite are drastically quenched. Instead, we observe highly asymmetric Raman peaks that we attribute to the second-order vibrational density of states. The

observed peaks are assigned to the degenerate LO/TO phonons at the Γ point, LA/LO and TO phonons from the M point, and to the overbending of the LO phonon branches. We simulate the Raman spectra and explain the scattering paths which are different from those of graphite under visible excitation. Excitations close to the M-point energy of $\sim 4.7\,\mathrm{eV}$ lead to the activation of double-resonant Raman modes. Although exhibiting very low intensities, we can observe the beginning of the $2D$ mode involving the shortest phonon wavevectors possible. We determine the $2D$ mode to stem from close to the Γ point exhibiting frequencies of around $3050\,\mathrm{cm}^{-1}$. Further, the second-order vibrational density of states from multilayer graphene is analyzed. We find that the frequencies of the degenerate LO/TO phonons at the Γ point and the LO phonon overbendings only depend marginally on the layer number.

The last part focuses on low-intensity modes in the Raman spectra of carbon nanotubes. In detail, we analyze the $\sim 1950\,\mathrm{cm}^{-1}$ and $2450\,\mathrm{cm}^{-1}$ modes in an ensemble sample that were controversially discussed in the past. We find that both modes are dispersive over an excitation range of 1.71 eV-2.73 eV, partly exhibiting bimodal peak structures. With the help of DFT + zone-folding calculations, we assign their dispersions to an ensemble effect, *i.e.* each varied excitation energy is in resonance to a certain CNT species in the ensemble sample, probing individual electronic and vibrational properties. The same argument is true for the observed bimodal peaks structures. For excitation energies between 2.1 and 2.5 eV, both metallic and semiconducting species are probed. Due to their different structures of one-dimensional electronic bands, metallic and semiconducting carbon nanotubes have different diameters for likewise transition energies. Consequently, we measure CNT specific vibrational properties with a monochromatic excitation which lead to characteristic fingerprints in the Raman spectra. With the support of DFT + zone-folding and non-orthogonal tight-binding calculations, we assign the $2450\,\mathrm{cm}^{-1}$ band to a double-resonant iTOLA mode originating from close to the K point. Instead, DFT + zone-folding calculations indicate that the $1950\,\mathrm{cm}^{-1}$ band is a LOLA mode from close to the Γ point. The underlying assignment is done via the analysis of both the dispersions and intensities of all possible $6 \times 6 = 36$ combination modes in the initial graphene structure. Non-orthogonal tight-binding calculations, however, indicate this mode to be a TOZO (ZO: transverse optical, out-of-plane optical) combination mode from close to the K point. As the DFT + zone-folding approach requires the initial electron-phonon matrix elements from graphene, we believe that possible ZO contributions are underestimated in this approach. In graphene, the out-of-plane ZO phonon mode is symmetry forbidden. Therefore, we attribute the $1950\,\mathrm{cm}^{-1}$ band to a TOZO combination from close to the K point.
We introduce an "extended Kataura plot", *i.e.* we show a calculated plot on how the optical transition energies from CNTs depend on their diameters up to the highest possible $\pi \rightarrow \pi^*$ Γ-point transitions. We will see on the one hand that quantum confinement and trigonal warping determine the transition energies, even in the deep-UV region. Based on the calculations of optical matrix elements, we will see on the other hand, that several optical transitions energies higher than the M-point energy are dipole forbidden. This is not known from transitions from below the M-point energy. In the end, we discuss and explain a way to utilize deep-UV light and carbon nanotubes to oxidize iron clusters to

Siderite which we have explored in another systematic study. We base our statements on the analysis of the Raman footprint of Siderite and show different spectra with varied external parameters such as different reaction gases, different excitation energies, or different exposure times.

List of publications

1 Double-resonant LA phonon scattering in defective graphene and carbon nanotubes
Felix Herziger, Christoph Tyborski, Oliver Ochedowski, Marika Schleberger, and Janina Maultzsch
Physical Review B, **90**, 245431 (2014)

2 Raman spectroscopy of nondispersive intermediate frequency modes and their overtones in carbon nanotubes
Christoph Tyborski, Felix Herziger, and Janina Maultzsch
physica status solidi (b), **252**, 2551-2557 (2015)

3 Beyond double-resonant Raman scattering: Ultraviolet Raman spectroscopy on graphene, graphite, and carbon nanotubes
Christoph Tyborski, Felix Herziger, Roland Gillen, and Janina Maultzsch
Physical Review B (R), **92**, 041401 (2015)

4 From isolated diamondoids to a van-der-Waals crystal: A theoretical and experimental analysis of a trishomocubane and a diamantane dimer in the gas and solid phase
Christoph Tyborski, Reinhard Meinke, Roland Gillen, Tobias Bischoff, Andre Knecht, Robert Richter, Andrea Merlin, Andrey A. Fokin, Tetyana V. Koso, Vladimir N. Rodionov, Peter Schreiner, Thomas Möller, Torbjörn Rander, Christian Thomsen, and Janina Maultzsch
The Journal of Chemical Physics, **147**, 044303 (2017)

5 Electronic and vibrational properties of diamondoid oligomers
Christoph Tyborski, Roland Gillen, Andrey A. Fokin, Tetyana V. Koso, Natalie A. Fokina, Heike Hausmann, Vladimir N. Rodionov, Peter Schreiner, Christian Thomsen, and Janina Maultzsch
The Journal of Physical Chemistry C, **121**, 48 (2017)

6 Tunable quantum interference in bilayer graphene in double-resonant Raman scattering
Felix Herziger, Christoph Tyborski, Oliver Ochedowski, Marika Schleberger, and Janina Maultzsch
Carbon, **133**, 254-259 (2018)

7 Double-resonant Raman scattering with optical and acoustic phonons in carbon nanotubes
Christoph Tyborski, Asmus Vierck, Rohit Narula, Valentin N. Popov, and Janina Maultzsch
Physical Review B, **97**, 214306 (2018)

8 Reductive Diazotation of Carbon Nanotubes: An Experimental and Theoretical Selectivity Study
Milan Schirowski, Christoph Tyborski, Janina Maultzsch, Frank Hauke, Andreas

Hirsch, and Jakub Goclon
accepted for publication in Chemical Science

9 Vibrational properties of single-bond diamondoid dimers
Christoph Tyborski, Tobias Hückstaedt, Tommy Otto, Roland Gillen, Andrey A. Fokin, Tetyana Koso, Lesya V. Chernish, Pavel A. Gunchenko, Peter Schreiner, and Janina Maultzsch
in preparation, based on Chapter 4.3

10 Electronic and vibrational properties of [2](1,3)Adamantano[2](2,7)pyrenophane
Tao Xiong, Christoph Tyborski, Tobias Hückstaedt, Stefan Kalinowski, Janina Maultzsch, Paul Kahl, Philipp Wagner, Ciro Balestrieri, Jonathan Becker, Heike Hausmann, Graham Bodwell, Peter Schreiner, and Peter Saalfrank
in preparation, partly based on Chapter 4.5

Contents

1. Introduction

Although being known for several centuries, the element carbon still evokes a tremendous scientific interest. It seems from a physicist's point of view, that its attention was even rapidly growing in the last 30 years. The first successful isolation of a sp^2 conjugated, complete two-dimensional carbon system is only 14 years ago, but its famous article "Electric Field Effect in Atomatically Thin Carbon Films" is already cited more than 42000 times[1] [1]. A lot of the interest can be understood from the fact that two-dimensional systems were not considered to be stable at all. According to Mermin and Wagner, a perfectly flat crystal could not exist due to thermal fluctuations in the range of the lattice constant [2]. Irregular deformations in graphene, however, reduce its long-range symmetry, leading to a stable crystal. The discovery of graphene can thus be seen as a starting point for the search of other two-dimensional crystals, such as hexagonal boron nitride [3] or MoS_2 [4], opening a complete new field of solid state physics.
On the other hand, a lot of the scientific interest of graphene can be understood from the fact that it combines many extraordinary properties, such as a linear electronic band dispersion that is otherwise only known from massless Dirac particle or surface states in topological insulators [5], its ballistic charge carrier transport at room temperatures [6], or its high mechanical stability of 42 N/m [7]. All its characteristics make graphene a promising candidate for applications in the field of electronics, sensors, composites, coatings or membranes. However, graphene can also be considered as the starting material for graphitic, one-dimensional carbon nanotubes (CNT) as well as other graphitic carbon. CNTs can be seen as rolled-up graphene with a perfect, seamless contact at the graphene edges, exhibiting diameters in the range of $\sim$ nm [8]. The reduction of dimensionality in carbon nanotubes leads to a confinement of their electronic states, while widely maintaining the traits of graphene. Surprisingly, only their rolling-up angle and their diameter determines whether a carbon nanotube is metallic or semiconducting. This aspect, in particular, distinguishes them from graphene, making carbon nanotubes a future candidate for possible semiconductor applications.
Among many other experimental approaches, especially Raman spectroscopy was utilized to gain access to both the electronic and vibrational properties of graphene and carbon nanotubes. The electronic band structure of graphene opens the possibility to investigate phonons with arbitrary wave vectors from a large area of the 1. Brillouin zone [9]. Together with the broad availability of compact Raman spectrometers, it is thus a comparably easy way to examine some of the peculiarities of graphene: At the one hand, its linear electronic band structure can be probed, but also, the breakdown of the Born-Oppenheimer approximation in graphene that leads to a strong Kohn-Anomaly [10]. In

[1] google scholar august 2018

Raman experiments, these characteristics can especially be addressed by excitation energies in the near infrared and visible optical region. Combined with the limited availability of laser light sources beyond the optical visible region, the focus on these specific excitation energies in the past, can be well understood. In this work, we have instead extended the Raman analysis of graphene, carbon nanotubes, and graphite to excitation energies in the deep-UV (ultraviolet) region. By this approach, we gain access to regions of the 1. Brillouin zone that are otherwise only accessible by way more complicated experimental approaches. It is interesting to note that the Raman response in the deep-UV region, *i.e.* away from the linear band structure, is systematically different compared to the response in the visible region. All well-known, second-order, double-resonant Raman modes, such as the D or the $2D$ mode, are not observable anymore. Instead, a new set of Raman peaks appears that we attribute to the second-order vibrational density of states. The Raman spectrum then resembles those from classical semiconductors like GaAs or ZnO [11–13]. By the careful choice of suitable excitation energies, we can manipulate the transition of the "unique" Raman response from graphene, graphite, and carbon nanotubes to a "conventional" Raman response known from other semiconductors. Until today, this transition has not been investigated yet and is again a new aspect of the rich characteristics of graphitic materials. The deep-UV Raman experiments presented in this thesis lead to a wider understanding of both Raman scattering in graphitic materials as well as their optical and vibrational properties.

Two-phonon scattering in graphitic materials allows for the analysis of many different phonon branches only by the careful choice of a certain mode in their Raman spectrum [14]. Compared to graphene, it has turned out that Raman spectra of carbon nanotubes exhibit more Raman peaks, mainly due to their altered symmetries. Rolling up a graphene sheet to a carbon nanotube, lifts the degeneracy of the Raman active E_{2g} mode on the one hand, but also leads to an altering of the strict Raman selection rules as present in graphene. For instance, this offers a way to analyze out-of-plane ZO phonon branches in carbon nanotubes, which is Raman forbidden in graphene [15, 16]. Although Raman spectra of carbon nanotubes have been analyzed for many years, several aspects concerning peak compositions, peak dispersion, or the origin of certain Raman modes still remain unclear. To some extent, this can be understood from the fact that typical CNT samples often contain more than one CNT species. The total Raman spectrum is thus a convolution of the intrinsic Raman response from each species, hindering an analysis on the basis of pure experimental data. This, of course, opens room for interpretations and leads to inaccuracies. Consequently, a thorough analysis of these ensemble samples requires time-demanding and sophisticated simulations. However, also the theoretical approaches used to calculate the electronic and vibrational properties of CNTs, suffer from inaccuracies. An often used approach is based on the zone-folding of graphene's two-dimensional reciprocal space in order to obtain the electron and phonon band structure. This widespread *a posteriori* approach offers reliable results for prominent peaks in the Raman spectrum of carbon nanotubes, but fails to describe structure-imposed Raman modes, such as the radial-breathing mode (RBM), which are not present in graphene. By combining sophisticated computational models, such as non-orthogonal tight binding, with an extensive experimental analysis, we analyze low-intensity Raman modes in car-

bon nanotubes and demonstrate the influence of ensemble effects on the measured Raman spectra. Our results show that species-specific properties determine the Raman spectra in terms of peak compositions and dispersion. Especially differences in the vibrational properties of metallic and semiconducting carbon nanotubes lead to distinguishable peaks of the analyzed low-intensity Raman modes. Further, it has turned out that the zone-folding approach underestimates out-of-plane ZO contributions in the Raman spectra of carbon nanotubes. This leads to a wrong assignment of an apparent, low-intensity mode in the Raman spectra of carbon nanotubes. However, with the help of a complementary computational approach, this somewhat misleading assignment can be rectified. These general findings can be utilized to understand the very large variety of Raman data available in literature to a greater extent. We believe our findings close a gap in the understanding of low-intensity Raman bands in carbon nanotubes on the one hand, but also in the understanding of ensemble effects. Especially the latter might be used to recap established Raman data widespread in current literature.

Besides graphene and carbon nanotubes, diamondoids can be seen as another extraordinary carbon allotrope. The smallest diamondoid, namely adamantane, has been known approx. 70 years longer than graphene or carbon nanotubes, but has not evoked such a large scientific interest. It was first discovered 1933 in crude oil [17] and can be seen as the smallest diamondoid possible, consisting of 10 carbon and 16 hydrogen atoms arranged in a diamond-cage structure. Since then, it has found its way particularly in medicine applications as drug carrier [18]. The scientific interest and possible applications, however, were back then limited to adamantane and the next two larger diamondoids, namely diamantane and triamantane. This can be understood from the simple fact that higher homologues were not available. Even today, higher homologues can be barely selectively fabricated, as differences in the thermodynamic stabilities of intermediate states in their synthesis are only very low. However, diamondoids experienced a renaissance in 2003 when Jeremy Dahl *et al.* [19] isolated different species of diamondoids up to undecamantane (11 cages) from crude oil. The availability of mono-fraction species allowed for their systematic analysis. For instance, it was found that the quantum confinement model has a limited validity in lower diamondoids [20] or that diamondoid passivated surfaces have a negative electron affinity [21]. Recent developments in diamondoid chemistry enabled their functionalization with specific groups. This in turn opens a way to tailor their electronic and vibrational properties, while maintaining their chemical inertness or their robustness. One possible route is the introduction of sp^2 defects in a way that lower diamondoids form dimers or trimers connected by a double bond [22]. Another way to form dimers is the connection by a single bond, that can be seen as an extension of the initial carbon cages [23]. The so obtained set of new diamondoid derivatives is both experimentally and theoretically analyzed to a large extent in this dissertation. For instance, we find that sp^2 defects in diamondoid dimers lead to a large redshift of their optical transition energies, compared to their pristine counterparts. The localization of the introduced π and π^* states further centralizes optically relevant orbitals between the diamondoid moieties. This particular aspect reduces the sensitivity of their lower, optical transitions to external influences such as neighboring molecules in diamondoid van-der-Waals crystals. Our findings might therefore help to design certain diamondoid derivatives that, one the

one hand exhibit desired electronic properties, but on the other hand, maintain those traits when they are brought into certain applications in a solid phase.

2. Structure and electronic properties of graphene, carbon nanotubes, and diamondoids

In this chapter, we discuss the structure and electronic properties of sp^2 graphene, sp^2 carbon nanotubes, and sp^3/sp^2 diamondoids. At first, we discuss the element carbon and its ability to form hybridized atomic orbitals as it is the basis of all analyzed materials in this dissertation. Findings for the electronic structures of sp^2 systems are generalized for periodic structures such as graphene or carbon nanotubes. We give a short introduction to the optical absorption in carbon nanotubes necessary to understand the optical responses in the ultraviolet range. In the end we introduce the structure and fundamental properties of diamondoids.

2.1 Carbon-Carbon bonds

Although the element carbon and its different appearances are partly known for more than two centuries, even in the recent past new configurations were found, namely carbon nanotubes [8] and graphene [24]. These modifications are periodic, low dimensional, fully unsaturated, and delocalized sp^2 carbon systems that were not expected to be stable for decades [2]. The basis of their stabilities are local deformations that destroy the long-range periodicity of the lattices [25,26], but also the comparably strong C=C double bond. The ability of carbon to form different hybrid orbitals creates the foundation of its rich modifications that are present in our daily environment. The carbon materials analyzed in this work only contain sp^2 and sp^3 hybridized carbon. We will therefore reduce the discussion on these two hybridizations and neglect the third type, the sp hybridization. It is important to note that the energies of the π and π^* orbitals (responsible for the second carbon-carbon bond in a carbon double bond) lie in between the energy gap of the σ and σ^* orbitals (responsible for the carbon-carbon bond in sp^3 configurations and the first carbon-carbon bond in a sp^2 configuration). This fact is very important for all carbon compounds analyzed in this dissertation as the low-lying orbitals determine the optical responses in the visible and near ultraviolet region.

A hybridization can be understood as a linear combination of atomic orbitals that form new, shared atomic orbitals. In the special case of carbon with its electron configuration [He]$2s^2 2p^2$, the spherical $2s$ and the dumbbell-shaped $2p$ orbitals are involved. Possible are also other combinations of atomic orbitals with *e.g.* 4, 5, 6d orbitals in complexes with

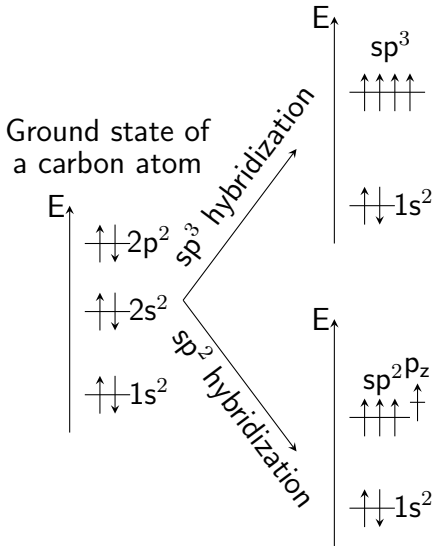

Figure 2.1: The electronic states of carbon core and valence electrons are schematically plotted. Left: Electron states of a carbon atom in the electronic ground state are shown. Right: Electron states of hybridized carbon is shown for a sp^3 hybridization (top) and for a sp^2 hybridization (bottom).

transition metals, but also very similar to carbon, the $2s$ and $2p$ orbitals in nitrogen [27].

The reorganization of atomic orbitals requires energy that is overcompensated by the large bonding energies [28]. This in turn enables the occurrence of stable, covalent, interatomic bonds. A schematic illustration of a sp^2 and sp^3 hybridization is given in Fig. 2.1.

A sp^3 hybridization leads to four equivalent hybrid orbitals that are mixed from $2s$ and $2p$ orbitals in the ratio of 1:3 [28]. Their spatial direction is determined by the respective contributions of $2p_x$, $2p_y$, or $2p_z$ orbitals within the hybrid orbitals [28]. In correspondence to the σ orbitals in diatomic orbitals, these hybrid orbitals are referred to as σ orbitals or rather the atomic bonds are referred to as σ bonds [28]. An equivalent atomic orbital mixing occurs between carbon and hydrogen atoms present at diamond and diamondoid surfaces [19, 29–31]. It is interesting to note that due to the $1s$ orbitals from hydrogen, the electronic states of the C-H σ-bonds lie energetically between those from the C-C σ-bonds with far-reaching consequences for the electronic structures of diamondoids [20, 28, 32]. They are discussed in more detail in Chapter 4.
Another hybridization, namely the sp^2 hybridization occurs from the mixing of a $2s$ and two of three $2p_x$ $2p_y$ $2p_z$ orbitals. This creates hybrid orbitals with a σ character aligned in a joint plane, in strong contrast to the sp^3 hybridization [28]. The second bond that originates from the out-of-plane p orbital is usually referred to as π bond and accordingly, the orbitals are referred to as π/π^* orbitals [28]. A schematic overview of their energy levels is given in Fig. 2.1. The twofold chemical bonds of a sp^2 hybridization lead to a comparably stiff and strong interatomic binding in carbon solids that explains the large vibrational frequencies of $\sim 1600\,\mathrm{cm}^{-1}$ ($\sim 198\,\mathrm{meV}$) that we measure within this dissertation. It further squeezes the remaining bond partners in one plane which in the end explains the two dimensional nature of graphene [24].

A heuristic and fast approach to understand the electronic structures of sp^2 systems was introduced by Erich Hückel [33–35] in 1931. The suggested approach reduces the problem to the out-of-plane p_z π/π^*-orbitals and parametrizes the Coulombintegral (Eigenenergies of the atomic orbitals) and the Resonanceintegral (interaction integral of neighboring

carbon atoms) with empirical data usually obtained from other theoretical methods or experiments [28, 33–35]. This approach only relies on next-nearest neighbors but still achieves considerable results [33–35]. For instance, with the help of the "Hückel method" it was possible to calculate the electronic structure of Benzol for the first time [33, 34].

Its power and range can be estimated when we examine the outcome for sp^2 carbon systems with a defined amount n of double bonds in a chain:

$$\Delta \mathrm{E} \sim 4\beta \sin\left(\frac{\pi}{2(n+1)}\right). \tag{2.1}$$

Eq. (2.1) describes the approximated energy value for the HOMO (highest occupied molecular orbital)-LUMO (lowest unoccupied molecular orbital) gap. β is a numeric value exhibiting $\sim 250\,\mathrm{kJ/mol}$ ($\sim 2.5\,\mathrm{eV}$) [36]. It already indicates that in the limit of an infinite chain of carbon double-bonds, as present in two-dimensional graphene, the energy difference of the lowest optical transition vanishes. A finding that holds true even for a material discovered in the 21$^{\text{th}}$ century and thus, almost 90 years after the theoretical prediction.
The profound considerations made by Erich Hückel can be generalized to conjugated carbon systems with arbitrary sizes. For instance, it can be applied to a periodic arrangement of hexagons forming one-dimensional linear chains or fully two-dimensional areas as present in graphene. The primary, discrete Eigenstates then turn into Bloch functions and accordingly, the discrete Eigenenergies turn into energy bands. Nowadays, this heuristic approach is widespread and also known as the tight-binding approximation, which is discussed on the next pages [37, 38].

2.2 Structure of graphene and tight-binding approximation

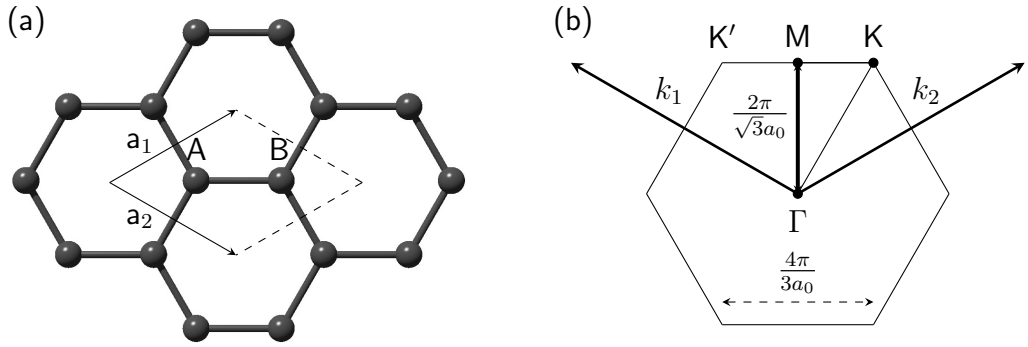

Figure 2.2: (a) A cutout of the real-space hexagonal graphene lattice is shown. a_1 and a_2 denote the lattice unit vectors in real space, respectively. The unit cell is spanned by the lattice vectors, indicated with the dashed lines. A and B show the carbon atoms within one unit cell. (b) The Brillouin zone of graphene is plotted with the high-symmetry points Γ, M, and K. k_1 and k_2 denote the reciprocal lattice unit vectors. Basic lengths between high-symmetry points are indicated.

As discussed above, the three σ and one π bonds of the sp^2 hybridized carbon lead to a triangular bond arrangement as shown in Fig. 2.2. If a sufficient amount of carbon atoms

forms such a triangular network, a honeycomb structure appears that is characteristic for the graphene lattice [24, 39]. Its unit cell contains two carbon atoms A and B with a distance a_{AB} of 1.422 Å resulting in a lattice constant of $a_0 = \sqrt{3}a_{\mathrm{AB}} \approx 2.463$ Å [39], as depicted in Fig. 2.2. In real space, the two-dimensional unit cell is spanned by the lattice vectors a_1 and a_2 [40]:

$$a_1 = \frac{a_{\mathrm{AB}}}{2}(3, \sqrt{3}) \qquad a_2 = \frac{a_{\mathrm{AB}}}{2}(3, -\sqrt{3}). \tag{2.2}$$

In reciprocal space, the Brillouin zone is given via:

$$k_1 = \frac{2\pi}{3a_0}(1, \sqrt{3}) \qquad k_2 = \frac{2\pi}{3a_0}(1, -\sqrt{3}). \tag{2.3}$$

The Fourier transformation of the real-space honeycomb lattice is again a honeycomb lattice in which the unit cell is rotated by 90° [40]. Reciprocal lattice vectors k_1 and k_2 are given in Fig. 2.2 and are plotted from the zone center (Γ) pointing to the middle of a neighboring hexagon of the reciprocal space's honeycomb structure. Particular high-symmetry points of the unit cell, namely the Γ point at the zone center, the K point at the edge of a hexagon and the M point between two K point edges are marked in Fig. 2.2. Further details can be found in Chapter 5, where the vibrational properties of graphene and graphite are discussed.

Tight-binding approximation

A fast way to obtain the electronic band structure of graphene is the tight-binding approximation that goes back to Wallace in 1947 [41]. It considers only valence electrons that are tightly bound to the atoms they belong to. The interaction with adjacent atoms is supposed to be only weak in a way that the electron wave functions resemble those from the atomic orbitals. Ensuing Bloch functions are then linear combinations of atomic wave functions [41]. When only the next-nearest neighbors are taken into account, already reasonable electronic band structures can already be achieved [41]. However, a considerable improvement can be obtained, when several interacting neighbors are considered in the calculations [38, 40, 41]. Only considering next-nearest neighbors in the easiest case, the energy bands for the valence electrons in graphene have the form:

$$E_{\pm}(\mathbf{k}) = \pm t\sqrt{3 + f(\mathbf{k})} - t' f(\mathbf{k}) \tag{2.4}$$

where t describes the nearest-neighbor hopping energy when the sub lattice is changed (A $\rightarrow$ B in Fig. 2.2). t' is the hopping parameter when the sub lattice is not changed (next-nearest neighbor). Both t and t' are empirical parameters that were found to exhibit $t = 2.7\,\mathrm{eV}$ and $0.02t \leq t' \leq 0.2t$ [38, 42]. $f(\mathbf{k})$ can be divided in its two-dimensional components [40]:

$$f(\mathbf{k}) = 2\cos(\sqrt{3}k_y a) + 4\cos(\frac{\sqrt{3}}{2}k_y a)\cos(\frac{3}{2}k_x a) \tag{2.5}$$

A one-dimensional plot of the electronic band structure of graphene along the Γ-K-M high-symmetry line is depicted in Fig. 2.3. The inset shows a magnification of the band dispersion around the K point. It can clearly be seen that in the proximity of the K

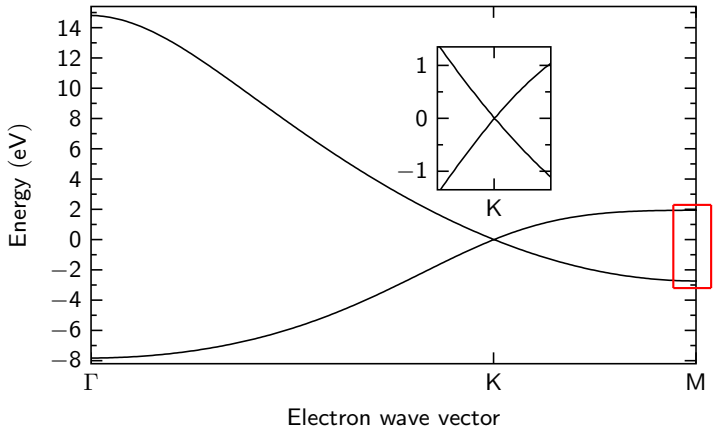

Figure 2.3: A one-dimensional plot of the electronic band structure of graphene within a next-nearest neighbor approximation is plotted for $t = 2.7\,\text{eV}$ and $t' = 0.1\,\text{eV}$, respectively [40, 42]. Denoted are the high-symmetry points Γ, K and M at the edges of the reciprocal unit cell. The inset shows a magnification of the linear band structure in the proximity of the K point.

point, both the electron and hole bands are linear. This particular behavior is well known from massless Dirac particles and is one of the reasons why graphene has evoked such a great interest in the past. Electrons in graphene are therefore often referred to as "massless Dirac particles" [43]. The electron band dispersion deviates from its linear behavior around the K point for larger and smaller electron momenta. The analogy to massless Dirac particles therefore only holds true in the direct proximity of the K points [38, 43, 44]. The deviation from the linear behavior is anisotropic, *i.e.* the slope of the electron bands in the $K-M$ direction is smaller compared to the dispersion along the $K-\Gamma$ direction [38, 43, 44]. In graphene and graphite, this anisotropy of the electron band structure is referred to as the "trigonal warping effect" with far-reaching consequences for their electronic properties [40, 44].
The one-dimensional electron band structure, as shown in Fig. 2.3, is used for various calculations of double-resonant Raman spectra in graphene as discussed in the Chapters 5 and 6.

2.3 Structure and electronic properties of carbon nanotubes

A paper tube can be made when a sheet of paper is rolled up. In analogy, single-walled carbon nanotubes can be thought of rolled-up graphene sheets that do not overlap at the edges, *i.e.* they have a seamless contact. Since the rolling-up angle can be chosen arbitrarily, there is an infinite amount of carbon nanotubes possible. Each one has an unique rolling-up angle and consequential, unique electronic and vibrational properties. The way a carbon nanotube is rolled up is defined by the chiral vector $\mathbf{c}$ measured in units of the graphene lattice vectors:

$$\mathbf{c} = \mathrm{n}_1 a_1 + \mathrm{n}_2 a_2 \tag{2.6}$$

Rolling up a sheet of graphene can be seen as an introduction of a boundary condition that quantizes the electronic states along the circumference of such a tube. It further reduces the dimensionality in comparison to graphene from continuous 2-dimensional states to constrained 1-dimensional states. The boundary condition reads as follows [45]:

$$m \cdot \lambda = |\mathbf{c}| = \pi \cdot d \qquad \Leftrightarrow \qquad \mathbf{k}_{\perp,m} = \frac{2\pi}{\lambda} = \frac{2\pi}{|\mathbf{c}|} \cdot m = \frac{2}{d} \cdot m. \tag{2.7}$$

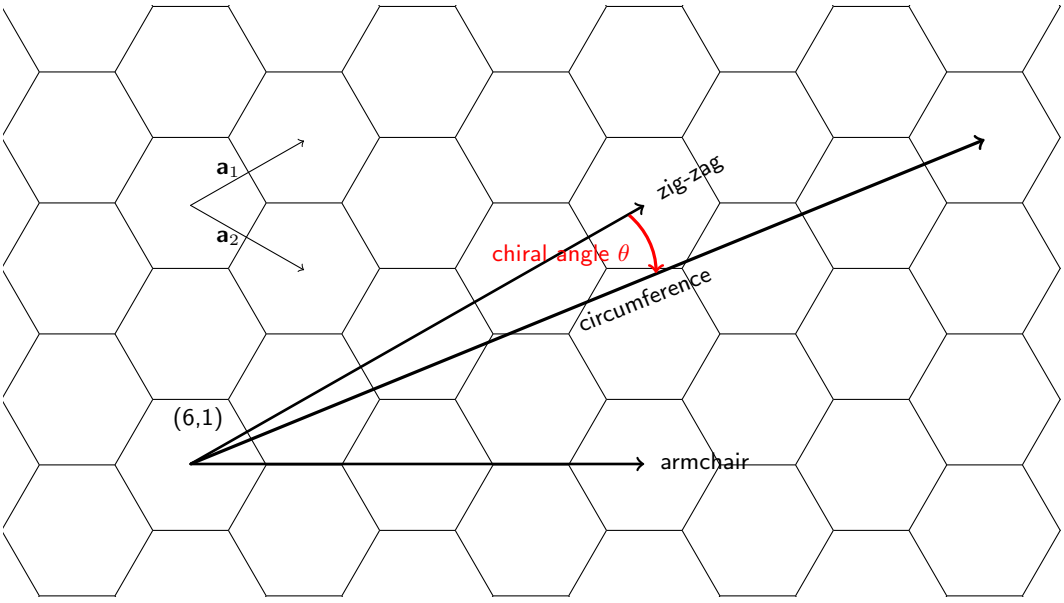

Figure 2.4: The chiral vector **c** (circumference) of a (6,1) carbon nanotube is plotted onto the hexagonal graphene lattice. The armchair and zig-zag high-symmetry directions are indicated by arrows and by the edges of the graphene lattice (top and bottom: armchair, left and right: zig-zag). The chiral angle is θ is indicated, $\mathbf{a}_1$ and $\mathbf{a}_2$ are the lattice vectors of the hexagonal graphene lattice, respectively.

With m being the quantum number for each electronic state $\mathbf{k}_{\perp,m}$, also named the band index. Electronic states in the direction of the tube axis are continuous and only depend on the translational period a [45]:

$$\mathbf{k}_z = \frac{2\pi}{a}. \tag{2.8}$$

The diameter d in Eq. (2.7) can be parametrized by the chiral indices n_1 and n_2 [45]:

$$d = \frac{|\mathbf{c}|}{\pi} = \frac{a_0}{\pi}\sqrt{n_1^2 + n_1 n_2 + n_2^2}. \tag{2.9}$$

Eq. (2.7) shows that the quantized electronic states are more separated in $\mathbf{k}$ space for smaller tube diameters and vice versa. An example of the chiral vector **c** of a (6,1) carbon nanotube plotted onto the hexagonal graphene lattice is depicted in Fig. 2.4.

Two high-symmetry chiral vectors and therewith two distinct directions can be found in the honeycomb lattice structure of graphene. They are named the zig-zag and armchair direction as given in Fig. 2.4. Any other direction in the honeycomb lattice can be defined with a so called chiral angel θ, defined relative to the high-symmetry zig-zag direction:

$$\cos\theta = \frac{n_1 + n_2/2}{\sqrt{n_1^2 + n_1 n_2 + n_2^2}}. \tag{2.10}$$

The six-fold symmetry of the graphene lattice only allows for distinguishable chiral angles θ between 0° (armchair) and 30° (zig-zag). All carbon nanotubes with chiral angles $\theta \neq 0°$ and $\theta \neq 30°$ are referred to as chiral carbon nanotubes. If the first chiral index is larger than the second chiral index, the helix of the respective tube is right-handed, if the order of the indices is changed, the helix will change to be left-handed, accompanied by a shift of the chiral angle to the interval between 30° and 60° [45]. The chiral angle of the

depicted (6,1) tube in Fig. 2.4 ($d \sim 5.1\,\text{Å}$) exhibits $\theta \sim 7.6°$ measured from the zig-zag direction.

Depending on the carbon nanotube sample, typical diameters exhibit values between 6 Å and 17 Å [46–48]. The scientific progress on carbon nanotubes since their discovery has lead to a broad availability of versatile samples. This especially includes highly enriched samples containing just certain species of carbon nanotubes or even just one chirality [49–51]. Ensemble samples, such as the HipCO sample, introduced and analyzed in Chapter 6, usually have a Gaussian diameter distribution and evenly distributed chiralities [45, 52, 53]. Carbon nanotube lengths up to 55.5 cm are reported in our days resulting in length-to-diameter ratios of 132.000.000:1 [54, 55], clearly showing their one-dimensional character. Until now, there has no material been discovered that exhibits higher aspect ratios. However, typical lengths of carbon nanotube reach from several 100 nm up to several μm [56, 57] with clearly lower aspect ratios. Still, carbon nanotubes are considered to be one-dimensional material systems.

2.3.1 Electronic band structure of carbon nanotubes

A convenient approach to obtain the electronic band structure of carbon nanotubes is the zone-folding approximation [38]. It requires the two-dimensional electronic band structure of graphene in the first place and can be seen as an *a posteriori* approach with the introduction of boundary conditions to the continuous electron wavevectors of graphene. The so emerging one-dimensional reciprocal space can be constructed by the the reciprocal space vectors $\mathbf{k}_z$ and $\mathbf{k}_\perp$ consisting of continuous lines $\mathbf{k}_z$ equidistantly spaced by $|\Delta\mathbf{k}_\perp| = 2/d$, orthogonal to the direction of the continuous electron wave vectors $\mathbf{k}_z$ [45, 53]. Their number, lengths, spacing, and their orientation depend on the chiral indices n_1 and n_2 [45, 53] as shown before. In this way, each carbon nanotube has a characteristic electronic band structure and can either be metallic or semiconducting [58]. Via the family index ν, carbon nanotubes can be classified into three different families [45, 53, 58]:

$$\nu = (n_1 - n_2) \bmod 3 \tag{2.11}$$

If one of the one-dimensional cutting lines crosses a K point in the reciprocal space of graphene, the respective carbon nanotube will be metallic. For reasons of symmetry, this always happens for $\nu = 0$ [45, 53, 58]. If the closest subband to the K point lies in the $K - \Gamma$ direction, the family index will be $\nu = -1$. If the closest subband to the K point lies in the $K - M$ direction, the family index will be $\nu = +1$ [45, 53]. In both cases, the carbon nanotubes will be semiconducting. One third of all imaginable carbon nanotubes are metallic, the other two thirds are semiconducting [45, 53, 58].
The alignment of subbands for three zig-zag carbon nanotubes belonging to the $\nu = +1, -1, 0$ families are plotted onto a contour plot of the electronic band structure of graphene in Fig. 2.5. The spacing of subbands for different nanotubes increases for decreasing diameters, but due to the same directions of the chiral vector, their orientations are the same. In case of the (9,0) tube, one cutting line passes the K point and thus the (9,0) tube is metallic. Cutting lines responsible for the first optical transitions E_{11} are denoted. Slopes of the corresponding electron and hole bands depend on the one-dimensional electron wave vector $\mathbf{k}_z$ and can be followed in Fig. 2.5 on the right side.

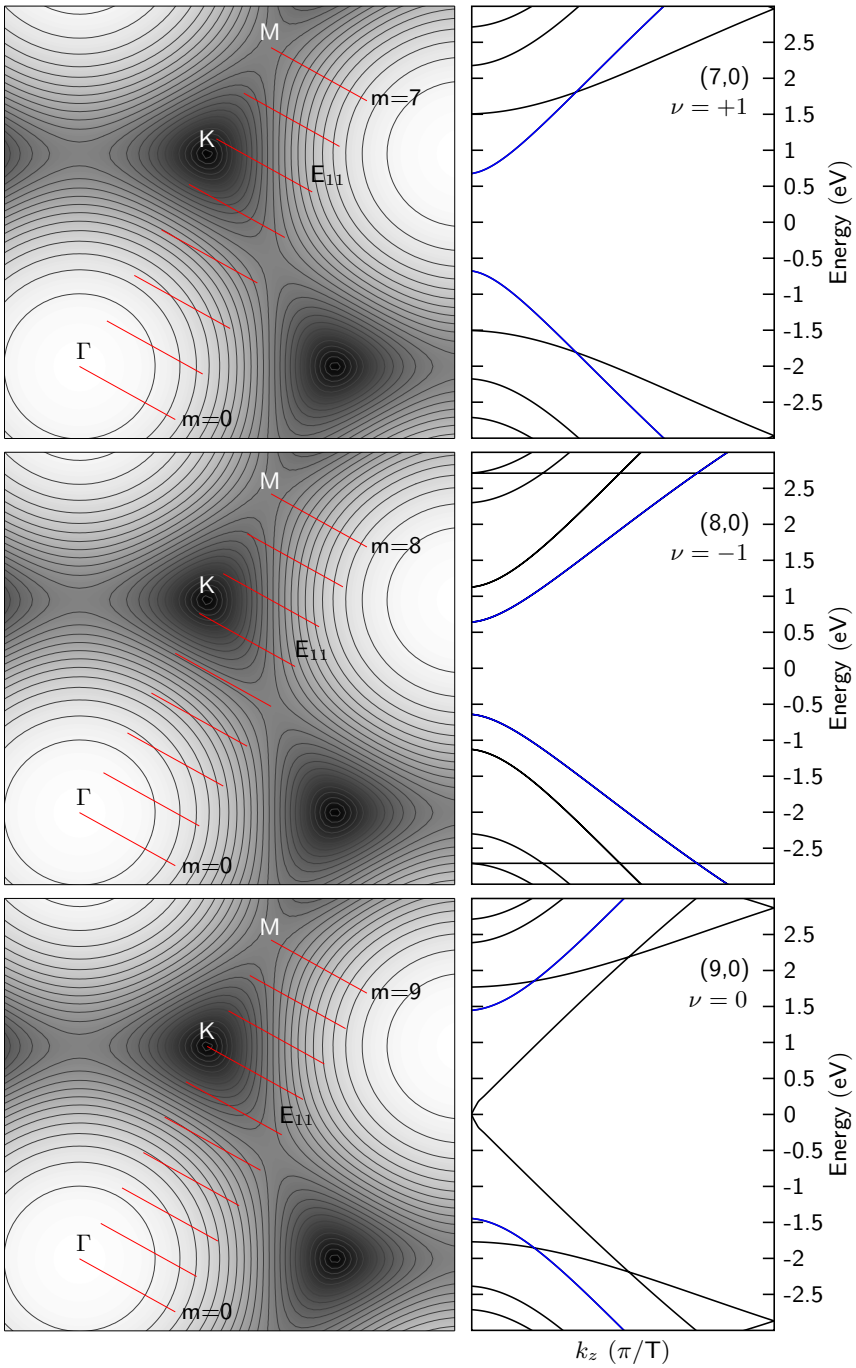

Figure 2.5: Left: Confined electronic bands of a (7,0), (8,0), and (9,0) carbon nanotube are plotted onto the two-dimensional contour plot of the electronic band structure of graphene, respectively. All carbon nanotubes belong to different families ν as indicated in the right boxes. The high-symmetry points Γ and K are highlighted. Band indices m of the subbands are given for each carbon nanotube. The subbands responsible for the lowest optical transitions E_{11} are labeled. Right: Electronic band structures of the respective carbon nanotubes are plotted. The bands responsible for the lowest optical transitions E_{11} are plotted in blue. Electronic bands are calculated within a next-nearest neighbor tight-binding + zone-folding approach.

Higher optical transitions generally occur for electron and hole bands with other band indices m and are named by ascending indices E_{nn}, *i.e.* E_{22}, E_{33}, ... Due to a lesser confinement of electronic states, the k-space distance to the closest K point for the (8,0) tube is smaller in comparison to the (7,0) tube, resulting in a smaller optical bandgap of $E_{11}^{(8,0)} = 1.28\,\text{eV}$, compared to $E_{11}^{(7,0)} = 1.392\,\text{eV}$, obtained within a next-nearest neighbor tight-binding + zone-folding approach. The K-point distance of the metallic nanotubes is even larger, resulting in an optical bandgap of $E_{11}^{(9,0)} = 2.914\,\text{eV}$. For commercially available nanotubes samples, the optical bandgaps are usually lower than 1 eV [45, 59, 60]. Excitation energies in the visible optical range are therefore usually in resonance with the E_{22} or E_{33} optical transitions.

The correlation between bandgap and diameter of a carbon nanotube with defined chiral indices n_1 and n_2 was first given by Kataura *et al.* [59], simply referred to as the "Kataura plot". In this plot, carbon nanotubes are arranged in branches reflecting both, quantum confinement effects and trigonal warping [59]. The strong dependence of optical transition energies on the chiral indices n_1 and n_2 and the diameter is discussed in Chapter 6 where we show a theoretical Kataura plot extended by optical transition energies up to the highest possible value.

2.3.2 Optical matrix elements in carbon nanotubes

Ensemble carbon nanotube samples contain a large variety of different carbon nanotubes. These samples can be seen as a mixture of disjunct material systems that can individually be probed by different optical excitation energies, as previously discussed. However, their optical responses do not only depend on the optical excitation energy but also on their coupling to optical light fields. We will see that the coupling strengths depend on the chiral indices n_1 and n_2 and the particular optical transition probed by a certain excitation energy. This is of great importance for the understanding of the optical responses of ensemble samples as discussed in detail in Chapter 6. Only when each carbon nanotube in an ensemble with its unique electronic properties is considered in the simulations, we are able to understand the complex optical responses. We will therefore discuss the optical matrix elements in carbon nanotubes on the next pages.

Following Ref. [61], the z-component of optical matrix elements as a function of the chiral index (n_1, n_2), band index m, and the wave vector along the $\mathbf{k}_z$ axis in a tight-binding approximation are given by:

$$\mathcal{M}_{e-r}^{n_1,n_2}(m,\mathbf{k}_z) = \frac{1}{2\sqrt{N}\,|e(k)|}\Big[(n_1-n_2)\cos\Psi_3 - (2n_1+n_2)\cos\Psi_1 + (n_1+2n_2)\cos\Psi_2\Big] \tag{2.12}$$

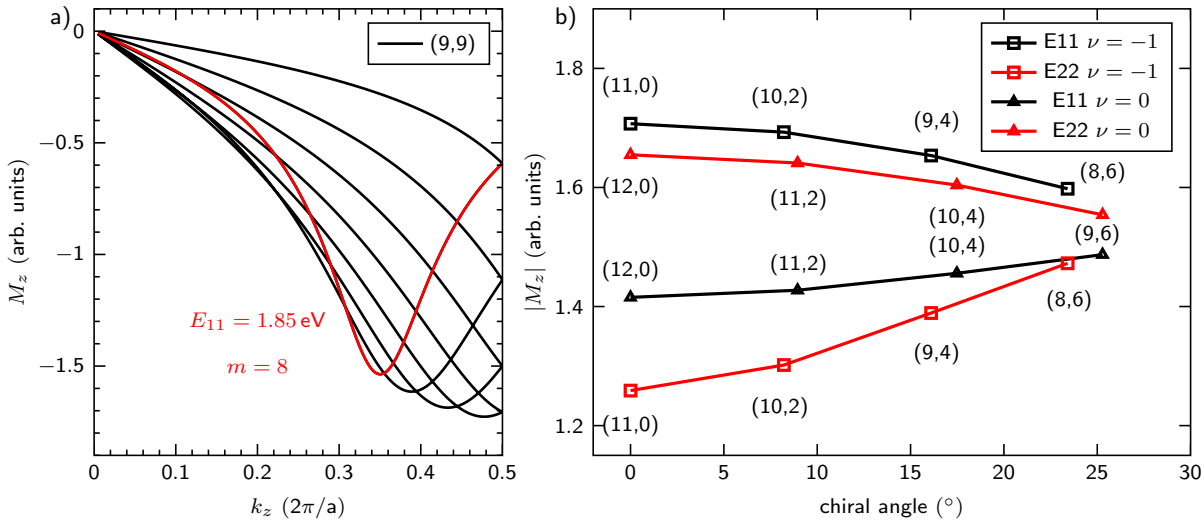

Figure 2.6: a) Calculated optical matrix elements of a (9,9) carbon nanotube tube as a function of the electron wavevector are plotted. Different curves correspond to different electronic subbands of a (9,9) tube. Highlighted in red is the band responsible for the optical matrix element of the lowest optical transition with the band index $m = 8$. b) Calculated optical matrix elements of various carbon nanotubes belonging to the $\nu = 0$ and $\nu = -1$ families are plotted as a function of the chiral angle θ. All carbon nanotubes have comparable diameters. Matrix elements of the first (E_{11}, black) and second (E_{22}, red) optical transition are plotted, respectively. The matrix elements are obtained with a next-nearest neighbor tight-binding approximation [61].

with

$$\Psi_1 = \pi m \frac{2n_1 + n_2}{N} - 2\pi \frac{n_2}{q} k_z \tag{2.13}$$

$$\Psi_2 = \pi m \frac{n_1 + 2n_2}{N} + 2\pi \frac{n_1}{q} k_z \tag{2.14}$$

$$\Psi_3 = \pi m \frac{n_1 - n_2}{N} - 2\pi \frac{n_1 + n_2}{q} k_z. \tag{2.15}$$

$|e(k)|$ describes the energy of an optical transition as a function of the chiral index (n_1, n_2) and the band index m. It is determined via:

$$|e(k)| = \sqrt{3 + 2\cos\Psi_1 + 2\cos\Psi_2 + 2\cos\Psi_3}. \tag{2.16}$$

The chiral indices n_1 and n_2 determine the values for N and q according to the following expressions:

$$N = n_1^2 + n_1 n_2 + n_2^2 \qquad \text{and} \qquad q = \frac{2N}{n\mathcal{R}}, \tag{2.17}$$

where $\mathcal{R} = 3$ if $(n_1 - n_2)/3n$ is integer and $\mathcal{R} = 1$ otherwise. n is the greatest common divisor of n_1 and n_2. Only light is considered that is polarized along the tube axis, *i.e.* only transitions between electronic states with $\Delta m = 0$ are allowed [61].

The so obtained optical matrix elements are plotted in Fig. 2.6. We show in a) the electronic matrix elements of an armchair (9,9) tube as a function of the band index m and the electron wavevector $\mathbf{k}_z$. Highlighted in red are the matrix elements for the optical

transition with the band index $m = 8$. The concrete electron wavevector responsible for the optical matrix element of the E_{11} transition is determined via the bandgap of the respective electron and hole bands [61]. This approach can be used to compare the optical matrix elements of different carbon nanotubes with almost similar diameters of $\sim 9\,\text{Å}$ as shown in Fig. 2.6 b). Keeping the diameter constant, enables the direct analysis of the trigonal warping effect as the distance to the closest K points is almost similar for all nanotubes within one family. The largest optical matrix elements are found for the E_{11}, $\nu = -1$ and E_{22}, $\nu = 0$ transitions accompanied by a decreasing coupling strength for larger chiral angles θ. Those are the optical transitions that mainly stem from the proximity of the high-symmetry $K - M$ direction in graphene (compare Fig. 2.5). A larger chiral angle moves the linear cutting lines away from the $K - M$ high-symmetry line, accompanied by a decrease of oscillator strength of the respective optical transitions [45,62]. In contrast, the lowest optical matrix elements are found for the E_{22}, $\nu = -1$ and E_{11}, $\nu = 0$ transitions, increasing for increasing chiral angles θ. Those mainly stem from the $K - \Gamma$ high symmetry line in graphene and increase the more their direction is moved to the $K - M$ high-symmetry line. Although not plotted in Fig. 2.6, it can generally be said that optical matrix elements for tubes belonging to the $\nu = -1$ family are larger than those from tubes belonging to the $\nu = +1$ family. Depending on the optical transition, metallic carbon nanotubes have larger/smaller optical matrix elements than those from the ± 1 tubes [61] (compare Fig. 2.6).

The unlike couplings to optical light fields affect the Raman experiments performed within this dissertation. Optical experiments alone are not able to display the correct distribution of chiralities within an ensemble. The Raman experiments predominantly cover "inner" optical transitions, *i.e.* those transitions that predominantly stem from the proximity of the $K - M$ high-symmetry direction. This fact has far-reaching consequences for the understanding of double-resonant Raman features in carbon nanotubes that are widely discussed in Chapter 6. We also show calculated optical matrix elements for deep-UV transitions *i.e.* E_{55}, E_{66}, E_{77}, ... transitions to understand the optical responses of carbon nanotubes in that spectral region.

2.4 Structure and fundamental properties of diamondoids

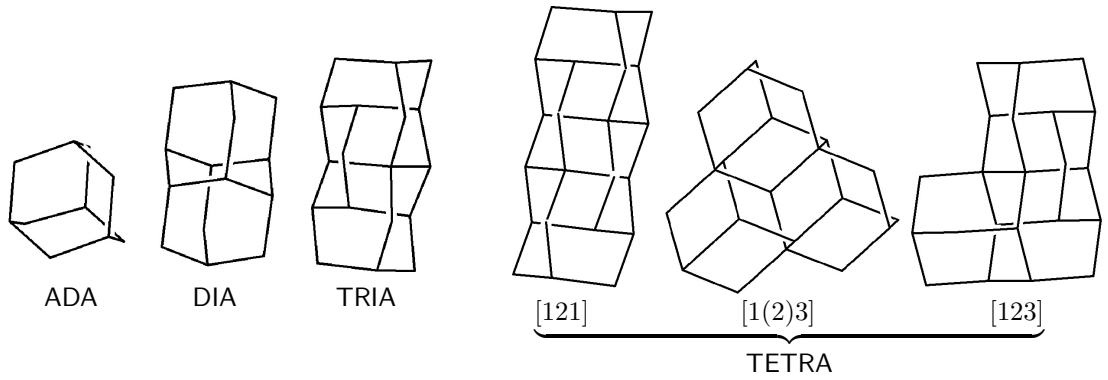

Figure 2.7: Lower diamondoids are pictured, with increasing size from left to right. ADA, DIA, TRIA, and TETRA stand for adamantane, diamantane, triamantane, and tetramantane, respectively. Numbers in brackets denote the nomenclature for isomers of one species after Balaban and Schleyer [63].

In contrast to the trigonal carbon structure present in graphene and carbon nanotubes, the sp^3 hybridization defines the tetrahedron-like arrangement of the carbon bonds in diamondoids [28]. Each bond exhibits a bond angle of 109.5 ° to its three neighbors. The smallest possible formation of a closed carbon cage in which every carbon atom exhibits a triangular pyramid bond structure consists of 10 carbon atoms and is named adamantane [64]. It can be seen as a cage-shaped cutout of the diamond lattice [19]. The remaining dangling bonds are either saturated with one or two hydrogen atoms, depending on the position of the carbon atom within the cage [19]. Its empirical formula is therefore $C_{10}H_{16}$. By adding another diamond crystal lattice cage to adamantane, a larger carbon molecule can be prepared that still conserves the tetrahedron diamond lattice structure. This procedure can be repeated over again, resulting in the formation of the homologous series of diamondoids [19]. Depending on the amount of containing face-fused cages, the lower diamondoids are named adamantane (one cage), diamantane (two cages), triamantane (three cages), tetramantane (four cages), and so on. Selected diamondoids are shown in Fig. 2.7. In the case of diamantane and triamantane, the direction in which the additional diamond cages are attached to adamantane does not change their structures. However, already for tetramantane, there are three different ways to attach a diamond carbon cage to triamantane, as depicted in Fig. 2.7. The amount of possible isomers drastically increases for higher diamondoids [19]. To distinguish between different isomers, Balaban and Schleyer suggested a nomenclature in which Arabian numbers determine the direction new carbon cages are added starting from adamantane [63].
Bond lengths of the C-C and C-H bonds have values of 1.54 Å and 1.112 Å, respectively. As a consequence, the diameter of an adamantane molecule exhibits ~ 5 Å. All diamond molecules smaller than 1 nm are named lower diamondoids, for diameters between ~ 1 and 2 nm they are named higher diamondoids, and large molecules with diameters from ~ 2 nm to μm are named nanodiamonds.

The availability of homogeneous species has made diamondoids to an object of broad

scientific interest. Their gradually increasing size for instance allows for a step-by-step analysis of quantum confinement effects. Interestingly, it was shown that the unoccupied states in diamondoids do not exhibit a size-dependent blueshift as known for other group IV semiconductors [20]. Their optical absorptions however are partly determined by quantum confinement effects, leading to size-dependent band gaps of $\sim 5.8\,\text{eV}$ (Pentamantanes) up to $\sim 6.6\,\text{eV}$ in adamantane [32, 65]. For comparison, the indirect wide-bandgap semiconductor diamond has an optical gap of $5.47\,\text{eV}$ [66]. It was found that the highest occupied states are referred to C-C σ states, spatially limited to the insides of the carbon cages, whereas the lowest unoccupied states are rather diffuse C-H σ^* states surrounding the diamondoids [32, 65, 67]. The diameter of their average distribution is several times larger than the confined C-C σ states and thus quantum confinement predominantly effects the occupied electronic states. Due to their distinct symmetries, not all vertical, optical transitions are dipole allowed [65]. For this reason, their optical responses are determined by quantum confinement, superimposed by optical selection rules. For instance, the HOMO (A_{1g}) $\rightarrow$ LUMO (A_{1g}) transition is symmetry-forbidden in diamantane [65]. The first allowed transition HOMO (A_{1g}) $\rightarrow$ LUMO + 1 (A_{2u}) is $\sim 0.6\,\text{eV}$ higher and exceeds that of adamantane although the carbon cage has twice its size [65].

Vörös *et al.* theoretically demonstrated that the substitution of the hydrogen passivisation with high-electronegativity atoms induce both, a charge transfer and symmetry braking, significantly reducing the lowest optical transitions in diamondoids [68]. In case of adamantane four sulfur atoms are necessary to redshift its optical gap to the visible range whereas in [1(2,3)4] pentamantane, already one sulfur atom suffices for the same downshift [68]. An experimental verification however is still absent. Downshifts of optical transition energies for other functional groups, such as -SH, -NH_2, and -OH groups are instead reported experimentally, but do not exceed energies lower than $1\,\text{eV}$ [69, 70]. Combining diamondoids to diamondoid oligomers with an introduction of sp^2 defects constitutes another way to alter the electronic properties of diamondoids [22, 71–73]. The fundamentally different structure of the double-bond related electronic states that lie in between those from the σ and σ^* in pristine diamondoids lead to fundamentally different optical responses that are in detail discussed in Chapter 4.

The vibrational properties of pristine diamondoids up to [121321] heptamantane are widely understood both experimentally and theoretically [30, 65, 74, 75]. Their distinct symmetries were used for a profound group-theoretic analysis with a great accordance to experimental Raman spectra [30, 74]. However, functionalizations significantly lower their symmetries and therefore alter the allowed vibrational modes of chemically modified diamondoids [72, 73, 76]. We will give a detailed introduction and analysis of the changes induced by sp^2 defects in diamondoid oligomers in Chapter 4.

3. Experimental methods

This chapter discusses inelastic light scattering in graphitic materials. We will introduce first-order Raman scattering in molecules and periodic solid state bodies. In graphitic materials, additional Raman features beyond the first-order scattering can be observed. They are characterized by considerable phonon wave vectors involved in the higher-order scattering process. This process, also named double resonant Raman scattering, is discussed in detail. In the end, we show the experimental setup and shortly discuss the second harmonic generation of light.

3.1 First-order Raman scattering - Raman spectroscopy

A small fraction of light that interacts with matter can be inelastically scattered, caused by atomistic vibrations in the material. In solid state bodies, these collective vibrations are referred to as phonons. They can be seen as vibrations in which the entire lattice is involved. This leads to the appearance of distinct phonon band structures in which the energy of a lattice vibration depends on the wavelength of the collective atom displacements. Instead, the lack of periodicity in molecules preludes the appearance of phonons with an arbitrary wavelength. From a solid state physics point of view, phonons in molecules always originate from the Γ point, *i.e.* they are atomic vibrations with no phonon wavevector involved.

The periodic, atomic vibrations affect the electric susceptibility of the analyzed material system. This in turn allows for an access to the vibrational properties of materials via optical spectroscopy methods. These spectroscopy methods with their large variabilities on the one hand and the striking sensitivities of current spectrometers on the other hand, can be utilized to map even smallest changes in optical responses. This also and, in particular, counts for changes induced by atomic displacements.
Inelastic scattering involving atomic vibrations was the first time experimentally observed by Raman 1928 [77]. Back then, it was called "A new type of Secondary Radiation" and was theoretically predicted even several years earlier by Smekal [78]. In honor of its discoverer, inelastic light scattering is today usually associated with the Raman effect. Although the effect is referred to as light scattering with phonons, it is on a microscopic level, rather the interaction of charge density coupling to light. To understand the Raman effect within a classical description, we assume an incoming light field:

$$\mathbf{E}(\mathbf{r}, t) = \mathbf{E}_i(\mathbf{k}_i, \omega_i) \cos\left(\mathbf{k}_i \mathbf{r} - \omega_i t\right) \tag{3.1}$$

An incoming electromagnetic wave with a wavevector $\mathbf{k}_i$ and frequency ω_i induce a polarization within the interacting material:

$$\mathbf{P}(\mathbf{r},t) = \mathbf{P}_i(\mathbf{k}_i,\omega_i)\cos\left(\mathbf{k}_i\mathbf{r} - \omega_i t\right) \tag{3.2}$$

The induced polarization $\mathbf{P}(\mathbf{r},t)$ as a function of the driving light field is a material specific physical quantity, also referred to as the electric susceptibility χ:

$$\mathbf{P}_i(\mathbf{k}_i,\omega_i) = \chi(\mathbf{k}_i,\omega_i)E_i(\mathbf{k}_i,\omega_i) \tag{3.3}$$

The susceptibility χ in turn slightly varies as a function of periodic atomic displacements, such as phonons in a lattice. In the following the displacements of the atoms are described by normal coordinates $\mathbf{Q}_k$:

$$\mathbf{Q}_k(\mathbf{r},t) = \mathbf{Q}_k(\mathbf{q},\omega_0)\cos\left(\mathbf{q}\mathbf{r} - \omega_0 t\right), \tag{3.4}$$

where ω_0 describes the frequency of a lattice vibration that belongs to the eigenvector. The susceptibility χ can further be expanded in a Taylor series depending on the normal coordinates of a lattice vibration:

$$\chi(\mathbf{k}_i,\omega_i,\mathbf{Q}_{k,m}) = \chi_0(\mathbf{k}_i,\omega_i) + \sum_k \left(\frac{\partial\chi}{\partial\mathbf{Q}_k}\right)_0 \mathbf{Q}_k(\mathbf{r},t) + \sum_{k,m}\left(\frac{\partial^2\chi}{\partial\mathbf{Q}_k\partial\mathbf{Q}_m}\right)_0 \mathbf{Q}_k(\mathbf{r},t)\mathbf{Q}_m(\mathbf{r},t) + \ldots \tag{3.5}$$

where the sums run over all normal coordinates. The first term χ_0 describes the susceptibility without distortions from atomistic displacements. In the second term, an atomic displacement along the normal coordinate $\mathbf{Q}_k$ is considered, defining the first-order expansion term. Further, higher-order terms can be considered in order to describe atomic displacements along more than one normal coordinate.
Inserting the nonlinear susceptibility [Eq. (3.5)] into the general expression for the polarization as given in Eq. (3.3) yields:

$$\mathbf{P}(\mathbf{r},t,\mathbf{Q}) = \mathbf{P}_0(\mathbf{r},t) + \mathbf{P}_{\mathrm{ind}}(\mathbf{r},t,\mathbf{Q}) \tag{3.6}$$

$\mathbf{P}_0$ describes the undistorted polarizability. For reasons of simplification, $\mathbf{P}_\mathrm{i}$ only considers the first order of the nonlinear susceptibility:

$$\mathbf{P}_{\mathrm{ind}}(\mathbf{r},t,\omega_0) = \left(\frac{\partial\chi}{\partial\mathbf{Q}_k}\right)_0 \mathbf{Q}_k(\mathbf{r},t)E_i(\mathbf{k}_i,\omega_i)\cos\left(\mathbf{k}_i\mathbf{r} - \omega_i t\right) \tag{3.7}$$

$$= \left(\frac{\partial\chi}{\partial\mathbf{Q}_k}\right)_0 \mathbf{Q}_k(\mathbf{q},\omega_0)\cos\left(\mathbf{q}\mathbf{r} - \omega_0 t\right)E_i(\mathbf{k}_i,\omega_i)\cos\left(\mathbf{k}_i\mathbf{r} - \omega_i t\right). \tag{3.8}$$

The product of two cosine functions in Eq. (3.8) can be rewritten using addition theorems via:

$$\mathbf{P}_{\mathrm{ind}}(\mathbf{r},t,\omega_0) = \frac{1}{2}\left(\frac{\partial\chi}{\partial\mathbf{Q}_k}\right)_0 \mathbf{Q}_k(\mathbf{r},t)E_i(\mathbf{k}_i,\omega_i) \cdot \left[\cos\left((\mathbf{k}_i+\mathbf{q})\mathbf{r} - (\omega_i+\omega_0)t + \cos\left((\mathbf{k}_i-\mathbf{q})\mathbf{r} - (\omega_i-\omega_0)t\right)\right]. \tag{3.9}$$

Three components of the induced polarizability can be distinguished that specify the measurable optical response. The first term $\mathbf{P}_0$ only depends on the frequency ω_i of the driving

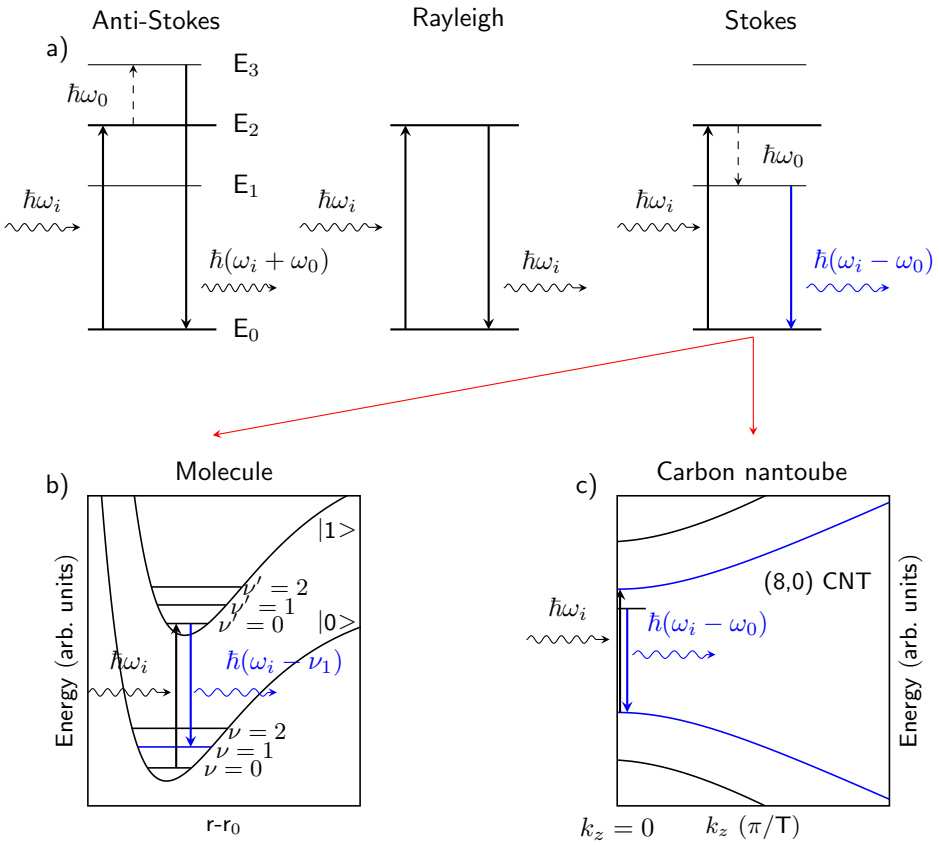

Figure 3.1: a) Anti-stokes, Rayleigh, and Stokes scattering are schematically plotted. The energy of the incoming photon is $\hbar\omega_i$; the phonon energy is denoted by ω_0. E_0 denotes an electronic ground state, $E_{1,2,3}$ are excited states. b) Stokes scattering is illustrated for a resonant excitation in a molecule. $|0>$ and $|1>$ are Morse potentials exemplary for the ground and the first excited electronic state of a simple molecule [79]. ν and ν' are vibrational states within the electronic ground and excited state, respectively. c) Resonant Stokes scattering is illustrated for a (8,0) zig-zag carbon nanotube (CNT).

light field. This elastically scattered light is usually referred to as Rayleigh scattering. $\mathbf{P}_{\text{ind}}$ contains two components in which the frequency of the scattered light is shifted by the phonon energy ω_0. In case there is a constructive interaction $(\omega_i + \omega_0)$, the Raman scattering is referred to as Anti-Stokes Raman scattering, in case there is a destructive interaction $(\omega_i - \omega_0)$, the Raman scattering is referred to as Stokes scattering.

As can be seen in the expression for the induced polarizability $\mathbf{P}_{\text{ind}}$ in Eq. (3.9), the nonlinear susceptibility contains its derivative after the normal coordinates of an atomic vibration. As a consequence, only those vibrations contribute to a Raman signal, that change the polarizability. The second derivative can be seen as a higher-order process in which two phonons are involved. They can either correspond to the same atomic vibration or can correspond to different atomic vibrations as generally described in Eq. (3.5).

A schematic overview of resonant Raman and Rayleigh scattering is given in Fig. 3.1 a). The excitation occurs from an electronic ground state E_0 to an excited state E_2. A more detailed view on a resonant Stokes Raman process in a molecule and in a (8,0) carbon nanotube is shown in Fig. 3.1 b) and c). Both ground and excited electronic states in molecules exhibit a vibronic fine structure as denoted with ν and ν' in Fig. 3.1. In

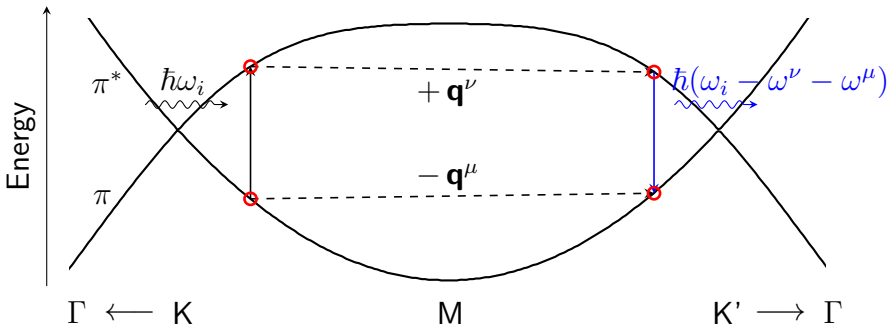

Figure 3.2: A representation of a second-order, two-phonon Raman scattering process in graphene is illustrated. The scattering occurs along the $\Gamma - K - M - K' - \Gamma$ high-symmetry direction. As both the K and the K' points are involved, the scattering process is also named an intervalley Raman process. The involved phonon energies are ω^ν and ω^μ with the momentum $\mathbf{q}$, respectively. Illustrated is a process in which both electrons and holes are scattered.

diatomic molecules, the electronic states are Morse potentials [79] that get much more complex in larger molecules [80]. The energy spacing of vibronic states in excited electronic states (ν' in Fig. 3.1) is usually smaller as the nuclei separation is larger in the excited states accompanied by reduced restoring forces for the atomic vibrations [80]. This fact is of great importance as we measure shifted bond lengths via the analysis of altered Raman frequencies in Chapter 4 [81]. Only the momenta of the incoming and outgoing light are involved in such a process. The small momentum difference due to the resonant scattering is transferred to the nuclei of the molecule.

The conservation of momentum during a first-order Raman process in carbon nanotubes requires that both the excited electron and remaining hole do not change their momentum. In case of a (8,0) tube, the absorption and emission therefore both occur at $\mathbf{k}_z = 0$ as depicted in Fig. 3.1. Only for reasons of visibility, the emission arrow (blue) is slightly shifted.
All Raman measurements performed within this dissertation are Stokes processes, *i.e.* we always measure reduced energies of the re-emitted photons.

3.2 Double-resonant Raman scattering

The Raman signature of graphitic sp^2 carbons contains several high-frequency modes exhibiting energies way above those from individual lattice vibrations. Intriguingly, some of these modes even show anomalous shifts as a function of the laser excitation energy that cannot be explained only by first-order Raman scattering. First observations of the unusual shift rate of a certain Raman peak were done by Tuinstra *et al.* [82]. It was related to defects in the graphite lattice which is why this mode is today named the defect mode, or simply the D mode [82, 83]. The exact origin of this peak however was unclear for a long time until Thomsen and Reich gave a conclusive explanation [9]. They suggested the concept of double-resonant Raman scattering that explained the D mode on the one hand but was also capable to explain various high-frequency peaks in the Raman spectrum of graphite on the other hand [9,45,53]. It was further successfully applied to other graphitic sp^2 materials, such as graphene, multilayer graphene, and carbon nanotubes [45, 53].

Double-resonant Raman scattering is a second-order process in which either two phonons or one phonon and one defect are involved. In quantum mechanics the lattice vibrations (phonons) can be treated as a perturbation of the light-matter interaction [53]. This fourth-order perturbational approach yields an expression in which the scattered photon rates depend on the square of a detuned Lorentzian oscillator [9, 14, 45, 53]. Following authors in Ref. [14] the two phonon Raman cross section in graphene can be written as:

$$
\begin{aligned}
&I^{\mu\nu}_{\mathbf{q}}(\epsilon_L,\gamma) \propto \\
&\Bigg| \sum_{\mathbf{k},e,h,\ldots} \frac{\langle \mathbf{k}\pi|D_{out}|\mathbf{k}\pi^*\rangle \langle \mathbf{k}\pi|\Delta H_{-\mathbf{q},\mu}|\mathbf{k}+\mathbf{q},\pi^*\rangle \langle \mathbf{k}+\mathbf{q},\pi^*|\Delta H_{\mathbf{q},\nu}|\mathbf{k}\pi^*\rangle \langle \mathbf{k}\pi^*|D_{in}|\mathbf{k}\pi\rangle}{(\epsilon_L-\epsilon^{\pi^*}_{\mathbf{k}}+\epsilon^{\pi}_{\mathbf{k}}-\hbar\omega^{\nu}_{-\mathbf{q}}-\hbar\omega^{\mu}_{\mathbf{q}}-i\frac{\gamma^C_{\mathbf{k}}}{2})(\epsilon_L-\epsilon^{\pi^*}_{\mathbf{k}+\mathbf{q}}+\epsilon^{\pi}_{\mathbf{k}}-\hbar\omega^{\nu}_{-\mathbf{q}}-i\frac{\gamma^B_{\mathbf{k}}}{2})(\epsilon_L-\epsilon^{\pi^*}_{\mathbf{k}}+\epsilon^{\pi}_{\mathbf{k}}-i\frac{\gamma^A_{\mathbf{k}}}{2})} \\
&- \sum_{\mathbf{k},e,h,\ldots} \frac{\langle \mathbf{k}+\mathbf{q}\pi|D_{out}|\mathbf{k}+\mathbf{q}\pi^*\rangle \langle \mathbf{k}\pi|\Delta H_{-\mathbf{q},\mu}|\mathbf{k}+\mathbf{q},\pi\rangle \langle \mathbf{k}+\mathbf{q},\pi^*|\Delta H_{\mathbf{q},\nu}|\mathbf{k}\pi^*\rangle \langle \mathbf{k}\pi^*|D_{in}|\mathbf{k}\pi\rangle}{(\epsilon_L-\epsilon^{\pi^*}_{\mathbf{k}+\mathbf{q}}+\epsilon^{\pi}_{\mathbf{k}+\mathbf{q}}-\hbar\omega^{\nu}_{-\mathbf{q}}-\hbar\omega^{\mu}_{\mathbf{q}}-i\frac{\gamma^C_{\mathbf{k}}}{2})(\epsilon_L-\epsilon^{\pi^*}_{\mathbf{k}+\mathbf{q}}+\epsilon^{\pi}_{\mathbf{k}}-\hbar\omega^{\nu}_{-\mathbf{q}}-i\frac{\gamma^B_{\mathbf{k}}}{2})(\epsilon_L-\epsilon^{\pi^*}_{\mathbf{k}}+\epsilon^{\pi}_{\mathbf{k}}-i\frac{\gamma^A_{\mathbf{k}}}{2})} \\
&+\cdots\Bigg|^2 . \qquad (3.10)
\end{aligned}
$$

ω^{μ} and ω^{ν} denote different phonon energies with respect to their momentum $\mathbf{q}$. All electron and hole states in $\mathbf{k}$ space are summed up for each individual phonon momentum $\mathbf{q}$. The first term considers electron-electron scattering where an electron is first scattered by the $-\mathbf{q}\nu$ phonon and then backscattered by the $\mathbf{q}\mu$ phonon. The same can occur both to electrons and holes as considered in the second term: The electron is scattered by the $-\mathbf{q}\nu$ phonon with a consecutive backscattering of the hole by the $\mathbf{q}\mu$ phonon [14]. Involved in the complex scattering process can either be just electrons, just holes, or both electrons and holes. Further, the succession of involved phonons in each individual scattering process can vary allowing for overall eight different scattering processes [14]. ϵ^{π^*} and ϵ^{π} denote the energy of the electrons in the valence bands and holes in the conduction band, respectively. The broadening γ can be seen as the inverse lifetime of individual electronic states involved and explicitly depends on the electron wavevector $\mathbf{k}$, but is often considered to be constant. The optical matrix elements ($\langle \mathbf{k}(\pm\mathbf{q})\pi|D_{out}|\mathbf{k}(\pm\mathbf{q})\pi^*\rangle$ and $\langle \mathbf{k}\pi^*|D_{in}|\mathbf{k}\pi\rangle$) describe the coupling strength to optical light fields. Electron-phonon coupling elements are expressed via $\langle \mathbf{k}\pm\mathbf{q}\pi|\Delta H_{\pm\mathbf{q},\mu,\nu}|\mathbf{k}\pm\mathbf{q}\pi^*\rangle$. Both can be found in Ref. [14].

A large Raman cross section is achieved when one of the denominators gets very small. This happens when two or more of the intermediate electronic states within this higher order process are real states. In this case, the particular Raman mode is resonantly enhanced and exceeds those with other phonon momenta involved by magnitudes [9, 14]. For this reason, this process is often referred to as a double-resonance, or even to a triple resonance process.

In contrast to first-order Raman scattering, double-resonant Raman scattering can involve phonons with an arbitrary momentum. The conservation of momentum in a double resonance Raman process is preserved, when two phonons with likewise momenta, but

with opposite signs contribute:

$$\hbar\mathbf{k}_s = \hbar\mathbf{k}_i + \hbar(\pm\,\mathbf{q}_1^{\nu,\mu} \mp \mathbf{q}_2^{\nu,\mu}) \tag{3.12}$$

The requirement of the conservation of momentum $\mathbf{k}_s \approx \mathbf{k}_i$ automatically implies the following relation for the phonons involved: $|\mathbf{q}_1| \approx |\mathbf{q}_2|$. As a consequence, zone-center phonons with very small momenta, as well as zone-boundary phonons with the largest momenta possible can possibly contribute to the Raman spectrum. This fact is of particular interest to understand the density-of-states related Raman spectra as discussed in Chapter 5.

The second-order Raman process as described in Eq. (3.10) can be divided into four steps as illustrated in Fig. 3.2. (*i*) At first, an electron/hole pair with momentum $\mathbf{k}$ is created in the π/π^* bands. (*ii*) The excited electron is scattered into a different electronic state with momentum $\mathbf{k}+\mathbf{q}$. (*iii*) The same occurs to the hole that is scattered to an electronic state with momentum $\mathbf{k}-\mathbf{q}$. (*iv*) In the end, electron and hole recombine by emitting a photon with a reduced energy $\hbar\omega_s = \hbar(\omega_i - \omega^\nu - \omega^\mu)$ [14]. The process illustrated in Fig. 3.2 is called an intervalley process as two distinguishable K and K' points are involved. Scattering can also occur within one Dirac cone; it is then referred to as intravalley scattering [14].

The introduced concept of double-resonant scattering could finally explain the shift rates of Raman modes in graphitic sp^2 materials. A certain laser excitation energy determines the electron momentum and therefore the $\mathbf{k}$-space distance to another real electronic state. As phonons mediate between these two unlike electronic states, their momentum necessarily needs to be different for different laser excitation energies in a second-order Raman process. Depending on the phonon dispersion, the phonon energies involved in such a process are therefore different for each individual laser excitation energy.

We show calculated Raman spectra of low-intensity Raman modes in carbon nanotubes in Chapter 6. They are modeled via the transition matrix $\mathcal{T}_{fi}[\mathbf{q}]$ with $I \propto |\mathcal{T}_{fi}[\mathbf{q}]|^2$, equivalent to the fourth-order perturbational approach as shown in Eq. (3.10) [84]. Different to Eq. (3.10), electron, holes, and phonon bands for each individual tube are altered according to the zone-folding constraints as introduced in section 2.3.1.

3.2.1 Characteristic Raman spectra of graphite, graphene, carbon nanotubes, and diamantane

Raman spectra of carbon nanotubes, graphite, graphene, and diamantane for an excitation energy of $\varepsilon_\mathrm{L} = 2.73\,\mathrm{eV}$ are plotted in Fig. 3.3. All modes in diamantane, the radial-breathing mode (RBM), and the G mode are first-order Raman scattering processes. The other modes can be referred to second-order Raman modes. The G mode is the most pronounced peak in the Raman spectra of graphite, graphene, and carbon nanotubes. It is referred to a C=C stretch vibration and is characteristic for all graphitic carbons. This mode can already be observed, if only two double bond sp^2 hybridized carbon atoms are present in the analyte. The D, and $2D$ modes are breathing modes of entire sp^2

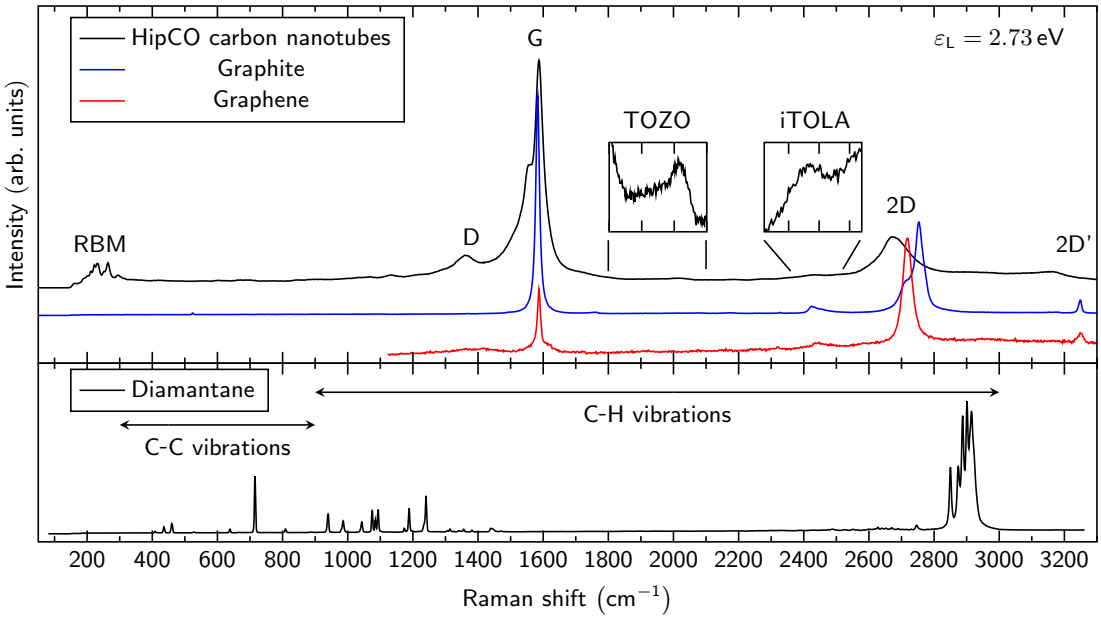

Figure 3.3: Raman spectra of HipCO-produced carbon nanotubes, graphite, graphene (top), and diamantane (bottom) are plotted for an excitation energy $\varepsilon_L = 2.73\,eV$. Characteristic modes for carbon nanotubes and graphite are indicated. The TOZO and iTOLA modes are discussed in detail in Chapter 6. Characteristic modes in diamantane are generally assigned by the atom species involved. A detailed analysis can be seen in Chapter 4. RBM stands for radial-breathing modes. All diamantane modes, the RBM, and the G mode are first-order Raman processes, the D, $2D$, $2D'$, TOZO, and iTOLA modes are double-resonant, second order Raman modes.

hybridized carbon hexagons [82]. In case of the D mode, its intensity depends on the defect density and therefore, it is often referred to as the defect mode [14,82,85]. The low-intensity, double-resonant Raman modes TOZO (transverse optical, out-of-plane optical) and iTOLA (in-plane transverse optical, longitudinal acoustic) are in detail discussed in Chapter 6. The structure-induced altering of vibrational properties of carbon nanotubes, leads to generally more complex Raman spectra. For instance, curvature effects lift the degeneracy of the two-fold degenerate E_{2g} mode in graphene, leading to various G modes in their Raman spectra (compare Fig. 3.3). Raman modes in diamantane are generally assigned by the species of atoms involved in the vibrations (C: carbon, H: hydrogen). Because of lower masses, the high-frequency modes are usually attributed to the C-H vibrations. A closer analysis of the vibrational properties in diamondoids and diamondoid derivatives is given in Chapter 4.

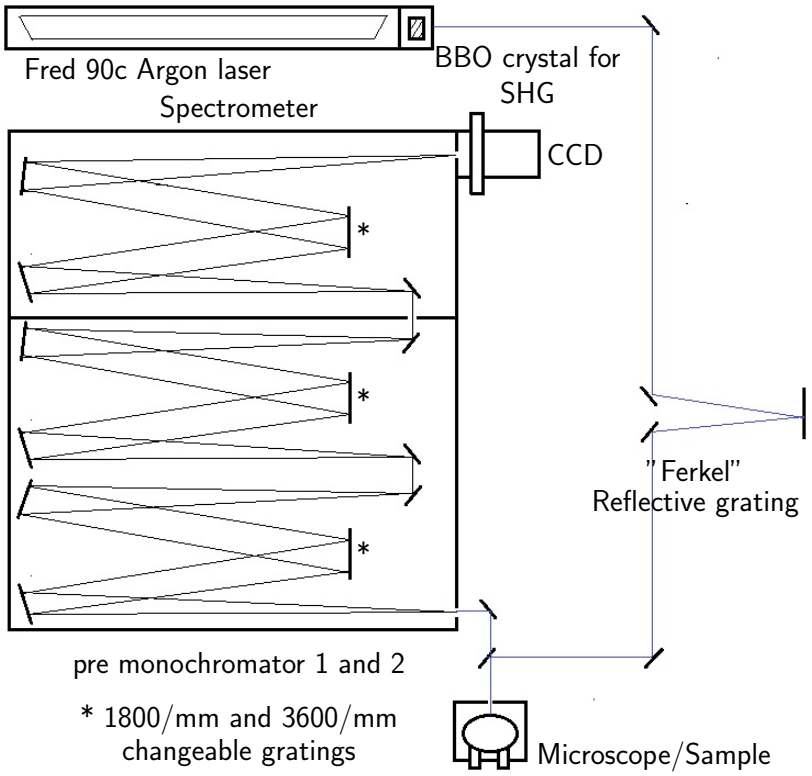

Figure 3.4: The experimental Raman setup is schematically plotted. Key optical elements are named. SHG and CCD stand for second harmonic generation and charge-coupled device, respectively.

3.3 Experimental setup

The key requirement for an experimental Raman setup is the suppression of the elastically scattered light of the exciting laser. This can be achieved via a notch filter, or via the application of pre monochromators. The latter has the advantage of flexibility, *i.e.* it can continuously be adjusted according to the laser wavelength. In our case, we have used a HORIBA T64000 triple monochromator that has two pre monochromators and a final spectrometer. The pre monochromators are coupled in a subtractive configuration, very efficiently suppressing these parts of the spectrum that are not required. The final resolution of the scattered light is carried out in the spectrometer.
For all measurements in the UV range, we have used a Coherent 90c Fred Argon ion laser supporting frequency doubling. We could use all fundamental wavelengths from 454.4 nm up to 528.7 nm with the possibility of frequency doubling of each individual line. Different BBO (beta-Barium borate) crystals were available exhibiting different cutting angles to achieve phase matching for each laser line [86]. The so covered photon energies range from 4.69 eV up to 5.46 eV.
All measurements with UV excitation energies have been done with the HORIBA T64000 as schematically plotted in Fig. 3.4. To achieve resolutions up to 1.5 cm^{-1}, we could change the 1800/mm to a 3600/mm grating in the ultraviolet region. The final signal was collected by a Symphony Cryogenic Back Illuminated UV sensitive CCD Detector. The incident UV light beam was focused by a Thorlabs LMU-40X-UVB CaF_2 objective, providing spot sizes up to 1 μm in diameter in the applied UV range. Raman measurements in the optical visible region have been performed with a LABRAM HR800 spectrometer. In contrast

to the T64000 spectrometer, it has a notch filter providing better signal-to-noise ratios but lacking the possibility to use variable light sources. All measurements have been performed in a backscattering geometry.

3.3.1 Second harmonic generation

One of the key features that is discussed in this dissertation is the ultraviolet optical response of graphitic materials. Although there is much progress in the field of compact UV laser LEDs, continuous-wave, narrow-bandwidth, and high-intensity light sources for wavelengths down to 200 nm are still not commercially available. A convenient and well established workaround for the generation of deep-UV radiation is the second harmonic generation (SHG) utilizing the fact that laser light sources in the desired visible range ($\sim 450 - 600\,\mathrm{nm}$) are very well available.
The already introduced polarization $\mathbf{P}$ can be expanded as follows [86, 87]:

$$\mathbf{P} = \epsilon_0 \sum_n \chi^{(n)} \mathbf{E}^n = \epsilon_0 \chi^{(1)} \mathbf{E}^1 + \epsilon_0 \chi^{(2)} \mathbf{E}^2 + \dots \tag{3.13}$$

$\chi^{(1)}$ denotes the linear susceptibility, χ^2 is the second-order term. In general, even higher order contributions can be important for nonlinear optic effects, such as the Kerr-nonlinearity [88] ($\chi^{(3)}$ effect). However, the relevant second harmonic generation is a $\chi^{(2)}$ process that is forbidden in systems with an inversion symmetry [86]. For strong light fields, the absorption of photons leads to excitations that are above their locally parabolic potentials. This in turn can activate additional restoring forces responsible for higher-order terms in the electric susceptibility [86].
Again, the light can be seen an oscillating wave:

$$E(t) = E_0 \sin(\omega t) \tag{3.14}$$

resulting in the second-order polarization:

$$\left|\mathbf{P}^2\right| = \epsilon_0 \chi^{(2)} E^2 = \epsilon_0 E_0^2 \chi^{(2)} \sin^2(\omega t) = \frac{\epsilon_0 E_0^2 \chi^{(2)}}{2} \cdot \left(\frac{1 - \cos(2\omega t)}{2}\right). \tag{3.15}$$

It can be seen that Eq. (3.15) contains two contributions: a constant term and a second term that explicitly depends on the doubled frequency 2ω responsible for the higher-order radiation.
The secondary radiation can only be emitted if all oscillators from an excited medium interact constructively [86]. This can solely be achieved when both the fundamental and the second harmonic light beam have the same refractive indices, although their wavelengths are different: $n_\omega \sim n_{2\omega}$. Therefore, nonlinear crystals are used for second harmonic generation that have different refractive indices both for the ordinary and extraordinary light beams. For instance, the refractive indices of the utilized BBO crystals for the ordinary and extraordinary rays are $n_o = 1.679$ (488 nm) and $n_e = 1.632$ (244 nm), respectively [89].

4. Diamondoid derivatives

Parts of this section are published in Refs. [81] and [73]

This chapter discusses the electronic and vibrational properties of functionalized diamondoids. Especially in the focus are diamondoid derivatives consisting of two or more lower diamondoids that are covalently connected. Analyzed are various structures: On the one hand chemically blended sp^2/sp^3 hydrocarbons are discussed in which diamondoids are connected by carbon double bonds. The carbon double bonds are either attached directly to the diamondoids or they are between two carbon atoms forming small chains connecting the oligomers. On the other hand, various diamondoid dimers are analyzed that are connected by single carbon bonds. In contrast to the double-bond oligomers, they are fully saturated hydrocarbons with fundamentally other electronic properties. Further, a graphene/adamantane composite, namely [2](1,3)Adamantano[2](2,7)pyrenophane is analyzed. It can be seen as a bridge between a fully saturated diamondoid and a fully unsaturated graphene flake with interesting properties merged from both constituents.

The nearly unlimited availability of carbon and the variety of its allotropes make carbon even in the 21^{th} century to an object of a broad scientific interest. Recent developments in the functionalization of diamondoids seem to offer a whole new path for carbon derivatives to find their way in applications. The essential requirement however is a deep understanding of the electronic and vibrational changes that are accompanied by the modification of their structures. It may be even more important to first understand the self-caused altering of electronic properties as diamondoids tend to form very stable van-der-Waals crystals with unusually high binding energies. The periodic arrangement in a crystal lattice leads to electronic and vibrational properties different from those in isolated molecules or in solutions diamondoids are available otherwise. For this reason, we also discuss the electronic properties of several diamondoid van-der-Waals crystals and report newly observed collective vibrational modes that are referred to librations in diamondoids van-der-Waals crystals.

4.1 Double-bond diamondoid oligomers - vibrational properties

An interesting way to tailor properties of diamondoids is the introduction of unsaturated bridges between neighboring sp^3 cage units [22]. These bridges can be seen as surface sp^2 defects and lead, due to their fundamentally different nature of the chemical bond, to widespread changes of their electronic and vibrational structure. Recently, a large

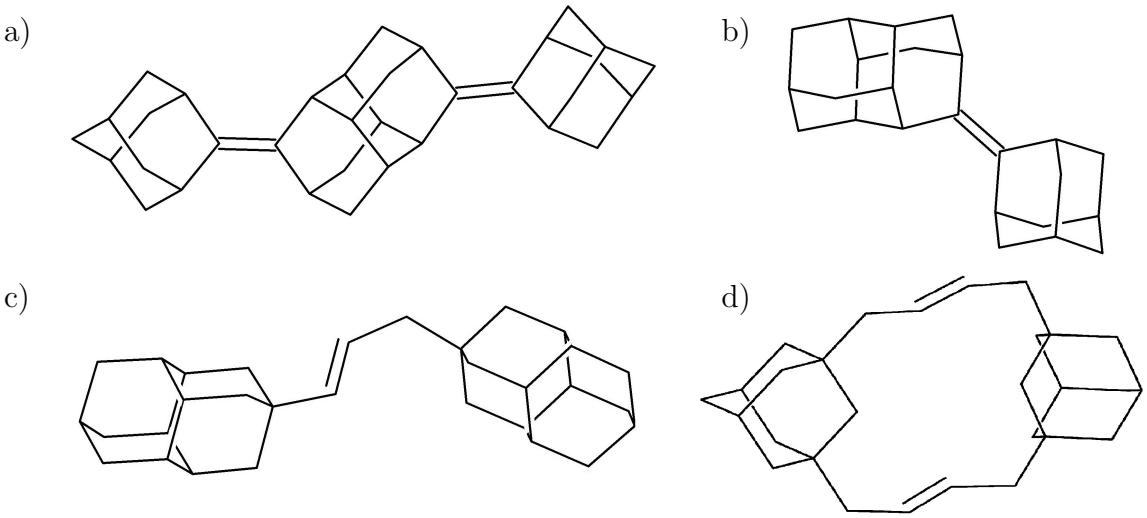

Figure 4.1: The analyzed sp^2/sp^3 hybrid diamondoid oligomers are plotted. They are namely: a) 3,10-bis-(2-adamantylidene)diamantane, b) 3-(2-adamantylidene)diamantane, c) 1,3-(bis-4-diamantyl)prop-1-ene, and d) [4.4](1,3)adamantanophan-*trans,trans*-1,8-diene. For reasons of simplicity, the hydrogen atoms are not plotted.

variety of diamondoid oligomers have been synthesized [22]. They consist of lower diamondoids, such as adamantane or diamantane and are connected either directly with a double bond or via carbon chains containing the C=C double bond. Simplified structures of the molecules are plotted in Fig. 4.1.
Another group of available cagelike hydrocarbons are the Pentacycloundecanes (Trishomocubanes) [90]. One isomer, namely the Pentacyclo[$6.3.0.0^{2,4}.0^{3,10},0^{5,9}$] is the only structure without three- or four-membered rings or other strain-inducing components [90]. It was therefore also used to fabricate sp^2/sp^3dimers [91] comparable to those with diamondoid constituents and is closer analyzed in section 1.4.1 and Refs. [72, 92].

The introduction of sp^2 defects as a connection between lower diamondoids results in a far-reaching change of their vibrational properties. On the one hand, the diamondoid oligomers exhibit lower symmetries compared to their constituents (T_d for adamantane or D_{3d} for diamantane [30]). This should generally result in much more complex Raman spectra in terms of the pure amount of visible Raman modes. On the other hand, we expect new, characteristic Raman modes that originate from the specific structure of the diamondoid derivatives.
A possible perspective to approach the vibrational properties of the diamondoid oligomers is the linear combination of distinctive, characteristic vibrational modes of their constituents. The sp^2/sp^3 blended oligomers can be seen as a combination of pristine adamantane/diamantane and ethylene, located between the diamondoids. Therefore, we expect characteristic Raman modes from both ethylene and adamantane/diamantane in the Raman spectra of the oligomers. For instance, reasonable are breathing-like modes that are already known for diamondoids [30] or other carbon sp^2 systems such as carbon nanotubes [93], or Fullerenes [94].
Adamantane has 72 vibrational modes, $11T_2+7T_1+6E+1A_2+5A_1$ of which the T_1 and A_2 are not Raman active, leaving 22 possible Raman modes [30]. In contrast, diamantane has 96 vibrational modes, $11A_{1g}+6A_{1u}+5A_{2g}+10A_{2u}+16E_g+16E_u$. In this case only the A_{1g}

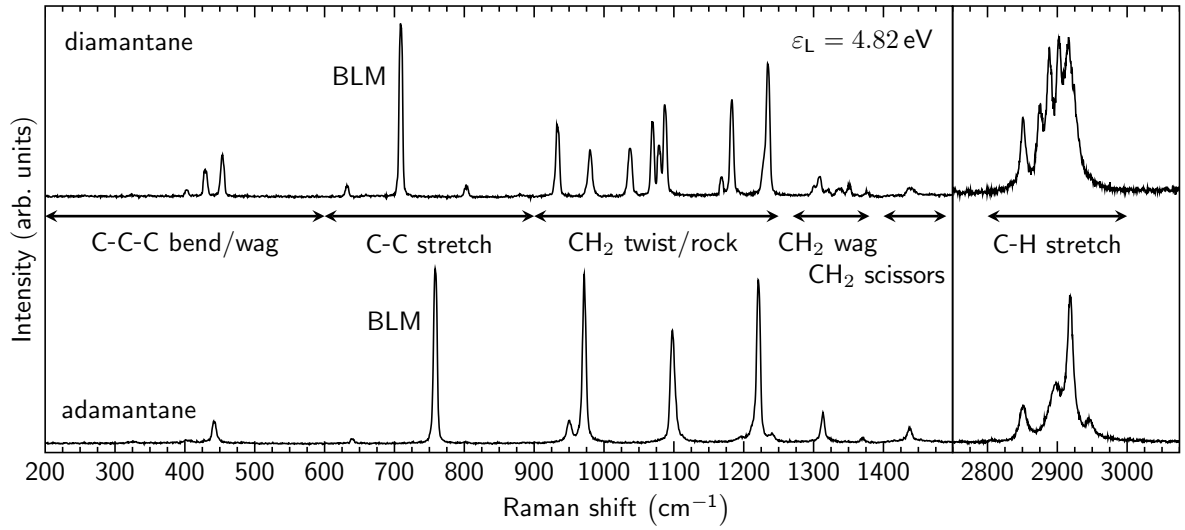

Figure 4.2: Raman spectra of diamantane (top) and adamantane (bottom) for an excitation energy of 4.82 eV are given. Characteristic modes and their frequency ranges are indicated. BLM stands for breathing-like mode.

and E_g species are Raman active, resulting in 27 possible Raman modes in the spectrum of diamantane [30]. Not all Raman-active modes are intense enough to be observed in an experiment, explaining the lower amounts of modes in Fig. 4.2. Ethylene has the point group D_{2h} and 12 vibrational modes: $3A_g+2B_{2g}+2B_{1u}+2B_{3u}+B_{3g}+A_u+B_{2u}$ of which the A_g, B_{2g}, and B_{3g} species are Raman active, resulting in six possible Raman modes [95]. The spectrum of diamondoids can be divided into characteristic vibrations as denoted in Fig. 4.2. They can be separated by carbon-carbon vibrations, namely C-C-C bend/wag and C-C stretch modes and carbon-hydrogen vibrations such as CH_2 twist/rock, CH_2 wag, or CH_2 scissor modes [30,74]. The latter generally have higher frequencies due to the lower masses involved in the vibrations. A species-characteristic mode is the breathing-like mode "BLM", found at around $\nu \sim 600 - 700\,cm^{-1}$ as indicated in Fig. 4.2. In lower unfunctionalized diamondoids, it is a fully symmetric vibration whose frequency increases with a decreasing size and vice versa [30]. Its determination is therefore useful to characterize diamondoid species in an unknown sample. The functionalized diamondoid oligomers exhibit lower symmetries than their constituents: The lowest symmetry has the 1,3-(bis-4-diamantyl)prop-1-ene dimer with the C_1 point group. [4.4](1,3)adamantanophan-*trans,trans*-1,8-diene has C_2 symmetry, 3,10-bis-(2-adamantylidene)diamantane has C_{2h} symmetry, and 3-(2-adamantylidene)diamantane exhibits C_S symmetry.

By comparison to DFT computations we can separate the Raman modes into three classifications: (*i*) Raman modes from the unfunctionalized diamondoids, (*ii*) Raman modes from ethylene, and (*iii*) Raman modes from the relative movements of the entire monomers within the compounds. Further, compounds in which the double bond is directly attached to the monomers ([4.4](1,3)adamantanophan-*trans,trans*-1,8-diene and 3-(2-adamantylidene)diamantane) are separated from those where the double bond is connected to a carbon atom that does not belong to a diamondoid cage. The additional carbon atom enlarges the vibrational degree of freedom of the ethylene centers, leading to several highly localized Raman modes that are equivalent to those of pristine ethylene.

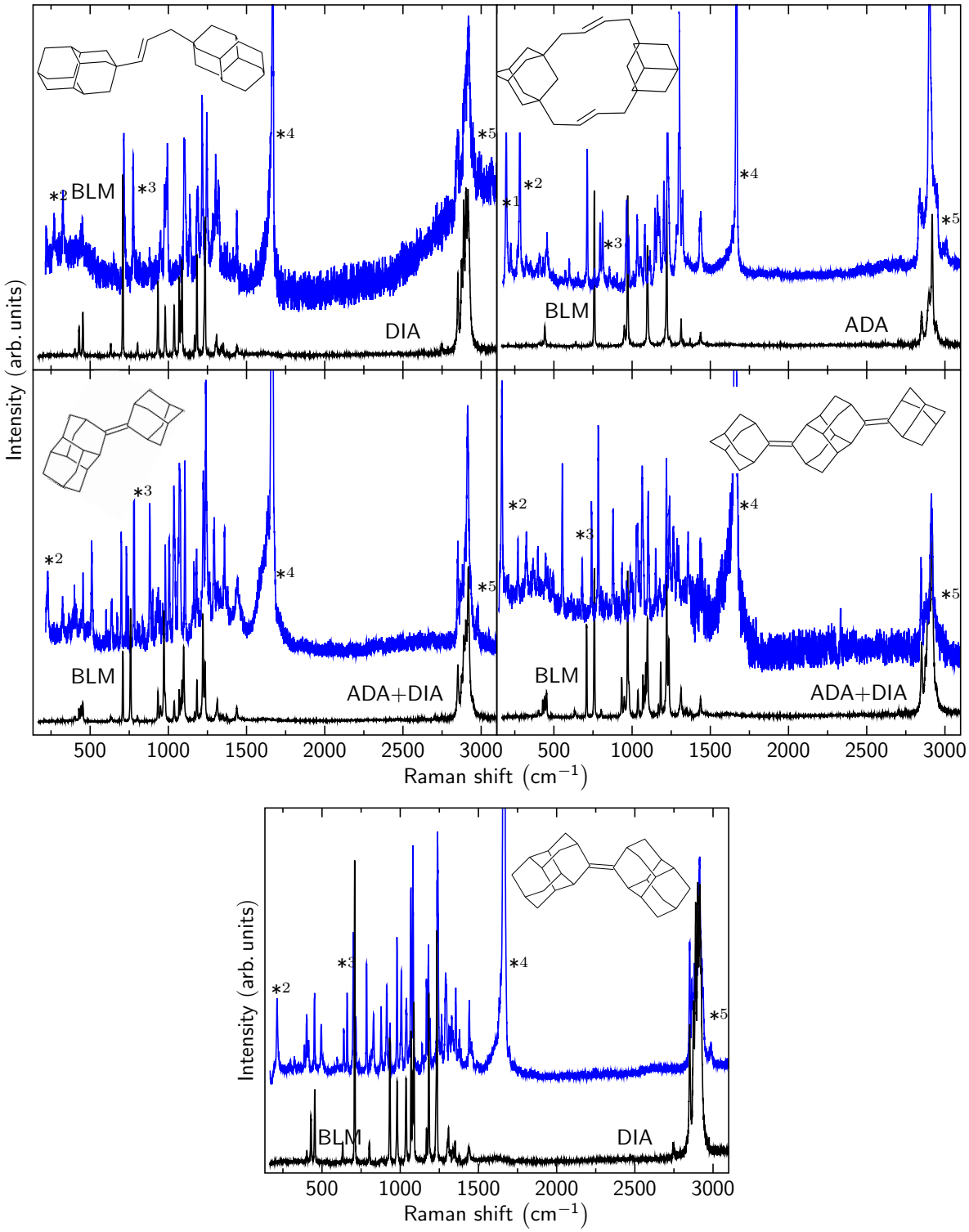

Figure 4.3: Raman spectra of diamondoid oligomers (blue) compared to unfunctionalized diamondoids (black) for an excitation energy of $\varepsilon_{\mathrm{L}} = 4.82\,\mathrm{eV}$ are given. In case the oligomers consist of different diamondoids, the sum of the constituents is given. Characteristic modes are labeled with asterisks and are summarized in Table 4.1. BLM, ADA and DIA stand for breathing-like mode, adamantane, and diamantane, respectively.

The reduced symmetries cause a lift of degenerated vibrational modes that can be seen in Fig. 4.3, where a comparison of Raman spectra from the analyzed diamondoid oligomers and unfunctionalized adamantane and diamantane is shown. In case the oligomers have two different constituents, the sum of their single contributions is given. All Raman spectra of the chemically blended oligomers show additional modes in the region of the carbon-carbon bend/wag, stretch and CH_2 twist/rock, wag modes that mainly originate from degenerated vibrational modes in the unfunctionalized constituents. Also, new carbon-carbon bend/wag, stretch modes of carbon atoms in the chains connecting single constituents are found. The characteristic BLM is a carbon-carbon stretch vibration that is, except for the 1,3-(bis-4-diamantyl)prop-1-ene, downshifted compared to the unfunctionalized diamondoids due to the larger inertiae. However, a top (4-position) functionalization [as in the case of the 1,3-(bis-4-diamantyl)prop-1-ene] only marginally affects the BLM frequencies [76]. The 4-position carbon atoms are not deflected during an oscillation of the BLM and thus inductive effects of the attached molecules lead to a slight upshift of the BLM rather than a downshift due to the additional mass attached [76].

The compounds generally exhibit all vibrational modes that are known from the unfunctionalized diamondoids [30, 74]. Frequencies of C-C-C bend/wag/stretch modes reach from $\sim 150-900\,\mathrm{cm}^{-1}$ and thus, compared to $\sim 300-900\,\mathrm{cm}^{-1}$ in pristine diamondoids, a larger region of frequencies is covered. This mainly accounts for the low-frequency region due to the generally larger inertia involved. CH_2 scissor modes around $1440\,\mathrm{cm}^{-1}$ are highly localized vibrations at the cage edges and are not affected by a functionalization. Both in the pristine and functionalized diamondoids, they exhibit the same frequencies (compare Fig. 4.3). The same accounts for the carbon-hydrogen stretch vibrations found at around $2900\,\mathrm{cm}^{-1}$. As in the unfunctionalized diamondoids, they can be separated into symmetric contributions (around $2850\,\mathrm{cm}^{-1}$) and anti-symmetric contributions (around $2915\,\mathrm{cm}^{-1}$). However, for all oligomers, an additional carbon-hydrogen stretch mode is found $50\,\mathrm{cm}^{-1}$ above the highest anti-symmetric stretch vibration in pristine diamondoid (labeled with $*^5$ in Fig. 4.3). These modes are referred to highly localized vibrations close to the C=C bridges. The sp^2 defects cause a local stiffening slightly increasing the frequency of surrounding C-H modes.
We further observe new modes that are not found in pristine diamondoids: A C=C stretch mode ($*^4$ in Fig. 4.3), a C=C torsional mode ($*^3$ in Fig. 4.3), a C=C rotational mode ($*^1$ in Fig. 4.3), and a newly observed breathing-like mode ($*^2$ in Fig. 4.3) in which the containing diamondoids oscillate towards each other. We will refer to that mode as dimer-breathing mode (DBM) [73]. The C=C stretch and torsional modes originate from the ethylene moieties and have a direct equivalent in ethylene (D_{2h} point group): The symmetric A_g stretching mode ($\sim 1720\,\mathrm{cm}^{-1}$) and a hydrogen-carbon-hydrogen out-of-plane wagging mode (B_{2g}) around $954\,\mathrm{cm}^{-1}$. Both in the computations and measurements we find these vibrations at lower frequencies, around $1660\,\mathrm{cm}^{-1}$ and around $754\,\mathrm{cm}^{-1}$ for the stretching and torsional modes, respectively. The masses attached to the ethylene moieties lead to a decrease of their frequencies, compared to ethylene.

The ethylene rotational modes exhibit frequencies around $200\,\mathrm{cm}^{-1}$ both in the com-

Table 4.1: Overview of experimental and theoretical frequencies of characteristic Raman peaks from the double-bond diamondoid oligomers. In the upper part, we show Raman modes that all diamondoid compounds have in common and compare them to the corresponding vibrational modes of ethylene [95]. In the lower part we compare Raman modes of dimers in which the double bond is not directly attached to the diamondoid cage to the characteristic vibrational modes of ethylene. Modes marked with asterisks can be found in the Raman spectra in Fig. 4.3. We used a GGA approach with the PBE functional and a plain-wave basis set with pseudopotentials for the computations. Intermolecular, long-range interactions are accounted for through the DFT+D3(BJ) method. All frequencies are given in cm^{-1}. ADA and DIA stand for adamantane and diamantane, respectively. Computations have been done by Roland Gillen [96].

Sample	Mode type	exp.	calc.	Mode type	exp.	calc.
ADA-2×{CH_2-CH=CH-CH_2}-ADA	DBM $*^2$	285/-	281/138	BLM	712	689 / 705
DIA-CH=CH-CH_2-DIA	DBM $*^2$	177	168	BLM	715	705 / 711
ADA=DIA	DBM $*^2$	200	191	BLM	698 / 779	689 / 772
ADA=DIA=ADA	DBM $*^2$	171	162	BLM	683 / 785	731 / 772
Ethylene	B_{2g}	944		A_g	1621	
ADA-2×{CH_2-CH=CH-CH_2}-ADA	C=C bend/twist $*^3$	803	811	C=C stretch $*^4$	1666	1663
DIA-CH=CH-CH_2-DIA	C=C bend/twist $*^3$	773	812	C=C stretch $*^4$	1667	1664
ADA=DIA	C=C bend/twist $*^3$	731	725	C=C stretch $*^4$	1661	1653
ADA=DIA=ADA	C=C bend/twist $*^3$	743	725 /694	C=C stretch $*^4$	1660	1639
Ethylene	B_{3u}	952		B_{3g}	1234	
ADA-2×{CH_2-CH=CH-CH_2}-ADA		-	967		-	1303
DIA-CH=CH-CH_2-DIA		-	968		-	1261
ADA-2×{CH_2-CH=CH-CH_2}-ADA	ethylene rotation $*^1$	189	194			
DIA-CH=CH-CH_2-DIA	ethylene rotation $*^1$	231	236			

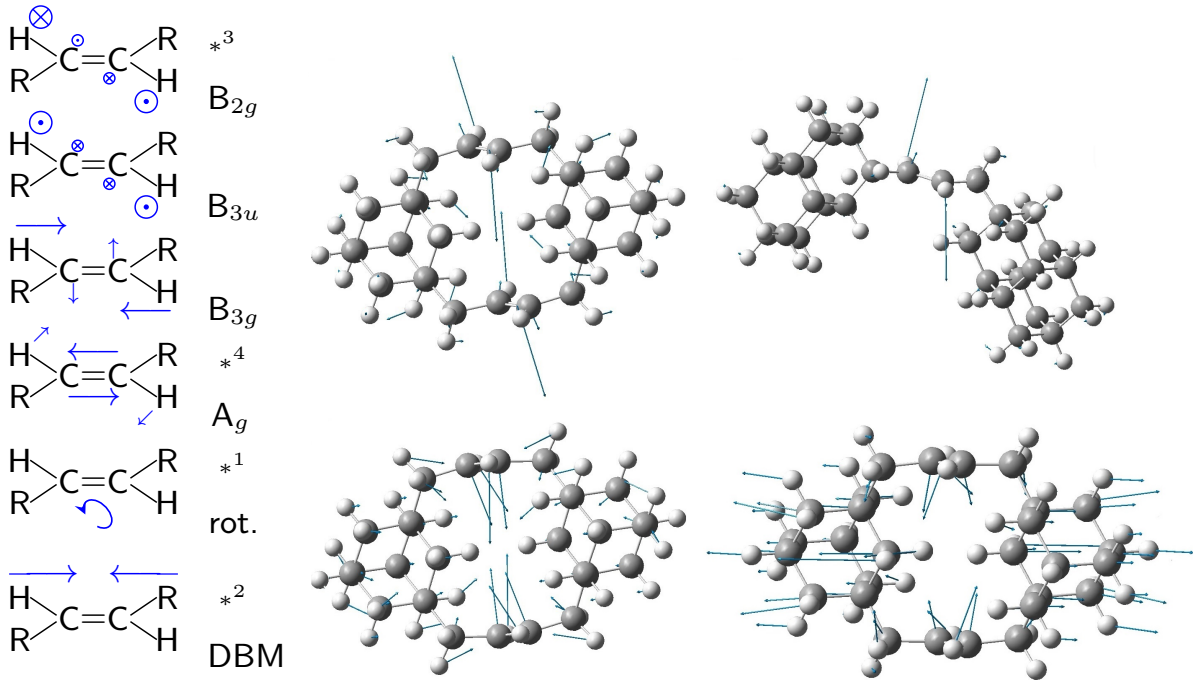

Figure 4.4: Left: Localized vibrational patterns of ethylene centers in two diamondoid dimers. R stands for diamantane [1,4-(bis-4-diamantyl)but-2-ene] or a carbon atom with an attached adamantane ([4.4](1,3)adamantanophan-*trans,trans*-1,8-diene). The irreducible representations of the equivalent vibrations in ethylene are given next to the simplified chemical structures. Corresponding frequencies of both ethylene and the diamondoid oligomers are summarized in Table 4.1. "rot." and "DBM" stand for (hindered) rotations of the entire ethylene centers and dimer breathing mode, respectively. Asterisks correspond to the modes in the Raman spectra of Fig. 4.3. Right: Several characteristic Eigenmodes (rot. and DBM) of two dimers are illustrated, taken from Ref. [73].

putations and measurements but only in the dimers where the carbon double bond is not directly attached to the diamondoid cages. It is a hindered rotation of entire ethylene moieties where the hydrogen atoms stay in the same plane as the carbon atoms. Since pure rotations are not Raman active, this rotational mode does not have an equivalent in pristine ethylene. The dimer-breathing modes are oligomer specific modes that can neither be found in ethylene nor in diamondoids. Their frequencies are around $200\,\mathrm{cm}^{-1}$ because of the comparably high masses of entire carbon cages. The ring-like structure [4.4](1,3)adamantanophan-*trans,trans*-1,8-diene has two BLMs with frequencies of $138\,\mathrm{cm}^{-1}$ and $285\,\mathrm{cm}^{-1}$ of which only the latter was experimentally accessible. The broad shoulder on the low-energy sides of the C=C peaks ($\sim 1660\,\mathrm{cm}^{-1}$ in Fig. 4.3) is attributed to amorphous carbon due to a sample degeneration under UV exposition [97]. An overview of some characteristic displacement vectors can be seen in Fig. 4.4.

In the computations, we have used experimentally obtained geometrical structures of the van-der-Waals crystals, as shown in Ref. [91]. It has been found, that depending on the diamondoid derivatives, the unit cell of the van-der-Waals crystals contain either two or four molecules. Therefore, in the computations, we find several similar C=C stretching/torsional modes and carbon-hydrogen stretching modes that are localized in different molecules within the unit cell of the van-der-Waals crystals. In case of the ring-like [4.4](1,3)adamantanophan-*trans,trans*-1,8-diene the modes are further split into intramolecular in-phase and out-of-phase vibrations. However, the separation is $\sim 1.5\,\mathrm{cm}^{-1}$

and should therefore not be resolvable in a standard experiment. Table 4.1, summarizes several characteristic sp^2/sp^3 diamondoid oligomer vibrational modes with their corresponding experimental and calculated Raman frequencies. All vibrations are compared to those of ethylene; the irreducible representations are given in Fig. 4.4 next to the patterns.

4.2 Double-bond diamondoid oligomers - electronic properties

The electronic structures of sp^2/sp^3 diamondoid oligomers are only marginally explored. By valence photoelectron spectroscopy in the gas phase, the highest occupied electronic states of various compound have been measured by Tobias Bischoff (birth name Zimmermann) *et al.* [98]. It was found that the ionization potential (IP) is much smaller compared to those of unfunctionalized diamondoids or single-bond diamondoids. Further, it was found that the ionization potential does not depend on the size of the dimers, but is rather fixed in a small energy region around 7.2 eV [98]. This stands in contrast to the experimentally explored IPs of unfunctionalized diamondoids that are determined by quantum confinement effects, *i.e.* the IP redshifts with increasing size of the diamondoids [98]. This even counts for the single-bond diamondoid dimers [98].

Optical transition energies of a trishomocubane dimer and a diamantane dimer in the solid phase have been explored by Reinhard Meinke *et al.* [72, 92]. Via the analysis of selectively enhanced Raman intensities of C=C stretch vibrations, it was found that the optical transition energies of both systems are ~ 1.5 eV downshifted, compared to their unfunctionalized counterparts. These findings agree well with theoretical predictions by Shiladitya Banerjee *et al.* [65,71], who computed optical absorption energies and resonance Raman spectra within a time-dependent correlation function approach. They find that the optical transitions in chemically blended diamondoid oligomers are downshifted by ~ 2 eV compared to their unfunctionalized counterparts [65,71]. The optical responses are generally determined by the $\pi \rightarrow \pi^*$ transitions with oscillator strengths of $f \sim 0.8$ and higher [65, 71]. In all computed oligomers, the HOMOs are the π orbitals, but in none of them the first excited state has a π^* character. They are always σ-like excited states with a diffuse localization towards the outer periphery of the molecules [65,71]. The consequential low overlap of HOMOs and LUMOs results in very low oscillator strengths $f \sim 0.004$ of the direct HOMO→LUMO transitions (compare Fig. 4.5) [65,71]. In the computations, the π^* orbitals are higher excited electronic states, namely the LUMO+2 in the *anti*-diamantane dimer (*anti*-diamantylidenediamantane), the LUMO+1 in the *syn*-diamantane dimer (*syn*-diamantylidenediamantane), or the LUMO+2 in the trishomocubane dimer [65, 81, 92]. These are clear predictions from theory and until now they have not been experimentally confirmed.

Various molecular orbitals of three different diamondoid oligomers are plotted in Figs. 4.5 and 4.6. The computations are done within the General-gradient approximation (GGA) using the PBE (Perdew-Burke-Ernzerhof) functional [99] implemented in Material studios 6.0. The π-like character of the highest occupied molecular orbitals can be clearly seen for

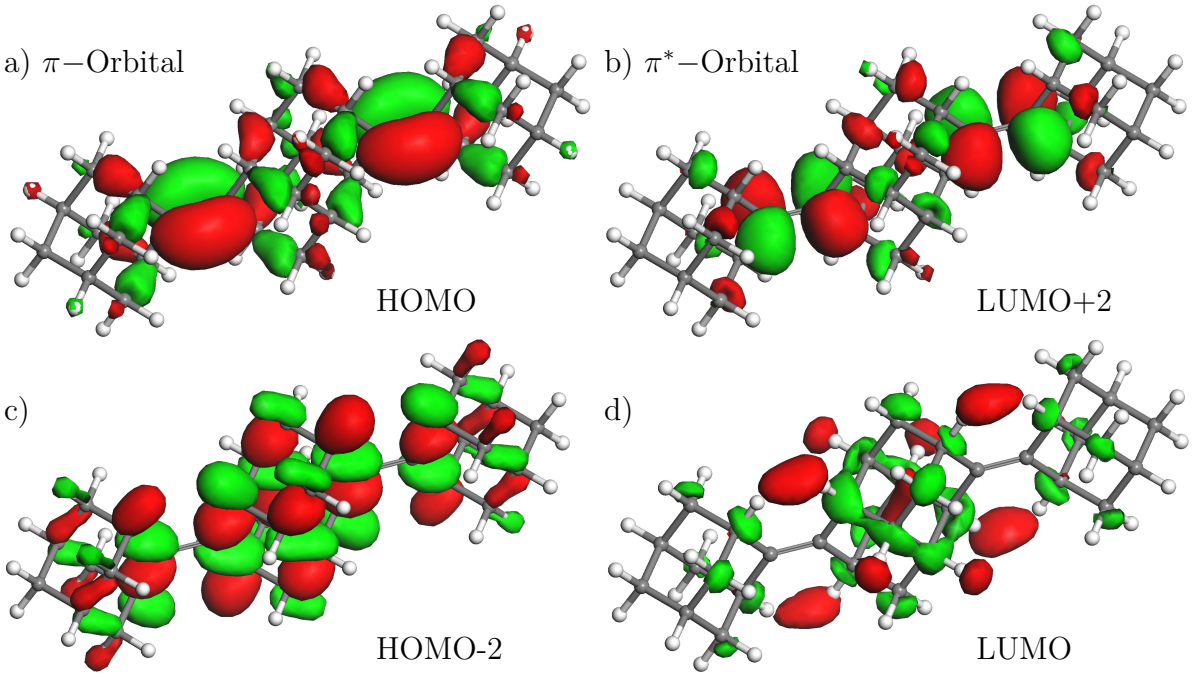

Figure 4.5: Equi-energy surfaces of the electron density from molecular orbitals are plotted. The diamondoid derivative is the 3,10-bis-(2-adamantylidene)diamantane trimer. Orbitals are named according to their energetic levels. π and π^* orbitals are labeled. Lobes corresponding to negative values of the electron wavefunctions are indicated in red, green lobes correspond to electron wavefunctions with positive values. DFT computations are done within a GGA approach using the PBE functional [99], implemented in Material studios 6.0.

all computed oligomers. Instead, the LUMO for the 3,10-bis-(2-adamantylidene)diamantane is rather diffuse and located at the C-H bonds of the diamantane centered in the middle of the molecule. Within the computational approach, the π^* orbitals are higher molecular orbitals, namely the LUMO+2 for 3,10-bis-(2-adamantylidene)diamantane, the LUMO+1 for 4.4](1,3)adamantanophan-*trans,trans*-1,8-diene, and the LUMO+2 for the 3-(bis-4-diamantyl)prop-1-ene.

The excited electronic states $S_{1,2,\ldots,n}$ of diamondoid oligomers generally exhibit other geometries than those of the electronic ground states S_0 because of different potential energy surfaces of each individual state [65, 71]. This behavior can be generally observed in molecules and was first extensively discussed in the publication "*Electronic Spectra and Electronic Structure of Polyatomic Molecules*" by Gerhard Herzberg [100]. The geometries of electronic states in the smallest molecule containing a double bond, namely ethylene, was analyzed to a large extent [101–103]. For instance, it was found that the electronic ground state exhibits D_{2h} symmetry whereas the geometry in the first excited state changes to a D_{2d} symmetry, accompanied by a torsion of neighboring hydrogen atoms and an elongation of the C=C double bond [101–103]. To a certain extent, the analyzed diamondoid oligomers can be understood as a combination of two diamondoids and ethylene forming the centers in all molecules. We therefore generally expect that electronic and vibrational properties of the ethylene moieties are transferred to the complex diamondoid molecules. And in fact, a comparable elongation of the C=C double bond in the excited π^* state was found in the diamondoid oligomers both experimentally and theoretically [71, 81]. The increase of bond length was found to exhibit ~ 0.1 Å in good

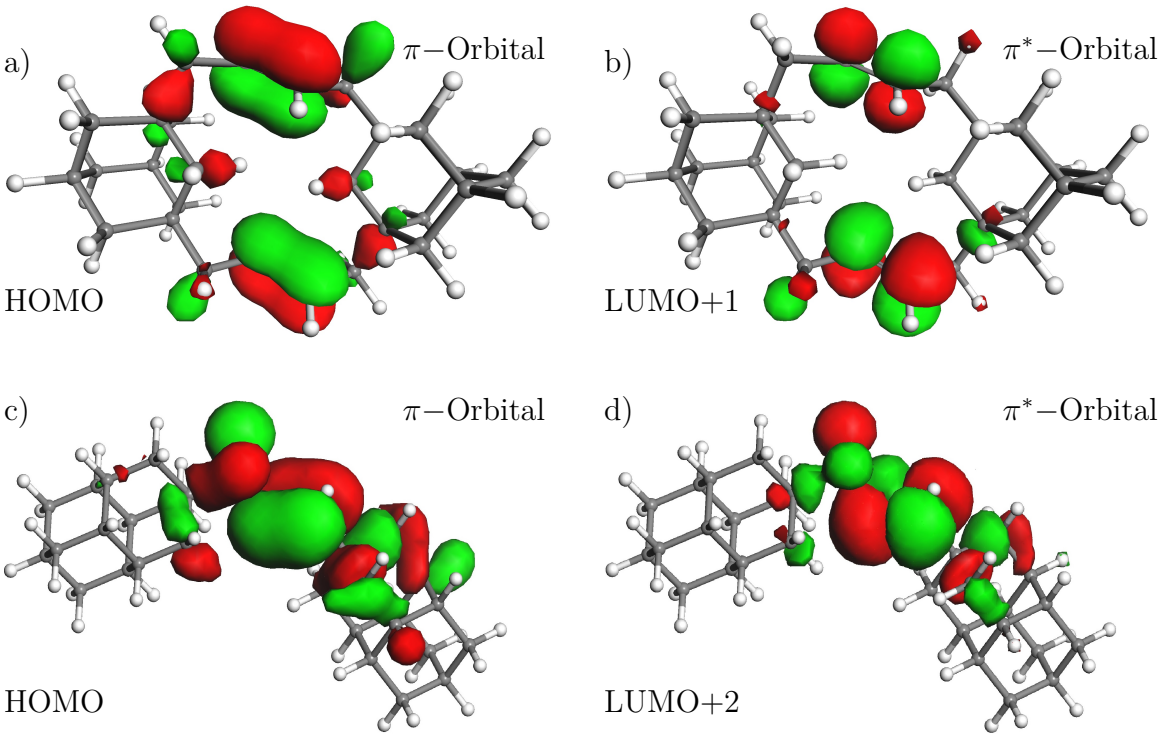

Figure 4.6: Equi-energy surfaces of electron density from π and π^* orbitals are plotted. They belong to the following dimers: [4.4](1,3)adamantanophan-*trans,trans*-1,8-diene dimer [a) and b)] and 1,3-(bis-4-diamantyl)prop-1-ene [c) and d)] dimer. Orbitals are named according to their energetic level. Lobes corresponding to negative values of the electron wavefunctions are indicated in red, green lobes correspond to electron wavefunctions with positive values. DFT computations are done within the GGA using the PBE functional [99] implemented in Material studios 6.0.

agreement to the computations [71, 81]. The main reason is the displaced electron density from the center to the periphery of the double bond in the corresponding excited state.

The geometry change of molecular orbitals in the excited state can be used experimentally to determine the $\pi \rightarrow \pi^*$ transition. Analyzing the Raman intensity of a certain vibrational mode in which the equilibrium conformation of the molecule is distorted along its normal coordinate, gives insights to the geometry of the molecule [97, 104]. The Raman intensity of a vibrational mode is resonantly enhanced when its change in geometry resembles the change in geometry of electronic states going from a ground to an excited state [65, 71, 97, 104]. For instance, ethylene has a twisted conformation in the excited state and therefore the C=C stretch vibration and a torsional oscillation are resonantly enhanced [104, 105]. As a consequence, a careful analysis of the Raman intensity of the C=C stretch vibration in diamondoid oligomers allows for an experimental access to the energy of the $\pi \rightarrow \pi^*$ transition. We have therefore performed resonant Raman measurements in which we have varied the laser excitation energy and analyze the intensity ratios of the C=C stretch vibrations to the breathing-like modes for each excitation energy. In the unfunctionalized diamondoids, the breathing-like modes have a fully symmetric character that is partly conserved in the diamondoid oligomers. Such a normalization reduces the systematic error occurring from the orientation of the molecules. Further, the breathing-like modes are not resonantly enhanced when resonantly probing the $\pi \rightarrow \pi^*$ transition [65, 71] and are therefore a suitable candidate for the normalization. This relative normalization has two advantages: It cancels out the different spectral sensitivities

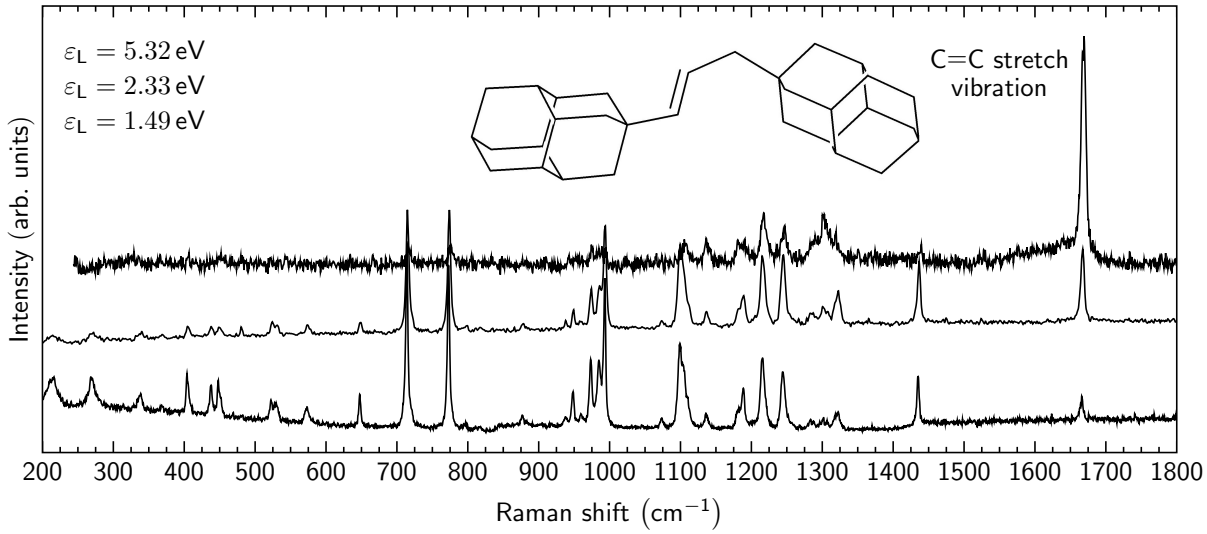

Figure 4.7: Raman spectra of 1,3-(bis-4-diamantyl)prop-1-ene for three different laser excitation energies are plotted. The characteristic C=C stretch vibration is indicated.

of the experimental setup and the systematic error due to sample degradation. All measured samples are not stable under UV irradiation causing a huge intensity drop of the Raman signal after exposure, making an absolute normalization via CaF_2 or diamond not feasible. However, this relative normalization contains the assumption that all Raman modes suffer from an equal intensity loss under UV irradiation. Further, we believe that the degradation does not influence our results as they were reproducible for all measured samples.

Fig. 4.7 shows Raman spectra of the 1,3-(bis-4-diamantyl)prop-1-ene dimer for three different excitation energies. A clear resonant enhancement of the characteristic C=C stretch vibration can be observed when tuning the laser excitation energy from the near infrared to the ultraviolet spectral range. In contrast, for lower excitation energies, all Raman active vibrational modes below the C=C stretch vibration, *i.e.* below $\sim$1660 cm^{-1} gain importance. It is therefore recommendable to choose very low laser excitation energies when only the characteristic Raman active vibrational modes of the sp^3 moieties within the blended diamondoid oligomers are of interest. This behavior corresponds well with computed Raman spectra of various sp^2/sp^3 diamondoid oligomer from Banerjee *et al.* [65, 71].
In Fig. 4.8 resonant ($\varepsilon_L = 4.82\,eV$) and non-resonant ($\varepsilon_L = 2.33\,eV$) Raman spectra of all measured sp^2/sp^3 diamondoid oligomers are plotted. Simplified structures of the oligomers are given as insets. For all samples, a clear enhancement of the intensities from C=C stretch vibrations can be observed when resonantly excited with $\varepsilon_L = 4.82\,eV$. Further, two other vibrational modes are resonantly enhanced: the C=C bend/twist modes and the dimer breathing modes DBM, as indicated in Fig. 4.8 d). In both cases, the vibrational patterns are accompanied by an elongation of the C=C double bond and are thus resonantly enhanced. However, the enhancement factor of these modes is significant but lower compared to that of the C=C stretch vibration since their eigenvectors only have a projection in the direction of the C=C double bond. Other modes, such as CH_2 twist and wag vibrations ($\sim 1100 - 1350\,cm^{-1}$) are also resonantly enhanced. In the

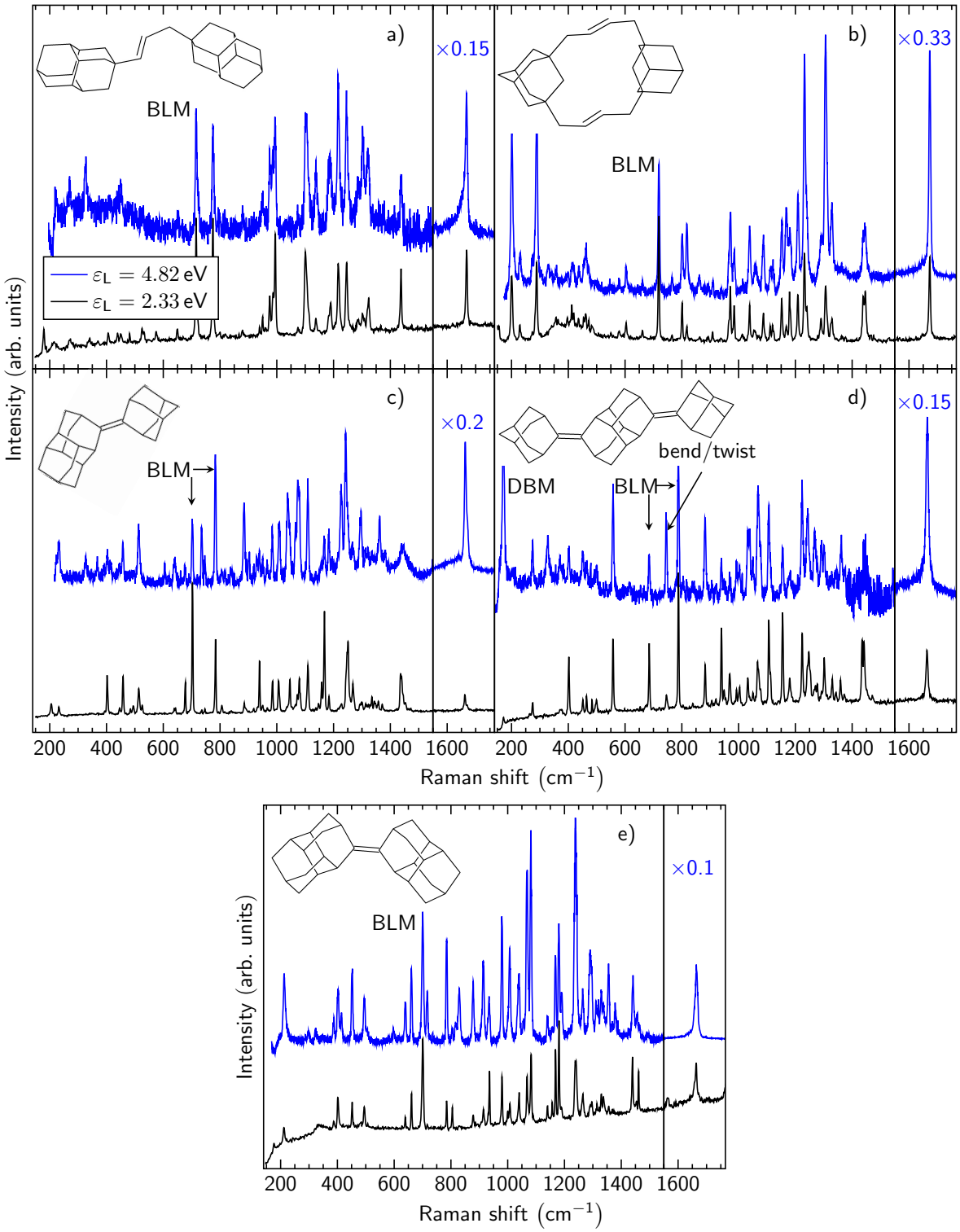

Figure 4.8: Raman spectra of 1,3-(bis-4-diamantyl)prop-1-ene [a)], [4.4](1,3)adamantanophan-*trans,trans*-1,8-diene [b)], 3-(2-adamantylidene)diamantane [c)], 3,10-bis-(2-adamantylidene)diamantane [d)], and *syn*-diamantylidenediamantane [e)] for two different laser excitation energies as given in the figure are plotted. BLM stands for breathing-like mode. The intensities of the C=C stretch mode for a laser excitation energy of $\varepsilon_L = 4.82\,eV$ are scaled for clarity. Simplified chemical structures of the diamondoid derivatives do not contain hydrogen atoms.

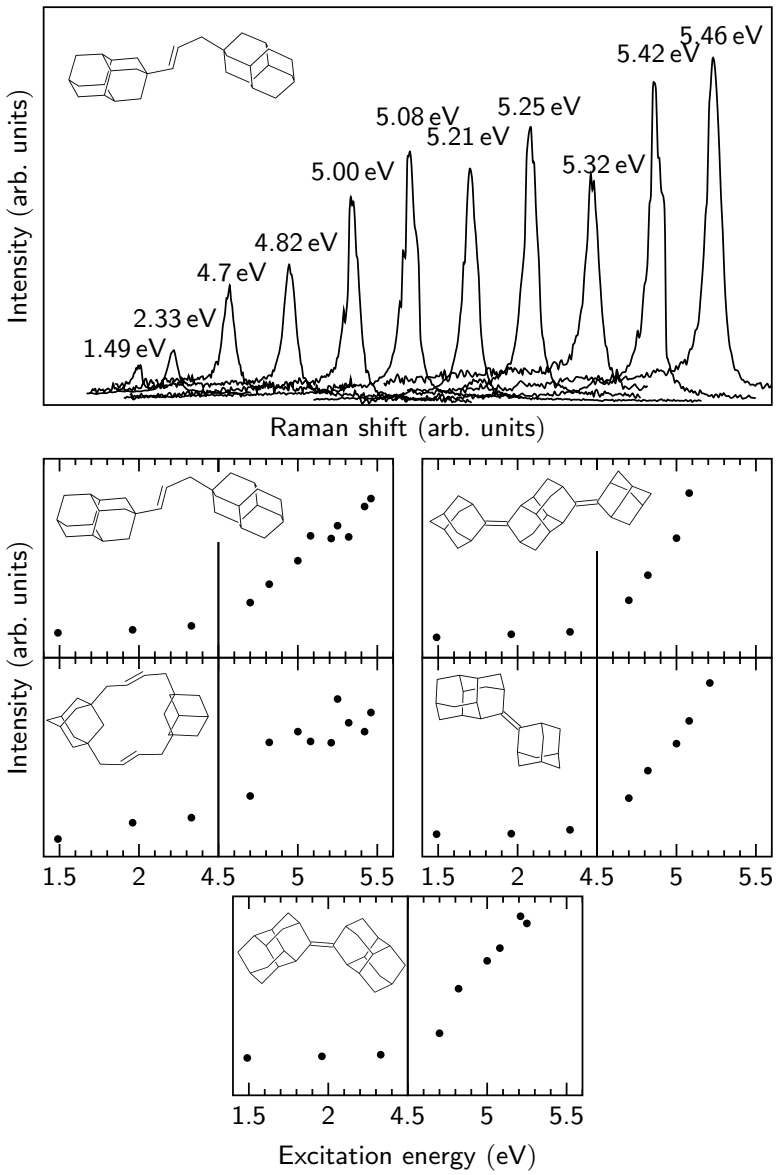

Figure 4.9: Top: Normalized Raman intensities of the C = C stretch vibrations of the 1,3-(bis-4-diamantyl)prop-1-ene are plotted. For a better overview, Raman peaks are shifted by $30\,\mathrm{cm}^{-1}$, respectively. Middle and bottom: Normalized Raman intensities of the C = C stretch vibrations for all measured diamondoid oligomers. The simplified structures are given in the figures.

computations, we find several localized modes with a strong deflection of carbon atoms forming the C=C double bond. These vibrations cause a displacement of the double bond carbon atoms along its direction and thus these modes are also resonantly enhanced for suitable excitation energies.

The intensity progression of the C=C stretch vibrations for various excitation energies of the measured diamondoid oligomers can be seen in Fig. 4.9. The upper part shows normalized and horizontally shifted Raman spectra of the C=C stretch mode for the 1,3-(bis-4-diamantyl)prop-1-ene for various laser excitation energies. The lower parts only show the normalized intensities of the C=C stretch mode of the other measured systems. For all oligomers, an intensity increase can be observed from $\sim 4.7\,\mathrm{eV}$ that directly corresponds to the $\pi \rightarrow \pi^*$ transition. This value is in good agreement to Refs. [65, 71, 72, 81] where resonance Raman spectra for various diamondoid dimers and trimers are computed and experimentally determined. By these measurements, we can determine the adiabatic E_{0-0} transition, *i.e.* the energy difference between the π and π^* states [65, 71] to exhibit 4.7 eV. Excitation energies above the E_{0-0} transition lead to a strong increase of absorption and therefore to an increase of the Raman intensity of the C=C stretch vibration [65, 71]. The $\pi \rightarrow \pi^*$ transition energy does not depend on the size or on the structure of the diamondoid oligomer (compare Fig. 4.9). With these results, we show that the π orbitals (HOMO) and π^* orbitals in chemically blended sp^2/sp^3 diamondoid oligomers are highly localized at the C=C double bond and that the influence of the surrounding constituents to the $\pi \rightarrow \pi^*$ transition energy is only marginal due to screening effects. These findings agree well with those from Ref. [98], where the measured ionization potentials of sp^2/sp^3 diamondoid oligomers are not affected by the size or shape of the molecules.
The high localization of both the π and π^* orbitals can exemplary be seen in Figs. 4.5 and 4.6 for 3,10-bis-(2-adamantylidene)diamantane and [4.4](1,3)adamantanophan-*trans,trans*-1,8-diene. Equi-energy plots of electron densities from other sp^2/sp^3 diamondoid oligomers can be found in Refs. [22, 72, 98].
In comparison to unfunctionalized diamondoids, optical transition energies of the chemically blended oligomers are donwshifted by at least 1.5 eV. The nature of the optical transitions are single-orbital $\pi \rightarrow \pi^*$ transitions with very high oscillator strengths up to $f_\alpha \sim 0.83$ [65, 71]. These values are approximately one magnitude higher than those in adamantane or diamantane [65, 71].

In summary, we can conclude that the nature of the optical responses of chemically blended oligomers are fundamentally different compared to unfunctionalized diamondoids. We find that the optical absorption is downshifted by $\sim 1.5\,\mathrm{eV}$ and originates from $\pi \rightarrow \pi^*$ rather than from $\sigma \rightarrow \sigma^*$ transitions.

In the beginning, we introduced the Hückel method that is capable of giving an estimation of the energies of the lowest optical transitions in sp^2 carbon systems, namely:

$$\Delta\mathrm{E} \sim 4\beta \sin\left(\frac{\pi}{2(n+1)}\right) \tag{4.1}$$

When we want to apply this expression to the sp^2/sp^3 diamondoid oligomers, we need to insert $n = 1$, as the longest sp^2 chain only consists of one double bond. Further inserting

$\beta = 2.5\,\text{eV}$ [36], we find a transition energy of $\Delta\text{E} \sim 5\,\text{eV}$. This value is already very close to our experimentally obtained value of 4.7 eV for all diamondoid oligomers and again shows the power of the Hückel method.

4.3 Single-bond diamondoid dimers - vibrational properties

Another approach to form diamondoid dimers was recently shown by the Peter Schreiner group in Gießen [23, 106]. In contrast to the oligomers as shown before, the diamondoid dimers, have a single-bond between their single constituents [23, 106]. A highly interesting and somewhat surprising aspect of the single-bond dimers is the exceptionally long carbon-carbon distance between their monomers that exhibits up to 1.704 Å in case of a diamantane-triamantane dimer [23, 106]. It is the so far longest reported bond length in alkanes [23]. The average value of unstrained carbon-carbon bonds instead is found to exhibit 1.54 Å [107]. It is commonly assumed that larger bond lengths are accompanied by a considerable bond weakening making them unfeasible to appear [108, 109]. However, due to steric repulsions and ring strain, longer carbon-carbon bonds can be observed in various large molecules that often contain highly electronegative atoms [23, 107, 108, 110, 111].
The stability of the diamondoid dimers, as proposed in Ref. [23, 106], however, arises from attractive dispersion interactions. The strong carbon-carbon bond elongations are achieved by a shifting of the energy balance in favor of attractive dispersion interactions exceeding the repulsive dispersive contributions [23]. The attractive interaction mainly occurs between the intramolecular $\text{HC}\cdots\text{CH}$ surfaces in the proximity of the central carbon-carbon bond [106]. An increase of interaction is observed, when the area of opposite surfaces is enlarged, accompanied by an increase of the observed bond length, as shown for DIA-DIA (1.647 Å), ADA-TRIA (1.659 Å), and DIA-TRIA (1.704 Å) [23]. Although not yet fabricated, even larger bond lengths are predicted for diamondoid dimers containing larger monomers [23].

The impact of the structural characteristic on electronic or vibrational properties is still only barely investigated. Measurements of the ionization potential (IP) of various single-bond diamondoid dimers indicate that quantum confinement effects determine their electronic structures, *i.e.* larger IPs are found for smaller dimers and vice versa [32, 98]. DFT computations show that in case of homo dimers, the HOMOs are symmetrically distributed with no distinction between single CC-bonds [98]. Instead, in case of hetero dimers, the HOMOs seem to be rather localized in the larger moieties of the dimers, *i.e.* their electronic properties rather equal those from the the larger moieties [98]. Their vibrational properties, however, are till today not yet investigated.
In the following, we will show Raman spectra of various single-bond diamondoid dimers and compare characteristics in their vibrational properties to those from pristine diamondoids and double-bond diamondoid dimers. We compare our findings with DFT calculations on a PWC (Perdew-Wang) level.

In Fig. 4.10 we show Raman spectra of various single-bond diamondoid dimers, namely 1-(1-adamantyl)adamantane (C_{2V} point group), 2-(2-adamantyl)adamantane (C_2 point

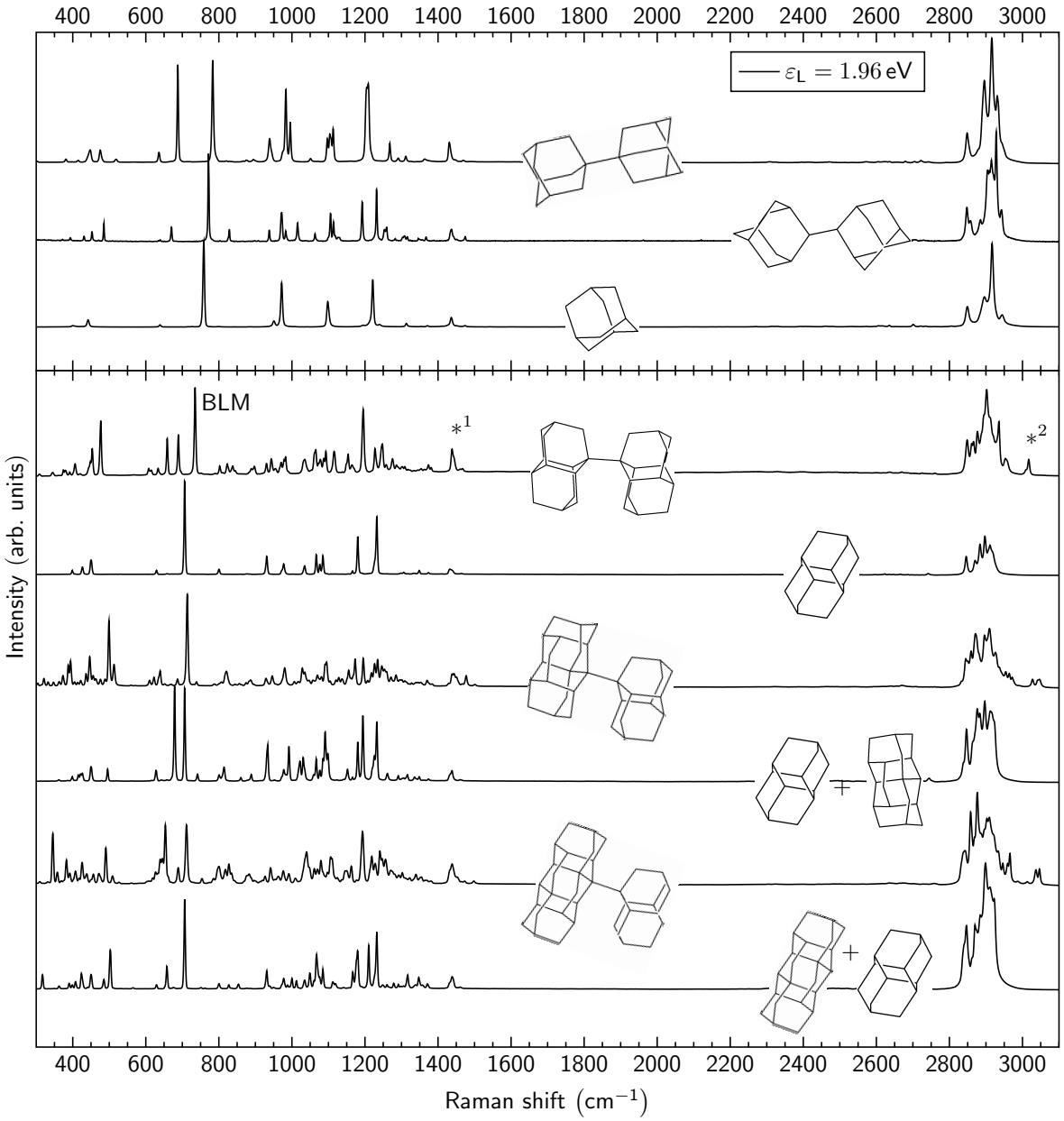

Figure 4.10: Raman spectra of single-bond diamondoid dimers are plotted for an excitation energy of $\varepsilon_L = 1.96\,eV$. The simplified chemical structures are given in the spectra, but do not contain hydrogen atoms. The + sign means that the spectrum is the sum of the respective pristine diamondoids as given in the figure. BLM stands for breathing-like mode. $*^1$ and $*^2$ indicate CH_2 scissors and CH stretch modes, respectively.

group), 1-(1-diamantyl)diamantane (C_{2V} point group), 2-(1-adamantyl)triamantane (C_S point group), 2-(1-diamantyl)triamantane (C_1 point group), and 2-(1-diamantyl)[121]-tetramantane (C_1 point group), enumerated from the top to the bottom [106]. The first three are homo dimers in which the constituents (adamantane, diamantane) are the same. In contrast, the other two dimers are hetero dimers.
We find many similarities in the Raman spectra of single-bond dimers when we compare them to pristine diamondoids: The spectra can again be divided into different spectral regions that can be attributed to characteristic vibrations in pristine diamondoids (compare Fig. 4.2). As also true for the double-bond oligomers, the addition of diamondoid cages via new carbon bonds leads to a symmetry reduction that lifts the degeneracy of vibrational modes in the unfunctionalized diamondoids [30, 73, 74, 76, 92]. As a result, the Raman spectra contain more distinguishable modes. This can especially be seen for the widely delocalized C-C-C bend/wag and C-C stretch modes between $\sim 300 - 800\,\mathrm{cm}^{-1}$ and for the CH_2 twist/rock modes between $\sim 900 - 1250\,\mathrm{cm}^{-1}$. C-C-C bend/wag modes can due to generally larger inertiae of the dimers, also be found at smaller frequencies (also see Fig. 4.11). Instead, the rather localized CH_2 scissor ($\sim 1450\,\mathrm{cm}^{-1}$) and C-H stretch modes ($\sim 2950\,\mathrm{cm}^{-1}$) seem to be widely unaffected by a functionalization ($*^1$ and $*^2$ in Fig. 4.10).

Characteristic breathing-like modes (BLM) can be observed for all diamondoid dimers. In terms of intensity, they are usually the most pronounced peaks in the C-C stretch region ($\sim 600 - 900\,\mathrm{cm}^{-1}$) and can be therefore well identified [30, 73, 76]. Within our DFT calculations, we always find two different breathing-like modes in the dimers. They are either localized in one or the other monomer of the molecules. In the case of homo dimers, the vibrations are split into in-phase and out-of-phase vibrations with almost equal frequencies. Hetero dimers, instead, have localized breathing-like modes with different frequencies, according to their constituents [30]. However, our calculations indicate that the fully symmetric character of the breathing-like modes gets lost under the functionalization. This especially counts for the larger counterparts of the dimers, *i.e.* triamantane and [121]tetramantane, where we observe a mixing with other C-C-C bend and wag modes.
In our Raman measurements, we only observe one pronounced breathing-like mode for each dimer although some contain two different diamondoid species. Instead, in a simple summation of the respective Raman spectra of pristine constituents, two breathing-like modes with clearly different frequencies are observable (compare Fig. 4.10). We tentatively attribute the absence of a clear, second BLM in the experimental Raman spectra to the mode mixing, accompanied by a loss of Raman intensity that is also known from large unfunctionalized diamondoids [30]. Our calculations indicate that both BLMs in the dimers are upshifted after a functionalization, but only a few cm^{-1}. The experimentally obtained upshifts therefore rather fit to the high-frequency BLMs in the dimers, *i.e.*, to the smaller diamondoids moieties. Both the calculations and experiments indicate that the BLM of the larger diamondoid moieties are intensity-wise more affected by a functionalization.

Equivalent to the double-bond diamondoid oligomers, we find high-frequency CH stretching modes that cannot be observed in pristine diamondoids. They are marked with $*^2$

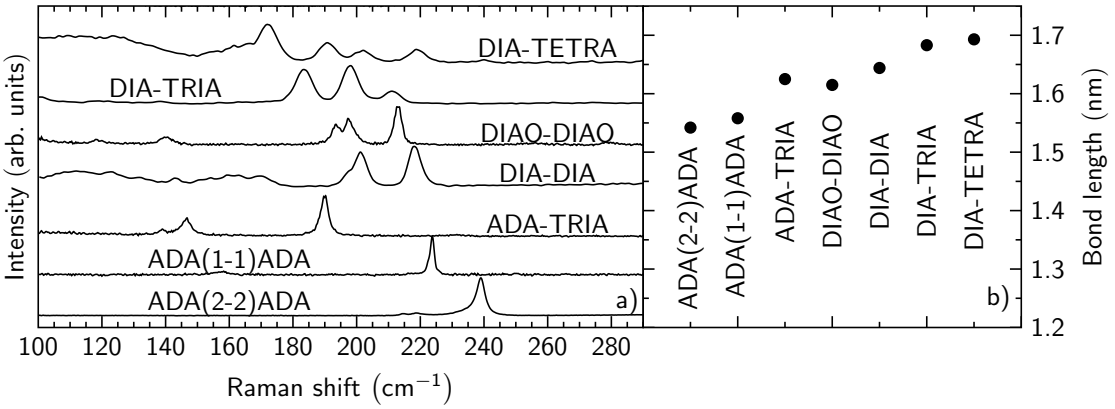

Figure 4.11: Low-frequency Raman spectra of single-bond diamondoid dimers are plotted for an excitation energy of $\varepsilon_{\mathrm{L}} = 1.96\,\mathrm{eV}$ in a). ADA, DIA, TRIA, and TETRA stand for adamantane, diamantane, triamantane, and [121]tetramantane, respectively. DIAO-DIAO is a 1-(1-diamantyl)diamantane dimer in which the 5$^{\mathrm{th}}$ position [112] carbon atoms are substituted by oxygen, respectively. b) The calculated bond lengths of the shared carbon bond is plotted for the different diamondoid dimers that are measured. Calculations are done in Dmol3 [113] on a PWC [114] level, implemented in Material studios 6.0.

in Fig. 4.10 but cannot be observed for the (adamantane) homo dimers. The experimentally obtained frequencies are $\sim 3050\,\mathrm{cm}^{-1}$ and thus $\sim 50\,\mathrm{cm}^{-1}$ larger than those in the double-bond dimers. Our calculations show that these localized vibrations only occur between the diamondoid moieties. Two opposite facets of the diamondoid moieties are due to a strong van-der-Waals interaction approximately aligned. Therefore, they create surfaces with pronounced repulsive forces for the hydrogen atoms of opposite diamondoid moieties [23, 106]. In case of the DIA-DIA and DIAO-DIAO dimers, the opposite surfaces are less aligned compared to dimers with larger diamondoid moieties. The reciprocal repulsion forces for the "inner" CH stretch vibrations are consequently slightly less pronounced accompanied by a lower frequency upshift. Both in the experiments and calculations, the highest CH stretch vibrations in DIA-DIA and DIAO-DIAO dimers are $\sim 30\,\mathrm{cm}^{-1}$ smaller than in larger diamondoid dimers. In the calculations, we again find in-phase and out-of-phase CH stretch vibrations of which the latter have slightly higher frequencies. Localized CH stretching modes that do not point in the direction of the neighboring, intramolecular diamondoid moieties are not affected by the additional repulsion forces. As a consequence, they are found at the same frequencies as in pristine diamondoids, both in the experiments and calculations. The (adamantane) homo dimers do not have pronounced, opposite facets (compare insets of Fig. 4.10). As a consequence, we cannot observe high-frequency CH stretching modes experimentally or in the calculations. In fact, the geometry optimized structure of the 1-(1-adamantyl)adamantane shows that both monomers are rotated by an angle of 60° around the shared carbon bond. This increases the distance of the hydrogen atoms of the neighboring adamantane monomers and therefore reduces the reciprocal repulsion forces.

These findings stand in clear contrast to those from the double-bond dimers. The stiff double bond aligns the diamondoid monomers in a way that the analyzed oligomers do not form pronounced, opposite facets. The observed increase of individual CH stretch vibrations is rather explained by a local stiffening [73]. This effect is smaller than the influence of the additional repulsion forces in the single-bond dimers. Therefore the high-frequency

Table 4.2: Overview of experimental and calculated frequencies of characteristic Raman peaks from the single-bond diamondoid dimers. ADA, DIA, TRIA, and TETRA stand for adamantane, diamantane, triamantane, and [121]tetramantane, respectively. DBM and BLM refer to dimer-breathing and breathing-like mode. We have used a LDA approach and the PWC [114] functional within the Dmol3 package implemented in Materials Studios 6.0. Asterisks belong to the Raman modes as marked in Fig. 4.10. All frequencies are given in cm^{-1}.

Sample	Mode type	exp.	calc.	Mode type	exp.	calc.
ADA(1-1)ADA	DBM	-	255	BLM	786	772
ADA(2-2)ADA	DBM	-	195	BLM	775	760
DIA-DIA	DBM	-	209	BLM	735	722 / 757
DIAO-DIAO	DBM	-	201	BLM	751	
DIA-TRIA	DBM	-	213	BLM	716	697
DIA-TETRA	DBM	-	190	BLM	712	722
ADA(1-1)ADA	$*^2$ CH stretch	-	-			
ADA(2-2)ADA	$*^2$ CH stretch	-	-			
DIA-DIA	$*^2$ CH stretch	3017	209			
DIAO-DIAO	$*^2$ CH stretch	3020	201			
DIA-TRIA	$*^2$ CH stretch	3050				
DIA-TETRA	$*^2$ CH stretch	3048	190			

CH stretch vibrations in the single-bond dimers exhibit $50\,cm^{-1}$ higher frequencies than those in double-bond dimers.

Our optimized geometries do not explicitly consider a dispersion correction that is supposed to be necessary for a correct description of the analyzed alkanes [23, 106]. We have rather chosen a functional that, without a dispersion correction, reproduces the very long central carbon-carbon bond considerably well. However, sophisticated DFT calculations and NMR (nuclear magnetic resonance) measurements show the existence of various conformational isomers of all analyzed diamondoid moieties [106]. Due to strong van-der-Waals interactions, the central C-C bond rotation barriers are shifted from ~ 7 to $\sim 33\,kcal\,mol^{-1}$ ($\sim$17.4 meV to $\sim$ 82.3 meV), depending on the dimers [106]. There are non-degenerate but isoenergetic rotation paths for various conformers found [106]. As a consequence, multiple conformational states can be populated that are not covered by our DFT calculations. Outcomes from our calculations can therefore deviate from the experimental findings.

We have plotted the central carbon-carbon bond length of the analyzed diamondoid dimers, ordered by their sizes in Fig. 4.11 b). In agreement to Refs. [23, 106], the central carbon-carbon bond length gets longer, the larger the diamondoids monomers are. Fig. 4.11 also contains an artificial (homo) diamantane dimer in which the 5^{th} [112] carbon atoms are substituted by oxygen atoms. The electronegativity causes a localization of the

HOMO to the functional group [68,69]. This in turn reduces the repulsive interaction between the diamondoid moieties, explaining the smaller carbon-carbon distance compared to the same structure without substituted carbon atoms.
In addition to the main carbon-carbon bond, also the low-frequency Raman modes of the diamondoid dimers are affected by their sizes as shown in Fig. 4.11 a). Following the lowermost to the top spectrum, we observe a downshift of Raman modes, *i.e.*, we generally observe Raman modes with lower frequencies for larger diamondoid dimers. Our DFT calculations indicate that in the analyzed spectral region, we mainly find rocking, stretching, and combined rocking/stretching vibrations of the whole diamondoid monomers within the molecule. As a consequence, their frequencies depend on the particular inertiae and exhibit generally lower frequencies for larger diamondoid monomers involved. This can exemplary be seen for the DIA-DIA and the DIAO-DIAO dimers of which the latter is due to substituted oxygen atoms slightly heavier. However, the vibrational characters of low-frequency modes are not affected by the chemical modification and, thus, they are slightly shifted to lower frequencies. The same behavior can be observed for d-16 adamantane in which all hydrogen atoms are replaced by deuterium [74].

Assimilable to the double-bond dimers, we find a dimer breathing mode (DBM) in the calculations for the single-bond diamondoids. However, we cannot assign a certain peak in the experimental low-frequency Raman spectra to the DBM. Within our DFT calculations, we find many Raman active, low-frequency modes up to $\sim 300\,\mathrm{cm}^{-1}$ that can experimentally not convincingly be distinguished from each other. This is in clear contrast to double-bond dimers, where a resonant intensity enhancement under UV excitations can be used to identify dimer-breathing modes [71–73]. The calculations further show that the breathing-like character of the DBM is altered compared to the double-bond dimers. The very stiff double bond defines a pronounced direction for the DBM resulting in clear, opposite vibrational pattern of the monomers within the diamondoid molecules. Instead, the BLM in single-bond dimers contains rotational, rocking, and stretching vibrations to variable extents. The highest symmetry of the analyzed dimers has the 1-(1-adamantyl)adamantane dimer (C_{2V} point group) in which the principal axis is along the central carbon-carbon bond (compare Fig. 4.11). The vertical mirror plane allows for a straight dimer-breathing mode resembling those from the double-bond dimers. The effect of repulsive interaction as a function of the distance between diamondoid dimers and the mode mixing superimpose the influence of the diamondoid masses to the DBM frequency. Calculated DBM frequencies, as given in Table 4.2, therefore deviate from the simple $f \sim m^{-1}$ proportionality.

Comparison of the vibrational properties of single- and double-bond diamondoid oligomers

The single and double-bond oligomers share many characteristics in their vibrational properties. These are mainly those vibrations that appear in pristine diamondoids, such as the C-C-C bend/wag/stretch, CH_2 twist/rock/wag/scissors, and CH stretch vibrations. All characteristic modes can be found in the functionalized diamondoid derivatives, but with partially altered frequencies. The more the carbon cage is involved in the vibrational patterns, the more their frequencies are affected by a functionalization. The arrangement

in dimers allows for dimer breathing modes in which the monomers oscillate against each other both in the single- and double bond dimers. However, the stiffer double bond defines the vibrational direction causing slightly higher frequencies and a lower mode mixing with other carbon cage vibrations for the double-bond oligomers. Further, due to their fundamentally different electronic structures, the DBM in double-bond oligomers can be resonantly enhanced with excitations energies above $\sim 4.7\,\mathrm{eV}$ making them distinguishable from other Raman modes. The ethylene centers in double-bond oligomers exhibit characteristic and very localized vibrational modes that cannot be observed in the single-bond dimers.
In both types of the functionalized diamondoids, we find high-frequency CH stretch vibrations that are separated by $\sim 50\,\mathrm{cm}$. The alignment of the monomers within the diamondoid dimers is determined by the van-der-Waals interaction in case of the single-bond dimers and by the comparably stiff C=C double bond in the double-bond oligomers. As a consequence, diamondoid facets are well aligned within the single-bond molecules. This in turn leads to additional repulsive forces that increase the frequencies of CH stretch vibrations that point in the direction of opposite diamondoid moieties. This effect exceeds the slight frequency increase caused by a local stiffening in case of the double-bond dimers.

4.4 Diamondoid van-der-Waals crystals

Parts of this section are published in Refs. [81, 92]

4.4.1 Electronic properties of chemically blended sp^2/sp^3 diamondoid van-der-Waals crystals

"Matter will always display attraction" used to be a basic principle of the 1910 Nobel prize winner Johannes D. van der Waals [23, 115]. The van-der-Waals interaction, that is often referred to as London dispersion, is an interaction between polarizable particles/matter in which (induced) electrostatic dipoles cause attractive forces [116]. Usual binding energies exhibit between 5 and 50 meV being responsible for the ability of trees to carry water to leaves that are more than 10 m above the ground or to simply write with a pencil.
It was found that the crystallization of super-saturated solutions of purified diamondoids in acetone leads to macroscopic, transparent crystallites [19]. They have a well-defined, long-range order with melting points about 540 K for the lowest $C_{10}H_{16}$ adamantane [67]. This value is considerably ($\sim$ 200 K) higher than those of other hydrocarbons with comparable molecular weights due to a strong van-der-Waals interaction of adjacent molecules within the crystal lattice [67]. In comparison to diamond, the van-der-Waals crystals from adamantane, diamantane, and triamantane are direct isolators with band gaps between 6 and 7 eV, decreasing for an increasing size of the diamondoid constituents [67]. Their optical properties are therefore difficult to experimentally access by usual laser setups. As discussed in the previous section, sp^2/sp^3 blended diamondoid oligomers have redshifted optical transition energies making them suitable candidates for optical experiments on diamondoid van-der-Waals crystals. By these measurements, we can determine the effect of van-der-Waals interaction to the optical properties of the analyzed crystals.

The arrangement of diamondoids in periodic van-der-Waals crystals leads to new, collective properties such as the formation of an electronic band structure or a phonon dispersion. Depending on the extension of electronic orbitals in the isolated molecules, their counterparts in the crystalline phase are different due to the overlap of adjacent molecular orbitals. This in turn changes the energetic levels of conduction and valence bands and generally reduces the band gap of the crystals compared to the isolated molecules [67, 81].
For a closer analysis of the diamondoid van-der-Waals crystals, optical absorption spectra of isolated molecules in the gas phase have been taken. The measurements have been conducted at the U125/2-NIM beam line [117] at the BESSY II synchrotron radiation facility (Helmholtz-Zentrum Berlin, Germany) [118] with the nice help of the AG Möller from the TU Berlin.
In Fig. 4.12 absorption spectra of a trishomocubane dimer $(PCU)_2$ and a diamantane dimer $(DIA)_2$ from molecules in the gas phase are plotted. A significant absorption increase starts from around 5.6 eV (plotted with dashed arrows) for both dimers. In good agreement to the absorption increase, a resonant enhancement of the Raman intensity of the C=C stretch vibration is also observed from around 5.6 eV (plotted with a red arrow in Fig. 4.12). In contrast, a resonant enhancement of the Raman intensity of the C=C stretch vibration in the crystalline phase is observed around 4.9 eV, *i.e.* at lower energies. In both cases, the strong absorption is caused by a $\pi \rightarrow \pi^*$ transition as shown for dia-

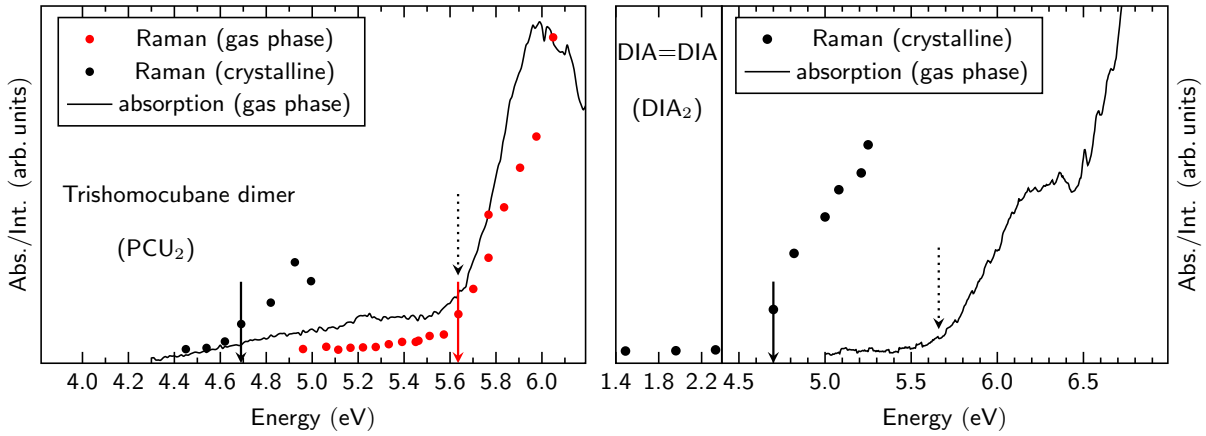

Figure 4.12: Absorption spectra of isolated molecules from a trishomocubane dimer [(PCU_2)] and a diamantane dimer [(DIA_2)] in the gas phase are given (continuous lines). Black dots represent normalized Raman intensities of the C=C stretch vibration in the solid phase. Red dots represent normalized Raman intensities of the C=C stretch vibration in the gas phase. Data is partly taken from Ref. [92]

.

mondoid oligomers in the previous section and by DFT computations in Refs. [65, 71, 92]. Due to the good agreement of Raman intensity and the optical absorption for $(PCU)_2$, we believe that we observe the same behavior in case of the diamantane dimer as shown in Fig. 4.12. Again, the resonant enhancement of the Raman intensity of the C=C in the solid phase begins at around 1 eV lower energies than the absorption in the gas phase.

DFT computations of the analyzed van-der-Waals crystals indicate that optical transition energies are downshifted compared to the isolated counterparts as can be seen in Ref. [81]. Since the experimental approach is only sensitive for optical transitions from the π to the π^* orbitals, experimental statements can only be derived for the corresponding valence and conduction bands in the crystal. In both crystals, the valence bands originate from π orbitals that have a lower dispersion compared to those from the σ orbitals [81]. Their high localization between the diamondoid moieties leads to a low interaction with orbitals from adjacent molecules and thus the dispersion is only weak [81]. The σ and σ^* orbitals, instead, are rather diffuse and outspread throughout the whole diamondoid moieties leading to a large interaction and thus a comparably high dispersion in the equivalent electron/hole bands in the crystals [67, 81]. Our DFT calculations indicate that the π^* orbitals are responsible for the conduction band in the PCU_2 and for the cb+3 band in the DIA_2 van-der-Waals crystal [81]. Their computed downshifts in the crystals exhibit 550 meV for PCU_2 and 400 meV for DIA_2, slightly lower than in the experiments [81]. The reason of the discrepancy might be the well-known underestimation of optical transition energies in DFT computations. The computed downshift of the direct valence band $\rightarrow$ conduction band transition in the DIA_2 van-der-Waals crystals is another $\sim$ 500 meV lower as the conduction band originates from σ^* orbitals that are much more affected by the neighboring molecules [81]. However, since the chosen experimental approach is not sensitive for these optical transitions, we cannot verify this outcome from the DFT computations. Calculated band structures and further information can be found in Refs. [81, 92].

The formation of van-der-Waals crystals can be used to tailor the electronic properties

of diamondoid moieties. It is an indirect way to downshift optical transition energies of the primary constituents. In principle, the induced downshift should depend on the extension of molecular orbitals forming the valence and conduction bands, as shown for the chemically blended sp^2/sp^3 diamondoid derivatives. By a certain functionalization, the localization of HOMO and LUMO and their electronic characters can be changed drastically [68,69,98]. This allows to tailor the overlap of adjacent molecular orbitals and therefore to tailor the downshift of optical transition energies in a diamondoid van-der-Waals crystal. Computations of sulfur-functionalized diamondoids indicate, that both HOMO and LUMO are highly located at the periphery of the carbon cages accompanied by a strong downshift of optical transition energies to the optical visible region [68]. A further introduction of sulfur atoms does not reduce the optical band gap, but leads to a slight upshift due to a reduced dipole-induced charge transfer from the sulfur atoms to the carbon cages [68]. However, the extension of electron orbitals towards the outer periphery further increases when more sulfur atoms are added. This might increase the van-der-Waals interaction between adjacent molecules in a crystal and thus the downshift of optical transition energies. Therefore, in such a crystal the optical band gap might decrease although the intrinsic optical transition energies increase when introducing more than four sulfur atoms to the diamondoid cages [68].
This general approach might be used to create diamondoid crystals that have tunable bandgaps from the optical visible up to ultraviolet spectral region.

4.4.2 Vibrational properties of diamondoid van-der-Waals crystals

The first Raman studies on diamondoid van-der-Waals crystals were performed 40 years ago [75, 119]. The already available knowledge of certain crystal structures allowed for their group theoretical analysis in a way that the Raman spectra from lower diamondoid crystals were understood even 40 years ago [120–122]. It was found that only diamantane has Raman active low-frequency modes at room temperatures [120, 122]. Adamantane and triamantane instead appear in a pre-melting plastic phase [119] with orientationally disordered molecules. Only for temperatures below 100 K (adamantane) or 20 K (triamantane), an ordered phase can be observed via pronounced peaks in the low-frequency Raman spectrum [119]. Although the crystal structures of higher diamondoids up to a hexamantane are known in our days, there are no Raman spectra available in the literature. The same accounts for the chemically blended sp^2/sp^3 diamondoid oligomers as discussed before.

The low-frequency Raman spectra of diamondoid van-der-Waals crystals are characterized by translatory displacements of entire diamondoid molecules or hindered rotational displacements around their axes of inertiae (librations) [119]. In case of diamantane, a group theoretical analysis at room temperature yields:

$$\Gamma_{\text{trans}}^{\text{opt}} = \mathrm{A}_u + \mathrm{E}_u + 2\mathrm{T}_u \tag{4.2}$$

$$\Gamma_{\text{lib}}^{\text{opt}} = \mathrm{A}_g + \mathrm{E}_g + 3\mathrm{T}_g, \tag{4.3}$$

of which only the librations (lib) are Raman active, *i.e.* their consideration is important for a comprehensive understanding of the low-frequency Raman regime.

Table 4.3: Overview of crystal structures of diamondoid van-der-Waals crystals as given in the top row. The numbers in brackets refer to the space group IT numbers, respectively. a, b, c, α, β, and γ are the lattice constants with the corresponding lattice angles. All lengths are given in Å. Data is provided by Franziska Emmerling [123].

[1234]Pentamantane	[121]Tetramantane	Triamantane
monoclinic	monoclinic	orthorhombic
space group P 21/c (14)	space group P 21/c (14)	space group Fddd (70)
$a = 7.7075$, $b = 12.5845$	$a = 7.6567$, $b = 7.9611$	$a = 12.6769$, $b = 17.9695$
$c = 17.7808$	$c = 12.7999$	$c = 21.9399$
$\alpha = 90°$, $\beta = 100.142°$	$\alpha = 90°$, $\beta = 104.881°$	$\alpha = 90°$, $\beta = 90°$
$\gamma = 90°$	$\gamma = 90°$	$\gamma = 90°$
units = 4	units = 2	units = 16

In order to understand the vibrational properties of diamondoid van-der-Waals crystals to a greater extent, we have started a cooperation with Franziska Emmerling [123] from the BAM (Bundesanstalt für Materialforschung). With a X-ray powder diffraction analysis, we could identify some crystallographic structures that are not available in the database of the Cambridge Crystallographic Data Centre (CCDC) or could be identified with a higher accuracy. They are listed in Table 4.3. Crystal structures of other chemically blended sp^2/sp^3 diamondoid crystals can be found in Ref. [91]. The structures are used for DFT calculations of both their vibrational and electronic structures and are partly still in progress. One of the purposes is the understanding of the low-frequency Raman spectra, as shown in Fig. 4.13.

In agreement to group theory based conclusions, we do not find any low-frequency Raman modes for adamantane or triamantane van-der-Waals crystals [119]. Instead, up to [12314]hexamantane, all other unfunctionalized diamondoid van-der-Waals crystals exhibit pronounced Raman modes in the low-frequency region. The same accounts for the chemically blended sp^2/sp^3 diamondoid oligomers. DFT calculations indicate that intramolecular (internal) vibrations in diamondoids occur at $\sim 200\,\mathrm{cm}^{-1}$, depending on their sizes [30, 73, 119]. The experimentally observed low-frequency Raman modes can be therefore solely attributed to intermolecular translational displacements or to librations. Interesting aspects of the van-der-Waals crystals that can be answered with the help of DFT calculations are the influences of size and shape of the diamondoid monomers to the low-frequency vibrations. Although the inertiae of the monomers noticeably increase going from adamantane up to [12314]hexamantane, we do not find a pronounced downshift of low-frequency Raman modes. A simple explanation for the observed trends might be that an increase of diamondoid intertiae is accompanied by an increase of the diamondoid surfaces and therefore their interaction surfaces. The larger inertness might cancel a frequency upshift due to an enlarged interactions resulting in only marginal frequency shifts of the low-frequency Raman modes.

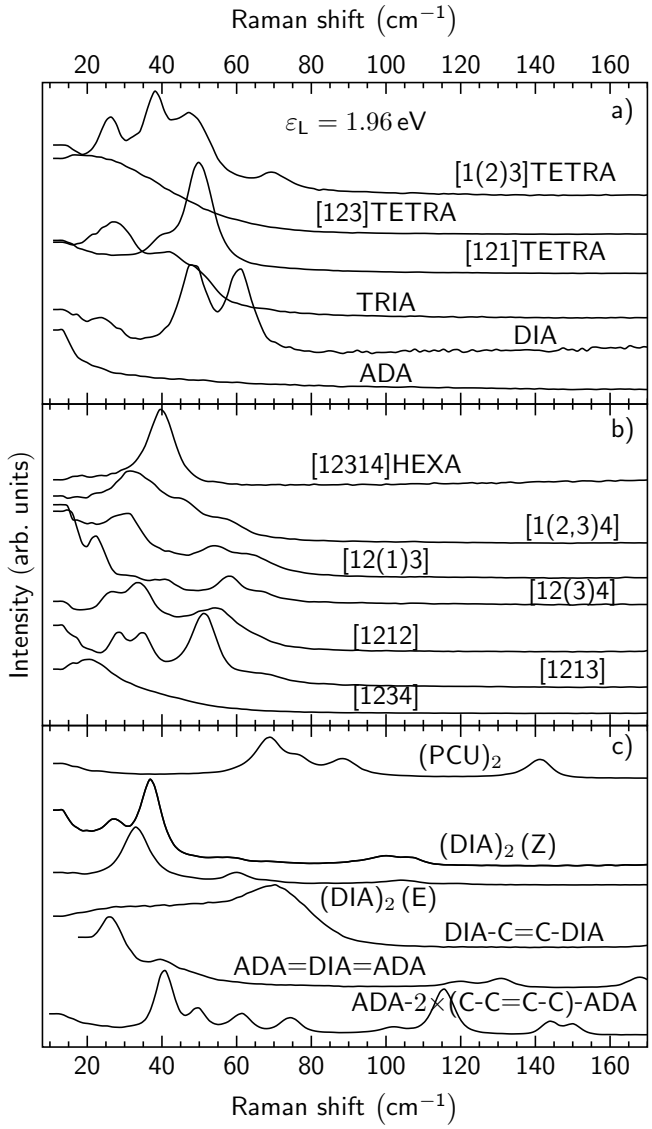

Figure 4.13: Low-frequency Raman spectra of pristine diamondoids (a)-(b) and sp^2/sp^3 diamondoid oligomers (c) for an excitation energy of $\varepsilon_L = 1.96$ eV are plotted. ADA, DIA, TRIA, TETRA, and HEXA stand for adamantane, diamantane, triamantane, tetramantane, and hexamantane, following the nomenclature given by Balaban and Schleyer [63]. In (b), all but the top spectra belong to pentamantanes. PCU stands for polycyclic undecane (compare previous section and Ref. [92]). (Z) and (E) denote the *anti*−, and *syn*−Isomers of diamantane.

In contrast, the diamondoid oligomers have intramolecular (internal) low-frequency Raman modes, such as the dimer-breathing modes [72, 73]. C-C-C vibrations are due to the attached masses generally shifted towards lower frequencies, explaining the rich Raman features in Fig. 4.13 c). However, even the functionalized diamondoids have pronounced crystal structures and therefore their low-frequency Raman spectra consist of both intermolecular and intramolecular vibrations.

Outlook

With the help of the DFT computations, we want to understand the low-frequency vibrational properties of the diamondoid van-der-Waals crystals. Furthermore, we want to understand their electronic structures. It was shown in Ref. [67] that the conduction bands in (unfunctionalized) diamondoid crystals originate from very diffuse C-H σ^* orbitals. The conduction band minima and valence band maxima occur at the Γ point (up to triamantane), *i.e.* the diamondoid crystals are direct insulators [67]. Bulk diamond instead is an indirect insulator, in which the conduction band originates from C-C σ^* orbitals. Further, it was shown that the bandgap in diamondoid crystals decreases with

increasing size of the diamondoid moieties [67]. Larger diamondoids than triamantane, however, have not yet been analyzed. Interesting questions are from our perspective if a diamondoid crystal exists that has a smaller bandgap compared to bulk diamond and how different isomers of tetra- and pentamantanes determine the electronic structure of the crystals.

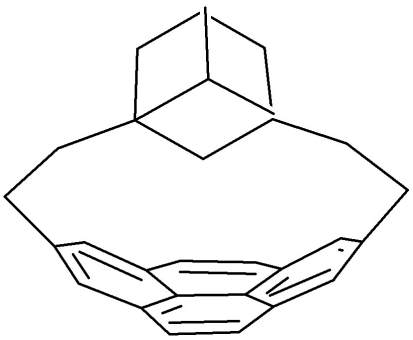

Figure 4.14: The ground state molecular structure of [2](1,3)adamantano[2](2,7)pyrenophane is shown. The remaining bonds are saturated with hydrogen, but are not shown for reasons of visibility.

4.5 Pyrene and diamondoids: Electronic and vibrational properties of [2](1,3)Adamantano[2](2,7)pyrenophane

In the last part of this chapter, we want to discuss a recently fabricated hydrocarbon that to some extent brings both diamondoids and graphene together. It is an aggregated sp^2/sp^3 hybrid structure of sp^2-hybridized pyrene and sp^3-hybridized adamantane connected by small carbon chains, namely [2](1,3)Adamantano[2](2,7)pyrenophane [124], see Fig. 4.14. The hybrid structure unifies the electron-acceptor and electron-donor abilities of bended sp^2 and diamondoid moieties, respectively [21, 124, 125]. When arranged in the ways as suggested in Ref. [124, 126], the actual non-polar carbon allotropes develop a considerable dipole moment pointing to the sp^2 moieties. This trait is for instance desirable for a controlled self-assembly on suitable surfaces [127]. Widely covered surfaces by adamantane containing compounds could then be used for high-brilliance electron beam sources [21, 128]. The electronic properties of diamondoids within the compounds, however, should not be altered too much to maintain their desired properties. It is therefore necessary to analyze their electronic properties with respect to similarities to pristine diamondoids. In the previous sections we could see that the chemically blended sp^2/sp^3 diamondoid oligomers exhibit both electronic and vibrational properties of the ethylene moieties and the diamondoids attached to each other. The same behavior appears in case of [2](1,3)Adamantano[2](2,7)pyrenophane, as we will see on the next pages.

4.5.1 [2](1,3)Adamantano[2](2,7)pyrenophane - vibrational properties

The ground state molecular structure of [2](1,3)Adamantano[2](2,7)pyrenophane exhibits a C_S symmetry being significantly reduced in comparison to adamantane (T_D) and pyrene (D_{2h}) [124, 129]. For that reason, we generally expect more complex Raman spectra in terms of the amount of allowed Raman active modes. The bending of the pyrene moiety in the ground state structure as shown in Fig. 4.14 further suggests that especially the in-plane C=C stretch vibrations should be altered compared to pristine pyrene. C-H vibrations at the edges should however be way less affected by the bending.

In the following, we compare the experimental Raman spectra to DFT calculations on a LDA level in DMol3 with the PWC functional [113, 114]. General assignments are done

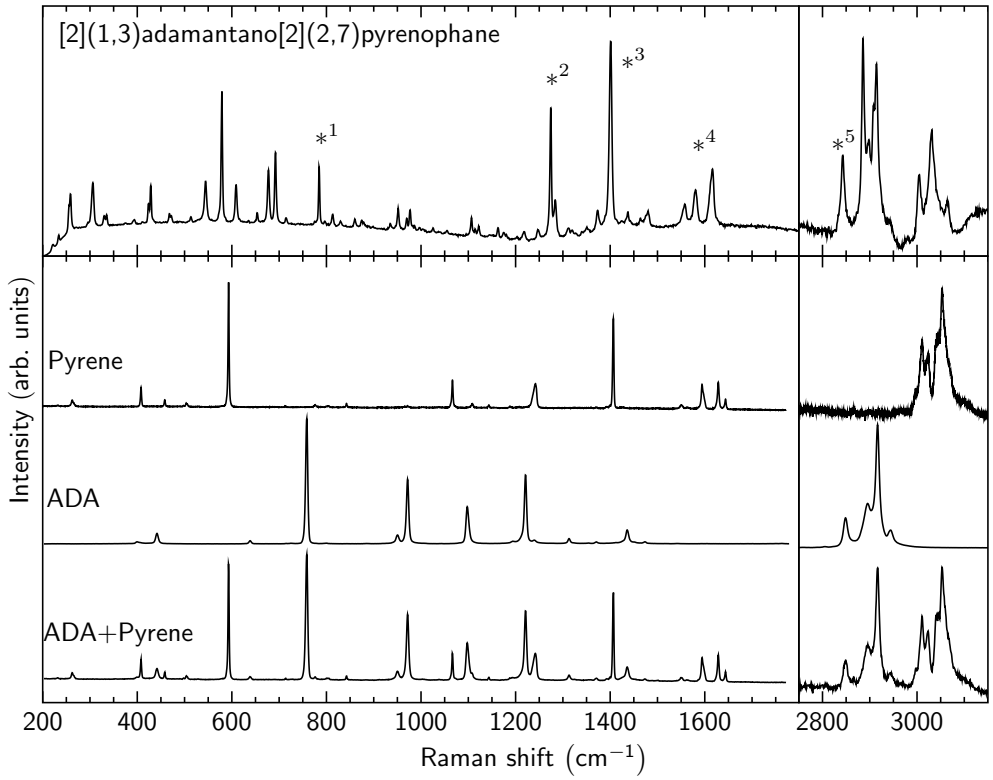

Figure 4.15: Raman spectra of [2](1,3)Adamantano[2](2,7)pyrenophane, adamantane (ADA), pyrene, and ADA + pyrene are plotted for an excitation energy of $\varepsilon_{\mathrm{L}} = 1.96\,\mathrm{eV}$.

via a careful analysis of each respective vibrational eigenmode.

Similar to the Raman spectra of the previously analyzed diamondoid oligomers, the Raman spectrum of [2](1,3)Adamantano[2](2,7)pyrenophane can again be decomposed in characteristic C-C cage, C=C, and C-H vibrations. Frequency-wise, characteristic C-H vibrations such as the C-H stretch ($\sim 3000\,\mathrm{cm}^{-1}$) and CH_2 scissor ($\sim 1450\,\mathrm{cm}^{-1}$) modes are widely unaffected in the artificial compound. In particular, this can be seen in the bottom spectra of Fig. 4.15, where the spectra of pristine adamantane and pyrene are added. Due to the stiff carbon double bonds, pyrene generally has high-frequency C-H stretching modes that are maintained in the [2](1,3)Adamantano[2](2,7)pyrenophane compound [130]. The same counts especially for the lowest C-H stretch vibration, denoted with $*^5$ in Fig. 4.15. In adamantane this mode is a fully symmetric breathing mode of hydrogen atoms that widely maintains its character in the measured compound [74]. C-C cage vibrations can again be found between $\sim$ 400 and $900\,\mathrm{cm}^{-1}$. The carbon chains between adamantane and pyrene can vibrationally-wise be seen as an enlargement of the sp^3 carbon cage of adamantane. For this reason, primary vibrations of the carbon cage are not substantially altered but extended by new modes in the frequency range C-C cage modes are usually found [30, 73, 74]. The well-known breathing-like mode BLM widely maintains its character and its frequency is slightly upshifted in the measured compound ($*^1$ in Fig. 4.15). Four C=C stretch vibrations are found at around $1600\,\mathrm{cm}^{-1}$ both in the experiments and calculations, denoted with $*^4$ in Fig. 4.15. They can directly be referred to one A and three A_g C=C stretch modes in pyrene (D_{2h} point group) [130]. Their frequencies, however, are downshifted due to the bond bending. We find seven

State	ΔE_{vert}	f
1	3.4623	0.0034
2	3.6718	0.0503
3	4.2282	0.1860
4	4.2665	0.0010

Table 4.4: Vertical transition energies ΔE_{vert} in eV and oscillator strengths f for [2](1,3)Adamantano[2](2,7)pyrenophane are shown for the first four excited states. Calculations are done on a B3LYP/TVZ level of theory. Data is taken from Refs. [129, 131].

other pronounced C=C modes in which the carbon atoms are deflected towards opposite carbon atoms and not along their shared C=C bonds as in the case of C=C stretch modes. Calculated frequencies range from 1340 cm^{-1} up to 1490 cm^{-1}. In the experimental spectra, these modes are found at slightly lower frequencies. The highest and lowest frequencies are denoted with $*^3$ and $*^4$ and Fig. 4.15. This is a clear difference to the diamondoid oligomers as previously discussed, since all vibrational modes between $\sim$ 900 and 1450 cm^{-1} could only be referred to C-H vibrations.

Another deviation to the vibrational modes of pristine diamondoids can be found in the range below 500 cm^{-1}. Between $\sim$ 250 and 500 cm^{-1}, we find collective vibrational modes in which the entire carbon rings are involved. Further, below $\sim$ 250 cm^{-1} many rotational modes of the entire adamantane moieties can be found, accompanied by a considerable stretching of the carbon chains between the pyrene and adamantane. Especially in the low-frequency region, we generally find an extensive mode mixing of the pyrene moiety with C-C cage modes of adamantane. This, however, does not count for the high-frequency modes above $\sim$ 1400 cm^{-1}, where the vibrational modes are rather distinguishable.

In the previous section, we showed that the vibrational modes of double-bond diamondoid oligomers can to some extent be understood as a linear combination of the vibrational modes of the ethylene moieties and diamondoids. The same occurs in [2](1,3)Adamantano[2](2,7)pyrenophane. Characteristic modes of both pyrene and adamantane are widely maintained and are only slightly altered in their frequencies. This can, in particular, well be seen when we compare the Raman spectrum of [2](1,3)Adamantano[2](2,7)pyrenophane to the sum of the Raman spectra of pyrene and adamantane in the bottom spectra of Fig. 4.15. However, the structure-induced change of vibrational modes leads especially in the low-frequency spectrum to a considerable mode mixing and allows for adamantane rotational modes that are only to a much lesser extent present in the double-bond diamondoid oligomers [73].

4.5.2 [2](1,3)Adamantano[2](2,7)pyrenophane - electronic properties

A very large dipole moment was theoretically found for [2](1,3)Adamantano[2](2,7) pyrenophane in the ground state exhibiting 2.3 D [124]. It is an interesting question if that large dipole moment is conserved in excited electronic states of the compound or

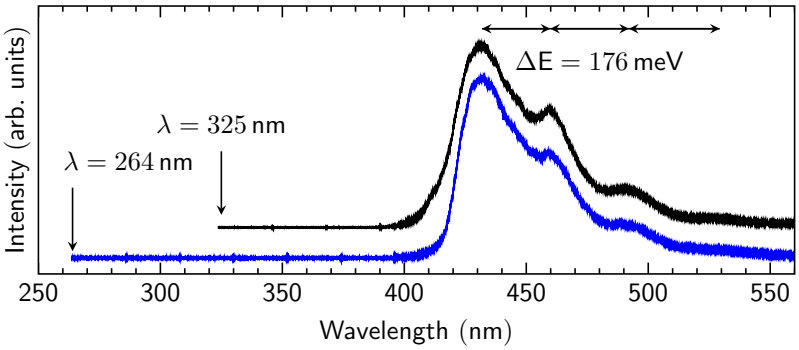

Figure 4.16: The PL (photo luminescence) spectrum of [2](1,3)Adamantano[2](2,7)pyrenophane is plotted for two excitation wavelengths as denoted in the figure. Arrows indicate the energy difference between maxima in the vibrational progression of the PL spectrum.

if the direction of the dipole moment can be reversed in higher electronic states. This could for instance offer new approaches for the self-assembly of diamondoids on various surfaces [127]. The reversal of dipole moments might be understood from the fact that the lower-lying excited electronic states are π^* states of the pyrene moiety, whereas very high excited states are σ^* states localized in the adamantane moieties, accompanied by a considerable shift of charge concentration.
Xiong *et al.* have calculated ground and excited states geometries with individual vertical transition energies within DFT on a B3LYP/TVZ level of theory [129]. Vertical transition energies and oscillator strengths for four excited states are listed in Table 4.4. Due to the significantly lower symmetry of the compound, no optically forbidden transitions were found [129]. The first allowed optical transition is considerably lower compared to adamantane [32] and those from double-bond diamondoid oligomers [71–73]. Interestingly, the first three excited states are accompanied by an increase of dipole moment of up to 18.22 % and a slight change in the direction of the internal field [129].
In contrast to lower diamondoids, the low-lying electronic states of the [2](1,3)Adamantano[2](2,7)pyrenophane compound allow for the experimental investigation with commercially available light sources [32]. All following experiments are performed in the solid phase, *i.e.*, the compound is measured in a van-der-Waals crystals. We therefore expect slightly lower transition energies compared to the isolated molecules [67, 81].

For excitation energies of $\varepsilon_L = 4.69\,\text{eV}$ (264 nm) and $\varepsilon_L = 3.81\,\text{eV}$ (325 nm), we have found a strong luminescence beginning from $\sim 420\,\text{nm}$ (2.95 eV) followed by a vibrational progression, as shown in Fig. 4.16. Following Kasha's rule [132], we attribute the measured onset of the luminescence to the E_{0-0} transition, *i.e.* the optical transition from the vibrational ground state in the first excited state S_1 to the vibrational ground state in the electronic ground state S_0 [65, 71]. The following maxima are referred to optical transitions from the vibrational ground state in the first electronic excited state to higher vibrational states in the electronic ground state (compare Fig. 3.1 in Chapter 3). They are separated by $\sim 176\,\text{meV}$ proportional to the dominant vibrational mode that alters the structure of the electronic ground state. In the calculations, the E_{0-0} transition is found at around 3.23 eV [129], slightly larger than in the experiments. The applied computational approach tends to overestimate transition energies as a comparable difference

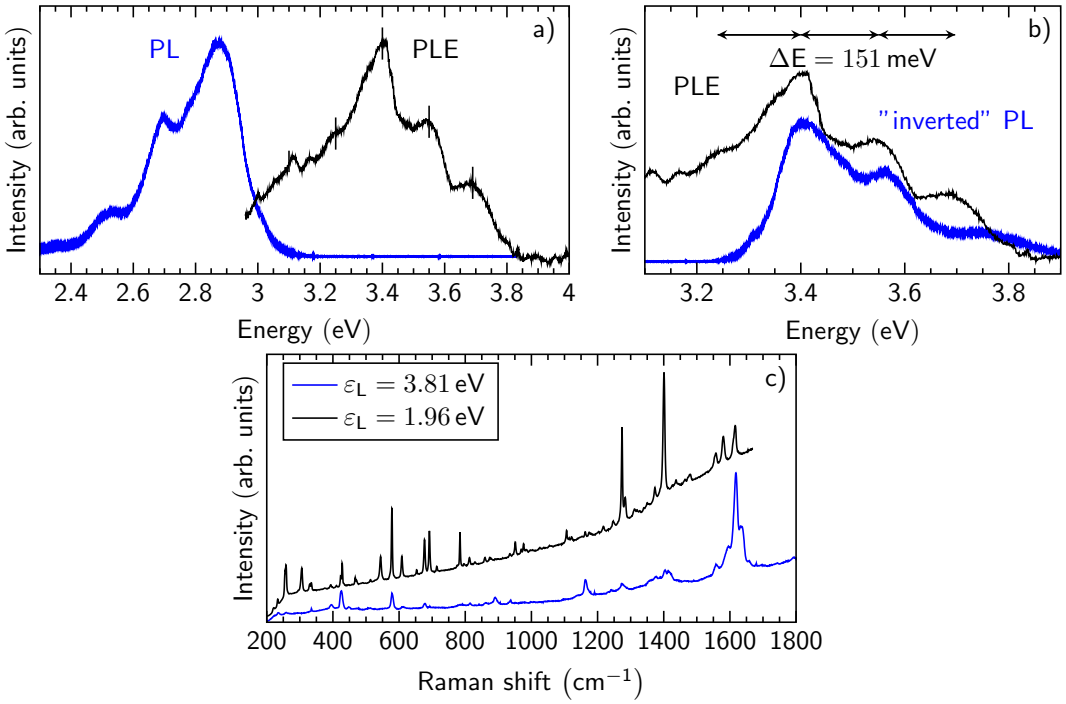

Figure 4.17: Photo luminescence a), photo luminescence excitation b), and Raman spectra c) of [2](1, 3)Adamantano[2](2, 7)pyrenophane are plotted. b) contains an inverted photo luminescence spectrum for a better comparison to the photo luminescence excitation spectrum.

of $\sim 0.3\,\text{eV}$ between calculations and measurements was also found for the double-bond diamondoid oligomers [71, 73].

To investigate the first excited state of the artificial pyrene + adamantane compound, we have performed photoluminescence excitation (PLE) measurements in the solid phase. This spectroscopic method is widely utilized in solid state physics but is rather unusual in molecular physics. It gives insights to the optical absorption of materials as the intensity of the luminescence directly corresponds to the strength of optical absorption. For molecules that are rather present in a gas phase, other spectroscopic methods, such as UV/Vis spectroscopy are more suitable giving a direct access to the optical absorption. However, since the [2](1,3)Adamantano[2](2,7)pyrenophane at room temperatures is present as small crystallites, PLE measurements can likely be applied.

A PLE spectrum vs. a PL spectrum of [2](1,3)Adamantano[2](2,7)pyrenophane is plotted in Fig. 4.17 a). We find a considerable absorption starting from $\sim 3.1\,\text{eV}$ up to $3.8\,\text{eV}$. The PLE spectrum also features a vibrational progression with maxima indicated by small lines in Fig. 4.17. Their energy spacing ΔE exhibits $\sim 151\,\text{meV}$, lower than in the vibrational progression of the PL spectrum. In more detail, this can be seen in Fig. 4.17 b), where the inverted PL spectrum is plotted against the PLE spectrum. The smaller energies of vibrational states can be understood from the fact that in absorption measurements, we observe vibrational states in the first excited electronic state S_1. Higher electronic states of molecules are accompanied by a considerable change of geometry [101–103] that usually leads to an altering of vibrational frequencies. In the first electronic state, the C=C bond lengths in the pyrene moiety are extended reducing restor-

ing forces and thus reducing the frequencies of relevant vibrational modes [129]. UV/Vis spectra of [2](1,3)Adamantano[2](2,7)pyrenophane in various solvents are available that show the same absorption onset but with a reduced spacing of vibrational states [124]. The fluorescence does not seem to depend on the solvent and is similar to that from [2](1,3)Adamantano[2](2,7)pyrenophane measured in the solid phase [124].

The measured absorption of [2](1,3)Adamantano[2](2,7)pyrenophane in cyclohexane exhibits a large increase from $\sim 3.5\,\mathrm{eV}$ up to higher energies, that we cannot observe in the PLE measurements. The increase of absorption correlates with an efficient absorption in the second excited electronic state S_2 [124, 129] that we can not probe with the PLE measurements. Internal conversion processes [28] allow for non-radiative relaxation channels when excited in higher electronic states that do not contribute to the $S_1 \rightarrow S_0$ optical transition that we cover by the PLE measurements. However, when excited to the first excited electronic state, all absorbed photons should contribute equally to the fluorescence, *i.e*, PLE spectroscopy can be seen as a measure of an optical absorption into the first excited electronic state [132]. It is interesting to note that both the absorption and fluorescence spectra of [2](1,3)Adamantano[2](2,7)pyrenophane are very similar to those from crystalline pyrene [133]. Except for the lifting of degenerate electronic states, the artificial compound does not substantially alter the electronic properties of the pyrene moiety. Both the vibrational and electronic properties of [2](1,3)Adamantano[2](2,7)pyrenophane are widely disjunct combinations of adamantane and pyrene.

Calculated Raman spectra indicate that C=C stretch vibrations should generally be enhanced under a resonant excitation [129]. It is often observed that those vibrational modes that are responsible for the vibrational progression in the fluorescence spectra, are enhanced under a resonant excitation [71, 97, 104, 129]. From the PL spectra, we obtain an energy of $\sim 1415\,\mathrm{cm}^{-1}$ (176 meV) corresponding well with the energies of the C=C stretch modes found in the DFT calculations. In fact, authors in Ref. [129] found that the geometry change of the first excited state agrees to the vibrational pattern in which the carbon atoms in the unbent carbon rings are deflected (compare Fig. 4.14). These modes should also be very well observable for lower excitation energies, explaining the large intensities of several modes between 1250 and $1400\,\mathrm{cm}^{-1}$ in the Raman spectra plotted in Fig. 4.15. Contradictory to the calculations, we observe a large intensity increase of the high-frequency C=C stretch modes in the Raman spectra when excited resonantly, as shown in Fig. 4.17. However, for an excitation energy of $\varepsilon_\mathrm{L} = 3.81\,\mathrm{eV}$, we are already close to the second excited electronic state exhibiting another geometry, compared to the first excited electronic state. As a consequence, other vibrational modes might be resonantly enhanced.

4.6 Summary

In summary we have analyzed the vibrational properties of various diamondoid derivatives. We have shown that they can be understood as linear combinations of the vibrational properties from the constituents involved. In particular, these are lower diamondoids and ethylene for the double-bond oligomers as well as adamantane and pyrene for

[2](1,3)Adamantano[2](2,7)pyrenophane. Since the connecting bond in the single-bond dimers can be seen as an extension of the carbon cage, their vibrational properties resemble those from the diamondoid species involved. Although the characteristic vibrational modes of the constituents are widely unaffected in the oligomers, we find new, structure-induced vibrational modes. On the one hand, this can be understood from the fact that the symmetry is clearly reduced. On the other hand, the new structures give rise to additional modes such as the dimer breathing mode (DBM) present in all oligomers or the high-frequency C-H stretching modes.

If a C=C double bond is existent in the diamondoids derivatives, the optical transition energies are substantially downshifted. In fact, they resemble those from the ethylene moieties in case of the double-bond dimers or those from pyrene in [2](1,3)Adamantano[2](2,7)pyrenophane, widely unaffected from the diamondoid species attached. By resonance Raman measurements, we could determine the $\pi \rightarrow \pi^*$ transition energies of C=C double bond connected oligomers to exhibit $\sim 4.7\,eV$. This value is a bit less than 2 eV smaller than in pristine, lower diamondoids. In [2](1,3)Adamantano[2](2,7)pyrenophane, the onset of the fluorescence was found at around 2.95 eV approximately resembling the value in crystalline pyrene.

In the crystalline phase, diamondoids and diamondoid derivatives form very stable vander-Waals crystals. We find that the arrangement in a periodic lattice structure leads to a downshift of the $\pi \rightarrow \pi^*$ transition energies of around 1 eV in diamondoid derivatives containing a carbon double bond. It further allows for collective, low-frequency phonon modes in which entire diamondoid moieties are involved.

5. UV Raman spectroscopy of graphite, graphene, and multilayer graphene

Parts of this chapter are published in Ref. [52].

5.1 UV Raman spectroscopy of graphite and graphene - a motivation

Raman spectroscopy has established itself as a very common technique to analyze fundamental properties of carbon allotropes, in particular, of graphene, graphite, and carbon nanotubes [45, 53, 134, 135]. From a simple point of view, it is surprising that the Raman effect in graphene can be experimentally observed since there is no effective scattering volume. However, graphene exhibits a reasonable, constant optical absorption of $\pi\alpha = 2.293\,\%$ (where $\alpha = e^2/\hbar c$ denotes the fine structure constant) for photon energies between 0.2 eV and 1.2 eV [136]. The optical absorption for higher energies deviates from the constant behavior due to considerably lower dispersions of electron and hole bands [137–139]. A lower dispersion along the $K - M$ direction leads to a higher density of states and thus, to a substantial increase of the optical absorption up to $4 \times \pi\alpha$ from a single sheet of graphene [137–139].
Both in graphene and graphite, excited charge carriers undergo an efficient coupling to optical phonons. The main reason is a strong Kohn Anomaly in both materials [10,140–142]. It causes a drastically enhanced electron-phonon coupling because of the reduced ability of electrons from the Fermi surface to screen the vibration of the carbon nuclei [10,140,143]. This in turn leads to a discontinuity of the derivative from certain phonon branches accompanied by a substantial softening of phonon frequencies close to the K and Γ points [10, 14, 140, 144]. Both the reasonable optical absorption and the strong electron-phonon coupling allow for the analysis of optical and acoustic phonons in these materials explaining the widespread usage of Raman spectroscopy.

A lot of interest has been put in the fundamental understanding of first- and second-order Raman processes in graphene, multilayer graphene, and graphite. Due to the broad availability of compact spectrometer and laser systems in the visible spectral range, many of the available publications concerning inelastic light scattering show experiments where a limited region of electron wave vectors around the Dirac points in graphene/graphite are

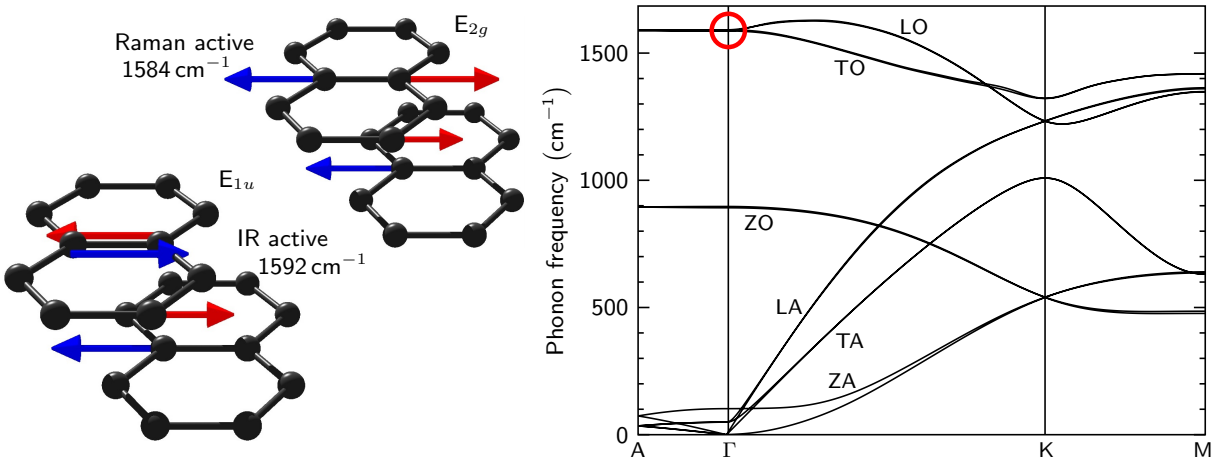

Figure 5.1: Left side: The structure of the graphite lattice with indicated eigenvectors of the Raman-active E_{2g} (top) and IR-active E_{1u} (bottom) modes is illustrated. Right side: The one-dimensional phonon dispersion of graphite is plotted along the high-symmetry lines. The red circle corresponds to the zone-center E_{1u} and E_{2g} vibrations as plotted on the left side. Calculations are done with a DFT/LDA approach and are provided by Roland Gillen [96].

probed [9, 14, 145–147]. This can also be well understood from the fact, that the electron dispersion in the proximity of the Dirac cones is linear - a behavior that is otherwise only known from massless Dirac particles or from surface states in topological insulators [5,148]. Since the two-dimensional electron dispersion is nearly isotropic in the proximity of the Dirac cones, in a double-resonant Raman process, the linearity can directly be probed by laser excitation energies below 2 eV [38]. Electrons with momenta beyond the proximity of the Dirac cones exhibit a sub linear behavior with a substantially lower dispersion in the $K-M$ direction compared to the $K-\Gamma$ direction [38]. This peculiarity in the electron band structure and its effect on the Raman spectra has been discussed in literature excessively [9, 14, 45, 144, 145, 149, 150]. An experimental and theoretical discussion of Raman processes away from the "usual" scattering paths, *i.e.* DR Raman processes that happen close to the M-point exciton, or far away from the proximity of the K points, are even today scarce in literature.
In this chapter, we will discuss and explain these "unusual" scattering paths. We will see that these processes will include phonons from all over the 1st Brillouin Zone of the analyzed materials. This aspect is a novelty in the analysis of DR Raman processes in graphene/graphite. By the careful selection of laser excitation energies, we can lift the usual restriction of phonon wave vectors fulfilling multiple resonance conditions in a double-resonant Raman process. This leads to fundamentally new insights into the vibrational properties of graphite, graphene, and carbon nanotubes.

5.1.1 Vibrational properties of graphene and graphite

The unit cell of the bulk material graphite consists of two single, two-dimensional planes of sp^2 hybridized carbon. They are arranged in a way that every second carbon atom is located above the center of a carbon six-ring from the adjacent layer. Their interlayer spacing is around 3.35 Å, *i.e.* around 1.5 times the distance of a carbon-carbon double bond (2.461 Å) [39, 151]. This stacking is also referred to as Bernal-stacking or simply as

AB-stacking. In other words, graphite consists of two sub lattices that are horizontally shifted by the length of a carbon-carbon bond along its fixed direction and vertically shifted by $\sim 1.5\times$ the length of the carbon-carbon double bond. A scheme of the arrangement of the two sub lattices can be seen on the left side in Fig. 5.1. The emerging crystal has a D_{6h}^4 symmetry and contains four atoms in the unit cell [152]. They are responsible for twelve phonon branches that are, due to the structure of the lattice, pairwise almost degenerate. An one-dimensional plot along the high-symmetry lines can be seen in Fig. 5.1.

The inversion center of graphite allows for new vibrational patterns compared to its single-layer constituent graphene (D_{6h}). The well known vibrational modes in graphene split up to in-phase and out-of-phase motions when changing the layer [153, 154]. For instance, this results in the IR activity of graphite or allows for Raman-active, low-frequency shear modes that originate from a zone boundary acoustic mode in the first place [153, 155]. The twelve allowed normal modes for $q = 0$ in graphite read as:

$$\Gamma_{\text{vib}}^{\text{Graphite}} = 2A_{2u} + 2B_{2g} + 2E_{1u} + 2E_{2g} \tag{5.1}$$

originating from the in-phase ($\Gamma_{\text{vib}}^{\text{graphene}} \otimes A_{1g}$) and out-of-phase ($\Gamma_{\text{vib}}^{\text{graphene}} \otimes B_{1g}$) combinations with the allowed normal modes of graphene [154]. The two double degenerate E_{2g} modes are Raman active and responsible for the well-known G-band and the shear modes in graphite [82, 155, 156]. The E_{1u} and A_{2u} modes are IR active whereas the B_{2g} modes remain optical inactive. The vibrational patterns of the high-energy E_{2g} and E_{1u} modes are illustrated in Fig. 5.1.
Based on Raman measurements in graphite, experimentally data is available for the LA, TA, TO, and LO phonon branches with gaps for phonon wave vectors between the high-symmetry points, *i.e.* far away from the high-symmetry points in the phonon dispersion. Other experimental approaches such as inelastic neutron scattering techniques [157], electron energy loss spectroscopy [158], and high-resolution electron energy-loss spectroscopy [159,160] also added insights into the out-of-plane ZO and ZA phonon branches. Deeper insights into the phonon dispersions of graphite were given by x-Ray Raman scattering several years later [152, 161]. These measurements could finally identify the unlike dispersions of the TO and LO phonon branches and therefore identify the phonon branch responsible for the D and $2D$ band in graphite, graphene, and carbon nanotubes [152,161]. This decisive assignment has finally led to a convincing and broad understanding of the second-order Raman scattering processes in the named carbon allotropes.

5.1.2 Beyond double-resonant Raman scattering: A UV analysis of graphite, graphene, and carbon nanotubes

Double-resonant Raman scattering is an essential concept for the understanding of the complex Raman spectrum of graphite [9]. It explains the large variety of modes that are usually visible in graphene and graphite as shown in Fig. 5.2 (bottom spectrum).
First-order processes such as the G-band (compare Fig. 5.2) are visible throughout a wide range of laser excitation energies [162,163]. Instead, second-order processes such as the D and $2D$ bands [9, 14, 164], the iTOLA [14, 149, 165–167], or other low-intensity bands [14]

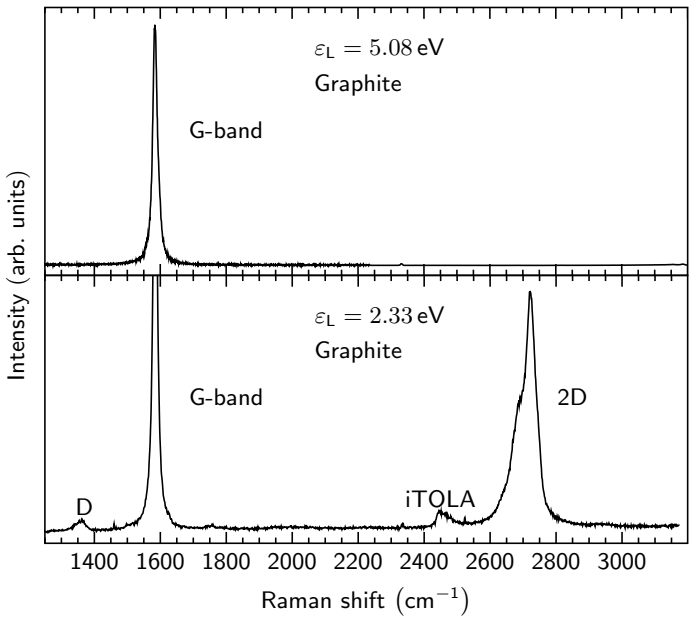

Figure 5.2: Raman spectra of graphite for a deep-UV and visible light excitation energy are plotted. The double-resonant D, iTOLA, and $2D$ modes disappear for an excitation energy of $\varepsilon_L = 5.08\,eV$ (upper spectrum).

like the D' band [14,85] or the LA defect band [168] are not present in a Raman spectrum when the excitation energy is chosen to exhibit 5.08 eV as shown in Fig. 5.2.
In the visible optical range, it further occurs that due to sharp resonances of reciprocal scattering processes, the intensity of second-order Raman modes exceeds that of the first-order process associated with the G-band [141, 169, 170]. This even happens although there is a strong Kohn Anomaly of the degenerate LO/TO phonon branches at the Γ point in the phonon dispersion of graphite [10,140]. For deep-UV excitation energies this behavior can not be observed anymore [52, 162, 163].
In the following, we will discuss and explain the drastic changes in the Raman spectra as shown in Fig. 5.2 and extend the discussion of Raman spectra from graphite to a larger set of laser excitation energies.

There has been a long-standing discussion about the phonon scattering paths of the dispersive Raman peaks in the spectra of graphene and graphite. The reason is the anisotropic electronic band structure of graphene/graphite allowing for various scattering paths with a broad range of different possible phonon wave vectors involved. In a simplified, one-dimensional scattering scheme, the different scattering paths can be associated with so called "inner" and "outer" processes when the optical excitation occurs along the $K - M$ direction ("inner") or along the $K - \Gamma$ direction ("outer"). An example for an outer process can be seen in Fig. 5.3 (b). As a consequence of the symmetry, the phonons involved then stem from the $\Gamma - K$ direction ("inner") or from the $K - M$ direction ("outer"). Herziger *et al.* gave a more general definition of "inner" and "outer" processes in the two-dimensional electronic band structure of bilayer graphene [144, 171] that can also be applied to graphene or graphite. According to the authors, a process is referred to as "inner" when the resonant phonon wave vectors come from a circular sector of $\pm 30°$ around

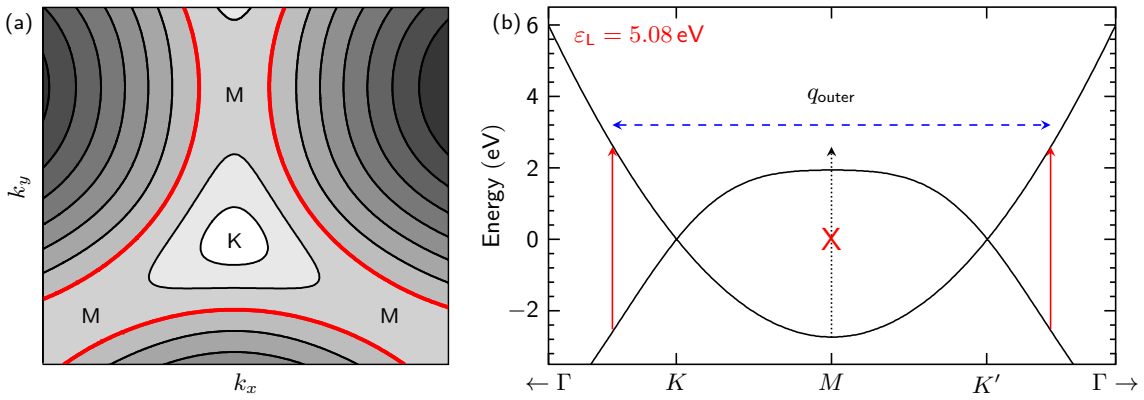

Figure 5.3: (a) A two-dimensional plot of the electronic band structure of graphene with the high-symmetry points K and M is shown. The red lines correspond to an equi-energy surface of $\varepsilon_L = 5.08\,\text{eV}$ whereas the triangle-shaped contour with edges in the middle between the $K - M$ high-symmetry line corresponds to an energy surface of $\varepsilon_L = 3\,\text{eV}$. (b) An One-dimensional plot of the electronic band structure of graphene is plotted. Indicated are optical excitations with an energy of $\varepsilon_L = 5.08\,\text{eV}$ and the length of a resonant phonon wave vector that mediates between two real electronic states in a double-resonant Raman process.

the $\Gamma - K$ high-symmetry direction in the proximity of the K points and from a circular sector of $\pm 30°$ around the $K - M$ high-symmetry direction for "outer" processes [144,171]. Authors in the most cited article concerning double-resonant Raman scattering in graphene and graphene layers claim that dominant processes are those where resonant phonon wave vectors mainly stem from the $K - M$ direction [164]. This interpretation, however, was done only by a tentative assignment to calculated phonon frequencies but without the support of sophisticated two-dimensional Raman calculations. Authors in Refs. [84, 172] also claim that the optical absorption occurs in areas with the "lowest curvature" in the electronic band structure which translates in optical excitations along the $K - \Gamma$ high-symmetry direction. Instead, with better agreement to experiments and with the support of extensive two-dimensional Raman calculations, the initial and somewhat general assignment was superseded by several authors [14, 144, 145, 149, 173, 174]. On the one hand, it was shown that the initial and simplified approach to calculate the second-order Raman spectra given by Thomsen *et al.* [9] was well justified. On the other hand, the full two-dimensional calculations, revealed that the main contributions of resonant phonon wave vectors originate from the $K - \Gamma$ high-symmetry line, *i.e.* the dominant processes are "inner" process [14, 144]. "Outer" processes, however, also give rise to contributions in second-order Raman modes but with generally lower intensities and unlike phonon frequencies compared to the "inner" processes. For instance, they are responsible for the asymmetric line shapes of the $2D$ band or the iTOLA in graphene [14, 149], but are generally less visible in carbon nanotubes as discussed in the next chapter.

A possible way to experimentally distinguish between both processes is to chose a laser excitation energy that is above the M-point energy, *i.e.* higher than 4.7 eV [136, 138, 174]. As illustrated in Fig. 5.3, this approach suppresses the inner scattering paths only allowing outer processes. It is noteworthy that equi-energy surfaces in the two-dimensional electronic band structure of graphene are fundamentally different for energies over the M-

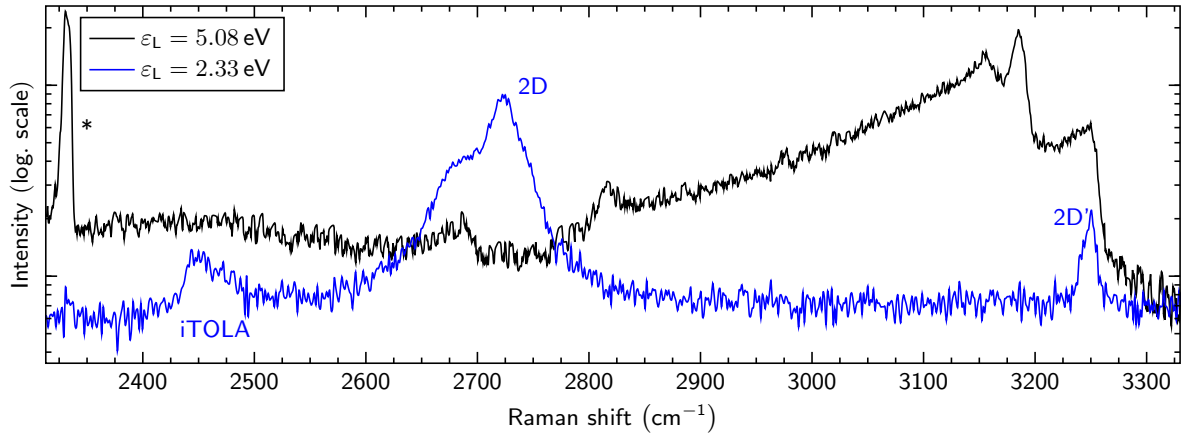

Figure 5.4: Raman spectra of graphite for an excitation energy of $\varepsilon_L = 5.08\,eV$ (black) and $\varepsilon_L = 2.33\,eV$ (blue) are plotted in a logarithmic scale. The marked peak (*) corresponds to a Raman mode from atmospheric nitrogen.

point energy compared to those below the M-point energy. Below 4.7 eV, the equi-energy surfaces correspond to the well-known triangles around the K points due to the trigonal warping effect [38]. Instead, equi-energy surfaces for energies over 4.7 eV are circles around the Γ points [compare Fig. 5.3 a)]. This topological change leads to a restriction of possible scattering paths in a double-resonant Raman process. In detail, the dominant "inner" scattering paths connecting unlike K and K' points at regions with the highest curvature are excluded due to the lack of real electronic states. As a consequence, Raman modes associated with these scattering processes are not present in a Raman spectrum anymore. This can clearly be seen in Fig. 5.2 where the excitation energy is 5.08 eV, *i.e.* way above the M-point exciton.

However, we still find Raman modes besides the first-order associated G-band in graphite for laser excitation energies above the M-point exciton but with a several magnitudes lower intensity compared to the G-band. A corresponding Raman spectrum for an excitation energy of $\varepsilon_L = 5.08\,eV$ is plotted in Fig. 5.4. Five, characteristic and asymmetric peaks between $2600\,cm^{-1}$ and $3300\,cm^{-1}$ are found. None of these peaks exhibits the typical Lorentzian line shape that is known from first-order or in a good approximation, the "Baskonian" line shape that is known from second-order processes in graphite [175]. Further, we find a strong Raman band around $2331\,cm^{-1}$ that is associated with a stretch vibration of the nitrogen molecule $^{14}N_2$ from the atmosphere [176]. This high-frequency peak can be used to calibrate the Raman spectra as it is independent from the laser excitation energy.
The asymmetric line shapes indicate that the nature of processes responsible for the Raman modes are fundamentally different compared to those present in the spectrum for excitation energies in the visible optical range. In fact, if we compare the Raman peaks to the phonon dispersion of graphite, we can assign these peaks to the second-order vibrational density of states [52]. Regions in the phonon dispersion exhibiting a very flat slope give rise to a high density of states being responsible for the peaks as shown in Fig. 5.4 and Fig. 5.5. These regions are namely the overbending of the LO phonon branch around the Γ point, the two pairs of TO/LO phonon branches at the Γ point, the TO

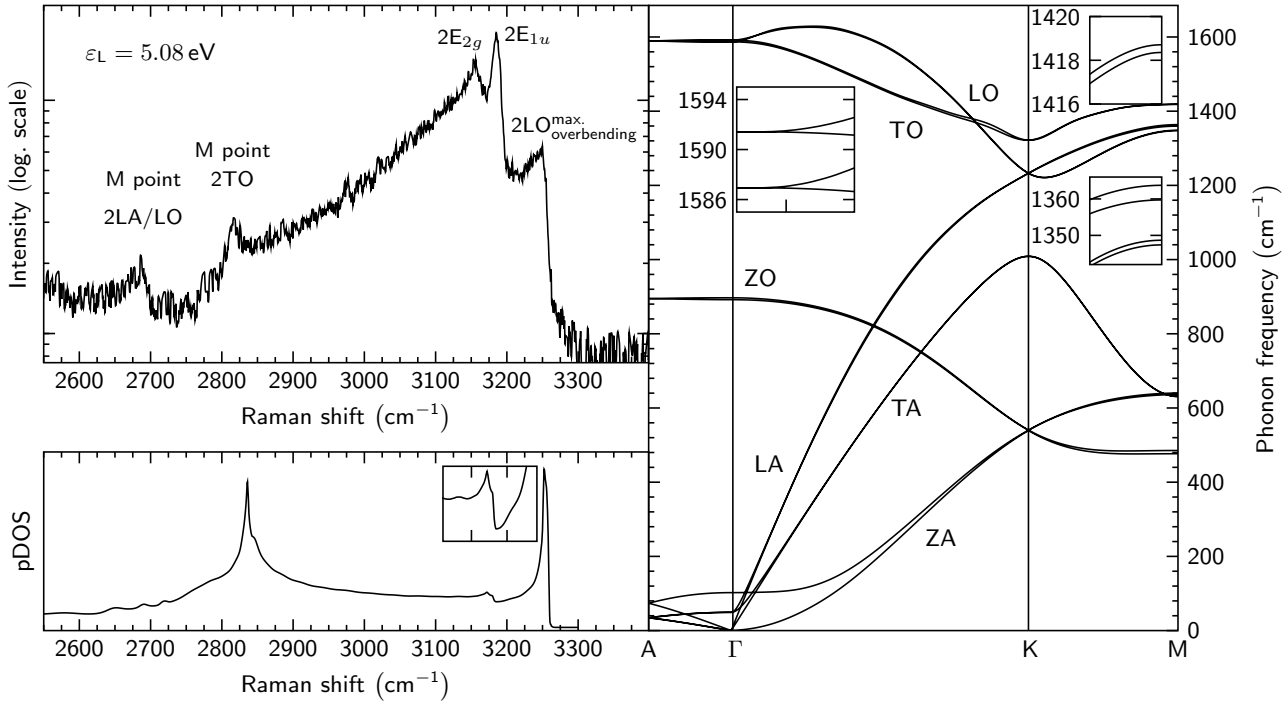

Figure 5.5: Left: The measured (top) and calculated (bottom) second-order vibrational density of states of graphite is plotted. The excitation energy is $\varepsilon_L = 5.08\,eV$. Peaks are assigned by a comparison to the calculated phonon dispersion of graphite (right). Insets show regions with a high density of states that can be seen in the experiments. Calculations are done with a DFT + LDA approach and are provided by Roland Gillen [96].

phonon branch at the M point, and the almost degenerate LA/LO phonon branches at the M point. The respective first-order frequencies can experimentally be determined with $1626\,cm^{-1}$ for the LO-overbending, $1592\,cm^{-1}$ for the Γ point E_{1u} mode, $1578\,cm^{-1}$ for the Γ point E_{2g} mode, $1408\,cm^{-1}$ for the M point TO phonon branch, and $1344\,cm^{-1}$ for the M point LO/LA phonon branches. We find an excellent agreement of the experimental values with data in the literature [82, 154, 161, 177]. Especially the calculated phonon frequencies of the TO, LO, and LA phonon branches at the M point can be verified [161]. This is of particular interest since this region of the phonon dispersion is barely accessible by optical spectroscopy.
Fig. 5.5 also contains the calculated vibrational (phonon) density of states named pDOS. We find similar asymmetric peaks as in the experimental Raman spectra, but with different intensities. In the pDOS calculations, no coupling elements are considered, leading to a strong underestimation of contributions from the Γ point. Its well-known Kohn Anomaly leads to a strong electron-phonon coupling giving rise to the E_{2g} and E_{1u} associated second-order peaks in the experimental Raman spectrum [10, 140].

The direct product of irreducible representations can be decomposed into a linear combination of irreducible representations belonging to the specific point group. Three examples of the product of the relevant irreducible representations E_{2g} and E_{1u} within the point

group D^4_{6h} are given below [178]:

$$E_{2g} \otimes E_{2g} = A_{1g} \oplus A_{2g} \oplus E_{2g} \tag{5.2}$$
$$E_{1u} \otimes E_{1u} = A_{1g} \oplus A_{2g} \oplus E_{2g} \tag{5.3}$$
$$E_{1u} \otimes E_{2g} = B_{1u} \oplus B_{2u} \oplus E_{1u} \tag{5.4}$$

The first two products contain the fully symmetric representation A_{1g} that is always Raman active. In fact, the direct product of irreducible representations always contains the fully symmetric representation A_{1g} [178]. The second order of a vibrational mode should therefore always be Raman active and its experimental access is not anymore restricted to the first-order scattering optical selection rules. It is consequently possible to measure both Raman active and non-Raman active modes in a joint experiment as shown for the E_{2g} and E_{1u} modes in graphite. Measuring IR active modes such as the E_{1u} otherwise requires more complicated experiments like reflectivity measurements at infrared beamlines [177].
In contrast, the product of the representations E_{1u} and E_{2g} does not contain a Raman active representation. We should therefore not be able to observe according second-order combination modes which holds true for the experiments as can be seen in Fig. 5.5

5.1.3 Raman scattering mechanism for deep-UV excitation energies

We will now turn the discussion to the mechanism of the scattering process and explain the different Raman spectra when the laser excitation energy is tuned from the deep-UV region down to the energy of the M-point exciton.
The well established concept of double-resonant Raman scattering proposed by Thomsen *et al.* [9] was initially used to understand and describe the second-order spectrum of graphite for laser excitation energies in the visible optical range. Double-resonance refers to two resonances, *i.e.* real electronic states that are namely the electron hole pair that is created by the incoming photon matching the energy difference of valence and conduction band ($h\nu \rightarrow a$) and the scattered electron/hole finding another real state in the conduction/valence band ($a \rightarrow b$) [9]. As a consequence of the dispersion of both electrons and phonons, the consecutive backscattering with a phonon ($b \rightarrow c$) is a non-resonant process with an usually small detuning for excitation energies in the optical visible range [9]. The scattering scheme can be seen in Fig. 5.6. For reasons of simplicity, we only explain the incoming resonance and electron-electron scattering in detail. Equivalent statements can be made for outgoing resonances and the predominant electron-hole scattering [14].

It is interesting to note that when the optical excitation approximately equals the M-point transition energy ($\sim 4.7\,\mathrm{eV}$) the flat dispersion of the valence band still impedes double-resonant scattering for "inner" processes. Phonon momenta necessary for the double resonance directly stem from the proximity of the Γ point and exhibit very large phonon energies of approximately 200 meV (compare Fig. 5.5). In a two phonon process the energy difference between the initial and final state then adds up to $\sim 400\,\mathrm{meV}$. For such a large energy difference, the electron momentum mismatch of k_{initial} and k_{final} is comparably vast, resulting in a large detuning of the entire double-resonant process.

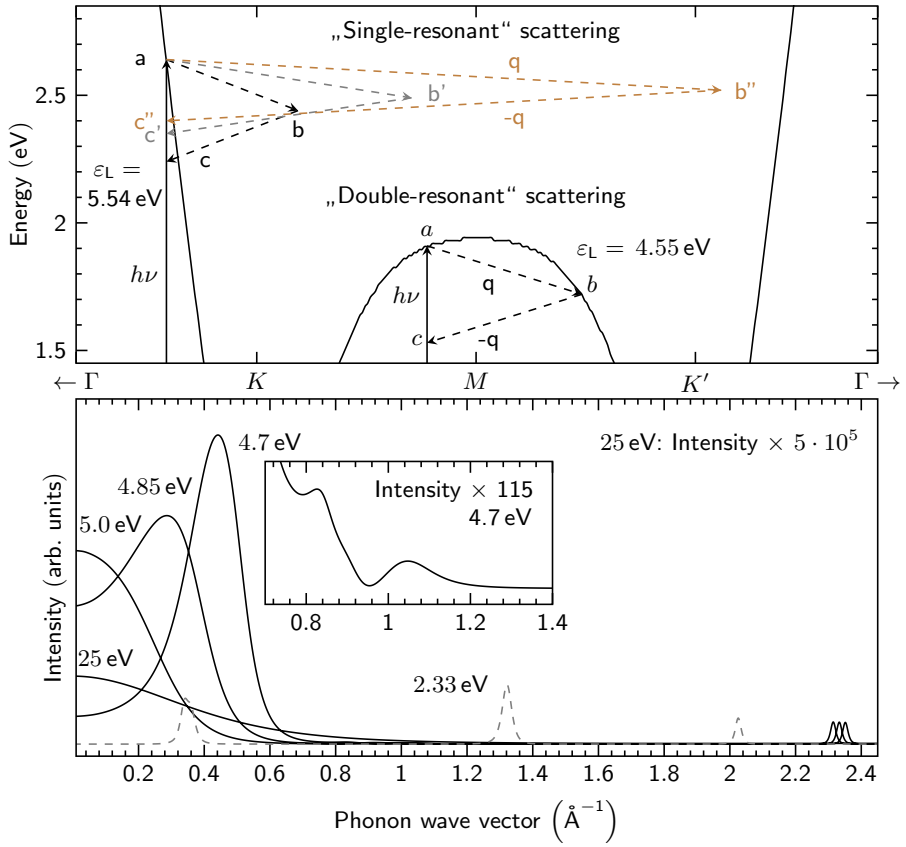

Figure 5.6: Top: Raman scattering schemes for excitation energies of $\varepsilon_L = 5.54\,\text{eV}$ and $\varepsilon_L = 4.55\,\text{eV}$ are plotted into the one-dimensional electronic band structure of graphene. In a single-resonant process, the intermediate states b, b', and b" are not real states whereas in a double-resonant process, the intermediate state (b) is a real state. Phonon momenta for various non-resonant processes are denoted with q and -q. Bottom: Calculated phonon wave vectors in a second-order Raman process for various laser excitation energies as given in the figure are plotted. The calculation is restricted to the high-symmetry lines with no coupling elements considered as shown in equation 2.5. The inset shows resonant phonon wave vectors for an intravalley scattering process. Electronic bands are calculated within a third-nearest neighbor tight-binding approach.

The large mismatch of electron momenta can be seen in the double-resonant scattering scheme in Fig. 5.6. In fact, due to the slope of the valence band, the mismatch of electron momenta is maximal for excitations close to the M-point transition energy compared to all other processes over the 1. Brillouin zone. Assuming a resonant scattering to a real state in the valence/conduction band, it is $\Delta k_{\text{final}}^{\text{initial}} \approx 1.5\, q^{\text{resonant}}$ (compare Fig. 5.6). Although the initial state is real, this aspect should reduce the intensity of the $2D$ peak in graphene/graphite when excited with $\varepsilon_L \sim 4.7\,\text{eV}$.

The concept of double-resonant Raman scattering allows for more scattering processes than its denotation suggests. It is a convenient concept since due to the very strong enhancement of subset scattering paths, all other possible scattering paths can be neglected when explaining the Raman spectra of graphene or graphite [9, 14].
Instead of being scattered to a real state, an excited electron in the valence band can be scattered to a non-real, intermediate state and backscattered to an electron state exhibiting the same momentum as that of the initially excited electron. We refer to such a process

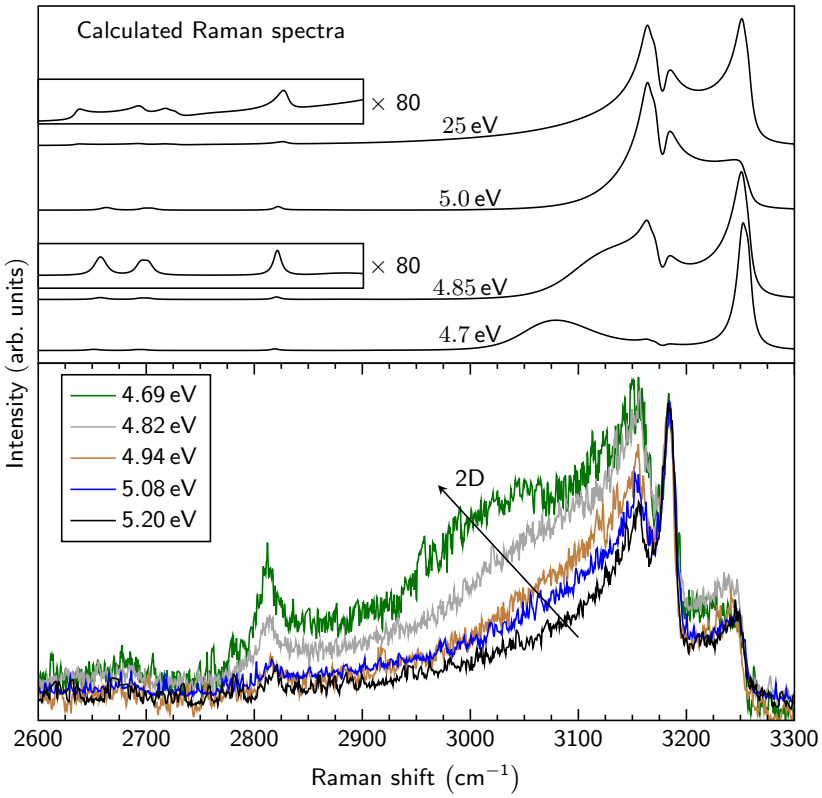

Figure 5.7: Raman spectra of graphite for different laser excitation energies. The arrow indicates the $2D$ mode for very small phonon wave vectors.

as a "single-resonant", second-order scattering process since only one real state is involved. For instance, if we assume an incoming resonance, only the initial state is a real electronic state. Various scattering paths are plotted in Fig. 5.6 entitled with "Single-resonant" scattering. In such a process, the phonon wave vector can exhibit values stemming from all over the 1. Brillouin zone and is not restricted to a small set of wave vectors connecting real electronic states as apparent in a double-resonant process. None of these processes is resonantly enhanced and thus, all of them contribute equally to a Raman spectrum. As a result, the spectrum of single-resonant, second-order Raman processes is weighted according to the vibrational density of states. In flat regions of the phonon dispersion, a broad range of phonon wave vectors exhibits equal energies and thus, these contributions add up to a considerable peak in the Raman spectrum. The asymmetry of the Raman peaks directly reflects the slope of the measured phonon branches. In order to understand the scattering process in more detail we have calculated the Raman spectra for excitation energies close and above the M-point exciton energy by using the following equation [9]:

$$\mathcal{I} \propto \sum_{\alpha=1}^{6} \left| \sum_{a,b,c} \frac{\mathcal{M}}{(E_L - E_{ai} - i\gamma)(E_L - E_{bi} - \hbar\omega_\alpha - i\gamma)} \times \frac{1}{(E_L - E_{ci} - 2\hbar\omega_\alpha - i\gamma)} \right|^2, \tag{5.5}$$

All coupling elements $\mathcal{M}$ are set to 1 and we restricted the scattering process only to the high-symmetry directions as shown in Fig. 5.3. The sum in the absolute value contains all possible states a, b, and c as denoted in Fig. 5.6. The outer sum considers the respective

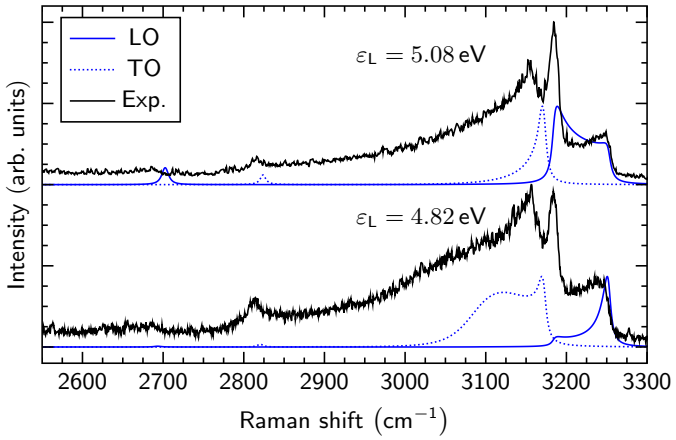

Figure 5.8: Calculated (blue) and experimental (black) Raman spectra are given for excitation energies of $\varepsilon_L = 5.08\,eV$ and $\varepsilon_L = 4.82\,eV$. TO (transverse optical)phonon contributions are plotted in dashed lines, LO (longitudinal optical) phonon contributions in continuous lines.

pairs of the TO, LO, and LA phonon branches.
Calculated resonant phonon wave vectors for excitations close and way above the M-point energy are plotted in Fig. 5.6. Due to the lack of reliable broadening parameters for such high excitation energies, we have assumed a broadening parameter of $\gamma/2 = 120\,meV$ for all calculated spectra in Fig 5.6. Considering a parabolic dependency of the broadening parameter γ on the laser excitation energy, as suggested by Venezuela *et al.* [14], we would end up with a broadening factor of $\gamma \sim 240\,meV$. This very high value is also predicted by Popov *et al.* [179], but an experimental verification is up to today still missing. However, since we mainly discuss single-resonant, processes that do not include resonant intermediate states, the influence of the broadening factor is comparably low [180].

As a consequence of the flat bands of both electrons and holes in the proximity of the M point, the resonant phonon wave vectors for such high excitation energies are short and very broad (compare Fig. 5.6). When the excitation energy is tuned above the M-point energy, the double-resonant Raman process vanishes accompanied by a reduction of both the length of the resonant phonon wave vectors and their intensities. For an artificially high excitation energy of 25 eV, there is no distinct resonant scattering process recognizable anymore. However, the scattering amplitude is small but nonzero leading to contributions with very low intensities.

An optical excitation close to the M-point leads to intervalley scattering processes with the shortest phonon wave vectors possible. Two-phonon Raman modes like the widely discussed $2D$ band will therefore be found at different phonon energies than usual for excitation in the optical visible range. In fact, we find the $2D$ band experimentally around $3050\,cm^{-1}$ as shown in Fig. 5.7. A tuning of the laser excitation energy from 5.2 eV down to 4.69 eV leads to a decrease of the phonon frequency, accompanied by an increase of $2D$-mode intensity. To some extent, we can speak of "the beginning" of the $2D$ mode as the phonons involved are zone-center phonons.
It is further interesting to note that intravalley scattering processes have the longest resonant phonon wave vectors possible for excitations close to the M point. A corresponding

inset with a magnification factor of 115 is given in Fig. 5.6. Further, due to the trigonal warping, the separation between the scattering paths $M \rightarrow \Gamma$ and $\Gamma \rightarrow M$ is also the largest possible. In the Raman spectrum, both peaks should therefore be very well distinguishable due to a comparably large separation of their phonon frequencies. However, in the experiments we are not able to see contributions of such a process that is usually referred to the $2D'$ band with two LO phonons involved [14] and very well observable for excitation energies in the visible range. In the discussed UV range, the corresponding Raman peak was around $3200\,\mathrm{cm}^{-1}$ and therefore, we believe it is screened by the second-order DOS peaks. To sum up, we can say that second-order Raman processes for deep-UV excitation close to the M-point energy in graphite involve unusual phonon wave vectors that lead to unusual Raman spectra.

In our calculations, we can distinguish between the phonon branches contributing to the overall Raman spectrum for a certain excitation energy. Fig. 5.8 shows a comparison of experimental and calculated Raman spectra where only the LO or the TO phonon branches are considered, respectively. As can be seen, the DOS peaks in the experimental Raman spectra can be assigned to both LO and TO contributions. The higher energy components generally originate from the LO phonon branch whereas the lower energy contributions stem from the TO phonon branch. An excitation energy near the M-point exciton leads to reasonable DR contributions associated with the $2D$ band but still exhibiting very low intensities in the order of the not resonantly enhanced DOS peaks.
In the DFT computations, we find the maximum of the LO phonon branch at a phonon wave vector of $0.46\,\mathrm{\AA}^{-1}$. The resonant phonon wave vector for an excitation energy of $\varepsilon_\mathrm{L} = 4.82\,\mathrm{eV}$ also exhibits $q \sim 0.46\,\mathrm{\AA}^{-1}$. As a consequence, the overbending related second-order Raman peak at around $3240\,\mathrm{cm}^{-1}$ is relatively enhanced for excitation energies around 4.82 eV, both in the experiments and calculations.

5.1.4 Deep-UV Raman measurements in graphene and carbon nanotubes

The introduced approach to investigate the vibrational density of states can also be applied to other sp^2 carbon systems such as graphene or carbon nanotubes as shown in Fig. 5.9. Similar to graphite, graphene also exhibits a six-fold rotation axis with a horizontal reflection symmetry but only consists of a single plane. Its point group is therefore D_{6h} [181]. The two atoms in the unit cell allow for six vibrational modes [153, 181]:

$$\Gamma_\mathrm{vib}^\mathrm{Graphene} = A_{2u} + B_{2g} + E_{1u} + E_{2g} \tag{5.6}$$

The degenerate high-energy mode (E_{2g}) does not split up into a phase and anti-phase vibration as in graphite and as a consequence only one peak should be observed in the second-order DOS Raman spectrum of graphene. This can nicely be seen in Fig. 5.9, where the calculated and measured second-order vibrational density of states are shown. Again, in the case of the calculated DOS, the E_{2g} @ Γ peak exhibits a lower intensity compared to other DOS peaks since within the simplified approach, the Kohn Anomaly [143] is not considered. We can determine the energy of the E_{2g} $\Gamma-$point vibration and the maximum of the LO phonon branch to exhibit $1581\,\mathrm{cm}^{-1}$ and $1623\,\mathrm{cm}^{-1}$, respectively [52].

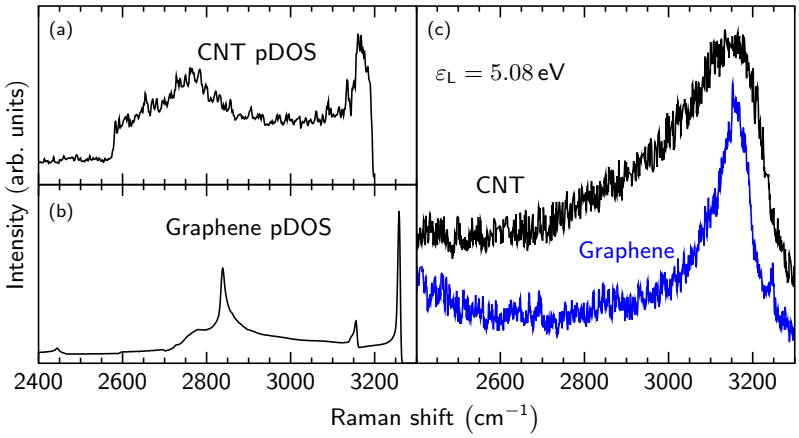

Figure 5.9: Left side: Calculated second-order vibrational density of states (pDOS) of carbon nanotubes (a) and graphene (b) are plotted. We have used the POLSYM code [182] for the calculations of the pDOS from carbon nanotubes and have only considered the chiralities as listed in Table 6.1. An equal distribution of all chiralities has been assumed. The pDOS of graphene has been calculated with a DFT/LDA approach by Roland Gillen [96]. Right side: Experimental, second-order vibrational density of states Raman spectra of an HipCO carbon nanotube sample (black) and graphene (blue) are plotted for an excitation energy of $\varepsilon_L = 5.08\,eV$.

Our findings have recently been confirmed by more complex ab initio calculations from Valentin Popov where the second-order vibrational density of states peaks can be observed for excitation energies above the π plasmon energy [179, 183].

Compared to graphene and graphite, the UV Raman spectrum of CNTs only consists of a single, broad, and asymmetric peak at around $3150\,cm^{-1}$. This experimental result is also reflected in the calculated pDOS for the CNT ensemble in Fig. 5.9 and can be understood from the fact that phonon frequencies in CNTs sensitively depend on the nanotube diameter and chiral angle [16]. The broad diameter distribution of the HipCO CNT ensemble (7 to 13 Å) directly results in a broad range of phonon frequencies. For instance, we infer a range of $2\Delta\omega = 80\,cm^{-1}$ for the second-order high-energy mode frequencies [182], well explaining the experimentally and theoretically observed broad peak centered at $3150\,cm^{-1}$. In contrast to graphene or graphite, we do not observe distinct peaks in our experimental Raman spectrum that are related to the LO overbending or the pDOS at the M point. Again, these phonon frequencies also show a dependence on tube diameter and chiral angle. The expected range of LO-phonon maxima in our CNT sample is [182] $\Delta\omega_{LO,max} = 10\,cm^{-1}$. Thus, all contributions will add up to a broad shoulder on the high-frequency side of the main peak. The broad Raman signal towards lower wavenumbers is attributed to LO-, LA-, and TO-derived phonon bands from the M point that cannot be separated in our experiments. The same counts for the calculated, second-order vibrational DOS of the carbon nanotube HipCO ensemble sample (compare Fig. 5.9). As already mentioned in the case of graphite, the calculated second order DOS does not contain electron-phonon coupling elements. As a result, the relative intensities of apparent Raman peaks are not reproduced correctly. Further, the used POLSYM code [182] underestimates the phonon frequencies, explaining the frequency gap between calculations and experimental data in Fig. 5.9.

Outlook

We believe that the discussed approach can also be applied to other graphitic materials possibly revealing new aspects of second-order Raman scattering. For instance, it could be used to tune the quantum interference of different scattering processes in bilayer graphene as recently shown by Herziger *et al.* [180]. The M-point transition energies of the π_1/π_1^* and π_2/π_2^* bands are different, allowing to address the higher transition individually by a suitable deep-UV laser energy [180]. This in turn eliminates a possible quantum interference between different scattering processes noticeably changing the line shape of the $2D$ band in bilayer graphene [144, 180]. The discussed approach might therefore help to understand the Raman spectrum of bilayer (multilayer-) graphene to a larger extent.

5.2 The second-order vibrational density of states in multilayer graphene

Although the phonon dispersions of graphene and graphite are well understood both theoretically and experimentally in our days, there is still a lack of experimental data concerning the phonon dispersions of multilayer graphene. First and second-order Raman processes can provide a broad access to their phonon dispersions [144, 155, 164, 184–187] but are limited due to optical selection rules. It takes more advanced approaches to break the symmetry of the multilayer systems in order to even get further insights into their vibrational properties: Layer-dependent doping [188], arbitrary twisting angles of adjacent layers [189], or tensile and compressive strain [190]. However, it is experimentally still unclear how for example the ZO related out-of-plane vibrations are affected by the number of adjacent layers and their interactions or if the Kohn Anomaly affects different Γ point vibrations differently in multilayer graphene.
On the other hand, the phonon dispersions of multilayer graphene have been calculated by various groups with DFPT (density-functional perturbation theory) approaches [191,192]. It is interesting to note that a DFT approach on the LDA (local density approximation) level gives a reasonable agreement to experiments even without the explicit consideration of a dispersion correction [156]. Instead, on the GGA (general gradient approximation) level, the interlayer distance is too large by 30 % and therefore the Raman active shear modes are predicted to exhibit way too small energies [156]. An *a posteriori* dispersion correction is needed to overcome these insufficiencies [156].
We have tried to utilize the possibility to measure the phonon density of states to find a new approach for a layer-number determination. Since every new layer in multilayer graphene adds six phonon branches including one pair of degenerate LO/TO phonon branches at the Γ point, it should be possible to observe the new peaks in the DOS Raman spectra. Measuring the second-order peaks again ensures Raman activity as discussed in the previous section.

On the following pages we discuss our findings and the challenges we had to encounter for reliable measurements.

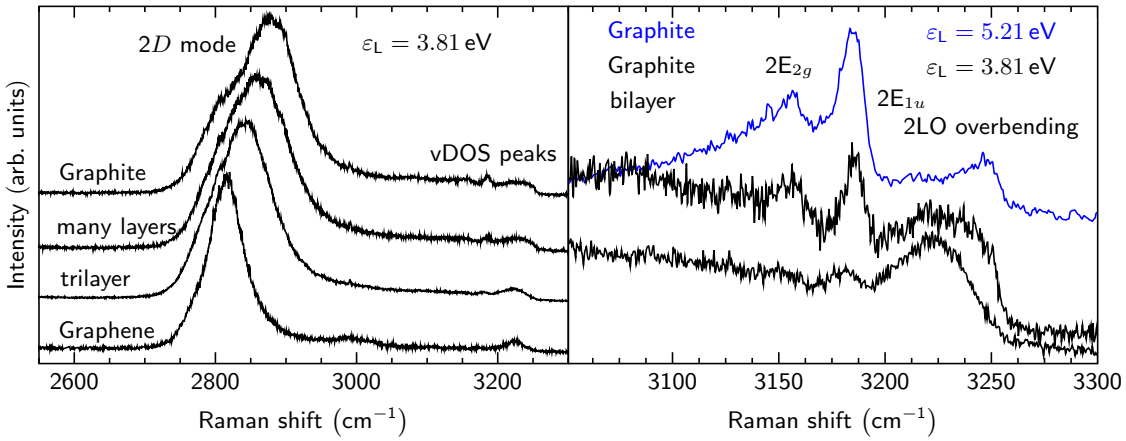

Figure 5.10: Left side: Raman spectra of Graphene, trilayer graphene, many layer graphene, and graphite for an excitation energy of $\varepsilon_L = 3.81$ eV are plotted. Denoted is the $2D$ band that was used for a layer-number determination. vDOS stands for the vibrational density of states. Right side: Close-up of the second-order density of states related Raman peaks as named in the figure are plotted. Shown are spectra for graphite ($\varepsilon_L = 3.81$ eV and $\varepsilon_L = 5.21$ eV) and for bilayer graphene ($\varepsilon_L = 3.81$ eV). As a protection layer, 30 nm Al_2O_3 layer has been deposited onto the silicon wafer with the graphene samples.

5.2.1 Layer-number determination and sample characterization

A sample characterization is necessary before we can measure the second-order density of states and assign the results to a multilayer graphene sample with a defined number of adjacent layers. We have used mechanically exfoliated graphene on a SiO_2/Si substrate. Several techniques are available to determine the amount of graphene layers of a sample: An analysis of the $2D$ line shape [164, 193], optical contrast measurements [194, 195], an analysis of shear modes [155], or an analysis of stoke/anti-stokes, double-resonant processes with out-of-plane phonons [187]. A first characterization was done via optical contrast measurements and was then verified by an analysis of the $2D$ line shape. Various spectra of the analyzed multi-layer graphene samples for an excitation energy of $\varepsilon_L = 3.81$ eV are plotted in Fig. 5.10. Note that the $2D$ line shapes for the shown excitation energy differ from those usually shown in literature. The characteristic low-energy contributions originating from symmetric processes in bi- and trilayer graphene will be less visible for very high excitation energies as the resonant phonon wave vectors of symmetric and anti-symmetric get more similar and the TO phonon splitting decreases [144, 193]. Also, mainly due to a higher electron-phonon-coupling, the electronic broadening for higher excitation energy increases leading to a strong destructive quantum interference of symmetric and anti-symmetric scattering processes [14, 144, 180]. This in turn pronounces high-wavenumber, symmetric contributions explaining the asymmetric line shapes of the $2D$ band as can be seen in Fig. 5.10 [144, 164, 180, 193].

With the sample characterization we can now advance the discussion to the layer number influence on the second-order density of states as shown in Fig. 5.10. Plotted are the second-order DOS peaks for bilayer graphene and graphite for an excitation energy of $\varepsilon_L = 3.81$ eV and for comparison, also the second-order DOS peaks of graphite for an excitation energy of $\varepsilon_L = 5.21$ eV. It can be seen that the second-order DOS peaks of the $2E_{2g}$ and $2E_{1u}$ modes are except of their intensity ratios similar. In fact, these

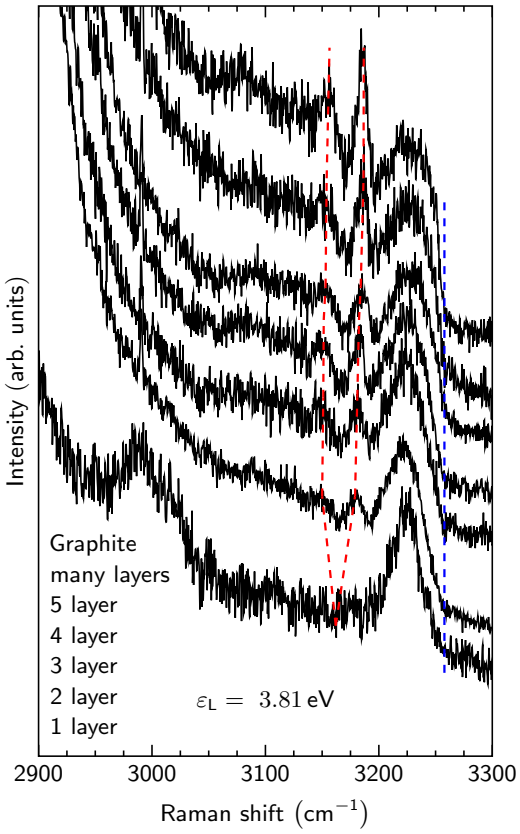

Figure 5.11: Raman spectra of graphene, multilayer graphene, and graphite as named in the figure are plotted. The laser excitation energy is $\varepsilon_L = 3.81\,\text{eV}$. The red dashed lines denote the slope of DOS peaks originating from the E_{2g} vibration in graphene [153, 154] as a function of the layer number. The blue dashed line corresponds to the maximum of the LO related second-order peak in graphite [52] (compare Fig. 5.5). As a protection layer, 30 nm Al_2O_3 layer has been deposited onto the silicon wafer with the graphene samples.

peaks should be observable for every excitation energy possible as the single-resonance Raman process described in the previous section involves phonons with arbitrary wave vectors. However, they tend to be screened by the $2D'$ mode [14, 196] and due to their single-resonance character, their intensities are magnitudes smaller compared to other second-order Raman modes [9, 14, 196]. Compared to graphite, the DOS related peaks in bilayer graphene are both downshifted to $3181\,\text{cm}^{-1}$ for the higher and to $3150\,\text{cm}^{-1}$ for the lower mode. Due to the reduced symmetry of the bilayer graphene lattice (D_{3d}), the observed peaks can be related to vibrations with the irreducible representations E_g (lower-frequency mode) and E_u (higher-frequency mode), different than those in graphite as denoted in Fig. 5.10 [153, 191, 192]. According to DFT calculations on a GGA or LDA level, the IR active, high-frequency anti-phase vibration in bilayer graphene (E_u) should exhibit a lower frequency compared to the E_{1u} mode in graphite [191, 192]. We find a difference of $\sim 5\,\text{cm}^{-1}$ in the second-order measurements translating into a downshift of $\sim 2.5\,\text{cm}^{-1}$ of the actual Γ-point frequency. This value is in very good agreement to DFT calculations where values between $2\,\text{cm}^{-1}$ and $3\,\text{cm}^{-1}$ are found [191, 192]. In the calculations, the frequency of the E_g mode in bilayer graphene is less affected compared to the E_{2g} mode in graphite but depending on the computational approach, a slight upshift is predicted [191, 192]. We instead also find a downshift of $\sim 2\,\text{cm}^{-1}$ for the E_g mode in bilayer graphene in the experiments as shown in Fig. 5.10.

A more comprehensive picture on how the DOS related second-order Raman peaks change as a function of the layer number is given in Fig. 5.11. The red, dashed lines indicate how the average frequencies of the DOS related peaks evolve from the E_{2g} mode in graphene. The dashed, blue line indicates the maximum of the 2LO overbending fre-

quency in graphite (compare Fig. 5.5).
From the presented measurements we can derive several statements: *(i)* For all multilayer samples, we observe two distinct, DOS related Raman peaks. This clear separation indicates, that the frequencies of new vibrational modes added by each new layer are very close to the initial E_u ($1591\,\mathrm{cm}^{-1}$) and E_g ($1576\,\mathrm{cm}^{-1}$) modes in bilayer graphene. *(ii)* We observe an upshift of the DOS peaks at around $3182\,\mathrm{cm}^{-1}$ and no significant shift of the $3152\,\mathrm{cm}^{-1}$ DOS peak when the layer number is increased. *(iii)* The intensities of the E_{2g} Γ-point related second-order peaks increase, compared to the LO overbending peaks for larger layer numbers. *(iv)* The maximum of the 2LO overbending frequencies only marginally change as a function of the layer number as indicated with the blue, dashed line in Fig. 5.11. *(v)* The FWHM of the 2LO overbending related peaks increase with increasing layer numbers. *(vi)* Compared to the deep-UV Raman spectra, the 2LO overbending related Raman peaks exhibit a Lorentzian line shape, *i.e.* they can rather be related to a double-resonant, second-order Raman process.

With the help of calculated phonon dispersions of graphene, AB bilayer graphene, and ABA trilayer graphene, we can understand the experimentally obtained Raman spectra as shown in Fig. 5.11. When the layer number is increased to three (black, trilayer graphene), a new pair of TO/LO phonon branches at the Γ point appears very close to the E_g mode in bilayer graphene (blue, bilayer graphene) as shown in Fig. 5.12 a). In contrast to graphene, trilayer graphene does not have an inversion center anymore, the six-fold rotational symmetry reduces to a three-fold rotational symmetry, but the horizontal reflection plane is conserved [153]. The reduced symmetry translates into the D_{3h} point group for trilayer graphene allowing for the irreducible representations $E^{'}$ and $E^{''}$ originating from the E_{2g} mode in graphene [153]. The two $E^{'}$ modes found in trilayer graphene are responsible for the highest and lowest pair of the three pairs of degenerate TO/LO phonon branches at the Γ point (compare Fig. 5.12). The third mode has the irreducible representation $E^{''}$ and is separated by less than $2\,\mathrm{cm}^{-1}$ from the lower $E^{'}$ mode at the Γ point [192]. All $E^{'}$ and $E^{''}$ modes are Raman active [192].

In the used DFT + LDA approach, we also find the new pair of degenerate TO/LO phonons at the Γ point very close to the lower $E^{'}$ in good agreement to our experimental findings (compare Fig. 5.12). When the layer number is increased, our experimental findings indicate that new pairs of degenerate phonon branches are very close to the E_{2g} and E_{1u} modes in graphite, even closer than predicted in theory [191, 192].
To understand the experimental Raman spectrum, we have calculated a Raman spectrum of graphene for an excitation energy of $\varepsilon_\mathrm{L} = 3.81\,\mathrm{eV}$ as shown in Fig. 5.12 d). We have used the approach as suggested in Ref. [9], have set all matrix elements to 1 and have only considered second-order processes involving LO phonons For comparison, we have plotted a smoothed experimental Raman spectrum of graphene for the same excitation energy next to the calculated Raman spectrum. We find a good agreement and thus it it tempting to assign the experimental peak to a second-order, double-resonant Raman process of the LO phonon branch. The bimodal peak structure in the calculated Raman spectrum originates from the anisotropic slopes of the electronic bands due to the trigonal warping effect. The double resonant process in which the initial electronic state is in

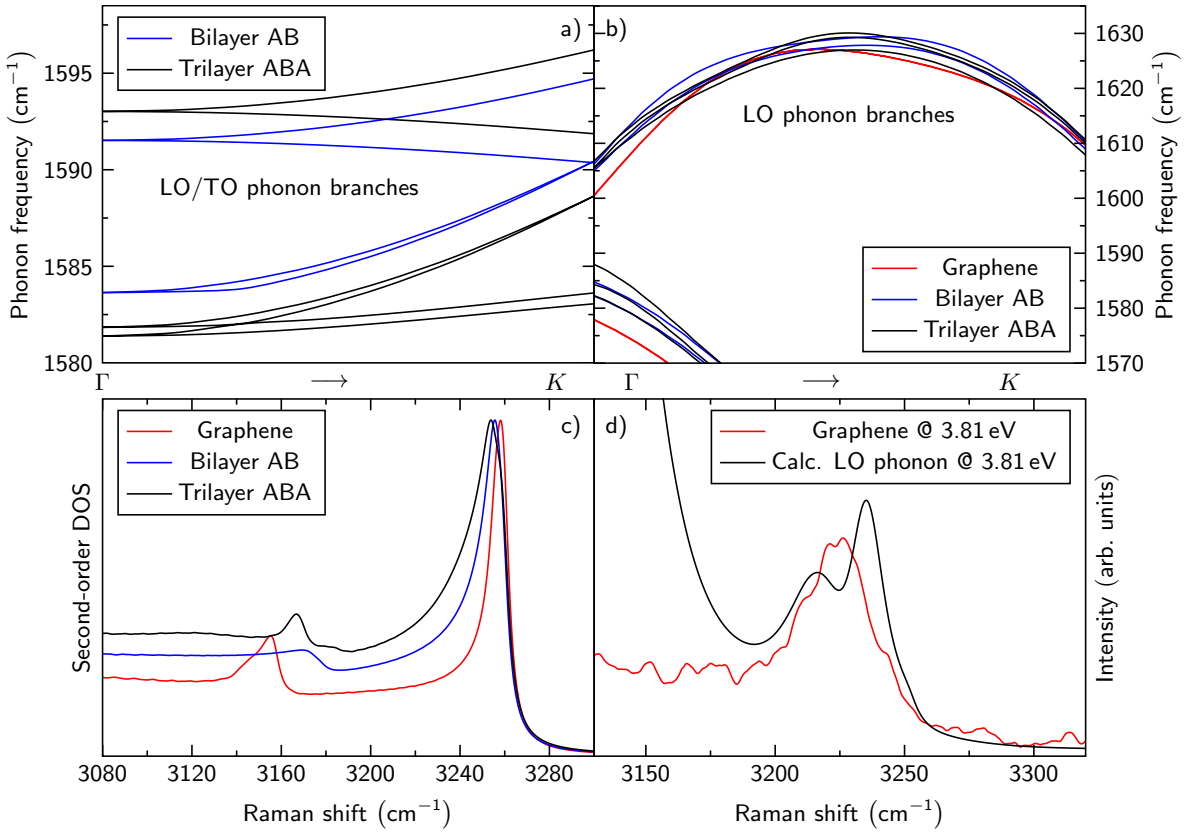

Figure 5.12: Top: Parts of the calculated phonon dispersions of graphene, bilayer graphene, and trilayer graphene are plotted. a) The LO/TO phonon branches at the Γ point from Bernal stacked bilayer graphene (blue) and from Bernal stacked trilayer graphene (black) along the $\Gamma \longrightarrow K$ direction are plotted. b) The maxima of the LO phonon branches of graphene (red), Bernal stacked bilayer graphene (blue), and Bernal stacked trilayer graphene (black) along the $\Gamma \longrightarrow K$ direction are shown. c) High-frequency parts of the, second-order vibrational density of states of graphene (red), Bernal stacked bilayer graphene (blue), and Bernal stacked trilayer graphene (black) are plotted. d) An experimental Raman spectrum of graphene is plotted (red). As a protection layer, 30 nm Al_2O_3 layer has been deposited onto the silicon wafer with the graphene sample. A corresponding calculated Raman spectrum for an excitation energy of $\varepsilon_L = 3.81$ eV just considering the LO phonon branch of graphene is shown in black. All matrix elements are set to 1. The phonon dispersions are calculated with a DFT/LDA approach, provided by Roland Gillen [96].

the proximity of the $K - M$ direction should be more dominant because of a reasonably higher oscillator strength [197]. In the experiment, we should therefore only observe a single peak in contrast to the simplified calculations. Its resonant phonon wave vector is shorter, accompanied by a slightly higher phonon frequency as plotted in Fig. 5.12 d). The situation gets more complicated for a larger number of layers as in general due to additional π and π^* electronic bands, more optical excitations are possible allowing for various double-resonant scattering paths. In all of them, slightly different resonant phonon wave vectors are involved, resulting in diverse Raman shifts. This somewhat general trend can be followed when comparing the Raman spectra in Fig. 5.11. The peak at around 3220 cm^{-1} broadens and gets more asymmetric when the number of layer increases.

The maxima of the LO phonon branches for the three calculated system are very close as can be seen in Fig. 5.12 b). However, they differ in the phonon wave vector exhibiting

the maximum frequency [191]. This should be observable in a double-resonant Raman process: The laser excitation energy required to observe the highest G′-mode frequency should be different in graphene compared to bi-, tri- or multilayer graphene. However, this is only a prediction from theory and, to our best knowledge, a corresponding experiment has not been performed yet. The additional LO phonon branches will cluster between the E_{2g} and E_{1u} modes in graphite when the layer number increases [191]. Therefore the maximum frequency does not reasonably change as a function of the layer number, but the vibrational density of states increases, especially for contributions slightly below the maximum of the LO overbending. A corresponding plot can be seen in Fig. 5.12 c) where the LO phonon related DOS peak ($\sim 1630\,\mathrm{cm}^{-1}$) broadens as a function of the layer number.

Experimental challenges with deep-UV measurements of graphene and related compounds

It is well known that there is a reasonable interaction of graphene and related compounds with UV light, especially in the presence of oxygen [198–201]. This has turned out to be a problem as, except for graphite, the carbon related compounds simply disappear after a short UV light exposition with an accompanying decrease of Raman intensity. This also applies to functionalized and pristine diamondoids as discussed in Chapter 4 although their bandgaps are partly above the used laser excitation energies. To circumvent this problem, we have not just integrated the Raman intensity over time, but also over an area. Resulting Raman spectra are then added up to increase the signal-to-noise ratios. For instance, graphene is only stable for about 25 s under an irradiation intensity of $\sim 1\,\mathrm{mW}$ independent from the laser excitation energy in the deep-UV region. In fact, we could not find any differences in its stability for photon energies between 4.69 eV and 5.46 eV. In contrast, graphite seems to be stable under UV irradiation. We however believe that also graphite degenerates in the focus volume of the laser spot but there are always sufficient graphite residuals left giving rise to a reasonable Raman signal. Although we have used integration times up to 4h, we could not observe changes in the Raman spectra of graphite throughout many samples.

Compared to graphene, multilayer graphene is supposed to be more stable in the face of external influences, mainly due to a strain reduction [202, 203]. In our UV-Raman experiments we have yet observed a fast degradation of the measured samples. We have therefore tried to measure the multilayer graphene samples in a nitrogen and in an argon atmosphere to avoid the contact to oxygen from the atmosphere. Nevertheless, we have still observed a sample degradation but with a lower rate. A last attempt to stabilize the samples has been done with the help of the Ralph Krupke group [204] from the KIT (Karlsruhe Institute of Technology) where atomic-layer deposition (ALD) has been used to deposit Sapphire (Al_2O_3) onto a pre-characterized Si/SiO_2 wafer with multilayer graphene samples. The Sapphire layers were supposed to encapsulate the multilayer graphene from extrinsic influences. We have tested thicknesses of 10 nm, 20 nm, and 30 nm.
Unfortunately, we have still not been able to stabilize the samples for a sufficient time of $\sim 1.5\,\mathrm{h}$ necessary for the deep-UV measurements. The Sapphire deposition however reduced the degradation rate.

In the end, we have not been able to convincingly distinguish between Raman spectra from multilayer samples in the deep-UV regions. In a degradation process, we remove the uppermost layers first, followed by a degradation of the next layers. For instance, this turns four-layer graphene into three-layer graphene, into bilayer graphene, and then into single-layer graphene, making assignment of appearing Raman peaks to a certain layer number unfeasible. To circumvent this problem, we have decided to measure in the near-UV rather than in the deep-UV as shown for the graphite, graphene, and carbon nanotubes samples. Although not discussed before, we have not observed a degradation for excitation energies of $\varepsilon_{\mathrm{L}} = 3.81\,\mathrm{eV}$ and a Sapphire layer thickness of 30 nm even for integration times up to 3 h and laser powers of $\sim 5\,\mathrm{mW}$. This has made layer-number dependent density of states measurements possible.

5.2.2 Temperature-dependent Raman measurements of the second-order vibrational density of states

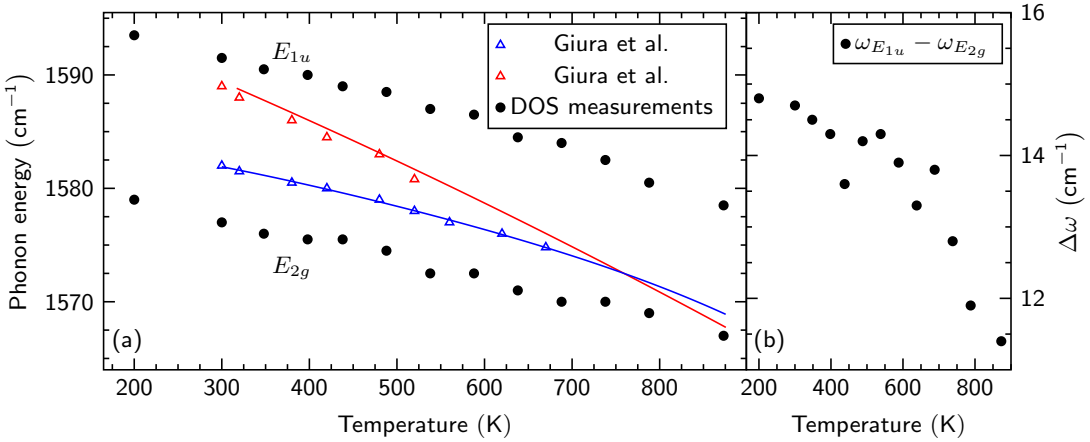

Figure 5.13: (a) Temperature-dependent Raman shifts of the E_{1u} and E_{2g} mode in graphite are plotted. Red and blue data points are taken from Ref. [177]. Circles correspond to density of states measurements as described in the sections before. (b) The energy difference $\Delta\omega$ of the E_{1u} and E_{2g} modes as shown in (a) is plotted.

The temperature-dependent frequency shifts of Raman-active lattice vibrations in sp^2 carbon materials were reported in detail during the last two decades. A general downshift of Raman frequencies with increasing temperature is observed for all Raman modes including the G-band, the D-band, and the radial-breathing mode (RBM) in carbon nanotubes [177, 205–210]. Reported temperature-dependent shift rates of the G mode in graphite, HOPG (Highly oriented pyrolytic graphite), or carbon nanotubes slightly differ, depend on the heating method, and usually exhibit $\chi \sim 2 \cdot 10^{-2}\,\mathrm{cm}^{-1}/\mathrm{K}$ [177,205–210]. A theoretical explanation for the temperature dependence of the E_{1u} and E_{2g} Γ-point vibrations in graphite is given by Giura *et al.* [177]. According to the authors, the observable downshift occurs due to a strong anharmonic, four-phonon interaction [177, 211]. This effect even superimposes the lattice expansion that leads to an upshift of the Raman frequency when the lattice is heated [177]. Different temperature-dependent shift rates are reported for the E_{1u} and the E_{2g} modes in graphite [177]. This difference is explained by the unlike four-phonon anharmonic coupling of the respective modes to the out-of-plane ZO' branch [177]. However, the calculations can only be partly confirmed by expensive experiments as shown in Ref. [177].

As discussed in the beginning of this chapter, the measurement of the second-order vibrational density of states allows for the contemporaneous measurement of both the IR active E_{1u} and the Raman active E_{2g} modes in graphite without the need of complicated experimental setups [52, 177]. We can further analyze the shift rates of phonon wave vectors away from the Γ point that, to our best knowledge, have not been reported in literature yet. By these measurements, we can more easily cover a larger temperature region compared to the measurements as shown in Ref. [177]. We will show that the temperature-dependent shift rates of the E_{1u} and E_{2g} modes are more similar and do not match for temperatures of 750 K as theoretically predicted [177]. In fact even for tem-

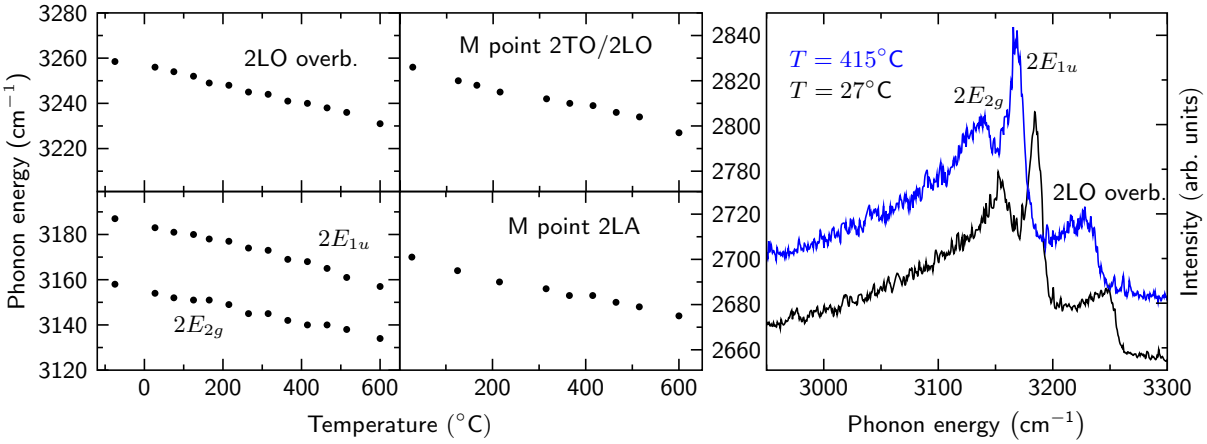

Figure 5.14: Right side: Raman spectra with density of states related Raman peaks of graphite are plotted for two different sample temperatures as given in the figure. Left side: Temperature-dependent shift rates of the second-order density of states peak as given in the figure. Compare Fig. 5.5.

peratures of almost 900 K, the frequencies of the E_{1g} and E_{2g} do not comply with each other. We compare the temperature-dependent Raman shifts of the E_{1u} and E_{2g} modes in graphite to the data shown in Ref. [177] in Fig. 5.13. Solid, colored lines correspond to a fit of the calculated temperature-dependent Raman shift calculated via the four-phonon spectral function [177, 211]. Black dots are measurements of the second-order density of states. Comparing both data sets, we find that there is a good agreement of the experimentally obtained shift rates for the E_{2g} mode. In contrast, the shift rate of the E_{1u} mode is weaker compared to the findings in Ref. [177] where the calculated slope exhibits twice the value of the E_{2g} mode. By linear fits, we find shift rates of $\chi^{E_{2g}} \sim 1.7 \cdot 10^{-2}\,\mathrm{cm}^{-1}/\mathrm{K}$ and $\chi^{E_{1u}} \sim 2.3 \cdot 10^{-2}\,\mathrm{cm}^{-1}/\mathrm{K}$. The blue Raman spectrum in Fig. 5.14 shows that for a temperature of T $\sim$ 700 K, there is still a significant energy gap between the E_{1u} and E_{2g}, contrary to the calculations in Ref. [177]. If we estimate the interception with the help of the fitted linear functions, we find a very high value of T $\sim$ 3100 K. This very high temperature is still below the melting point of graphene [212, 213] and might be realistic, from that point of view.

Various contributions lead to the downshift of both the E_{1u} and E_{2g} vibrational modes. They can be summarized as [177, 211]:

$$\omega_{\mathrm{ph}} = \omega_0 + \Delta\omega^{\mathrm{le}(T)} + \Delta\omega^{3p}(T) + \Delta\omega^{4p}(T) + O(\hbar^2) \tag{5.7}$$

The lattice expansion (le) leads to a slight upshift of phonon energies when the temperature is increased whereas the 3 - phonon contribution (3p) slightly decreases the phonon energies for temperatures above T $\sim$ 500 K [177]. Both contributions are equal for the E_{1u} and E_{2g} modes. The largest contribution has the 4 - phonon interaction giving rise to the overall negative slope [177]. The remaining term is referred to other higher-order contributions.
Since the lattice expansion contribution and the 3 - phonon coupling are the same for both shift rates and since we find a good agreement of both calculations and experiments for the E_{2g} mode, our experimental results suggest that either the anharmonic 4 - phonon coupling for the E_{1u} mode is overestimated or the higher-order contributions are not neg-

ligible. A further reconsideration of the calculations might be needed in order to achieve a better agreement to experiments.

The temperature-dependent shift rates of the M point 2LO/2TO, 2LA, and 2LO overbending phonon energies are $\chi^{q\neq 0} \sim 4.2 \cdot 10^{-2}\,\mathrm{cm}^{-1}/\mathrm{K}$, measured from the second-order peaks *i.e.* they approximately exhibit the same values as found for the Γ-point vibrations. From these measurements, we can say that the anharmonic coupling also counts for vibrations away from the Γ point. Vibrational modes with arbitrary phonon wave vectors away from the Γ point do not exhibit the same symmetry as group theory tells for the high-symmetry points. The area of validity for the model proposed in Ref. [177] is therefore larger than suggested in the article.

5.3 Summary

In summary, we have analyzed the ultra-violet Raman spectra of graphene, graphite, and carbon nanotubes. Different to the widely understood second-order Raman spectra in the optical visible range, we do not find any double-resonant Raman modes for excitation energies higher than 4.7 eV. Instead, we observe second-order vibrational density of states related Raman peaks between ~ 2650 and $3250\,\mathrm{cm}^{-1}$. On the one hand, deep-UV Raman spectra contain peaks from very high momentum M-point phonons that are otherwise not observable in Raman experiments. On the other hand, measuring the second order density of states, allows for the measurement of Raman inactive modes that are not visible in first-order measurements. Ultra-violet Raman spectroscopy therefore gives insights to the phonon dispersions of graphene, graphite, and carbon nanotubes that are otherwise only accessible by more complicated experimental setups.
For an excitation energy close to the M-point energy of $\sim 4.7\,\mathrm{eV}$, we observe the beginning of the $2D$ mode for the lowest phonon momenta possible. In contrast to excitation energies in the optical visible range, the TO phonons involved stem from the proximity of the Γ point with energies up to $1550\,\mathrm{cm}^{-1}$.

By second-order vibrational density of states measurements in multilayer graphene, we show that the layer-number dependent frequency shift of degenerate LO/TO phonons is only small. The LO overbending related second-order peak in multilayer graphene also depends only marginally on the layer number. By these measurements, we can show that the Kohn Anomaly induced downshift of Γ point LO/TO phonon frequencies in graphene and graphite also counts for Raman inactive vibrational modes. Temperature dependent Raman measurements show unlike shift rates of the E_{2g} and E_{1u} modes in graphite. However, we do not find a crossing of both phonon modes up to $\sim 900\,\mathrm{K}$ indicating that the anharmonic phonon coupling for the E_{1u} mode is overestimated in corresponding calculations.

6. Carbon nanotubes - Low-intensity Raman modes and UV spectroscopy

Parts of this chapter are published in Ref. [214]

This chapter discusses low-intensity Raman modes in the spectrum of carbon nanotubes between 1800 cm^{-1} and 2500 cm^{-1}. Although these modes are reported several times in the literature, there is no uniform assignment available. The lack of a comprehensive understanding is further confirmed by the lack of theoretical simulations in the denoted spectral range.
We show measurements with a broad range of excitation energies and calculate double-resonant Raman modes of an ensemble carbon nanotube sample with respect to each individual tube. By these simulations we can assign and understand the dispersions, peak intensities, and general compositions of double-resonant Raman modes. Especially the quasi-continuous dispersions of double resonant Raman modes in ensemble samples have not been theoretically addressed so far.
Raman spectra are simulated by a DFT + zone-folding and a non-orthogonal tight-binding approach with apparent differences in the assignment of the mode at around 1950 cm^{-1}. Both theoretical approaches are extensively discussed with respect to their initial assumptions necessary for the concrete calculations.

Even though carbon nanotubes have been spectroscopically analyzed for more than two decades, detailed data for their optical responses in the UV range are still very scarce in the literature. It is for instance widely unknown how their optical absorption changes for excitation energies close to the M-point energy. With a tight-binding approximation + zone-folding approach, we calculate optical transition energies and matrix elements for all allowed transitions up to those stemming from the Γ point. The so emerging "extended Kataura plot" is discussed in detail as it contains novelties that are not present when only the first optical transitions of carbon nanotubes are taken into account.
Coincidentally, we discovered how carbon nanotubes and UV radiation can be utilized to oxidize iron clusters and form the mineral siderite. We explain the mechanism and discuss its Raman footprint measured in a HipCO CNT sample.

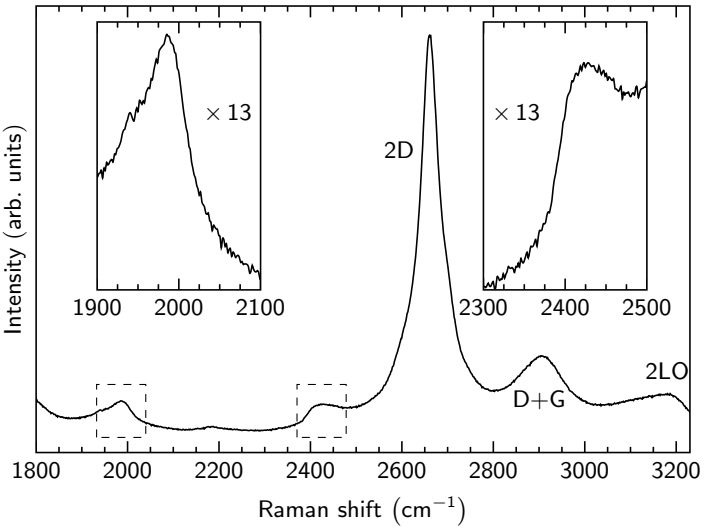

Figure 6.1: Second-order Raman spectrum of an HipCO buckypaper carbon nanotube sample. The laser excitation energy is $\varepsilon_{\mathrm{L}} = 2.41\,\mathrm{eV}$. Insets show a magnification of the analyzed double-resonant Raman modes.

6.1 Low-intensity Raman modes in carbon nanotubes

6.1.1 Low-intensity Raman modes - An introduction

The Raman spectra of carbon nanotubes are today well understood [45, 53, 134, 135, 215]. This counts, in particular, for the broad range of different carbon nanotube samples available where electronic and vibrational properties can differ significantly. In general, carbon nanotube samples used in experiments can be differentiated by their growth mechanism and further by their composition, *i.e.* ensemble samples or samples consisting of isolated carbon nanotubes [38, 216–222]. Ensemble samples can further be distinguished by their constellations: Ensembles with a large variety of chiralities [15, 52, 220, 223, 224], chirality-enriched ensembles [218, 225, 226], or metallic/semiconducting enriched ensembles [227–230]. In contrast, theoretical computations usually consider only particular properties of carbon nanotubes such as optical matrix elements [61, 197, 231], electronic properties [232–235], vibrational properties [16, 93, 232, 236], or electron-phonon coupling elements [80, 237, 238]. There is an obvious disparity between the Raman data that is experimentally obtained and the rather discrete aspects that are theoretically discussed. For the understanding of experimentally obtained Raman data of common samples, it is necessary to consider each individual tube with respect to its unique properties. This usually covers a large set of different electronic and vibrational properties rather than only distinct aspects. On the next pages, we will first give an overview on low-intensity Raman modes and then compare both spectra and calculations of two low-intensity Raman modes in ensemble samples.

A lot of effort has been put in the understanding of the most pronounced modes in the Raman spectra of carbon nanotubes such as the G^+/G^-modes, the D mode, or the radial-breathing mode RBM [215, 220, 229, 230, 238–241]. Instead, low-intensity Raman modes have not been of such a great interest and even today some question are still open. The intermediate-frequency range between the RBM ($\approx 300\,\mathrm{cm}^{-1}$) and the D mode ($\approx 1300\,\mathrm{cm}^{-1}$) exhibits many dispersive low-intensity modes with non-convincing explanations [242, 243]. A more conclusive explanation of the origin from the rich features in the intermediate-frequency region was given recently [244]. Instead, the only

non-dispersive, low-intensity mode found at around 850 cm^{-1} seems to be well understood [15, 16, 245]. The spectral range between the G bands ($\approx 1600\,\mathrm{cm}^{-1}$) and the $2D$ band ($\approx 2700\,\mathrm{cm}^{-1}$) also exhibits many low-intensity dispersive Raman modes that are not yet convincingly assigned. Two of them are highlighted in Fig. 6.1. Experimental works available in literature, tentatively assign these combination modes only by their dispersions in comparison to graphene. Corresponding Raman modes in carbon nanotubes have not been calculated before, impeding a concluding assignment. The Raman mode at around 1950 cm^{-1} is either attributed to a TO+LA or to a LO+LA combination mode from the Γ point. Fantini *et al.* [246] report a multipeak structure and assign the peaks in covalently functionalized carbon nanotubes to originate from scattering with both TO+LA and LO+LA phonons. Brar *et al.* [247] generally assign the mode to a TO+LA combination whereas Ellis *et al.* [248] state the Raman band in acid treated double-wall carbon nanotubes originates from scattering with LO+LA phonons. All articles suggest that the combination mode is an intravalley, process *i.e.*, a $\Gamma-$ point process. The dispersive peak at around 2450 cm^{-1} in graphene and bilayer graphene was explained by a TO+LA combination from the K point, *i.e.* it is an intervalley process with a very good agreement of both experiments and calculations [14, 149, 165, 166]. Its asymmetry can be well explained by the overall two-dimensional scattering process, involving phonon wave vectors adjacent to the high-symmetry directions. A second peak towards higher energies can be observed that was attributed to a LO+LA $@\,\Gamma$ combination with a much lower intensity [14, 149]. It is a quasi non-dispersive peak for the range of phonon wave vectors that can be accessed by excitation energies in the optical visible range. The very weak dispersion can be well understood from the fact that the TO and LA phonon branches in the proximity of the K point have almost similar slopes but with opposite signs [14, 161]. Former assignments stated this process is a 2iTO phonon mode involving $q = \mathbf{K}$ phonon wave vectors [165–167]. However, we believe that this assignment is questionable, since these processes should be canceled out due to destructive quantum interference [14, 145].

In contrast to carbon nanotubes, there is an uniform assignment of Raman modes in the spectral range between 1700 cm^{-1} and 2100 cm^{-1} for other graphitic materials, such as graphene and bilayer graphene. Calculated Raman spectra suggest many possible modes: LOZO$'$ $@\,\Gamma$, TOZO$'$ $@\,K$, LOTA $@\,\Gamma$, LOLA $@\,\Gamma$, TOZO $@\,K$ and a TOTA $@\,K$ in bilayer graphene [249] whereas in graphene LOTA $@\,\Gamma$, LOLA $@\,\Gamma$, 2LA $@\,K$, TOTA $@\,K$, and TOLA $@\,K$ combination modes are suggested [14, 149]. Hereby, the notation "$@\,\Gamma$" refers to an intravalley process, *i.e.* the phonon wave vectors involved stem from the proximity of the Γ point. "$@\,K$" refers to an intervalley process, *i.e.* the phonon wave vectors involved predominantly stem from the proximity of the K points. Due to its symmetry, optical out-of-plane vibrations are Raman forbidden in graphene lowering the amount of possible Raman active combination modes compared to bilayer graphene. Instead, bilayer graphene has an inversion center between the layers, making out-of-plane vibrations Raman active. This gives a reasonable contribution of combination modes with ZO phonons in the spectral region between 1600 cm^{-1} and 2700 cm^{-1} that have so far not been considered in the Raman spectra of carbon nanotubes [14, 249].

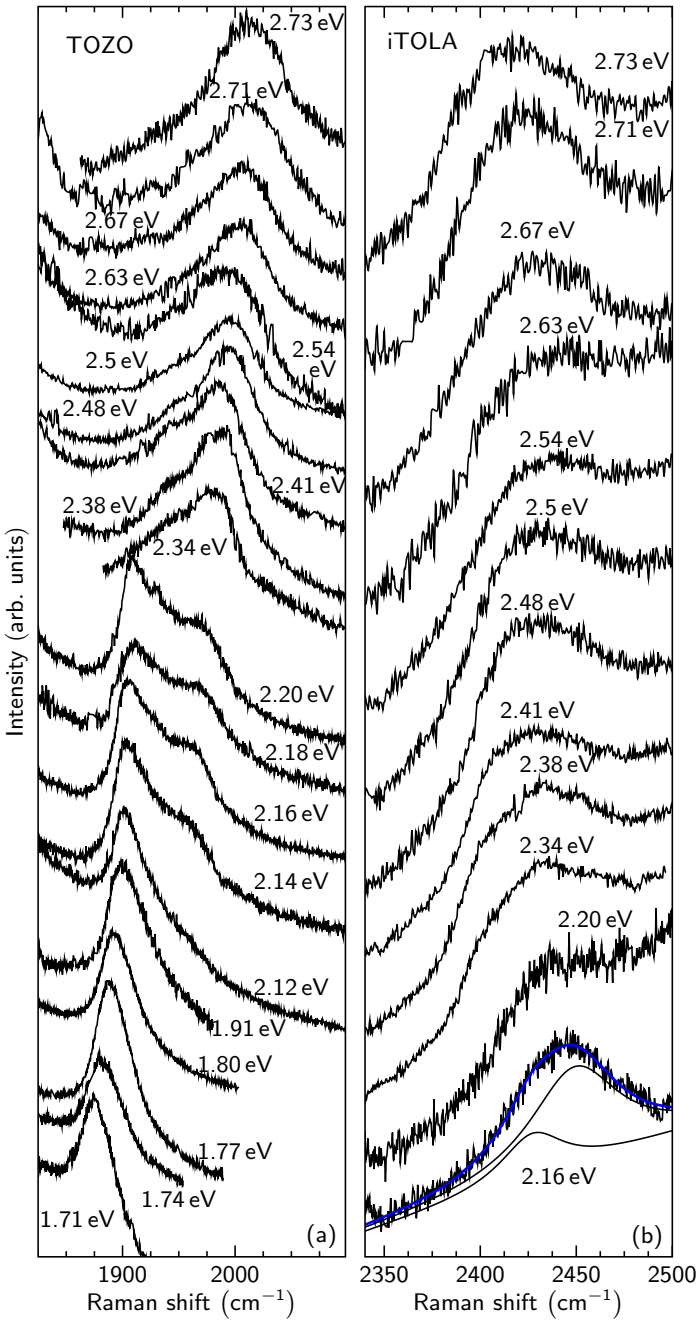

Figure 6.2: [(a) and (b)] Raman spectra of the low-intensity Raman modes as shown in Fig. 6.1 are plotted. Excitation energies are given next to the spectra. [(c) and (d)] Experimentally obtained dispersions for the 1950 cm^{-1} and the 2450 cm^{-1} Raman bands as a function of the laser excitation energy. Lines are linear fits of the bimodal peaks fitted with Lorentzian profiles as indicated in the Raman spectra.

6.1.2 Low intensity Raman modes - Experimental Raman spectra

In Fig. 6.2, we show different Raman spectra of the low-intensity Raman modes as highlighted in Fig. 6.1. A broad range of laser excitation energies between $1.7 - 2.7\,\mathrm{eV}$ is covered. We observe a clear bimodal peak structure for excitation energies between 2.14 eV and 2.5 eV in case of the Raman mode at around $1950\,\mathrm{cm}^{-1}$ (left panel). A change in the excitation energy results in a change of the peak composition. For higher and lower excitation energies, *i.e* below 2.14 eV and above 2.5 eV, the line shape corresponds to a single peak with a slight asymmetry. The low-frequency peak vanishes for increasing excitation energies, whereas the peak towards higher wave numbers arises at 1.9 eV and dominates the Raman spectra up to 2.73 eV. The average frequency difference between the two peaks is around $55\,\mathrm{cm}^{-1}$ for excitation energies between 2.14 eV and above 2.5 eV. Both peaks are highly dispersive, shifting towards higher frequencies with increasing excitation energy. The right panel of Fig. 6.2 shows the low-intensity Raman mode at around $2450\,\mathrm{cm}^{-1}$. For excitation energies between 2.16 eV and 2.73 eV, we observe Raman peaks that exhibit two contributions. They are separated by approximately $25\,\mathrm{cm}^{-1}$ for all measured excitation energies. Both peaks show a weak dispersion towards lower wave numbers increasing the laser excitation energy.
The experimentally obtained Raman frequencies are plotted as a function of the excitation energy in Fig. 6.2. In case of the $1950\,\mathrm{cm}^{-1}$ band, the twofold dispersions exhibit $73\,\mathrm{cm}^{-1}/\,\mathrm{eV}$ and $92\,\mathrm{cm}^{-1}/\,\mathrm{eV}$ for the upper and lower branch, respectively. The experimentally obtained dispersions are in contrast to a previous work where the reported dispersion is found to exhibit $230\,\mathrm{cm}^{-1}/\mathrm{eV}$ [135]. This extremely high value might be understood from the fact that the authors of Ref. [135] did not consider the twofold contributions of the Raman band as shown in Fig. 6.2: Not considering the 'step' in the dispersion would increase the overall dispersion, but only up to approximately $140\,\mathrm{cm}^{-1}/\,\mathrm{eV}$ (compare Fig. 6.4). The remaining gap of roughly $100\,\mathrm{cm}^{-1}$ maybe originates from wrong assignments of the modes in the first place. The experimentally obtained dispersion of the $2450\,\mathrm{cm}^{-1}$ band is $22\,\mathrm{cm}^{-1}/\,\mathrm{eV}$ in good agreement to the literature [14, 135].

6.1.3 Low-intensity Raman modes - DFT calculations

In the following, we will show simulations of both dispersive Raman bands and discuss their respective origins. We first assign the peaks and then discuss the overall line shape of the modes. The quasi-continuous slopes of dispersive Raman bands was a subject of discussion in the literature [135, 218, 220, 222, 251]. Measurements on chirality enriched samples suggest that carbon nanotubes probed within a range of $\approx 200\,\mathrm{meV}$ near their optical transition energies give rise to a reasonable Raman signal with no dispersion [218, 222, 251], due to the van-Hove-singularities in their electronic bandstructures. Off-resonance excitations result in Raman peaks with much lower intensities and only slight dispersions [218, 222, 251]. It was shown that because of the mixing of incoming and outgoing resonances, the intensity maximum of the $2D$ mode for a certain transition energy occurs at $\mathrm{E_{ii}} + \frac{\hbar}{2}\omega_{2D}$ and depending on the particular electronic structure with reasonable contributions from lower transitions $\mathrm{E}_{i-n\,i-n}$ [222]. A similar behavior for other double-resonant Raman modes can be seen in Fig. 6.3 where full Raman spectra of a

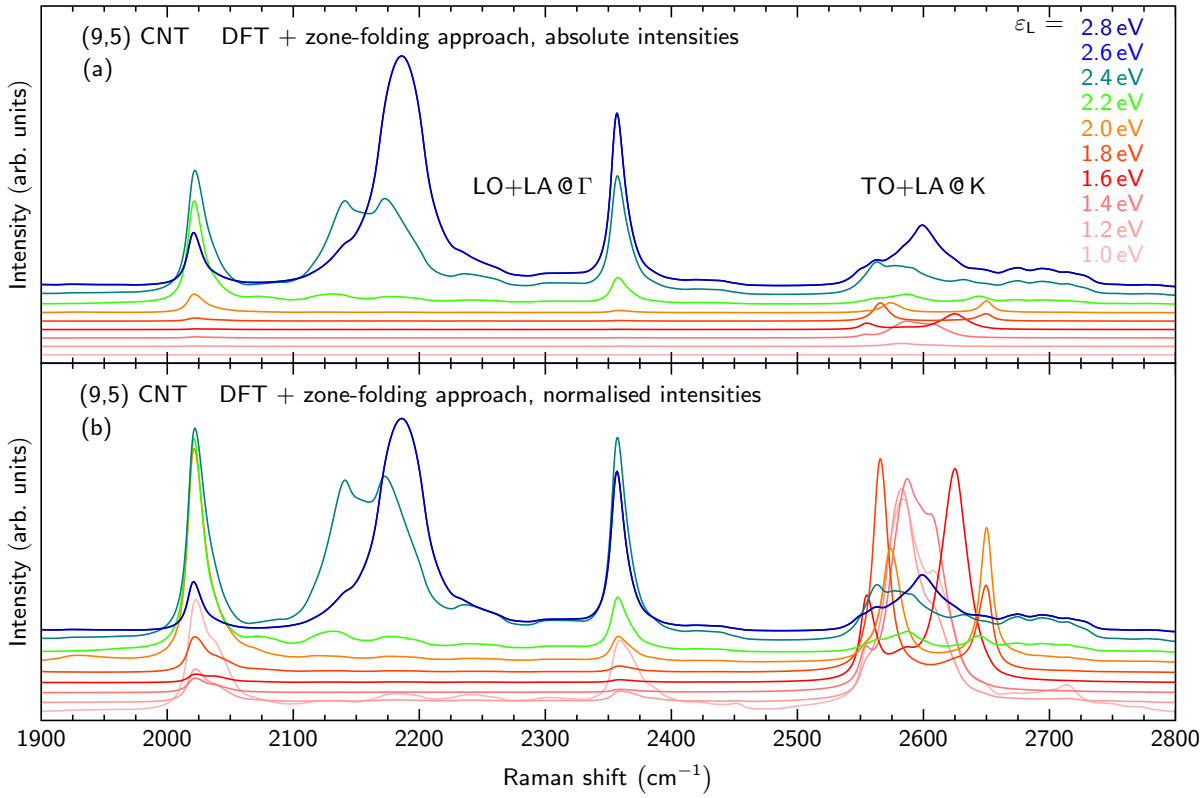

Figure 6.3: Raman spectra of a (9,5) carbon nanotube calculated in a DFT + zone-folding approach are plotted. Considered are an intravalley LO+LA @ Γ and an intervalley TO+LA @ K process. Calculations are done by Rohit Narula [250].

(9,5) carbon nanotube are calculated within a DFT + zone-folding approach by Rohit Narula [250]. The upper part shows Raman spectra with absolute intensities as a function of various excitation energies. According to the optical transition energies and the respective phonon energies, different Raman peaks show resonances with no perceptible dispersions although the excitation energies differ between 1.0 eV and 2.8 eV. This can even clearer be seen in Fig. 6.3 (lower panel) where the same calculations are shown but with a different normalization. In (b), the Raman spectra for each excitation energy are normalized to 1 in contrast to (a) where only the most intense peak of all Raman spectra is normalized to 1, *i.e.* in (a) the relative intensity ratios are correctly reproduced. However, the artificial normalization in (b) reveals low-intensity modes that only show marginal dispersions. The large variety of Raman peaks originates from the mixture of contributions from different optical transitions. For each optical transition, a likewise probing of confined phonon branches with different band indices contributes to the overall spectra as well as contributions from inner and outer processes [222, 251]. For higher excitation energies, intensities of the LO+LA @ Γ combination modes generally exceeds the TO+LA @ K combination due to an increasing joint density of states, in agreement to calculations for graphene [14].

We now advance the analysis from a single tube to an ensemble of carbon nanotubes. To simulate Raman spectra of an ensemble sample, we first need to know its specific composition. We have therefore performed Raman resonance profiles of the RBM between a range of 1.58 eV and 2.73 eV of a HipCO sample. By a comparison of experimentally

Table 6.1: List of carbon nanotubes considered for the calculations. Chiral indices were determined experimentally by resonance Raman profiles of the RBM. Detailed spectra can be found in Ref. [52]

semiconducting	metallic
(16,0) (12,2) (10,2) (10,6)	(7,7) (12,0) (10,4) (9,9)
(9,1) (8,3) (8,6) (7,6)	(9,3) (8,5) (9,6) (11,2)
(11,1) (7,5) (10,3) (9,5)	(11,5) (12,6) (13,1) (10,7)
(11,4) (9,8) (14,1) (12,5)	(13,4) (11,8)
(13,3) (11,7)	

obtained optical transition energies and RBM frequencies to calculations, we can identify individual CNTs with their chiral indices [93, 232, 234]. This approach was first suggested by Hagen Telg and is also referred to as pattern recognition [220]. A list of the so found chiral indices can be seen in Table 6.1. The diameter range is $\approx 7\,\text{Å} - 13\,\text{Å}$ with both semiconducting and metallic nanotubes [52]. With the used set of excitation energies, we optically excite metallic (E_{11}^{M}) as well as semiconducting (E_{22}^{S}, E_{33}^{S}, and E_{44}^{S}) carbon nanotubes.

Similar to the calculations of the (9,5) tube as shown in Fig. 6.3, we have calculated Raman spectra of every individual carbon nanotube listed in Table 6.1. To simulate the ensemble sample, we have then added up each individual spectrum. The resulting Raman spectra are shown in Fig. 6.4. Individual Raman spectra in the first row are normalized to 1 and then summed up to one common Raman spectrum. This reveals low-intensity contributions that are not visible in the bottom row where the Raman spectra of all carbon nanotubes are summed up and then normalized to 1 for each excitation energy. In the latter case, contributions from carbon nanotubes with a low absorption or low electron-phonon coupling elements contribute less to the overall spectrum. Dot sizes in (b) and (d) correspond to the peak intensities in (a) and (c). From the calculations in Fig. 6.4, we can derive several statements: (*i*) We observe a highly dispersive, multimodal Raman band at $\approx 2000\,\text{cm}^{-1}$. Its origin is an LO+LA combination from the Γ point, *i.e.* it is an intravalley process. The Raman bands also contain TO+LA contributions from the Γ point but with a much lower intensity. (*ii*) We find a multimodal TO+LA combination mode at around $2580\,\text{cm}^{-1}$. In contrast to the experiments, it exhibits a weak positive dispersion of $70\,\text{cm}^{-1}/\text{eV}$ and can be referred to an intervalley process. The weak dispersion both in the experiments and calculations can be attributed to the likewise dispersions of the TO and LA phonon branches in the proximity of the K point, but with different signs [14, 152, 161]. (*iii*) The dispersion of the Raman bands from the ensemble measurements originates from different carbon nanotubes that are in resonance to the excitation energy. Each CNT adds an unique contribution depending on its chirality, the excitation energy, and the lengths of the relevant phonon wave vectors involved in the second-order Raman process. The relevant double-resonant Raman modes of a single carbon nanotubes do not show a substantial dispersion. Thus, the dispersion can be explained by an average Raman spectrum of all carbon nanotubes in the sample [218, 222]. (*iv*) The zone-folding calculations considered all 6 graphene derived phonon branches against each other for a

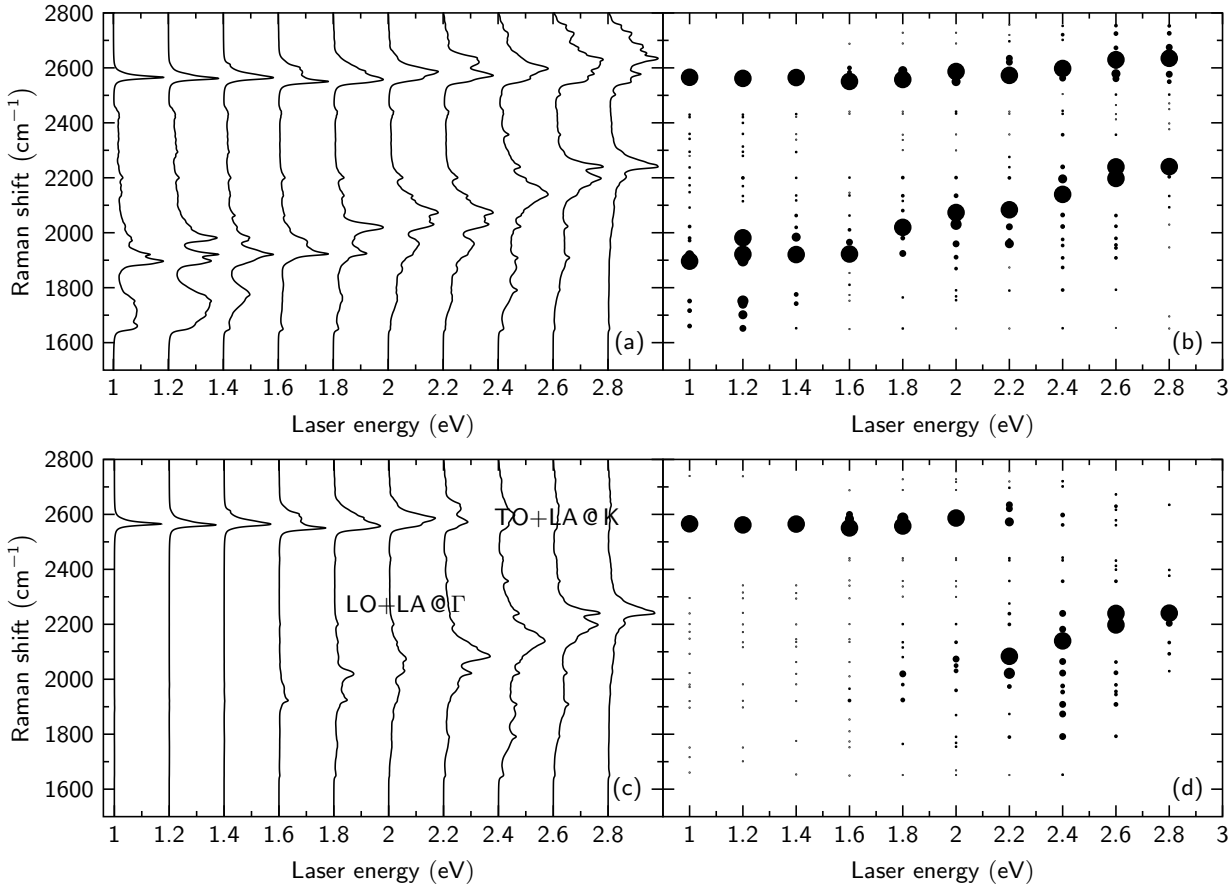

Figure 6.4: Calculated Raman spectra in a DFT + zone-folding approach are plotted. The dot diameters represent intensities of single peaks. In (a) and (b), the intensities of the combinations modes are separately normalized to 1 and then composed to a spectrum. In (c) and (d), the combination modes are summarized and then normalized to 1. According to the used approach, the 2450 cm^{-1} mode can be assigned to a TO+LA @ K and the 1950 cm^{-1} mode to a LO+LA @ Γ process as denoted in the figure. Calculations were carried out by Rohit Narula [250].

total of 36 possible combinations modes. The assignment of combination modes was done analyzing the Raman intensities and dispersions of all possible processes. As a consequence, the calculations indicate that the combination modes LO+LA @ Γ (1950 cm^{-1}) and TO+LA @ K (2450 cm^{-1}) are responsible for the two low-intensity Raman bands observed in the experiment, in agreement to former assignments in graphene [14]. This explicitly excludes a possible TO+ZO @ K process, as suggested by A. Vierck, due to ultra-low electron phonon coupling elements. Joint phonon energies of such a process would be close to those from a LO+LA @ Γ process and thus, it must be considered in the discussion. However, the zone-folding approach is known to give incorrect results especially for the acoustic modes. For instance, it fails to predict the twiston acoustic mode or the transition of the out-of-plane ZA acoustic mode into an optical phonon in carbon nanotubes (RBM) [45]. Moreover, scattering processes with out-of-plane ZO phonons in graphene are forbidden by symmetry [14] which does not necessarily counts for carbon nanotubes [15, 16, 52]. Therefore, the contributions of a possible TO+ZO @ K process might be underestimated in a DFT + zone-folding approach. (v) Calculated phonon energies are systematically higher than the experimental values due to the well-known underestimation of both electron and phonon energies on account of the employed LDA

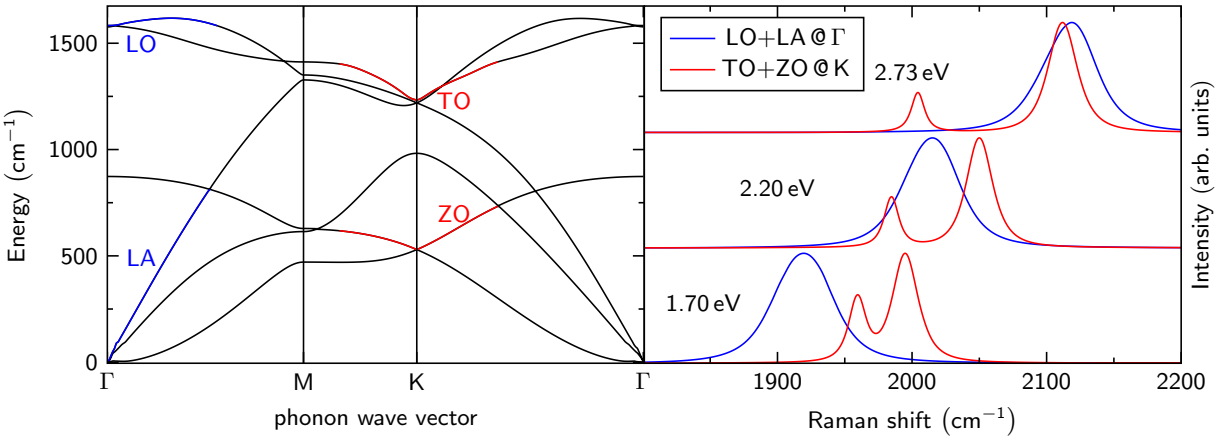

Figure 6.5: Left: The phonon dispersion of graphene along the high-symmetry directions of the 1. Brillouin zone is plotted. Highlighted are parts of the LO/LA and TO/ZO phonon branches that are used to calculate Raman spectra for various excitation energies on the right side. The calculations are done to visualize the likewise dispersions of the two different processes and do not contain any coupling elements [14]. In graphene, a TO+ZO process is forbidden by symmetry [14]. Within the energy range of 1.7 eV and 2.73 eV the LO+LA @ Γ (blue) and TO+ZO @ K (red) processes have comparable frequencies and dispersions.

calculations. This explains the slightly too large frequencies and dispersions, compared to experiments. Especially the energy of the TO and LO derived phonon branches is overestimated, leading to a positive instead of a negative dispersion in case of the TO+LA combination mode.

The LO derived phonon branches in metallic carbon nanotubes exchange their frequencies with those from the TO derived phonon branches at the Γ point, compared to semiconducting carbon nanotubes [215, 252–257]. The reason is a strong Kohn Anomaly reasonably softening the LO derived phonon frequencies. The degeneracy of the TO/LO phonon branches at the Γ point in graphene is in metallic carbon nanotubes predominantly lifted due to confinement effects [252] whereas in semiconducting tubes the degeneracy is rather lifted due to curvature effects [252], explaining the fundamentally different Raman spectra from both types of carbon nanotubes. However, the exchange of related phonon frequencies only counts for a very limited region of phonon wave vectors close to the Γ point [252]. Resonant phonon wave vectors probed in a LO+LA @ Γ double-resonant Raman process with excitation energies in the optical visible range are usually larger and thus our DFT + zone-folding computations indicate that the DR Γ−point processes involve the higher frequency LO derived phonon branches. It is therefore sufficient to reduce the discussion on the LO derived phonon branches for intravalley processes.

6.1.4 Low-intensity Raman modes - Non-orthogonal tight-binding calculations

An assignment of the 1950 cm^{-1} band only by its dispersion and frequency cannot convincingly be done. As shown in Fig. 6.5, a LO+LA @ Γ (blue) and a TO+ZO @ K (red) process have assimilable frequencies and dispersions when optically excited with usual laser excitation energies in the optical visible range. The calculations do not contain any

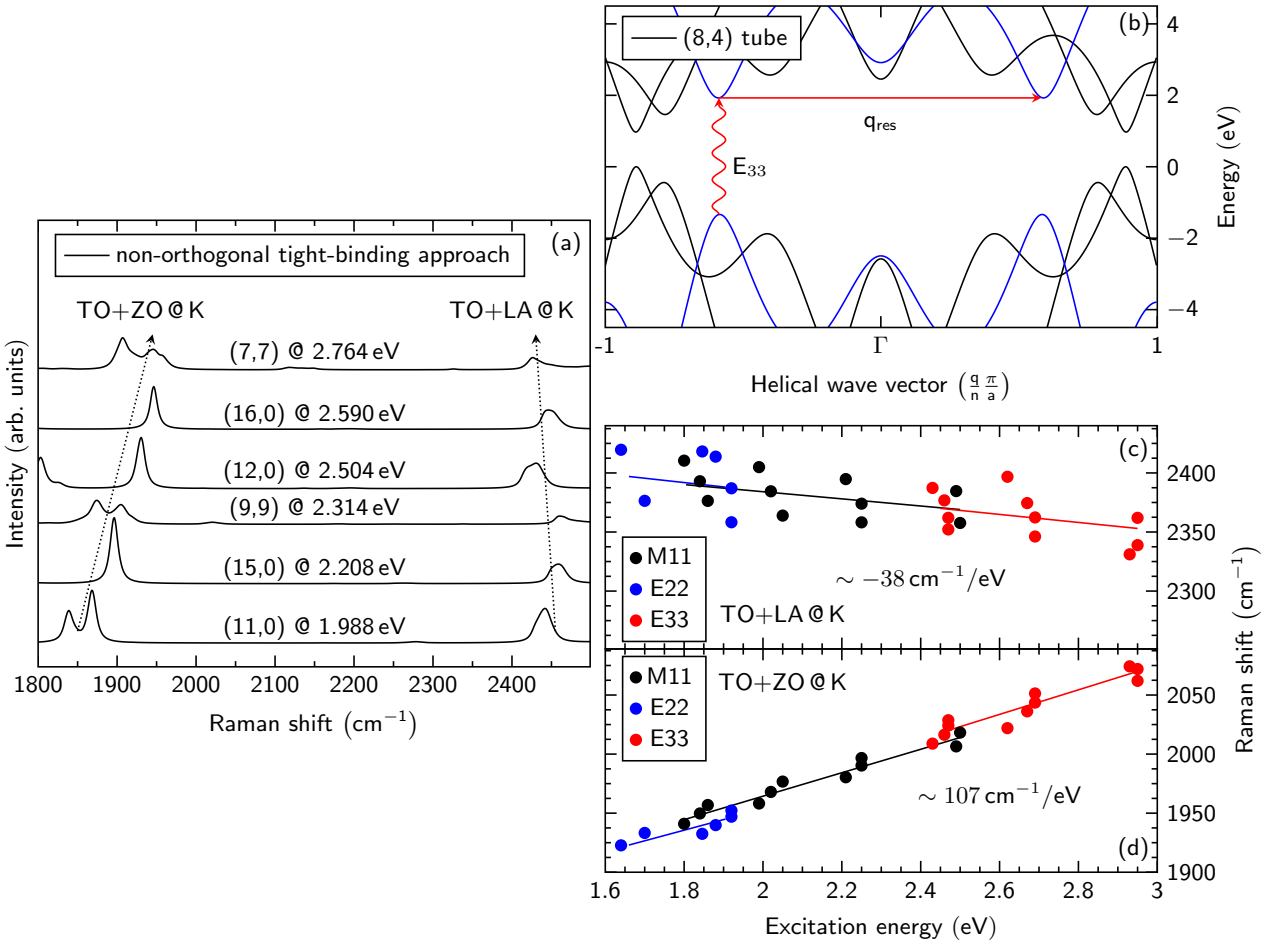

Figure 6.6: (a) Calculated Raman spectra of various carbon nanotubes excited at their E_{11} transition energies within a non-orthogonal tight-binding approach are plotted. Calculations have been done by Valentin N. Popov [258]. The symmetry-based approach suggests that the 1900 cm^{-1} band is a TO+ZO @ K process as indicated in the figure; the 2400 cm^{-1} band is assigned to a TO+LA @ K process. (b) Illustration of the simplified scattering process used for the calculations in (c) and (d) is plotted. The initial idea for that approach was brought up by Felix Herziger [259]. (c) and (d): Calculated phonon frequencies of the TO+LA (c) and TO+ZO (d) combination modes for the E_{11}^{M}, E_{22}^{S}, and E_{33}^{S} transition energies are shown. Considered are only "inner" processes and carbon nanotubes as shown in Table 6.1. Indicated are the quasi-linear slopes of the dispersions, equivalent to those in Fig. 6.2.

coupling elements and therefore, the Raman intensities are not predicted correctly. A TO+ZO @ K process is forbidden in graphene due to symmetry reasons [14]. The large line width of the LO+LA @ Γ process originates from the very large joint density of states probing the overbending of the LO phonon branch around the Γ point in the 1st Brillouin zone.

Since the DFT + zone-folding approach requires the initial electron-phonon matrix elements calculated for graphene, the coupling elements for carbon nanotubes might be reproduced incorrectly. We have therefore also calculated double-resonant Raman spectra of various carbon nanotubes within a non-orthogonal tight-binding approach. All calculations are done by Valentin N. Popov [258] and are summarized in Fig. 6.6. A dispersive mode at around 1950 cm^{-1} can be observed that is assigned to a TO+ZO @ K combination mode in the used approach. This assignment is a clear difference to the results of the

DFT + zone-folding calculations as discussed before. The 2400 cm^{-1} band is assigned to a TO+LA @ K combination in agreement to the assignment before. However, in contrast to the DFT+zone-folding approach a slight negative dispersion is observed. This outcome describes the experimentally observed negative dispersion better compared to the other computational approach. The calculations explicitly contain the Kohn Anomaly in metallic carbon nanotubes leading to both a strong softening of LO phonon frequencies and an increase of the electron-phonon coupling [257]. Still, we do not find a LO+LA @ Γ process in carbon nanotubes.

A final assignment of the band at around 1950 cm^{-1} only based on the computations cannot convincingly be done. Due to the well-known shortcomings of the DFT+zone-folding approach describing curvature-induced changes of vibrational properties, a tentative assignment of the mode to a TO+ZO @ K process as suggested within the non-orthogonal tight-binding approach seems feasible [260]. However, we believe that more experimental data is needed. For instance, it might help to perform measurements on isolated carbon nanotubes as appearing Raman modes can be identified and more certainly assigned, compared to ensemble samples. A contemporaneous measurement of both Stokes/Stokes and Stokes/anti-Stokes, double resonant Raman processes as shown by Herziger *et al.* [187] and suggested in Ref. [246] might help to distinguish between a LO+LA @ Γ and a TO+ZO @ K process. This idea utilizes the fact that due to the different phonon energies involved, the combined Stokes/anti-Stokes phonon energies of a LO+LA @ Γ process should be systematically higher than for a Stokes/anti-Stokes TO+ZO @ K process. Thus, an assignment could be done more easily and was then a strong argument for the correct assignment of the $\approx 1950\,\mathrm{cm}^{-1}$ band as discussed before.

6.1.5 Low-intensity Raman modes - Dispersions and line shapes

We now continue with a discussion of the line shapes of the measured, double-resonant Raman modes. The bimodal peak structures of the observed modes originate from distinctive contributions from different species of carbon nanotubes. Due to the specific ensemble of the HipCO sample, mainly semiconducting tubes are probed below $\varepsilon_\mathrm{L} \approx 2.1\,\mathrm{eV}$ ($\mathrm{E}^\mathrm{S}_{22}$) and above $\varepsilon_\mathrm{L} \approx 2.5\,\mathrm{eV}$ ($\mathrm{E}^\mathrm{S}_{33}$). In the intermediate range, both semiconducting and metallic ($\mathrm{E}^\mathrm{M}_{11}$) carbon nanotubes are probed. Different tubes having likewise transition energies but are either semiconducting or metallic necessarily need to have different diameters. Compared to $\mathrm{E}^\mathrm{S}_{22}$ ($\mathrm{E}^\mathrm{S}_{33}$) transitions, metallic tubes with $\mathrm{E}^\mathrm{M}_{11}$ transitions have larger (smaller) diameters for similar transition energies and therefore different phonon energies [45, 59, 232, 234, 259]. Hence, we attribute different peaks in the Raman bands to carbon nanotubes with different diameters. In detail, due to the specific ensemble analyzed, we can attribute Raman peaks to semiconducting tubes for excitation energies below $\varepsilon_\mathrm{L} \approx 2.1\,\mathrm{eV}$ and above $\varepsilon_\mathrm{L} \approx 2.5\,\mathrm{eV}$. The Raman peaks for excitation energies between 2.1 eV and 2.5 eV can be assigned to both metallic and semiconducting carbon nanotubes. Thus, the origin of the observed multimodal band is the concurrent probing of carbon nanotubes. Within our analysis we can explicitly exclude the assignment done by Brar *et al.* [247] where the bimodal peak of the 1950 cm^{-1} band was attributed to both LO+LA @ Γ and TO+LA @ Γ processes. To understand the bimodal peak structure in more detail, we have also modeled Raman frequencies of TO+ZO @ K and TO+LA @ K

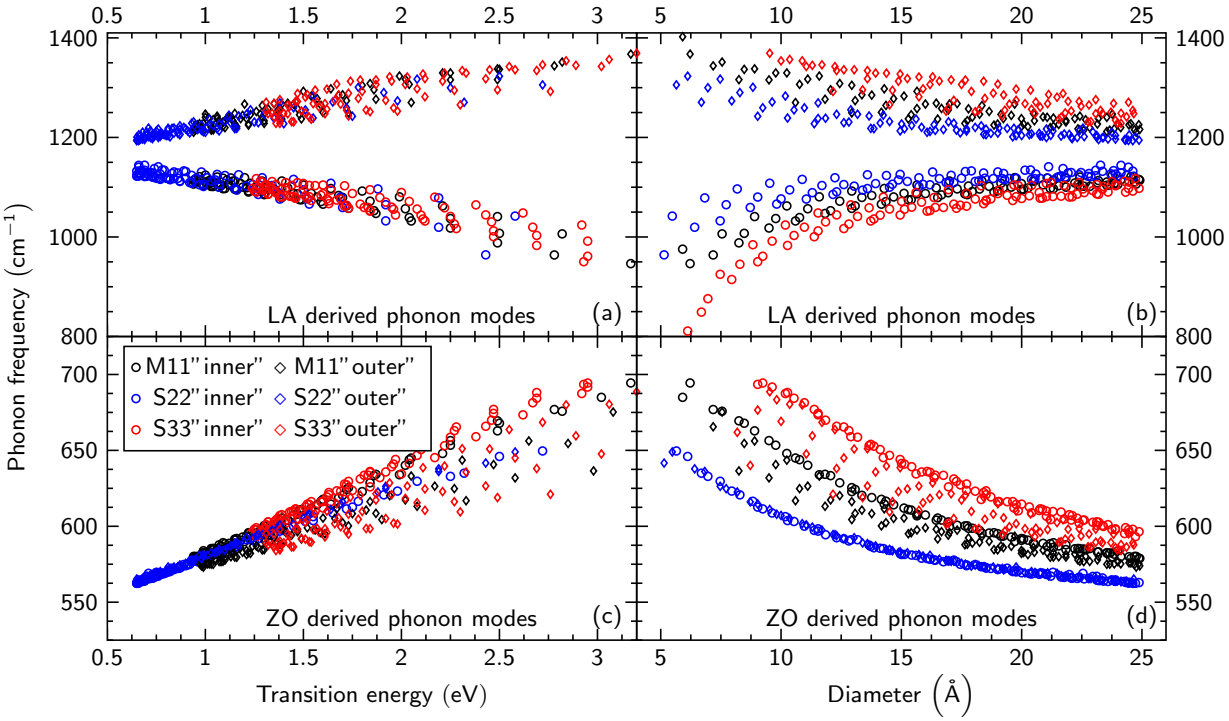

Figure 6.7: Calculated frequencies of the out-of-plane ZO derived and of the in-plane LA derived phonon branches in carbon nanotubes are plotted. Optical transition energies and phonon frequencies were obtained from a six-nearest-neighbor tight-binding approach using the POLSYM code [182]. For the calculations of the frequencies, we have used the model proposed by Herziger *et al.* [259]. Different colors stand for different optical transitions, circles are referred to "inner" processes whereas diamonds are referred to "outer" processes.

processes with a different computational approach. The model was brought up by Felix Herziger [259] and is only based on the symmetry of the hexagonal lattice and geometric considerations. An illustration of the simplified scattering process is given in Fig. 6.6 (b). A resonant phonon wave vector q_{res} mediates between equivalent minima in the electronic band structure. Its length is $q_{res} = 2k$ and visualizes the usual assumption "$q_{res} = 2k$" for M point centered, double-resonant Raman scattering processes in carbon nanotubes [171]. The scattering pass always traverses the Γ point due to the symmetry of the hexagonal lattice. This approach does not include phonon energies and limits the scattering only to extrema in the electronic bands. However, predictions for the frequencies of the *D* mode in carbon nanotubes are convincing and are very close to experimental results [171,259,261]. The model was initially introduced for the description of the *D* band in carbon nanotubes but it is also capable of predicting correct phonon frequencies of other *K* point centered scattering processes, such as the TO+ZO @ K or the TO+LA @ K process as discussed above. Corresponding calculations can be seen in Figs. 6.6 (c) and (d). We have only considered "inner" processes and those tubes that we have found in the sample (compare Table 6.1). Electronic and phonon band structures, and therefore respective optical transition energies and phonon frequencies, were obtained from a six-nearest-neighbor tight-binding approach using the POLSYM code [182]. For the TO+ZO @ K process, we observe frequency "steps" between E^S_{22}/E^M_{11} and between E^M_{11}/E^S_{33} transitions, indicated with linear fits in Fig. 6.6 (c) and (d). In contrast, there are no clear "steps" observable

in case of the TO+LA @ K process. This effect is mainly caused by the opposite influence of curvature to the in-plane LA derived and out-of-plane ZO derived phonon energies as can be seen in Fig. 6.7. Overall, we find a good agreement to the experimental findings. The geometry-based approach gives reasonable results describing both the dispersions and line shapes of the TO+ZO @ K and TO+LA @ K processes. In fact, the so obtained dispersions of $\sim -38\,\mathrm{cm}^{-1}/\mathrm{eV}$ (TOLA @ K) and $\sim 107\,\mathrm{cm}^{-1}/\mathrm{eV}$ (TOZO @ K) are very close to the experimental values of $\sim -22\,\mathrm{cm}^{-1}/\mathrm{eV}$ and $\sim 80\,\mathrm{cm}^{-1}/\mathrm{eV}$ (averaged). We will therefore extent the discussion to a broad range of carbon nanotubes with diameters between 5 Å and 25 Å.

In the following, the discussion is reduced to the influences of chirality and diameter only to the ZO and LA derived phonon branches as these components are different in the TO+ZO @ K and TO+LA @ K processes. A comparable discussion of the TO derived phonon branches in carbon nanotubes can be found in Refs. [171, 259, 261].
At first, only "inner" processes are discussed *i.e.* processes where the phonons predominantly originate from the $K - \Gamma$ direction. ZO derived phonon energies in carbon nanotubes increase with an increasing optical transition energy [Fig. 6.7 (c), circles]. In general, the phonon energies follow the slope of the out-of-plane ZO phonon branch in graphene [14], *i.e.* in a M centered double-resonance process, larger excitation energies result in shorter resonant phonon wave vectors automatically leading to higher phonon energies since the ZO phonon branch has its maximum at the Γ point in the 1$^{\mathrm{st}}$ Brillouin zone. Further, carbon nanotubes with smaller diameters generally exhibit higher ZO-derived phonon energies for likewise optical transitions [Fig. 6.7 (d)]. A clear separation of phonon energies between the "inner" $\mathrm{E}_{11}^{\mathrm{M}}$, $\mathrm{E}_{22}^{\mathrm{S}}$, and $\mathrm{E}_{33}^{\mathrm{S}}$ transitions can be observed. The findings agree with those of the TO derived phonon branches in carbon nanotubes [171, 259, 261], *i.e.* smaller carbon nanotubes generally have higher TO derived phonon energies and the phonon energies of different optical transitions for likewise diameters are separated by several cm^{-1}. These general trends are enhanced in the TO+ZO @ K combination mode since both phonon branches follow the same proportionalities. In particular, the separation of phonon energies as shown in Fig. 6.7 (d) are increased and cause "steps" in the continuity of the TO+ZO @ K dispersion as indicated with linear fits in Fig. 6.6 (d). In contrast, the energies of the LA derived phonon modes show an opposite behavior [Fig. 6.7 (b), circles]. Increasing excitation energies result in lower phonon energies since the LA phonon branch along the $\Gamma - K$ high-symmetry line in graphene has its maximum at the K point [14]. Smaller diameters generally have lower phonon energies with a comparably large overlap from different optical transitions [compare Fig. 6.7 (b)]. This stands in strong contrast to both the TO and ZO derived phonon modes where the phonon energies are clearly separated.
The opposite behavior of the curvature-induced changes to the LA derived phonon modes compared to TO derived phonon modes in carbon nanotubes leads to a softening of the overall influence of the diameter to the TO+LA @ K combination mode. This explains the uniform peaks in the experimental Raman spectra of the TO+LA @ K combination mode although the analyzed range of excitation energies is large and the sample contains carbon nanotubes with many different chiralities.

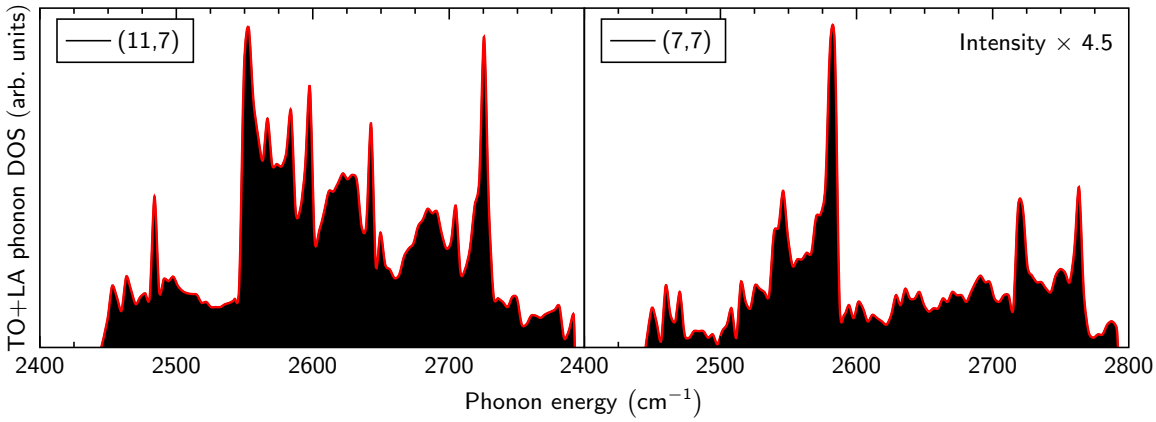

Figure 6.8: Calculated joint TO+LA phonon density of states for a (11,7) and a (7,7) carbon nanotube in a DFT + zone-folding approach is shown. The scale is the same for both spectra. Calculation are done by Rohit Narula [250].

Using the same approach, we have also calculated phonon energies of "outer" processes, *i.e.* scattering processes where phonons originate from the $K - M$ direction (compare Fig. 6.5) indicated with diamonds in Fig. 6.7. In case of the ZO derived phonon energies, the deviations to energies of the "inner" processes are only small since the slopes of the ZO phonon branch in the $K - \Gamma$ and in the $K - M$ directions are almost similar in the relevant range of phonon wave vectors (compare Fig. 6.5). Instead, the LA phonon branch increases in energy along the $K - M$ direction (compare Fig. 6.5) resulting in systematically higher phonon energies for the "outer" processes (indicated with diamonds in Fig. 6.7). Depending on diameter and the optical transition of the carbon nanotubes, the gap between "inner" and "outer" LA derived phonon energies can be several hundred cm^{-1}. As a result "outer" TO+LA @ K processes in the observed HipCO sample should be observed at around 2600 cm^{-1} and higher energies. This however can not experimentally be observed. These findings agree with a computational and experimental analysis of the TO+LA @ K process in graphene [149]. By a comparison of measured joint phonon energies and sophisticated computations, it was found the TO+LA combination mode is an "inner" process, *i.e.* that the involved phonon stem from the $K - \Gamma$ direction [149]. The absence of a double-resonant Raman mode at around 2600 cm^{-1} confirms again that Raman spectra of carbon nanotubes are predominantly determined by "inner" scattering processes.

6.1.6 Low-intensity Raman modes - Intensity ratios

We now continue with a discussion of Raman intensities of the measured combination modes. The intensity progressions of low-intensity Raman modes in graphene are still only barely discussed in the literature and are usually given as ratios in comparison to the strong $2D$ mode [14]. Still, exact experimental values are even today not available. This also counts for carbon nanotubes samples where an accurate analysis of the intensity progression of a particular Raman mode gets even more complicated. An exact calculation of the intensity progression of the measured HipCO sample is given in Figs. 6.4 (c) and (d) regarding an LO+LA @ Γ and a TO+LA @ K combination process. Although the non-orthogonal tight-binding approach suggests that a LO+LA @ Γ process should not

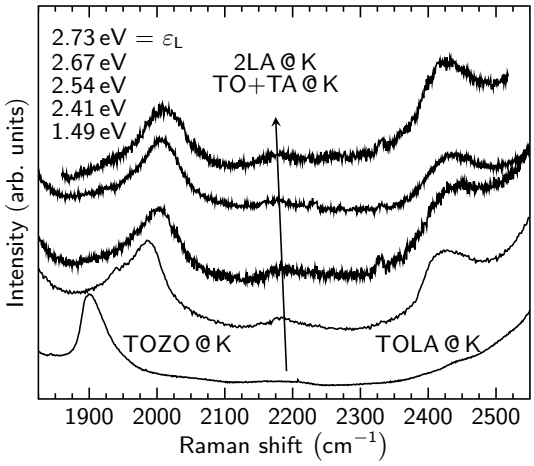

Figure 6.9: Second-order Raman spectra of an HipCO buckypaper carbon nanotube sample for various excitation energies given next to the spectra are shown. The arrow indicates a possible TO+TA @ K or a 2 LA @ K combination for the observed Raman mode.

be visible in carbon nanotubes, general statements can still be derived from the DFT calculations. The relatively low intensity of the TO+LA @ K process for high excitation energies is due to an increasing joint density of states (jDOS) of the LO+LA @ Γ mode within this computational approach. It can mainly be referred to the LO derived phonon branch that has a very low slope in the probed $\Gamma \rightarrow M$ direction (compare Fig. 6.5). Instead, the jDOS of TO+LA @ K processes does not show a clear dependence comparing a large range of phonon wave vectors. This behavior is shown in Fig. 6.8 where the jDOS of TO+LA @ K process for a (11,7) and a (7,7) carbon nanotube are calculated in a DFT + zone-folding approach. Only for very large excitation energies above 3 eV and higher (and therefore lower frequencies of the TO+LA combination mode) the jDOS tentatively decreases since the gradient of the LA phonon branch increases in the $K \rightarrow \Gamma$ direction. In contrast, both the ZO and TO phonon branches run parallel in the region of phonon wave vectors that is usually probed by excitation energies in the visible range (compare Fig. 6.5). As a result the jDOS should be comparably high and widely independent from the excitation energy.
In a double resonance process, only a very small range of resonant phonon wave vectors is responsible for particular modes in the Raman spectra of carbon nanotubes [45, 53, 218]. Therefore, the jDOS of a certain combination mode only gives a qualitative trend on how the corresponding Raman intensity evolves as a function of the excitation energy. Considering the slopes of the discussed phonon branches and therefore the jDOS, we would only expect small deviations of the intensity ratios from a TO+LA @ K and a TO+ZO @ K process.
Besides the jDOS, only the respective electron-phonon coupling elements of the ZO and the LA derived phonons are different that determine the intensity ratios of the discussed combination modes. However, neither computational nor experimental values of the respective coupling elements are available today and therefore we can not make reliable quantitative statements. Since in graphene there is no coupling to the optical out-of-plane phonons, we believe that the electron-phonon coupling of the ZO derived phonons in carbon nanotubes should generally decrease for larger diameters.

In Fig. 6.9, Raman spectra of the HipCO sample for various excitation energies are plotted showing both the TO+LA @ K and TO+ZO @ K combination modes. The spectra are normalized to the TO+ZO @ K mode. For all spectra, the TO+ZO @ K has a larger

intensity. Between 2.41 eV and 2.73 eV, the intensity ratios are likely the same and do not depend on the excitation energy. In contrast, the intensity of the TO+LA @ K for $\varepsilon_{\mathrm{L}} = 1.49\,\mathrm{eV}$ is only very low. We tentatively attribute the low intensity to the comparable low LA electron-phonon coupling elements of the carbon nanotubes probed. Interestingly, the frequency of the TO+ZO @ K mode exhibits $\nu \approx 1900\,\mathrm{cm}^{-1}$ although the laser excitation energy is below 1.5 eV. This value stands in contrast to that from the measurements shown in Fig. 6.2 where the lowest frequency $\nu \approx 1875\,\mathrm{cm}^{-1}$ was found for a higher excitation energy of 1.71 eV. Considering the diameter range of 7 Å to 13 Å of the HipCO sample, we start to probe the $\mathrm{E}_{\mathrm{S}}^{11}$ transition with $\varepsilon_{\mathrm{L}} = 1.5\,\mathrm{eV}$. Again, a concurrent probing of different optical transitions in carbon nanotubes is only possible, when the tubes involved exhibit different diameters. This again results in different phonon frequencies and therefore to different measured Raman shifts.

All spectra showed an additional low-intensity Raman mode at around $2200\,\mathrm{cm}^{-1}$. It exhibits a small negative dispersion with intensities about two magnitudes smaller than those from the TO+ZO @ K or TO+LA @ K combination modes. In the literature, this mode in carbon nanotubes has not been reported before. Experimental data in graphene is also not available. However, DFT calculations in graphene suggest the existence of a TO+TA @ K and a 2LA @ K combination mode in the discussed range of phonon frequencies [14]. Both are supposed to exhibit a negative dispersion in agreement to the measurements. Experimental data for the D" mode (defect mode with LA phonons) in carbon nanotubes and graphene is available where a dispersion of $100\,\mathrm{cm}^{-1}/\mathrm{eV}$ was measured [168]. The dispersion for the corresponding second-order ($2D''$) process should amount to $\sim$200 $\mathrm{cm}^{-1}/\mathrm{eV}$, confirming the theoretical findings for the dispersion of the $2D''$ mode in graphene [14]. However, this value is larger than the experimentally obtained dispersion as shown in Fig. 6.9. We therefore rather attribute this mode to a TO+TA @ K combination [14] as the calculated dispersion only exhibits $\sim 30\,\mathrm{cm}^{-1}/\mathrm{eV}$. A closer analysis is necessary to make a final assignment.

6.2 UV Raman spectroscopy: Extended Kataura plot and RBM measurements

Even in nowadays, the optical transition energies of carbon nanotubes in the UV range are neither experimentally nor theoretically discussed. The topological change of equi-energy surfaces in graphene when excited above the M-point energy also leads in carbon nanotubes to interesting new findings.
On the next pages we discuss how we get access to higher optical transitions above the M-point exciton, calculate the corresponding optical matrix elements and show calculated absorption spectra. With the understanding of the respective optical absorptions, we show and discuss UV Raman spectra of the radial-breathing mode from a HipCO sample.

6.2.1 Optical transitions energies above the M-point energy

The Kataura plot of carbon nanotubes gives a general overview on how optical transition energies in carbon nanotubes are affected by their diameters [59, 262]. The diameter in turn can be parametrized by the chiral indices and, therefore, the Kataura plot also gives information on how the diameter determines optical transitions [59, 262]. For the usual range of optically visible transition energies, some general findings can be made: *(i)* Quantum confinement determines the general dependence on the diameter, *i.e.* tubes with smaller diameters have larger transition energies and vice versa [59, 263]. *(ii)* The transition energies are arranged in larger and smaller branches: The optical transition index E_{ii} is constant along a larger branch. Smaller branches only contain a certain type of carbon nanotubes. Within such a branch, the chiral indices follow the relation: $2n_1+n_2 =$ constant. *(iii)* Smaller branches appear pairwise with optical transitions rather stemming from the $K-M$ direction in graphene and transitions rather stemming from the $K-\Gamma$ direction. Transition energies from the $K-M$ direction are systematically smaller than from the $K-\Gamma$ direction. *(iv)* There is a clear separation between metallic and semiconducting nanotubes. The larger branches only contain either metallic or semiconducting carbon nanotubes [59, 262]. A calculated Kataura plot can be seen in Fig. 6.11.

Optical transitions in carbon nanotubes occur between van-Hove singularities [264, 265] that have a strong excitonic character [233, 266–268]. The singularities in the absorption spectra are a consequence of the one-dimensional electronic density of states [264,265] and arise from electronic bands that locally exhibit no dispersion. Below the M-point exciton, the areas where the band dispersions disappear are always minima in the electron bands as can be seen in Fig. 6.10 where the linear electron bands of a (8,0) carbon nanotube are plotted, calculated in a next-nearest neighbor tight-binding + zone-folding approach. Red dots indicate the electron momentum for each subband where the optical transition originates from. In the case of a zig-zag carbon nanotube, the minima are always located at the $k = 0$ and every subband ($n = 8$) exhibits an extremum where an optical transition is allowed. However, depending on the chiral vector in a general CNT, not every electron subband exhibits an extremum which limits the amount of allowed optical transitions [45, 53, 178].

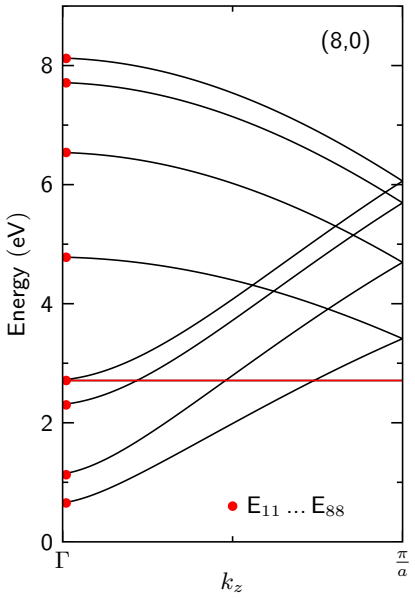

Figure 6.10: Electron bands of a (8,0) carbon nanotubes are plotted. Red dots correspond to optical transition from E_{11} to E_{88}. Note: Zigzag tubes where n_1 is even, always have one electron and one hole band with no dispersion. The optical transition is therefore independent from k_z. Optical transitions higher than the M-point energy (5.42 eV within the used next-nearest neighbor tight-binding + zone-folding approach), are located at maxima of the combined electron/hole bands rather than at minima as apparent for excitations below the M point.

Electronic bands higher than the M-point energy do not have a minimum with a disappearing gradient anymore, but possibly exhibit a maximum, depending on the chiral indices n_1 and n_2 (maxima only refer to areas where the gradient disappears). This point can be seen in Fig. 6.10 where the five highest bands exhibit a maximum, respectively. The red line corresponds to a subband with the band index $m = 5$ that exhibits no dispersion (discussed later), but by definition also contains a maximum (minimum).

We have calculated all allowed optical transition energies of carbon nanotubes with chiral indices n_1, n_2 between 2 and 21 within a next-nearest neighbor tight-binding + zone-folding approach and have explicitly allowed transitions between minima and maxima. They are plotted in Fig. 6.11. Allowing transitions between maxima, we get access to optical transitions higher than the M-point energy (5.42 eV within the used approach). Below an energy of 5.42 eV, we find the known arrangement of transitions energies as apparent in the usual Kataura plot. However above 5.42 eV, the arrangement drastically changes. We again find larger and smaller branches but this time they seem to have an opposite dependence on the diameter, *i.e.* larger diameters have larger transition energies and vice versa. Black dots represent allowed optical transitions with $|M_z| > 0$, red dots represent forbidden optical transitions with $|M_z| = 0$ that are for reasons of completeness, also plotted into the extended Kataura plot. Analyzing the chiral indices of the respective carbon nanotubes, we can derive several statements from the extended, calculated Kataura plot:

- In contrast to optical transitions below the M-point, we find possible optical transitions that are forbidden by symmetry. (Indicated with red dots in Fig. 6.11.)

- Smaller branches do not appear pairwise as they do for optical transitions below the M-point. All transitions originate from the proximity of the steep-slope $\Gamma - K$-direction and not from twofold $K - M$ and $K - \Gamma$ directions with different slopes of the electron and hole bands.

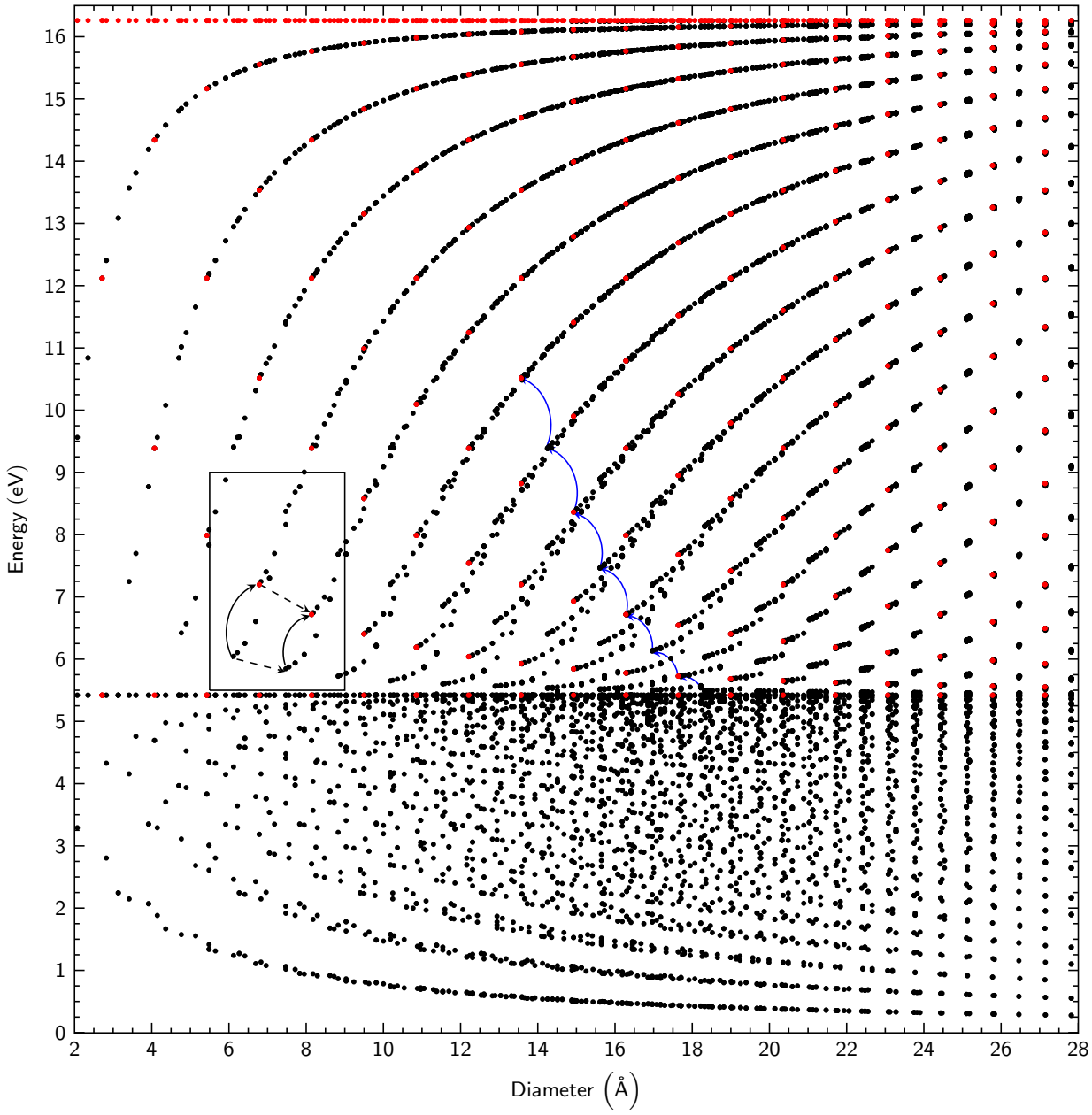

Figure 6.11: The extended Kataura plot is shown. Black dots represent optical transitions of carbon nanotubes with chiral indices (n_1, n_2) between 2 and 21 and optical matrix elements $|M_z| > 0$. Red dots represent optical transitions with no oscillator strength, *i.e.* optically forbidden transitions. Carbon nanotubes are sorted by their diameter. All optical transitions above 5.42 eV correspond to transitions above the M-point energy. A zoom-in of the inset can be seen in Fig. 6.12. Black arrows indicate starting points of different smaller branches, respectively. The blue arrows connect starting points of smaller branches in which the optical transition E_{ii} is always the same. Calculations are done in a next-nearest neighbor tight-binding + zone-folding approach.

- $n_1 + n_2$ = constant for all carbon nanotubes within a smaller branch (compare Fig. 6.12). All semiconducting tubes within a smaller branch have the same transition E_{ii}; the metallic carbon nanotubes generally have a lower transition $E_{(i-1)(i-1)}$. The low-energy end of the branches always belong to a carbon nanotube with the largest chiral angle. The high-energy end always belongs to a zig-zag tube, *i.e.* to a tube with the smallest chiral angle.

- Larger branches consist of smaller branches where the optical transition E_{ii} and the sum $n_1 + n_2$ change by +1 for increasing diameters, respectively (compare Fig. 6.12 and solid, black arrows in Fig. 6.11).

- The chiral indices of neighboring, smaller branches change by +1 both for n_1 and n_2 as indicated with dashed arrows in Fig. 6.11. (Compare Fig. 6.12.)

- We find a clear separation between carbon nanotubes that have the same optical transition E_{ii} as indicated with blue arrows. They follow the same trend as below the M-point energy, *i.e.* smaller tubes have higher transition energies and vice versa. For each new smaller branch the sum $n_1 + n_2$ changes by +1 for larger diameters. (Follow the blue arrows in Fig. 6.11.)

- Due to reasons of symmetry, the extended Kataura contains M-point and Γ-point transitions for each carbon nanotube. However, the Γ-point transition is forbidden in every carbon nanotube. This is a direct consequence of the dipole-forbidden $\Gamma-$point transition in graphene. Additionally, all optical transitions above the M-point are forbidden in armchair tubes. In armchair tubes, all conduction and valence bands for $k = 0$ have the same parity with respect to the σ_h mirror plane. Z-polarized light, however, reverses the parity for the horizontal mirror plane σ_h and therefore, independent from the band index m, all optical transitions above the M-point are forbidden [61].

- Following the blue arrows in Fig. 6.11 (identical transition E_{ii} but smaller diameters for each new arrow), the energy separation between the arrows increases up to $\sim 13\,\mathrm{eV}$ followed by decreasing gaps.

Although the Kataura plot looks different for energies above the M-point energy, we find three major similarities with the usual Kataura plot: *(i)* Again, quantum confinement determines the general dependence of transition energies on the diameter. This can be seen following the blue arrows in Fig. 6.11 where the optical transition index E_{ii} is kept constant. Further, the increasing energy separation (up to $\sim 13\,\mathrm{eV}$) followed by a decreasing energy separation reflects the $\propto 1/d$ dependence, but also the dispersion of the electronic band structure in graphene. The overall gradient towards the Γ point increases up to $\sim 13\,eV$ ($E_c - E_v$) from all directions but drastically decreases in its proximity [38]. *(ii)* Smaller branches do not appear pairwise since all transitions from the $K - M$ direction are excluded. Transition energies within smaller branches show the same dependence on the chiral angle as those from below the M-point energy. For the same optical transition, higher chiral angles have lower transition energies and vice versa.

In contrast to the transitions below the M-point energy, the chiral angle dependence

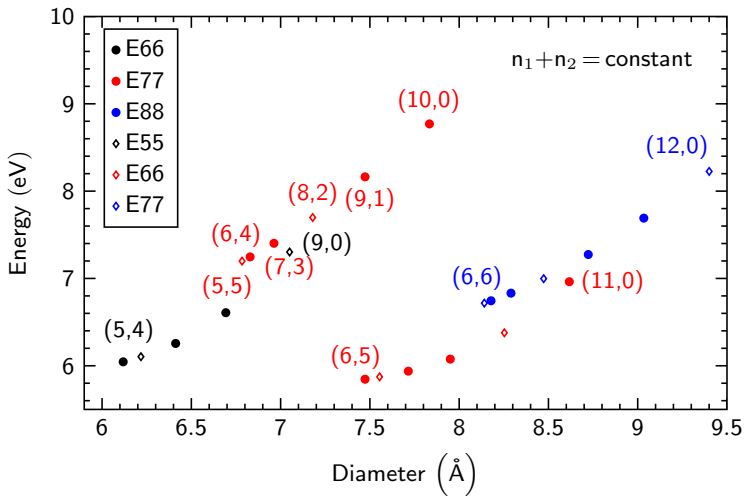

Figure 6.12: A zoom-in of the extended Kataura plot as shown in Fig. 6.11, is plotted. Different colors stand for different optical transitions. Semiconducting tubes are marked with circles, metallic ones are marked with diamonds. For reasons of completeness, the plot contains the (5,5) and (6,6) armchair tubes although all optical transitions above the M-point energy are forbidden by symmetry. The sum of n_1 and n_2 is constant within one branch. Calculations are done in a next-nearest neighbor tight-binding + zone-folding approach.

seems inverted. The inversion can be understood from the symmetry of the hexagonal graphene lattice. The helical vector cuts the hexagons of the graphene lattice the closer to the K points, the larger the chiral angle is. At the same time, the k-space distance to the various Γ points gets larger for larger chiral angles and vice versa. In other words, optical transitions for large chiral angles are rather close to the K points, but far away from the Γ points (translates into "lower" transition energies in both cases) and optical transitions for small chiral angles are rather away from the K points and close to the Γ points (translates into "higher" transition energies in both cases). Corresponding illustrations can be found in Refs. [45, 53, 62, 171]. All statements from above can be followed in detail in Fig. 6.12 where we show a zoom-in of the extended Kataura plot as indicated with the rectangle in Fig. 6.11. Chiral indices of the respective carbon nanotubes are indicated to highlight their arrangements within different branches in the extended Kataura plot.

6.2.2 Optical absorption above the M-point energy and UV Raman spectra

With a deeper understanding of the optical transition energies above the M-point exciton in carbon nanotubes, we can extend the analysis to the optical absorption and can compare these results to UV Raman spectra.

The absorption in carbon nanotubes has a strong excitonic character [233, 266–268]. Exciton binding energies can reach values up to 500 meV for small semiconducting tubes, where the holes and electrons are significantly confined [45,62,233,266–268]. Larger diameters lead to a reduced confinement, weakening the binding energies, but values usually still reach several hundred meV. Even in metallic tubes, exciton binding energies are observed that exceed $k_BT \sim 25$ meV for the usual optical transitions probed, although there is an efficient Coulomb screening of free electrons in metallic carbon nanotubes [62]. The experimental and theoretical analysis however usually covers excitation energies in the optical visible range. It was therefore interesting to know, how the optical matrix elements M_z and the consecutive absorption spectra of carbon nanotubes evolve in the ultra-violet region.

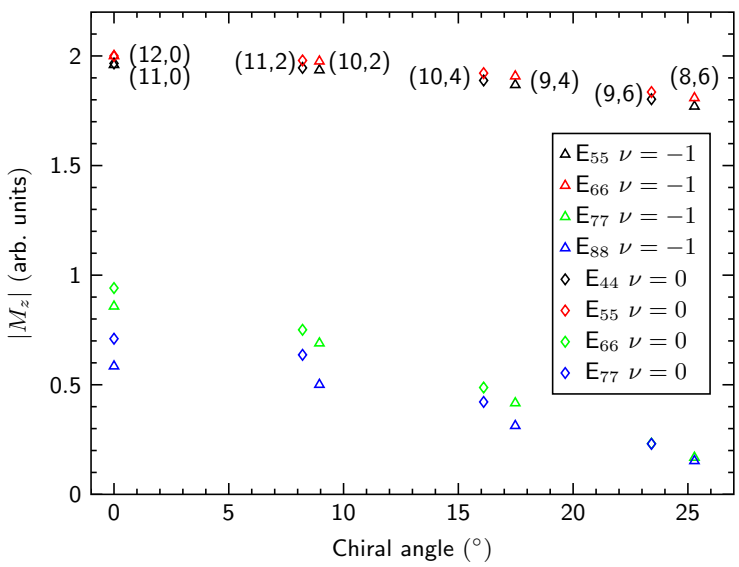

Figure 6.13: The magnitudes of different optical matrix elements $|M_z(k)|$ for several optical transitions E_{ii} are plotted as a function of the chiral angle. The lowest optical transitions E_{44} (metallic) and E_{55} are the last ones before the M-point transition. The M-point transitions for metallic tubes are therefore E_{55} and E_{66} for semiconducting tubes. Triangles belong to tubes with the family index $\nu = -1$, diamonds belong to tubes with the family index $\nu = 0$. The tubes have approximately the same diameter of $\sim 9\,\text{Å}$. Calculations are done in a next-nearest neighbor tight-binding + zone-folding approach.

We have plotted the linear band structure of a semiconducting (8,0) tube in Fig. 6.10 and for every subband we have marked the electron momentum k_z where an optical transitions occurs. In the case of a zig-zag tube, all optical transitions occur at $\mathbf{k}_z = 0$ (Γ point) as can be seen in Fig. 6.10. This is also true for every optical transition higher than the M-point energy in armchair tubes [45, 61, 62]. If n_1 is an even number, zig-zag tubes further have a band with no dispersion as their cutting lines on the hexagonal graphene lattice are parallel to a $M-M$ connection line. The non-existing dispersion can be understood from the fact that equi-energy surfaces of excitations above the M point in graphene are circles around the Γ point and triangles around the K point for excitations below the M-point energy. The curvatures have opposite signs, respectively. As a consequence, there is a zero-crossing of the curvatures resulting in piecewise straight equi-energy surfaces. In Chapter 5, Fig. 5.3, a corresponding contourplot of the two-dimensional band structure of graphene with depicted equi-energy surfaces can be seen.
The following high density of states results in a very strong absorption of zig-zag nanotubes with an even n_1 when excited at the M-point transition energy [61, 62].

From the calculated electron bands, we have also calculated the optical matrix elements M_z of each allowed optical transition as shown in the extended Kataura plot (details are given in Chapter 2). We have used the approach as given in Ref. [61], where the optical matrix elements are calculated within a next-nearest neighbor tight-binding approach. Some of them are plotted in Fig. 6.13, where we show the optical matrix elements for excitations below, at, and two above the M-point energy for various carbon nanotubes. We have chosen nanotubes with an approximate diameter of $d \sim 9\,\text{Å}$ but with chiral angles ranging from 0 to 25 degrees. The matrix elements for the highest transitions below the M-point energy E_{55} (E_{44} for metallic tubes, drawn in black) have very high values close to 2, decreasing for an increasing chiral angle. This reflects the trigonal warping effect also apparent for optical matrix elements of lower transitions [61, 62]. At the M-point transition, the respective matrix elements are systematically higher for all chiral angles (drawn in red). In case of the (12,0) zig-zag tube, the maximum value of $|M_z| = 2$ is reached, the values for tubes with higher chiral angles are again slightly lower. E_{77} and

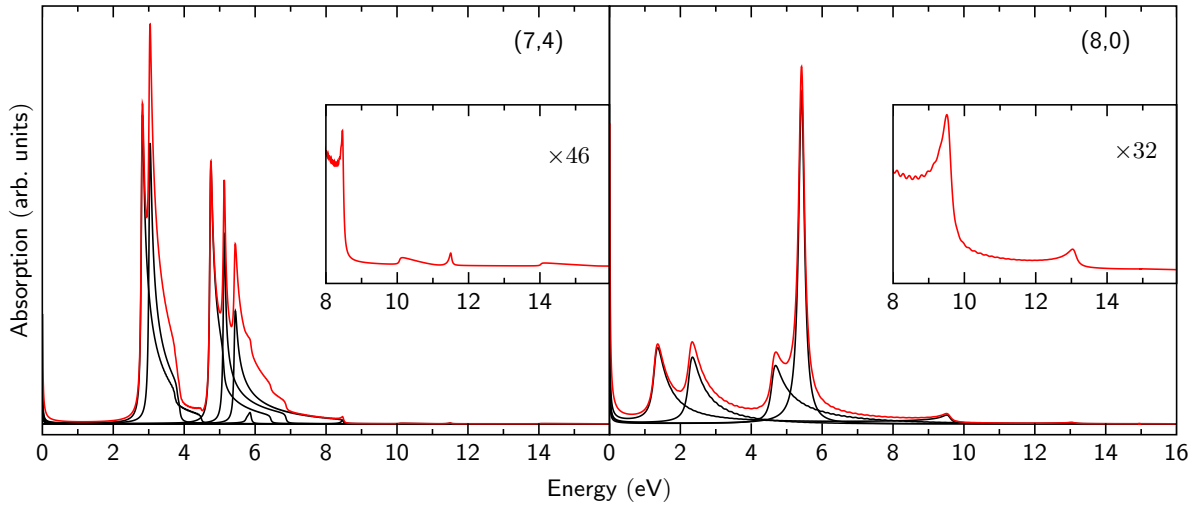

Figure 6.14: Calculated optical absorption spectra of a (7,4) and a (8,0) carbon nanotube are plotted as a function of the photon energy. Black spectra correspond to a band-to-band absorption with $\Delta m = 0$. The red spectra are the sum of all allowed optical transitions, respectively. The linear absorption spectra are calculated in a next-nearest neighbor tight-binding + zone-folding approximation. Insets show a magnification of the absorption in the UV range.

E_{88} (E_{66} and E_{77} in metallic tubes; green and blue) are the first transitions above the M-point energy with significantly lower coupling elements. It is known from graphene, that the optical absorption drastically decreases for energies above the M-point energy both due to a reduced electronic density of states and a lower oscillator strength [138]. The same occurs in carbon nanotubes. Again, we find higher values of $|M_z|$ for smaller chiral angles and vice versa. This can be understood from the fact that for the same optical transition, the bandgaps for higher chiral angles are significantly larger (compare Figs. 6.11 and 6.12). Equivalent transitions in graphene generally have lower oscillator strengths [62, 138]. From Fig. 6.13, we can see that the values for zig-zag tubes for the first two transitions above the M-point energy are roughly one magnitude smaller compared to the transition below and at the M point, *i.e.* the optical absorption is drastically reduced. Although not plotted in Fig. 6.13, all higher transitions exhibit even smaller optical coupling elements $|M_z|$.

From the optical matrix elements, we have calculated full absorption spectra to get further insights into the optical properties of carbon nanotubes in the UV range. For the calculations, we have mainly followed Ref. [61] where the linear absorption in the rotating-wave approximation is given by [61]:

$$\alpha(\omega) \sim \frac{\hbar e_0^2}{m_0^2 \omega} \sum_k |M_z(k)|^2 \frac{\gamma}{(\omega - \omega_{cv})^2 + \gamma^2} \tag{6.1}$$

The wave functions for $|M_z(k)|$ are given in Chapter 2, $\omega_{cv} = \omega_c - \omega_v$ (c and v stand for conduction and valence bands, respectively), and the broadening factor γ was set to 6 meV [62]. The absorption $\alpha(\omega)$ was then obtained by a numerical summation over k for every respective subband of the analyzed carbon nanotube.
Two absorption spectra for a semiconducting (8,0) and a metallic (7,4) CNT as a function of the photon energy are plotted in Fig. 6.14. In case of the metallic (7,4) nanotube, the

absorption peaks occur pairwise due to the trigonal warping effect. Except for the M-point transition of the (8,0) tubes, all absorption peaks are asymmetric mirroring the respective electronic band dispersion. The non-existing dispersion of the electron and hole bands with $m = 4$ leads to a very strong absorption when the (8,0) tube is excited in resonance with the M-point exciton. Including Coulomb-Coulomb interaction however, reduces the M-point absorption considerably but it should still exceed the absorption from electronic bands with other indices m, but also the absorption from other, chiral tubes [62].
The optical absorption of each transition above the M-point energy is more than one magnitude smaller than for absorptions below the M point as can be seen in Fig. 6.14. The closer the excitation occurs to the Γ-point energy ($\sim 16.2\,\mathrm{eV}$ in the used approach), the lower gets the optical absorption. Band dispersions of electron and hole bands are reversed for optical transitions above the M-point energy as we have considered maxima rather than minima in the combined transition energies. As a result, the van-Hove singularities for these transitions are also reversed as apparent in the insets of Fig. 6.14.

UV spectroscopy on carbon nanotubes

What can we learn from the analysis of both the extended Kataura plot and the UV absorption spectra? We can summarize our findings as follows:

- The difference of optical transition energies of carbon nanotubes with comparable diameters is generally larger for transition above the M point, compared to those below the M point. One should consequently observe a smaller amount of tubes in resonance to the laser excitation energy when a sample is excited in the deep-UV region.

- Due to optically forbidden transitions, all armchair carbon nanotubes are excluded from deep-UV spectroscopy.

- Because of symmetry reasons, all carbon nanotubes have the graphene M-point transition in common. As a consequence, all tubes except for the armchair tubes should be in resonance when excited with the M-point transition energy. However, if apparent in a sample, the optical absorption of zig-zag tubes with an even n_1 should dominate the overall absorption.

- Compared to excitations below the M-point energy, the optical absorption above the M-point energy is more than one magnitude smaller. It further decreases with an increasing photon energy. Hence, deep-UV spectroscopy of carbon nanotubes is supposed to be way more difficult than for excitations in the optically visible range.

Deep-UV Raman measurements

We have performed Raman measurements in the deep-UV range on HipCO produced carbon nanotubes. We have tried excitation energies in resonance with the M-point transition ($\sim 4.7\,\mathrm{eV}$), but also higher ones. Some spectra are plotted in Fig. 6.15 b) where the RBM and the G-mode for an excitation energy of 4.69 eV and 5.08 eV are shown. Although observable for an excitation energy $\varepsilon_\mathrm{L} = 4.69\,\mathrm{eV}$, the RBM disappears for an excitation energy of 5.08 eV whereas the G mode is still visible. Even though spectra

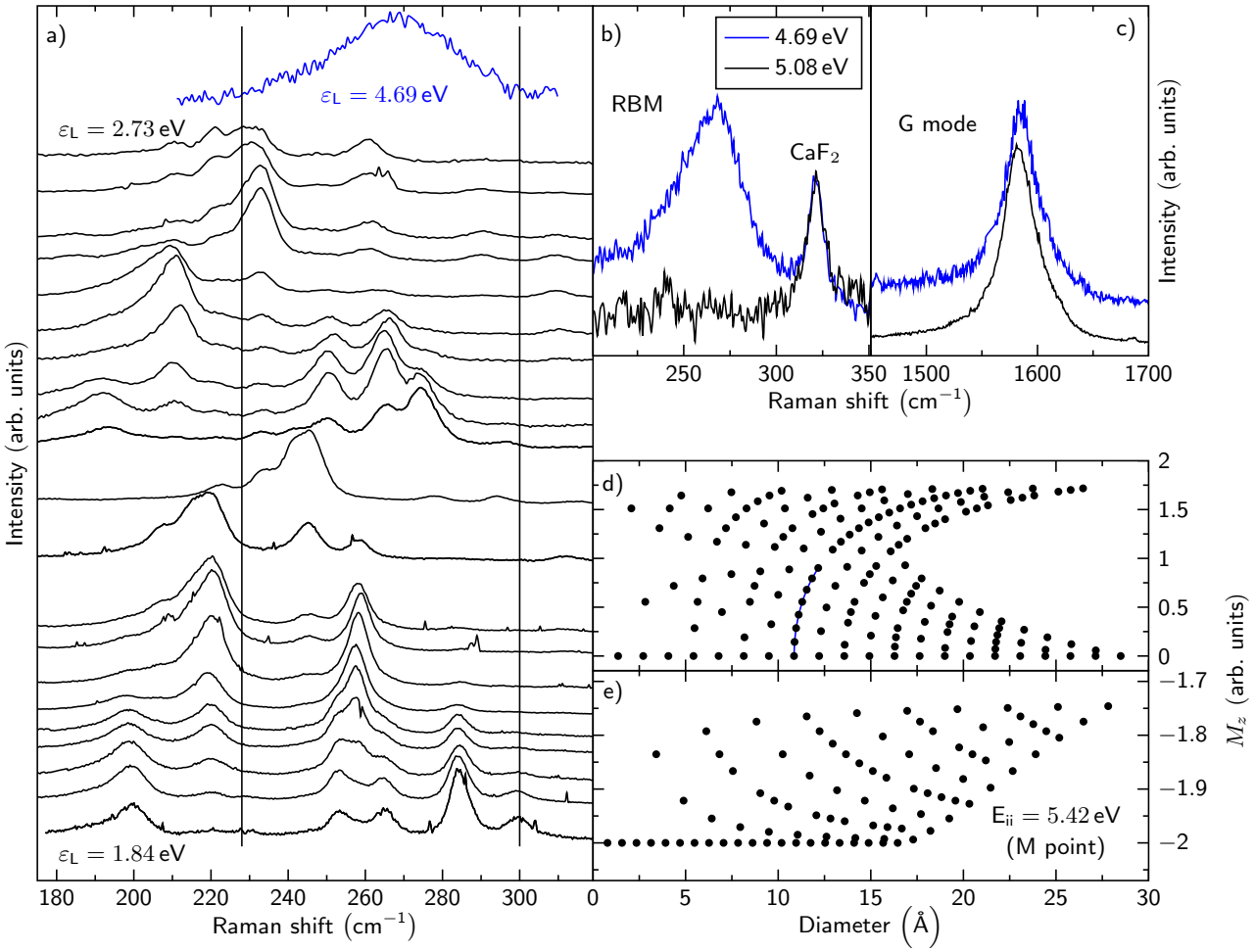

Figure 6.15: Raman spectra of a HipCO sample and optical matrix elements M_z are plotted. a) RBMs of the HipCO sample for many excitation energies between 1.84 eV and 2.73 eV (black) are plotted. The average energy difference between the the excitation energy is $\Delta\varepsilon_L \sim 45$ meV. The RBM for the same HipCO sample excited at the M-point transition (~ 4.7 eV) is plotted in blue. b) and c) RBM and G modes of the HipCO sample for two UV excitation energies are shown. d) and e) Optical matrix elements of carbon nanotubes for the M-point transition as a function of the diameter are plotted. Considered are chiral indices (n_1, n_2) between 2 and 21. Labeled are optical matrix elements for nanotubes where the sum of n_1 and n_2 equals 16.

are not shown, this is also true for higher excitation energies. We believe the absence of the RBM for very high excitation energies is due to the drastically decreasing optical absorption as discussed before. This effect is overcompensated by a very strong electron-phonon coupling due to the Kohn-Anomaly in case of the G mode explaining its presence throughout all deep-UV excitation energies [140, 143, 252]. Further G mode spectra of other carbon nanotube samples and deep-UV excitation energies can be seen in Figs. 6.17 and 6.18.

We find a very large FWHM (full width at half maximum) for the RBM as shown in Fig. 6.15 b) exhibiting $\sim 45\,cm^{-1}$. This very high value is not observed for any other excitation energies as shown in Fig. 6.15 a), in agreement with former findings [269, 270]. We generally attribute the large line width to the concurrent probing of various carbon nanotubes. As discussed before, except for the armchair tubes, all carbon nanotubes have

the M-point transition from graphene in common, allowing for their contemporaneous optical excitation. From that point of view, we might expect a broad and symmetric RBM Raman peak that represents the diameter distribution of carbon nanotubes within the sample, rather than small fractions of tubes in resonance to the laser excitation energy. The frequency range of the RBM measured at $\varepsilon_{\mathrm{L}} = 4.69\,\mathrm{eV}$ covers $\sim 230 - 300\,\mathrm{cm}^{-1}$ as denoted with black lines in Fig. 6.15. In contrast, for optically visible excitation energies between 1.84 eV and 2.73 eV, we find RBMs between $\sim 190 - 300\,\mathrm{cm}^{-1}$, *i.e.* a larger frequency range. Especially the lower frequencies can not be seen within the broad RBM peak in the UV region. A reason for the somewhat smaller frequency range remains unclear. A first explanation might be the fact that absolute values of the optical matrix elements $|M_z|$ of M-point transitions in carbon nanotubes range from 0 up to the overall maximum of 2, as plotted in Fig. 6.15. This also counts for the limited range of diameters $d \sim 8 - 12\,\text{Å}$ of the probed HipCO sample. A similar behavior can not be observed for lower optical transitions in the visible range [61, 62]. As a consequence, several chiralities should be way less visible than others when contemporaneously excited at the M-point transition. For instance, the branch where the sum of n_1 and n_2 equals 16 is marked in Fig. 6.15, in which all nanotubes have low optical matrix elements $|M_z|$. Thus their specific contribution to the optical absorption should be very small compared to other CNTs.

6.3 Ultra-violet light assisted functionalization

A lot of effort has been put in the exploration of paths for a covalent functionalization of carbon nanotubes [271–275]. It is a necessity for possible applications since by a subtle functionalization a solubility in organic or aqueous solvents can be achieved [276], one can separate metallic from semiconducting nanotubes [277], carbon nanotubes can be charged [272, 278], can be prepared for drug delivery [279] or they can be prepared for a far more complicated functionalization such as the growing of embryonic rat-brain neurons [280]. The development of possible reaction paths has defaulted to the broad and -in our days- common knowledge of the functionalization of other large sp^2 system such as fullerenes [271, 281, 282]. Due to their chemical inertness, their functionalization is rather difficult and often requires aggressive chemicals such as strong acids, elemental fluorine, or alkali metals [283, 284].
Another possible path is suggested in Refs [199–201] where photo-assisted functionalizations of carbon nanotubes are shown both theoretically and experimentally. By a solvent-free UVO (ultra-violet-ozone) treatment, esters, quinines, and hydroxyl functional groups could be attached to the surface of multi-walled carbon nanotubes while conserving an insignificant number of defects [201]. Authors in Ref. [200] simulated the UV-light accelerated interaction of carbon nanotubes and oxygen. They found that an UV-assisted excitation of the oxygen ground spin-triplet state to a higher spin-singlet state significantly lowers the activation energy for the molecular-oxygen chemisoprtion to the nanotube [200]. According to the authors, a predominant functionalization happens at defects, such as $7-5-5-7$ or Stone-Wales defects, accompanied by a charge transfer from the oxygen to the carbon nanotube [200]. The suggested methods are a convenient and straight-forward way to functionalize carbon nanotubes without using aggressive chemicals.

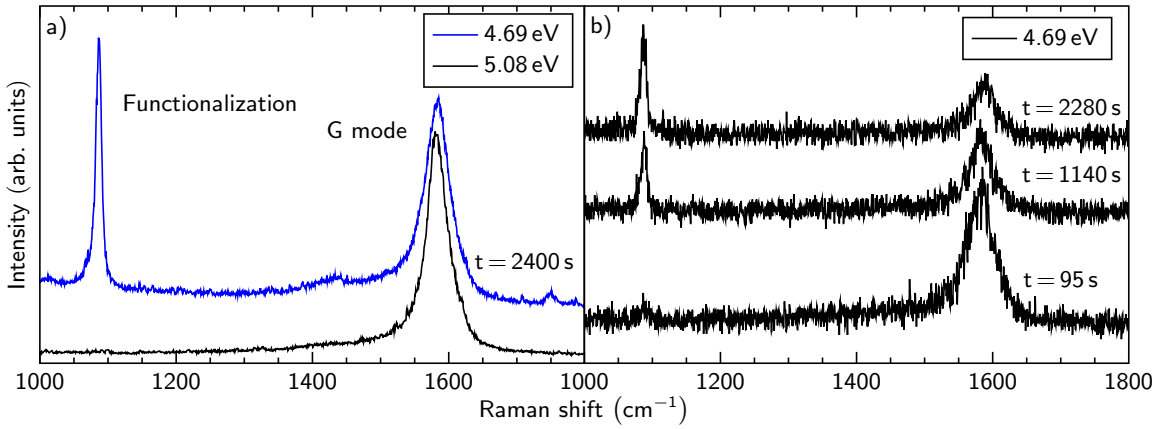

Figure 6.16: UV Raman spectra of a HipCO buckypaper carbon nanotube sample with different excitation energies a) and different exposure times b) are plotted. The G mode and the functionalization mode are denoted.

Based on the analysis of Raman spectra, we show that a HipCO CNT sample can be functionalized only by UV irradiation under standard ambient conditions. Further, we show that the iron clusters in the HipCO sample are oxidized in the presence of UV light and carbon nanotubes.

On the next pages we show experimental data of a newly found Raman mode that we attribute to a CNT and photo-assisted oxygen functionalization of iron clusters. We show experiments where we change external parameters such as the exposure time to UV-light, potential reaction gasses, and the carbon nanotube samples. Further, we demonstrate that the photo-assisted reaction depends on the laser excitation energy. For energies larger than 4.7 eV we can not observe a functionalization in the Raman spectra. In the end we give an explanation and explain the newly observed Raman mode.

6.3.1 Raman analysis of the functionalization

In Fig. 6.16 a) two Raman spectra of the same HipCO buckypaper carbon nanotube sample are shown. The integration times are the same, but the laser excitation energies are different. One is close to the M-point energy (blue) [52, 136, 138] whereas the second excitation energy is 400 meV higher, *i.e.* clearly above the M-point exciton. In the first case, a new Raman mode at around 1086 cm^{-1} can be observed that does not come up when excited with a photon energy of 5.08 eV, even for long exposure times of 40 min. This also counts for higher laser excitation energies. On the right hand side in Fig. 6.16 b), three Raman spectra are plotted with integrations times of 2×95 s, but with overall different UV exposure times as denoted in the figure. The spectra belong to a time series in which a new Raman spectra was taken every 190 s (2×95 s) from the same sample position, *i.e.* one can follow the time-dependent progression of the change in the Raman spectra. For longer exposure times, the intensity of the functionalization mode increases with a simultaneous decrease of the G-band intensity. This can be seen more clearly in Fig. 6.17 where both the absolute intensities of the Raman modes [a)] and their intensity ratios are plotted [b)]. The intensities refer to the area of the Raman peaks as shown in Fig. 6.16 fitted with one Lorentzian peak, respectively.

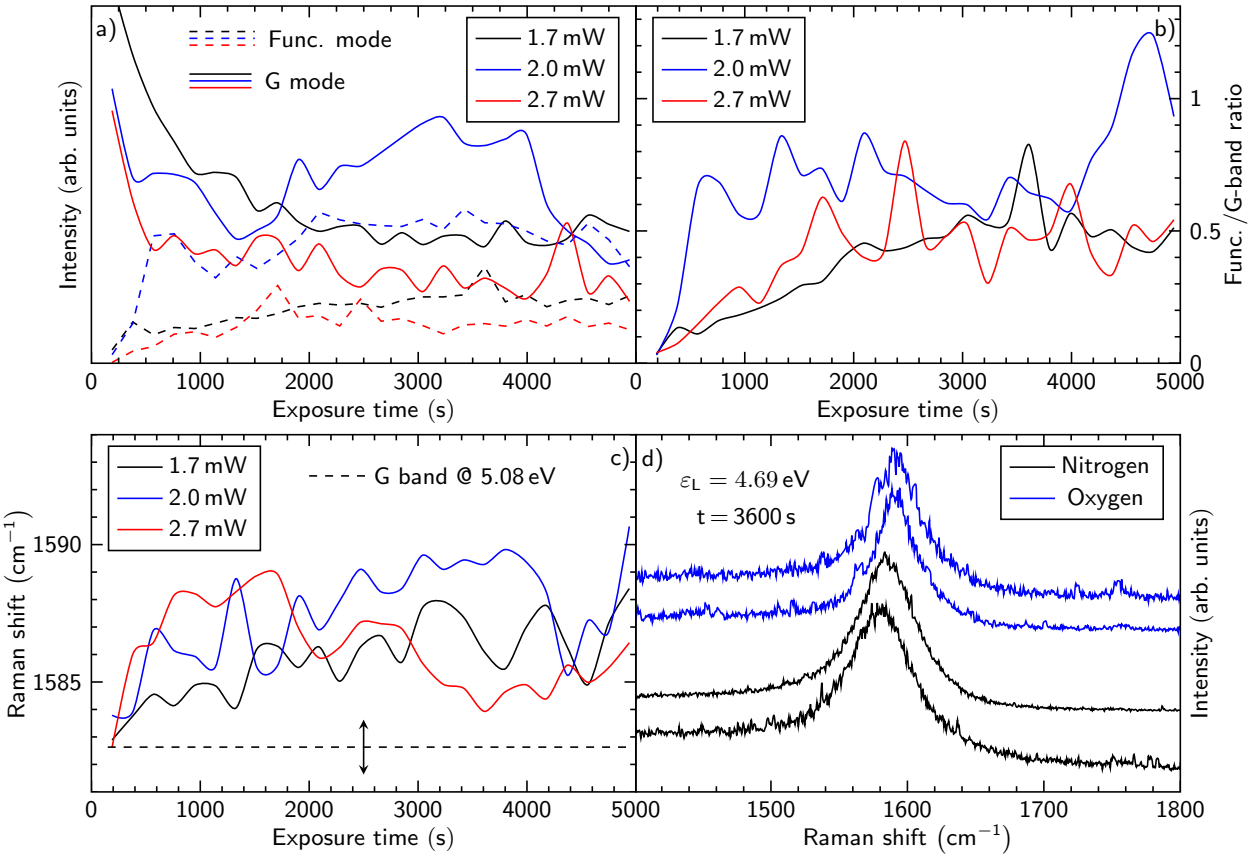

Figure 6.17: Raman intensities, intensity ratios, and Raman frequencies of the fitted functionalization mode and the G mode are shown. All spectra are taken with a laser excitation energy of $\varepsilon_L = 4.69\,\text{eV}$ under standard ambient conditions in ambient air. a) Raman intensities of the Func. mode (dashed lines) and the G mode for three different laser excitation powers are shown. b) Intensity ratios of the Func. mode and the G mode as a function of the exposure time are plotted. c) The Raman shifts of the G band as a function of the exposure time are plotted for difference laser excitation powers. The dashed line denotes the G band frequency at the beginning of the UV exposition, *i.e.* it corresponds to the G band of a widely unfunctionalized carbon nanotube sample. The arrows frame the experimental error. d) Raman spectra of the HipCO sample under UV exposition and irradiation times of $t = 3600\,\text{s}$ in an oxygen atmosphere (blue) and in a nitrogen atmosphere (black) are plotted.

After exposure times of $t \approx 750\,\text{s}$ the intensity of the functionalization mode saturates and stays approximately at the same level up to exposure times of 5000 s. In contrast, the intensity of the G band decreases with increasing exposure times. This explains the increasing Func. / G-band ratios in Fig. 6.17 b). Within the range of probed laser powers, the intensity ratios of the functionalization mode and the G band do not differ substantially. All show the same trends as discussed above.

The averaged G band of the carbon nanotube sample upshifts as a function of UV exposition time in ambient air. For all laser excitation powers, the lowest Raman frequencies are found at the beginning of the exposition followed by an increase of $\approx 4\,\text{cm}^{-1}$ (compare Fig. 6.17). We find the same behavior for graphene as illustrated in Fig. 6.18 d). An exposition to UV light with exposition times up to 5000 s results in an upshift of approximately $3\,\text{cm}^{-1}$ with a contemporaneous decrease of the G-band intensity (Fig. 6.18). Instead, the G-band frequency of graphite under UV exposition does not change as a function of the

exposition time [compare Fig. 6.18 d)]. Further, the intensity drop of the G band in graphite begins after longer exposition times and saturates after approximately $t = 2500\,\mathrm{s}$ in contrast to graphene where a saturation of the intensity drop cannot be observed.

Previous Raman studies on graphene observed a light-induced oxidation accompanied by a frequency increase of the G band [285, 286]. The frequency shift is attributed to an oxidation causing a p-doping in graphene [285–287]. From the shift of the G band, we can estimate the p-doping increase to exhibit $\Delta n = 3.5 \times 10^2\,\mathrm{cm}^{-2}$. Authors in Ref. [286] have found similar upshifts for the G band in graphene after a 10 min irradiation with UV light from a Hg lamp in an oxygen atmosphere corresponding to a hole doping of $n \sim 3.5 \times 10^2\,\mathrm{cm}^{-2}$. We therefore believe the frequency increase in the Raman spectra of the HipCO carbon nanotube sample can also be attributed to an oxygen-induced p-doping. To further analyze this assumption, we have performed likewise experiments in different atmospheres. Namely, we have used Argon, Nitrogen, and Oxygen atmospheres as shown in Fig. 6.18 a). Differently colored spectra correspond to spectra of a HipCO sample excited with $\varepsilon_L = 4.69\,\mathrm{eV}$ and exposition times of $t = 3600\,\mathrm{s}$, but in various atmospheres as denoted in the figure. The functionalization mode at $1086\,\mathrm{cm}^{-1}$ exhibits the largest intensity in the oxygen atmosphere. Instead, its intensity is comparably low in an Argon or in a Nitrogen atmosphere even after long exposition times of $t = 3600\,\mathrm{s}$.In an oxygen atmosphere, a significant increase of the G band frequency can be observed. We have repeated the measurements on various sample spots and show the G band after a $t = 3600\,\mathrm{s}$ UV irradiation in an Oxygen atmosphere (blue) and in a Nitrogen atmosphere (black) in Fig. 6.17 d). Similar to the spectra in Fig. 6.18 a), the UV exposition in Oxygen leads to an upshift of the G band.
Changing the sample to CoMoCat, Elicarb, or arc discharge produced carbon nanotubes we cannot observe the functionalization mode even after UV ($\varepsilon_L = 4.69\,\mathrm{eV}$) exposition times of $t = 3600\,\mathrm{s}$ [Fig. 6.18 b)]. The same accounts for graphene and for graphite as shown in Fig. 6.18 c).

In contrast to all other tested carbon nanotube samples, the HipCO produced carbon nanotubes contain iron as a catalyst for the synthesis [46,60,288]. The iron atoms are existent as iron clusters catalyzing the disproportionation: $CO + CO \xrightarrow{\mathrm{Fe}} CO_2 + C(\mathrm{SWNT})$ [46]. This reaction creates nanotubes that usually have open caps filled with the catalyst [271]. The direct contact to iron clusters might therefore enable possible UV-induced chemical reactions.

For a further investigation, we have patterned the HipCO sample with UV light ($\varepsilon_L = 4.69\,\mathrm{eV}$) as illustrated in Fig. 6.19 c). One can clearly observe the difference in contrast between the areas that have been illuminated and those that have not been illuminated. In the optical visible range ($\varepsilon_L = 2.71\,\mathrm{eV}$) we have then taken a Raman map of the illuminated area and show a map of the D/G ratio as a function of the location on the sample in Fig. 6.19 a). Throughout the entire area, we observe a high D/G ratio of 0.5 and above. However, we can not follow the pattern as visible in Fig. 6.19 c). In contrast, the ratio of the functionalization mode to the G mode does show the pattern illuminated via the UV light [b)]. Only at illuminated spots, we observe high intensities of the functionaliza-

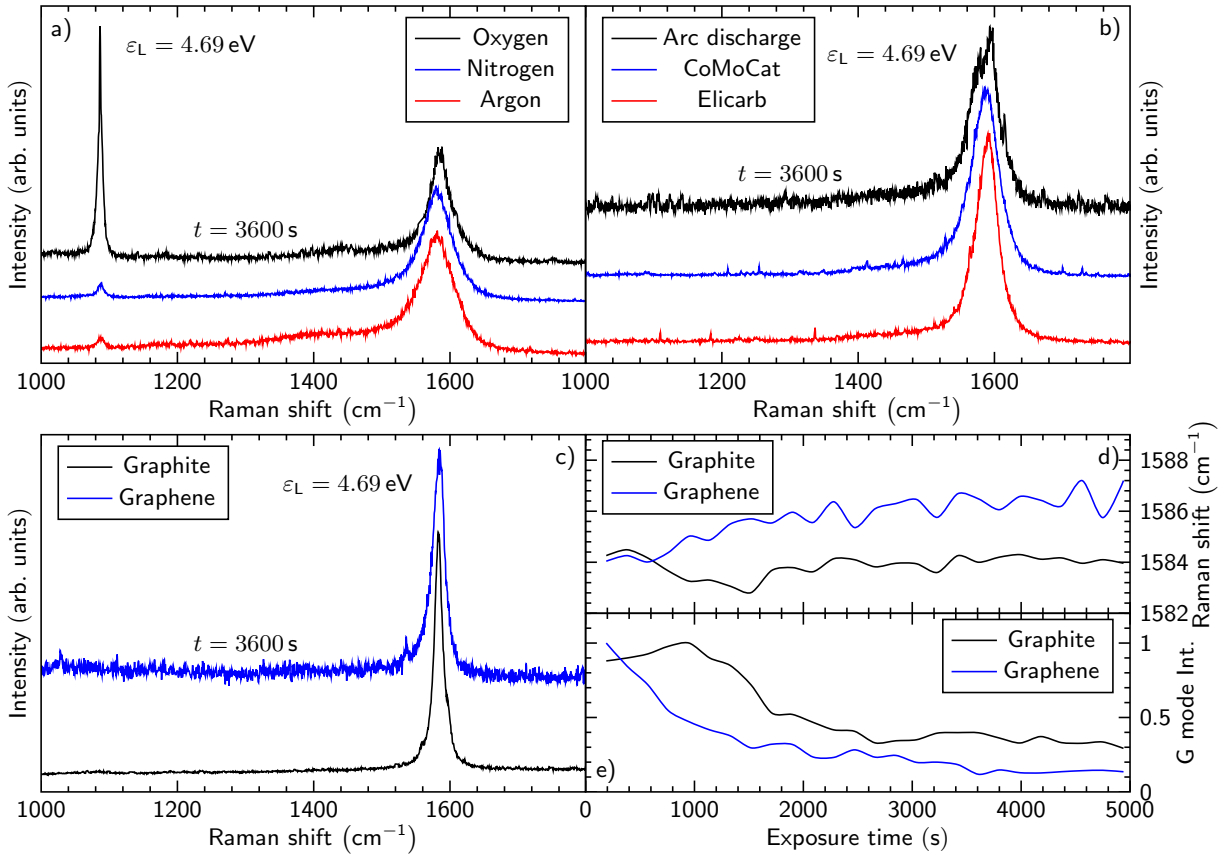

Figure 6.18: Raman spectra of carbon nanotubes, graphene, and graphite are shown. a) Raman spectra of a HipCO sample, an UV exposition of t = 3600 s, and a laser excitation energy of $\varepsilon_L = 4.69\,eV$ with different ambient gasses are plotted. b) Raman spectra of Arc discharge (black), CoMoCat (blue), and Elicarb (red) carbon nanotubes are plotted for a laser excitation energy of $\varepsilon_L = 4.69\,eV$ and an UV exposition of t = 3600 s under standard ambient conditions. c) Raman spectra of graphene (blue) and graphite (black) are shown for a laser excitation energy $\varepsilon_L = 4.69\,eV$ and an UV exposition time of t = 3600 s. d) Raman shift of the G mode under UV exposition and standard ambient conditions as a function of the exposition time for graphite (black) and graphene (blue) are plotted. e) Normalized intensities of the G mode under UV exposition and standard ambient conditions for graphite (black) and graphene (blue) are plotted. Different spectra correspond to different spots on the sample.

tion mode at $1086\,cm^{-1}$ as exemplary shown Fig. 6.19 d) for an excitation energy in the optical visible range. Zones with high func. mode/G mode ratios directly correspond to the illuminated area as shown in Fig. 6.19 c). This means that the functionalization can apparently be reproduced and is clearly UV-light induced. Moreover, as can be seen in the D/G Raman map, the functionalization does not further increase the defect densities in the carbon nanotubes. The already high defect densities usual for HipCO CNT are not further increased at UV-illuminated areas.

6.3.2 Explanation of the functionalization process

In the following we summarize the conditions in which we observe the functionalization and try to frame an explanation for its origin.

- The functionalization is UV induced and can only be initiated for an excitation energy of $\varepsilon_L = 4.69\,eV$. This energy is close to the M-point energy in graphene

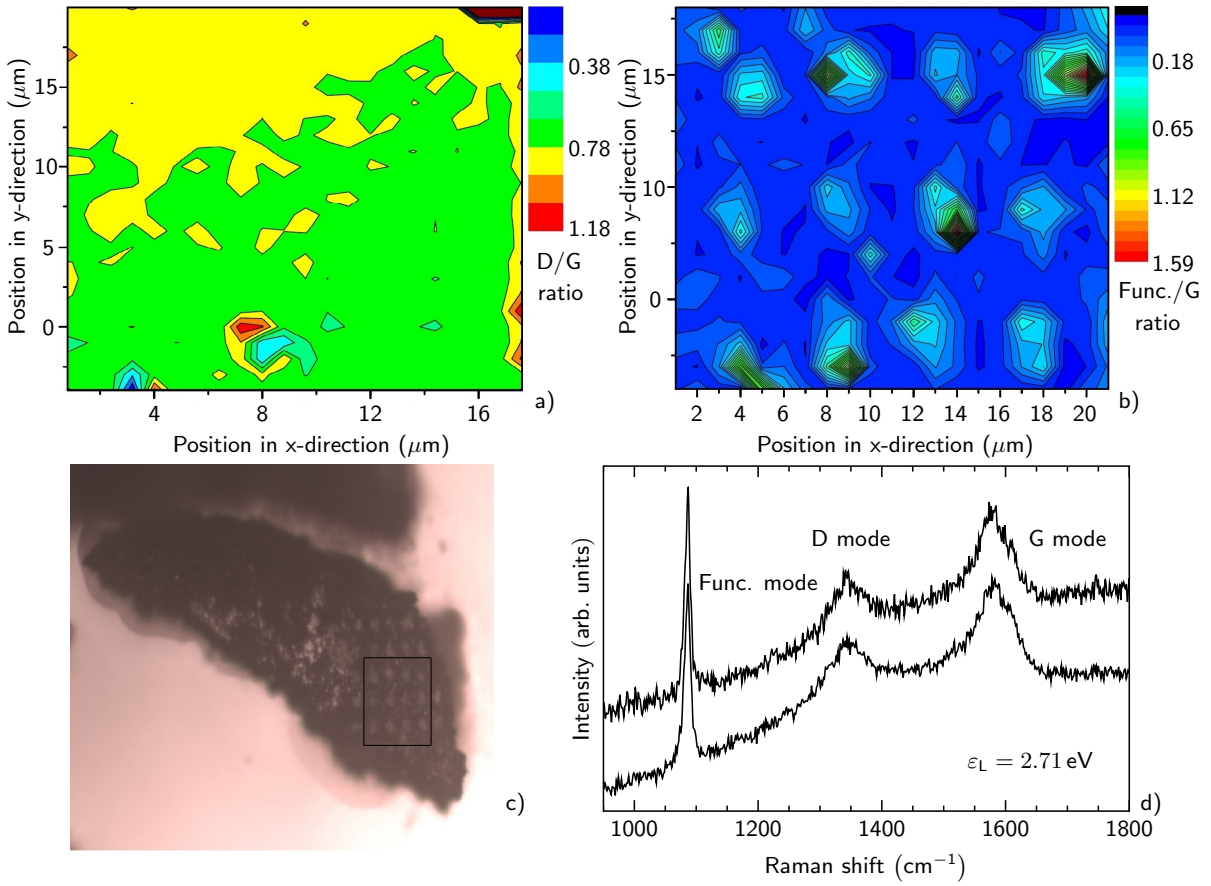

Figure 6.19: a) A Raman map of the D/G ratio @ $\varepsilon_L = 2.71\,\text{eV}$ from a HipCO carbon nanotube sample that was illuminated with UV ($\varepsilon_L = 4.69\,\text{eV}$) Light (step size in x-direction: $5\,\mu\text{m}$, step size in y-direction: $8\,\mu\text{m}$) is shown. b) A Raman map of the Func. mode/G ratio @ $\varepsilon_L = 2.71\,\text{eV}$ is shown after illumination as in a). The measured area on the sample is the same as before. c) Optical image ($50\times$ magnification) of the UV illuminated area on the HipCO nanotube sample. One can clearly see the irradiation pattern. The depicted rectangle corresponds to the measured areas as shown in a) and b). d) Representative Raman spectra of the HipCO sample showing the func. mode with a high intensity. They correspond to areas in b) with a high func. mode/G ratio. The laser excitation energy is $\varepsilon_L = 2.71\,\text{eV}$.

[52, 136], accompanied by a strong optical absorption [136, 138]. As a consequence of symmetry, all but armchair carbon nanotubes contain the M point of graphene, *i.e.* by an excitation energy of $\varepsilon_L = 4.69\,\text{eV}$ almost all carbon nanotubes within an ensemble sample are in an optical resonance. Further, this laser excitation energy equals the work function of graphene, graphite, and carbon nanotubes [38, 289–291], potentially providing charge carriers for a chemical reaction.

- For excitation energies higher than 4.69 eV, a functionalization can not be initiated. The optical absorption decreases considerably for energies higher than the M-point exciton [138], reducing the possible amount of charge carriers for a chemical reaction.

- The functionalization can only be observed in HipCO samples. It can not be seen in arc discharge, Elicarb, or CoMoCat carbon nanotube samples. Further, other carbon allotropes do not show the functionalization mode. We refer this behavior to the presence of iron in the sample.

- The defect densities in UV illuminated areas of the HipCO carbon nanotube sample do not increase.
- The presence of oxygen is essential for the chemical reaction.
- An analysis of the G band of the carbon nanotubes suggests that a p-doping after the functionalization occurs. This is a well-known behavior in graphene, an oxidation causes a p-doping attended by an upshift of the G band.
- The func. mode intensity saturates after certain UV exposition times, accompanied by a decrease of both G-mode and D-mode intensity. An advancing UV-assisted destruction of CNTs limits the possible supply of charge carriers for a chemical reaction, showing the clear necessity of the presence of carbon nanotubes for the reaction.

A strong Raman band at around $1086\,\mathrm{cm}^{-1}$ is characteristic for different calcite group structures [292–294]. The calcite group contains ionic minerals with the carbonate $[(CO_3)^{-2}]$ as the characteristic anion [295]. The anion is paired with comparably small cations, such as Li, Na, Mg, Zn, Fe^{2+}, or Cd forming a group of minerals with very similar crystallographic traits [295]. The symmetry of all its members is the trigonal $\bar{3}\frac{2}{m}$ point group (D_{3d} in the Schönflies notation) [295] allowing for six normal modes of which two are doubly degenerate [293]. One of them corresponds to a symmetric stretching vibration of the carbonate groups having the irreducible representation A_1' being Raman active and usually showing a strong, distinct Raman peak [292–294]. The vibrational pattern is illustrated in Fig. 6.20. It seems feasible that the strong Raman peak in the spectra of the UV-irradiated areas on the carbon nanotube sample can be referred to originate from one member of the calcite group, namely the siderite ($FeCO_3$). The iron and carbon residuals in the sample react under UV irradiation with oxygen and form the mineral siderite. Therefore, by a photo-induced chemical reaction, we produce a mineral whose strong Raman signal superimposes with that of the carbon nanotubes still present in the sample. However, this does not explain the clear upshift of the G band when the HipCO sample is UV-illuminated. We believe the upshift is also due to an oxidation of the carbon nanotubes in agreement with former observations [285–287].

The reaction path for the formation of the siderite remains unclear. In the presence of carbon nanotubes, it is clearly an UV-light induced process. The carbon nanotubes may provide the charge carriers necessary to reduce the pentavalent iron in the iron pentacarbonyl complex that is usually present in HipCO samples [46, 60, 288]. This would explain, why the strong Raman band at around $1086\,\mathrm{cm}^{-1}$ can only be observed when the sample is excited with $\varepsilon_\mathrm{L} = 4.69\,\mathrm{eV}$. An excitation energy of $\sim$4.7 eV on the one hand leads to a comparably strong absorption in carbon nanotubes but on the other hand it also is the energy of the work function in carbon nanotubes. Since this strong Raman band is not initiated for higher excitation energies, we believe that an electrophilic reaction causes a reallocation of both carbon and oxygen from the iron pentacarbonyl [$Fe(CO)_5$] to the Fe clusters present in the HipCO sample [46, 60, 288].
Authors in Ref. [200] refer the oxidation of carbon nanotubes in the presence of UV light to the more reactive singlet oxygen $O_2(^1\Delta_g)$ rather than to the ground spin-triplet state

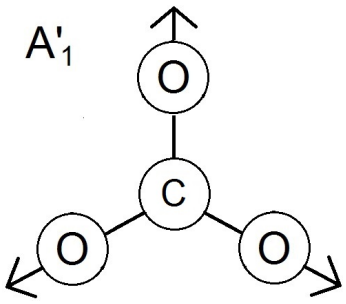

Figure 6.20: The vibrational pattern of the A_1' mode in siderite (D_{3d} point group) is illustrated [293].

oxygen $O_2(^3\Sigma_g^-)$. This may also be a feasible explanation for the UV-induced formation of the siderite. However, since we cannot observe the siderite Raman peak for excitation above ∼4.7 eV this explanation is questionable. It was recently shown, that the UV-induced formation of the reactive singlet state oxygen $O_2(^1\Delta_g)$ states occurs between $\sim\ 230 - 290$ nm with comparable yields [296]. Higher excitation energies than 4.69 eV (264 nm) would therefore provide similar amounts of excited oxygen molecules. Yet, we do not observe the functionalization peak for higher excitation energies. Hence, the carbon nanotubes are crucial for the UV-induced formation of the siderite in the HipCO sample. Since the work functions of graphene, graphite, and fullerenes are very close to those from carbon nanotubes, the UV-induced formation of siderite should also be possible with the just listed carbon allotropes. It might be interesting to repeat the UV exposure measurements with other carbon allotropes but with the same catalysts as needed for the growth of HipCO carbon nanotubes. However, this is beyond the scope of the present work.

6.4 Summary

We analyzed the low-intensity, double-resonant Raman modes at around 1950 cm^{-1} and 2450 cm^{-1} in an ensemble carbon nanotube sample. With the support of DFT + zone-folding calculations we modeled their dispersions, peak intensities, and general peak structures. We find that the complex dispersions can be understood from contributions of individual carbon nanotubes close to the resonance of the laser excitation energies. Depending on chirality and diameter, each carbon nanotube adds an unique share to the complex line shape of the low-intensity Raman modes. Since metallic and semiconducting tubes necessarily exhibit unlike diameters when both species are in resonance to the laser excitation energy, their vibrational properties need to differ accordingly. As a consequence, the contemporaneous probing of both species results in bimodal peak structures of the analyzed double-resonant Raman modes. This effect is a clear ensemble effect and especially occurs for the $\sim 1950\,cm^{-1}$ band since the frequencies of the phonons involved highly depend on the tube diameter.

The assignment of both low-intensity modes has been discussed controversially in the past. Especially the 1950 cm^{-1} mode was only tentatively assigned without the support of calculations. In a DFT + zone-folding approach, we find a LO+LA @ Γ combination mode responsible for the mentioned mode. Instead, in a non-orthogonal tight-binding approach, the 1950 cm^{-1} mode is rather attributed to a TO+ZO @ K combination. The out-of-plane ZO phonon mode is symmetry forbidden in graphene resulting in very low electron-phonon coupling elements in the zone-folding calculations. This in turn might

lead to an underestimation of its contribution to the mode at around 1950 cm^{-1} in comparison to the LO+LA @ Γ mode. The non-orthogonal tight-binding approach however does not have this insufficiency as it is an *ab initio* approach and takes the CNT into account without initial assumptions. We therefore tentatively the 1950 cm^{-1} band to a TO+ZO @ K combination mode. In contrast, the 2450 cm^{-1} mode is uniformly assigned to a TO+LA @ K combination mode in both computational approaches.

We have introduced the "extended Kataura plot" containing optical transitions way above the M-point energy in carbon nanotubes. This is a clear contrast to the usual Kataura plot that only contains optical transitions in the visible range, *i.e.* below the M-point energy. By simulating the matrix elements, we find that above the M-point energy, several optical transitions are forbidden - a clear difference to those transitions that are lower than the M-point energy. In particular, these are all transitions from armchair nanotubes, but also all transitions stemming from the Γ point. Although the arrangement of optical transitions above the M-point energy appears to be different compared to those from below the M-point energy, they also follow the well known trends caused by the quantum confinement and trigonal warping effect.

Raman measurements of the RBM (radial-breathing mode) for an excitation energy close to the M-point energy show a broad peak that cannot be observed for excitation energies in the visible range. We generally attribute the large FWHM to the concurrent probing of many carbon nanotube chiralities since the M-point transition is except for armchair tubes included in all carbon nanotubes. Higher excitation energies lead to a drastic quenching of RBM intensity that we generally attribute to the low optical absorption for very high excitation energies.

In the end we showed how UV light and carbon nanotubes can be used to fabricate siderite. Its Raman footprint can only be observed in the presence of oxygen, photon energies of $\varepsilon_{\mathrm{L}} = 4.69\,\mathrm{eV}$, and the iron catalyst as present in a HipCO carbon nanotube sample. We believe the formation of Siderite is caused by two reasons: On the one hand, CNT have a very strong optical absorption around 4.7 eV. On the other hand, 4.7 eV corresponds to the work function of CNT possibly providing the charge carriers necessary for the oxidation of the iron clusters.

7. Conclusion

Diamondoid derivatives

By (resonance) Raman scattering experiments, we have turned the attention to zero-dimensional diamondoid derivatives. In particular, we have focused on the effect of sp^2 defects in the electronic structure of otherwise fully saturated diamondoids. The structural changes cause energetically low-lying π and π^* orbitals, resulting in optical transition energies of 4.7 eV that are around 2 eV smaller than in pristine diamondoids. Studying a large variety of diamondoid oligomers connected by sp^2 defects, we have found the optical transitions energies of 4.7 eV to be independent of their sizes or structures. These experimental outcomes are in a very good agreement with sophisticated DFT calculations on the one hand, but also with absorption and valence photoelectron spectroscopy measurements on the other hand.
Along with the lifting of the degeneracy of certain vibrational modes, new structural-induced eigenmodes could be found in the vibrational Raman spectra of sp^2 diamondoid oligomers. Some of them can directly be assigned to the ethylene sp^2 moieties, such as the intensity-wise strong C=C stretch vibration, or a combined twisting/stretch mode of the C=C double bond. However, the new structures of diamondoid oligomers lead to unusual high-frequency C-H stretch vibrations but also to vibrational modes in which the entire diamondoid moieties are deflected along their shared carbon-carbon double bond. We refer these modes to Dimer breathing modes (DBM) that have only small frequencies in the range of $\sim 190\,\mathrm{cm}^{-1}$ caused by the comparably large masses of the diamondoid moieties. To sum up, Raman spectra of sp^3 diamondoid oligomers are generally more complex compared to pristine diamondoids. The covered frequency range of Raman active vibrations is further enlarged due to new, structural-induced vibrational modes.

In analogy, we find a similar altering of the vibrational characteristics in diamondoid dimers that are connected by single-bonds. Again, high-frequency C-H stretch vibrations are found that are caused by additional restoring forces of neighboring diamondoid moieties within the dimers. This is a clear difference to the sp^2 diamondoid oligomers as their comparably stiff double bond determines the angle and distance between the diamondoid moieties. This, in turn, impedes the formation of pronounced facets that induce additional van-der-Waals forces in single-bond dimers. We again find Dimer breathing modes in the frequency range around $\sim 200\,\mathrm{cm}^{-1}$. However, due to the loose single bond, the vibrational modes are slightly modified because of a considerable mode mixing with other low-frequency modes.

Diamondoid and diamondoid derivatives form very stable van-der-Waals crystals at room

temperatures, accompanied by a self-altering of their electronic properties. With absorption and resonance Raman measurements, we could determine a downshift of optical transition energies in sp^2 diamondoid dimer crystals of around 1 eV, compared to isolated molecules. This value, in particular, counts for the $\pi \rightarrow \pi^*$ transition that was experimentally accessible. DFT calculations, however, indicate that the reduction of transition energies related to the more widespread $\sigma \rightarrow \sigma^*$ transitions can even be larger. We believe that this particular aspect in the electronic properties of diamondoids is of great importance. Thinkable applications in devices for instance, require not just isolated molecules, but rather diamondoids in a solid phase.

Graphite, graphene, and multilayer graphene

Raman intensities of the well-known, double-resonant Raman modes such as the D or the $2D$ mode in graphitic sp^2 materials are drastically quenched for excitation energies in the range between $\varepsilon_\mathrm{L} = 4.69$-$5.46$ eV. We, instead, find new Raman peaks that we attribute to the second-order vibrational density of states. Optical excitations higher than the M-point energy (~ 4.7 eV) lead to an absorption far away from the $K - M$ high-symmetry line, accompanied by a large decrease of oscillator strength. The reduced absorption combined with a drastically reduced electron-phonon coupling then results in a strong quenching of double-resonant Raman processes. In fact, their quenching is so strong, that not resonantly enhanced second-order processes exceed their intensities. These "single-resonant" processes involve two phonons with arbitrary phonon wave vectors that can stem from all over the 1. Brillouin zone. However, it turned out that only those phonon wave vectors contribute to a deep-UV Raman spectrum that have a large density of states. In particular, these are the LO/TO phonon branches from the Γ point, the LO overbending area around the Γ point, and the TO/LA as well as the LO phonon branches at the M point. Especially the high-momentum M-point phonons are not accessible with excitation energies from the visible spectrum.
Although inactive in a first-order Raman process, the E_{1u} mode in graphite gets active in a second-order Raman process. As a consequence, we get a simultaneous access to the Raman active E_{2g} and Raman inactive E_{1u} modes in graphite. We find analogies in the deep-UV Raman spectra of graphene and carbon nanotubes, but with altered phonon frequencies. This is even true for carbon nanotubes as we have measured an ensemble sample. To summarize, deep-UV Raman measurements give direct access to areas in the phonon dispersions of low-dimensional carbon materials that are otherwise only accessible by more complicated experimental methods such as elastic neutron scattering.

For excitation energies close to the M-point energy, we observe a fingerprint of the weakly emitting $2D$ mode. In contrast to measurements in the visible region, it is a very low-intensity peak found around $3050\,\mathrm{cm}^{-1}$. Due to the optical excitation close to the M point, the involved phonons have the smallest possible phonon wave vectors in a double-resonant process. As a consequence, the phonons stem from the Γ point rather than from the proximity of the K points as in the case of excitations in the visible range.

We have found that the second-order vibrational density of states in multilayer graphene only depends marginally on the layer number. By these experimental findings we can

conclude that Γ-point frequencies of degenerate pairs of LO/TO phonons in multilayer graphene are very close to those from graphite.

Carbon nanotubes

Low-intensity Raman modes at around 1950 and 2450 cm^{-1} have been analyzed in an ensemble sample. For a large range of excitation energies, we have found that the explored modes are dispersive exhibiting bimodal peak structures. Simulating the Raman modes in an ensemble sample with DFT + zone-folding calculations, we find that both dispersion and bimodal peak structures are clear ensemble effects. Due to their diverse electronic structures, metallic and semiconducting species have different diameters for likewise optical bandgaps. Their diameters determine distinct phonon energies resulting in pronounced Raman peaks that can be attributed to metallic or semiconducting tubes when excited contemporaneously.

Especially the assignment of the 1950 cm^{-1} mode was discussed controversially in the past. Our DFT calculations indicate that it can be referred to a LO+LA @ Γ process. However, a non-orthogonal tight-binding approach rather attributes this mode to a TO+ZO @ K process. As the DFT + zone-folding approach requires the initial electron-phonon coupling elements from graphene, we believe a ZO contribution to low-intensity Raman modes is generally underestimated. The out-of-plane ZO mode in graphene is symmetry forbidden that not necessarily holds true for carbon nanotubes. Therefore, we tentatively assign the mode at around 1950 cm^{-1} to a TO+ZO @ K process. In both approaches uniformly assigned, the mode at around 2450 cm^{-1} is a TO+LA @ K combination mode.

We have introduced an "extended Kataura plot" that contains optical transitions up to the highest possible $\pi \rightarrow \pi^*$ transition. Although appearing contrary on a first view, the arrangement of optical transitions as a function of the tube diameter follows the well-known quantum confinement and trigonal warping effect. However, in contrast to transitions in the visible range, we find that several transitions are forbidden. In particular, these are all transitions at and above the M point from armchair tubes and all transitions from the Γ point. The optical matrix elements of transitions way above the M point are generally orders of magnitudes smaller than those below the M point. We believe this is the reason why we do not observe a Raman signal of the RBM for excitation energies higher than 4.7 eV. Instead, a very broad Raman peak is observed for an excitation energy very close to the M-point energy. Because of symmetry, all but armchair nanotubes have the M-point transition in common which is why we excite a huge variety of nanotubes for $\varepsilon_{\mathrm{L}} = 4.69\,\mathrm{eV}$. This, in turn, leads to a very large FWHM of the RBM.
With our measurements and calculations, we can generally conclude that excitations in the visible range are more suitable for the characterization of a carbon nanotube samples than those in the deep-UV region. On the one hand, the amount of carbon nanotubes excited with a deep-UV excitation energy is generally smaller than for excitations in the visible range. On the other hand, the optical absorption drastically decreases for deep-UV excitation energies. We rather believe deep-UV Raman spectroscopy of carbon nanotubes is a complementary characterization tool that reveals new aspects such as the second-order vibrational density of states. However, deep-UV excitations may open a new way of car-

bon nanotube chemistry as shown for the light and carbon nanotube-induced formation of Siderite. We have found that excitations close to both the absorption maximum and the work function of carbon nanotubes in the presence of iron and atmospheric oxygen, lead to the formation of iron-carbonate clusters.
In many ways, the Raman response from carbon nanotubes in the deep-UV region differs from that in the visible region. Deep-UV Raman spectroscopy can especially be utilized to observe phonons that are not accessible by visible light. In particular, this might be interesting for isolated carbon nanotubes since ensemble effects, as in the explored case, screen individual contributions.

List of Figures

Bibliography

[1] K. S. Novoselov, A. K. Geim, S. V. Morozov, D. Jiang, Y. Zhang, S. V. Dubonos, I. V. Grigorieva, and A. A. Firsov, "Electric field effect in atomically thin carbon films," *Science*, vol. 306, no. 5696, pp. 666–669, 2004. [Online]. Available: http://science.sciencemag.org/content/306/5696/666

[2] N. D. Mermin and H. Wagner, "Absence of ferromagnetism or antiferromagnetism in one- or two-dimensional isotropic Heisenberg models," *Phys. Rev. Lett.*, vol. 17, pp. 1133–1136, Nov 1966. [Online]. Available: https://link.aps.org/doi/10.1103/PhysRevLett.17.1133

[3] L. Song, L. Ci, H. Lu, P. B. Sorokin, C. Jin, J. Ni, A. G. Kvashnin, D. G. Kvashnin, J. Lou, B. I. Yakobson, and P. M. Ajayan, "Large scale growth and characterization of atomic hexagonal boron nitride layers," *Nano Letters*, vol. 10, no. 8, pp. 3209–3215, 2010. [Online]. Available: https://doi.org/10.1021/nl1022139

[4] K. F. Mak, C. Lee, J. Hone, J. Shan, and T. F. Heinz, "Atomically thin MoS2: A new direct-gap semiconductor," *Phys. Rev. Lett.*, vol. 105, p. 136805, Sep 2010. [Online]. Available: https://link.aps.org/doi/10.1103/PhysRevLett.105.136805

[5] L. Fu and C. L. Kane, "Superconducting proximity effect and Majorana fermions at the surface of a topological insulator," *Phys. Rev. Lett.*, vol. 100, p. 096407, Mar 2008. [Online]. Available: https://link.aps.org/doi/10.1103/PhysRevLett.100.096407

[6] A. S. Mayorov, R. V. Gorbachev, S. V. Morozov, L. Britnell, R. Jalil, L. A. Ponomarenko, P. Blake, K. S. Novoselov, K. Watanabe, T. Taniguchi, and A. K. Geim, "Micrometer-scale ballistic transport in encapsulated graphene at room temperature," *Nano Letters*, vol. 11, no. 6, pp. 2396–2399, 2011. [Online]. Available: https://doi.org/10.1021/nl200758b

[7] C. Lee, X. Wei, J. W. Kysar, and J. Hone, "Measurement of the elastic properties and intrinsic strength of monolayer graphene," *Science*, vol. 321, no. 5887, pp. 385–388, 2008. [Online]. Available: http://science.sciencemag.org/content/321/5887/385

[8] S. Iijima, "Helical microtubules of graphitic carbon," *Nature*, vol. 354, no. 56, 1991.

[9] C. Thomsen and S. Reich, "Double resonant Raman scattering in graphite," *Phys. Rev. Lett.*, vol. 85, pp. 5214–5217, Dec 2000. [Online]. Available: https://link.aps.org/doi/10.1103/PhysRevLett.85.5214

[10] S. Pisana, M. Lazzeri, C. Casiraghi, K. S. Novoselov, A. K. Geim, A. C. Ferrari, and F. Mauri, "Breakdown of the adiabatic Born-Oppenheimer approximation in graphene," *Nature*, vol. 6, no. 198, 2007. [Online]. Available: http://dx.doi.org/10.1038/nmat1846

[11] M. Lax, V. Narayanamurti, R. C. Fulton, R. Bray, K. T. Tsen, and K. Wan, "Raman scattering and the two-phonon density of states in GaAs," in *Phonon Scattering in Condensed Matter*, W. Eisenmenger, K. Laßmann, and S. Döttinger, Eds. Berlin, Heidelberg: Springer Berlin Heidelberg, 1984, pp. 133–135.

[12] R. Cuscó, E. Alarcón-Lladó, J. Ibáñez, L. Artús, J. Jiménez, B. Wang, and M. J. Callahan, "Temperature dependence of Raman scattering in ZnO," *Phys. Rev. B*, vol. 75, p. 165202, Apr 2007. [Online]. Available: https://link.aps.org/doi/10.1103/PhysRevB.75.165202

[13] J. Serrano, A. H. Romero, F. J. Manjón, R. Lauck, M. Cardona, and A. Rubio, "Pressure dependence of the lattice dynamics of ZnO: An ab initio approach," *Phys. Rev. B*, vol. 69, p. 094306, Mar 2004. [Online]. Available: https://link.aps.org/doi/10.1103/PhysRevB.69.094306

[14] P. Venezuela, M. Lazzeri, and F. Mauri, "Theory of double-resonant Raman spectra in graphene: Intensity and line shape of defect-induced and two-phonon bands," *Phys. Rev. B*, vol. 84, p. 035433, Jul 2011. [Online]. Available: https://link.aps.org/doi/10.1103/PhysRevB.84.035433

[15] V. Skákalová, J. Maultzsch, Z. Osváth, L. P. Biró, and S. Roth, "Intermediate frequency modes in Raman spectra of Ar+-irradiated single-wall carbon nanotubes," *physica status solidi (RRL) - Rapid Research Letters*, vol. 1, no. 4, pp. 138–140, 2007. [Online]. Available: http://dx.doi.org/10.1002/pssr.200701069

[16] E. Dobardžić, I. Milošević, B. Nikolić, T. Vuković, and M. Damnjanović, "Single-wall carbon nanotubes phonon spectra: Symmetry-based calculations," *Phys. Rev. B*, vol. 68, p. 045408, Jul 2003. [Online]. Available: https://link.aps.org/doi/10.1103/PhysRevB.68.045408

[17] S. Landa and V. Macháček, "Sur l'adamantane, nouvel hydrocarbure extrait du naphte," *Collect. Czech. Commun.*, vol. 5, pp. 1–5, 1933. [Online]. Available: http://dx.doi.org/10.1135/cccc19330001

[18] A. A. Spasov, T. V. Khamidova, L. Bugaeva, and I. S. Morozov, "Adamantane derivatives: Pharmacological and toxicological properties (review)," *Pharmaceutical Chemistry Journal*, vol. 34, pp. 1–7, 01 2000.

[19] J. E. Dahl, S. G. Liu, and R. M. K. Carlson, "Isolation and structure of higher diamondoids, nanometer-sized diamond molecules," *Science*, vol. 299, no. 5603, pp. 96–99, 2003. [Online]. Available: http://science.sciencemag.org/content/299/5603/96

[20] T. M. Willey, C. Bostedt, T. van Buuren, J. E. Dahl, S. G. Liu, R. M. K. Carlson, L. J. Terminello, and T. Möller, "Molecular limits to the quantum confinement model in diamond clusters," *Phys. Rev. Lett.*, vol. 95, p. 113401, Sep 2005. [Online]. Available: https://link.aps.org/doi/10.1103/PhysRevLett.95.113401

[21] S. Roth, D. Leuenberger, J. Osterwalder, J. Dahl, R. Carlson, B. Tkachenko, A. Fokin, P. Schreiner, and M. Hengsberger, "Negative-electron-affinity diamondoid monolayers as high-brilliance source for ultrashort electron pulses," *Chem. Phys. Let.*, vol. 495, no. 1-3, pp. 102–108, 2010. [Online]. Available: http://www.sciencedirect.com/science/article/pii/S0009261410008729

[22] T. S. Zhuk, T. Koso, A. E. Pashenko, N. T. Hoc, V. N. Rodionov, M. Serafin, P. R. Schreiner, and A. A. Fokin, "Toward an understanding of diamond sp^2-defects with unsaturated diamondoid oligomer models," *J. Am. Chem. Soc.*, vol. 137, no. 20, pp. 6577–6586, 2015. [Online]. Available: http://dx.doi.org/10.1021/jacs.5b01555

[23] P. R. Schreiner, L. V. Chernish, P. A. Gunchenko, E. Y. Tikhonchuk, H. Hausmann, M. Serafin, S. Schlecht, J. E. P. Dahl, R. M. K. Carlson, and A. A. Fokin, "Overcoming lability of extremely long alkane carbon-carbon bonds through dispersion forces," *Nature*, vol. 477, no. 308, 2011. [Online]. Available: http://dx.doi.org/10.1038/nature10367

[24] G. A. K. and K. S. Novoselov, "The rise of graphene," *Nature Materials*, vol. 6, no. 183, 2007.

[25] J. C. Meyer, A. K. Geim, M. I. Katsnelson, K. S. Novoselov, T. J. Booth, and S. Roth, "The structure of suspended graphene sheets," *Nature*, vol. 446, no. 60, 2007.

[26] A. Fasolino, J. H. Los, and M. I. Katsnelson, "Intrinsic ripples in graphene," *Nature Materials*, vol. 6, no. 858, 2007.

[27] G. L. Miessler, P. J. Fischer, and D. A. T. Tarr, *Inorganic Chemistry (5th eidtion)*. Pearson, 2014.

[28] I. Herztel and S. Claus-Peter, *Atome, Moleküle und optische Physik 2*. Springer Spektrum, 2010.

[29] J. Filik, J. N. Harvey, N. L. Allan, P. W. May, J. E. P. Dahl, S. Liu, and R. M. K. Carlson, "Raman spectroscopy of nanocrystalline diamond: An ab initio approach," *Phys. Rev. B*, vol. 74, p. 035423, Jul 2006. [Online]. Available: http://link.aps.org/doi/10.1103/PhysRevB.74.035423

[30] J. Filik, J. N. Harvey, N. L. Allan, P. W. May, J. E. Dahl, S. Liu, and R. M. Carlson, "Raman spectroscopy of diamondoids," *Spectrochim. Acta A Mol. Biomol. Spectrosc.*, vol. 64, no. 3, pp. 681–692, 2006.

[31] H. Kawarada, "Hydrogen-terminated diamond surfaces and interfaces," *Surface Science Reports*, vol. 26, no. 7, pp. 205 – 259, 1996. [Online]. Available: http://www.sciencedirect.com/science/article/pii/S0167572997800027

[32] L. Landt, K. Klünder, J. E. Dahl, R. M. K. Carlson, T. Möller, and C. Bostedt, "Optical response of diamond nanocrystals as a function of particle size, shape, and symmetry," *Phys. Rev. Lett.*, vol. 103, p. 047402, Jul 2009. [Online]. Available: http://link.aps.org/doi/10.1103/PhysRevLett.103.047402

[33] E. Hückel, "Quantentheoretische Beiträge zum Benzolproblem," *Zeitschrift fur Physik*, vol. 70, pp. 204–286, Mar. 1931.

[34] E. Hückel, "Quanstentheoretische Beiträge zum Benzolproblem," *Zeitschrift für Physik*, vol. 72, no. 5, pp. 310–337, May 1931. [Online]. Available: https://doi.org/10.1007/BF01341953

[35] ——, "Quantentheoretische Beiträge zum Problem der aromatischen und ungesättigten Verbindungen. III," *Zeitschrift für Physik*, vol. 76, no. 9, pp. 628–648, Sep 1932. [Online]. Available: https://doi.org/10.1007/BF01341936

[36] D. A. Bahnick, "Use of huckel molecular orbital theory in interpreting the visible spectra of polymethine dyes: An undergraduate physical chemistry experiment," *Journal of Chemical Education*, vol. 71, no. 2, p. 171, 1994. [Online]. Available: https://doi.org/10.1021/ed071p171

[37] G. F. Koster and J. C. Slater, "Wave functions for impurity levels," *Phys. Rev.*, vol. 95, pp. 1167–1176, Sep 1954. [Online]. Available: https://link.aps.org/doi/10.1103/PhysRev.95.1167

[38] S. Reich, J. Maultzsch, C. Thomsen, and P. Ordejón, "Tight-binding description of graphene," *Phys. Rev. B*, vol. 66, p. 035412, Jul 2002. [Online]. Available: http://link.aps.org/doi/10.1103/PhysRevB.66.035412

[39] P. Trucano and R. Chen, "Structure of graphite by neutron diffraction," *Nature*, vol. 258, no. 984, p. 136, 1975. [Online]. Available: http://dx.doi.org/10.1038/258136a0

[40] A. H. Castro Neto, F. Guinea, N. M. R. Peres, K. S. Novoselov, and A. K. Geim, "The electronic properties of graphene," *Rev. Mod. Phys.*, vol. 81, pp. 109–162, Jan 2009. [Online]. Available: https://link.aps.org/doi/10.1103/RevModPhys.81.109

[41] P. R. Wallace, "The band theory of graphite," *Phys. Rev.*, vol. 71, pp. 622–634, May 1947. [Online]. Available: https://link.aps.org/doi/10.1103/PhysRev.71.622

[42] R. S. Deacon, K.-C. Chuang, R. J. Nicholas, K. S. Novoselov, and A. K. Geim, "Cyclotron resonance study of the electron and hole velocity in graphene monolayers," *Phys. Rev. B*, vol. 76, p. 081406, Aug 2007. [Online]. Available: https://link.aps.org/doi/10.1103/PhysRevB.76.081406

[43] A. K. Novoselov, A. K. Geim, S. V. Morozov, D. Jiang, M. I. Katsnelson, I. V. Grigorieva, S. V. Dubonos, and A. A. Firsov, "Two-dimensional gas of massless Dirac fermions in graphene," *Nature*, vol. 438, no. 197, 2005.

[44] S. Ono and K. Sugihara, "Trigonal warping of the bands and hall effect in graphite," *Journal of the Physical Society of Japan*, vol. 24, no. 4, pp. 818–825, 1968. [Online]. Available: https://doi.org/10.1143/JPSJ.24.818

[45] S. Reich, C. Thomsen, and J. Maultzsch, *Carbon Nanotubes: Basic Concepts and Physical Properties*. Wiley-VCH, 2003.

[46] M. J. Bronikowski, P. A. Willis, D. T. Colbert, K. A. Smith, and R. E. Smalley, "Gas-phase production of carbon single-walled nanotubes from carbon monoxide via the HiPco process: A parametric study," *Journal of Vacuum Science & Technology A: Vacuum, Surfaces, and Films*, vol. 19, no. 4, pp. 1800–1805, 2001. [Online]. Available: https://doi.org/10.1116/1.1380721

[47] S. Iijima and T. Ichihashi, "Single-shell carbon nanotubes of 1-nm diameter," *Nature*, vol. 363, no. 603, 1993.

[48] S. M. Bachilo, L. Balzano, J. E. Herrera, F. Pompeo, D. E. Resasco, and R. B. Weisman, "Narrow (n,m)-distribution of single-walled carbon nanotubes grown using a solid supported catalyst," *Journal of the American Chemical Society*, vol. 125, no. 37, pp. 11 186–11 187, 2003. [Online]. Available: https://doi.org/10.1021/ja036622c

[49] M. S. Arnold, A. A. Green, J. F. Hulvat, S. I. Stupp, and H. M. C., "Sorting carbon nanotubes by electronic structure using density differentiation," *Nature*, vol. 1, no. 60, 2006.

[50] X. Tu, S. Manohar, A. Jagota, and M. Zheng, "DNA sequence motifs for structure-specific recognition and separation of carbon nanotubes," *Nature*, vol. 460, no. 250, 2009.

[51] Sanchez-Valencia, Juan Ramon and Dienel, Thomas and Gröning, Oliver and Shorubalko, Ivan and Mueller, Andreas and Jansen, Martin and Amsharov, Konstantin and Ruffieux, Pascal and Fasel, Roman, "Controlled synthesis of single-chirality carbon nanotubes," *Nature*, vol. 512, no. 61, 2014.

[52] C. Tyborski, F. Herziger, R. Gillen, and J. Maultzsch, "Beyond double-resonant Raman scattering: Ultraviolet Raman spectroscopy on graphene, graphite, and carbon nanotubes," *Phys. Rev. B*, vol. 92, p. 041401, Jul 2015. [Online]. Available: http://link.aps.org/doi/10.1103/PhysRevB.92.041401

[53] A. Jorio, M. Dresselhaus, R. Saito, and G. F. Dresselhaus, *Raman Spectroscopy in Graphene Related Systems*. Wiley-VCH, 2011.

[54] X. Wang, Q. Li, J. Xie, Z. Jin, J. Wang, Y. Li, K. Jiang, and S. Fan, "Fabrication of ultralong and electrically uniform single-walled carbon nanotubes on clean substrates," *Nano Letters*, vol. 9, no. 9, pp. 3137–3141, 2009. [Online]. Available: https://doi.org/10.1021/nl901260b

[55] R. Zhang, Y. Zhang, Q. Zhang, H. Xie, W. Qian, and F. Wei, "Growth of half-meter long carbon nanotubes based on Schulz-Flory distribution," *ACS Nano*, vol. 7, no. 7, pp. 6156–6161, 2013. [Online]. Available: https://doi.org/10.1021/nn401995z

[56] J. K. Streit, S. M. Bachilo, A. V. Naumov, C. Khripin, M. Zheng, and R. B. Weisman, "Measuring single-walled carbon nanotube length distributions from diffusional trajectories," *ACS Nano*, vol. 6, no. 9, pp. 8424–8431, 2012. [Online]. Available: https://doi.org/10.1021/nn3032744

[57] D. Hecht, L. Hu, and G. Grüner, "Conductivity scaling with bundle length and diameter in single walled carbon nanotube networks," *Applied Physics Letters*, vol. 89, no. 13, p. 133112, 2006. [Online]. Available: https://doi.org/10.1063/1.2356999

[58] R. Saito, M. Fujita, G. Dresselhaus, and M. S. Dresselhaus, "Electronic structure of chiral graphene tubules," *Applied Physics Letters*, vol. 60, no. 18, pp. 2204–2206, 1992. [Online]. Available: https://doi.org/10.1063/1.107080

[59] H. Kataura, Y. Kumazawa, Y. Maniwa, I. Umezu, S. Suzuki, Y. Ohtsuka, and Y. Achiba, "Optical properties of single-wall carbon nanotubes," *Synthetic Metals*, vol. 103, no. 1, pp. 2555 – 2558, 1999, international Conference on Science and Technology of Synthetic Metals. [Online]. Available: http://www.sciencedirect.com/science/article/pii/S0379677998002781

[60] B. Satishkumar, A. Govindaraj, R. Sen, and C. Rao, "Single-walled nanotubes by the pyrolysis of acetylene-organometallic mixtures," *Chemical Physics Letters*, vol. 293, no. 1, pp. 47 – 52, 1998. [Online]. Available: http://www.sciencedirect.com/science/article/pii/S0009261498007271

[61] E. Malić, M. Hirtschulz, F. Milde, A. Knorr, and S. Reich, "Analytical approach to optical absorption in carbon nanotubes," *Phys. Rev. B*, vol. 74, p. 195431, Nov 2006. [Online]. Available: https://link.aps.org/doi/10.1103/PhysRevB.74.195431

[62] E. Malic and A. Knorr, *Graphene and Carbon Nanotubes Ultrafast Optics and Relaxation Dynamics*. Wiley-VCH, 2013.

[63] A. T. Balaban and P. V. R. Schleyer, "Systematic classification and nomenclature of diamond hydrocarbons: Graph-theoretical enumeration of polymantanes," *Tetrahedron*, vol. 34, no. 24, pp. 3599 – 3609, 1978. [Online]. Available: http://www.sciencedirect.com/science/article/pii/0040402078884373

[64] P. Vlado and S. Rativoj, "Über die Synthese des Adamantans," *Berichte der deutschen chemischen Gesellschaft (A and B Series)*, vol. 74, no. 10, pp. 1644–1648, 1941. [Online]. Available: https://onlinelibrary.wiley.com/doi/abs/10.1002/cber.19410741004

[65] S. Banerjee and P. Saalfrank, "Vibrationally resolved absorption, emission and resonance Raman spectra of diamondoids: a study based on time-dependent correlation functions," *Phys. Chem. Chem. Phys.*, vol. 16, pp. 144–158, 2014. [Online]. Available: http://dx.doi.org/10.1039/C3CP53535E

[66] C. J. Wort and R. S. Balmer, "Diamond as an electronic material," *Materials Today*, vol. 11, no. 1, pp. 22 – 28, 2008. [Online]. Available: http://www.sciencedirect.com/science/article/pii/S1369702107703498

[67] T. Sasagawa and Z. xun Shen, "A route to tunable direct band-gap diamond devices: Electronic structures of nanodiamond crystals," *Journal of Applied Physics*, vol. 104, no. 7, p. 073704, 2008. [Online]. Available: http://aip.scitation.org/doi/abs/10.1063/1.2986637

[68] M. Vörös, T. Demjén, T. Szilvási, and A. Gali, "Tuning the optical gap of nanometer-size diamond cages by sulfurization: A time-dependent density functional study," *Phys. Rev. Lett.*, vol. 108, p. 267401, Jun 2012. [Online]. Available: http://link.aps.org/doi/10.1103/PhysRevLett.108.267401

[69] T. Rander, M. Staiger, R. Richter, T. Zimmermann, L. Landt, D. Wolter, J. E. Dahl, R. M. K. Carlson, B. A. Tkachenko, N. A. Fokina, P. R. Schreiner, T. Möller, and C. Bostedt, "Electronic structure tuning of diamondoids through functionalization," *J. Chem. Phys.*, vol. 138, no. 2, 2013. [Online]. Available: http://scitation.aip.org/content/aip/journal/jcp/138/2/10.1063/1.4774268

[70] L. Landt, C. Bostedt, D. Wolter, T. Möller, J. E. P. Dahl, R. M. K. Carlson, B. A. Tkachenko, A. A. Fokin, P. R. Schreiner, A. Kulesza, R. Mitrić, and V. Bonačić-Koutecký, "Experimental and theoretical study of the absorption properties of thiolated diamondoids," *J. Chem. Phys.*, vol. 132, no. 14, p. 144305, 2010. [Online]. Available: http://dx.doi.org/10.1063/1.3356034

[71] S. Banerjee, T. Stuker, and P. Saalfrank, "Vibrationally resolved optical spectra of modified diamondoids obtained from time-dependent correlation function methods," *Phys. Chem. Chem. Phys.*, vol. 17, pp. 19 656–19 669, 2015. [Online]. Available: http://dx.doi.org/10.1039/C5CP02615F

[72] R. Meinke, R. Richter, A. Merli, A. A. Fokin, T. V. Koso, V. N. Rodionov, P. R. Schreiner, C. Thomsen, and J. Maultzsch, "UV resonance Raman analysis of trishomocubane and diamondoid dimers," *J. Chem. Phys.*, vol. 140, no. 3, 2014. [Online]. Available: http://scitation.aip.org/content/aip/journal/jcp/140/3/10.1063/1.4861758

[73] C. Tyborski, R. Gillen, A. A. Fokin, T. V. Koso, N. A. Fokina, H. Hausmann, V. N. Rodionov, P. R. Schreiner, C. Thomsen, and J. Maultzsch, "Electronic and vibrational properties of diamondoid oligomers," *The Journal of Physical Chemistry C*, vol. 121, no. 48, pp. 27 082–27 088, 2017. [Online]. Available: https://doi.org/10.1021/acs.jpcc.7b07666

[74] J. O. Jensen, "Vibrational frequencies and structural determination of adamantane," *Spectrochim. Acta A Mol. Biomol. Spectrosc.*, vol. 60, pp. 1895–1905, Aug 2004.

[75] T. Jenkins and J. Lewis, "A Raman study of adamantane (C10H16), diamantane (C14H20) and triamantane (C18H24) between 10 K and room temperatures," *Spectrochimica Acta Part A: Molecular Spectroscopy*, vol. 36, no. 3, pp. 259 – 264, 1980. [Online]. Available: http://www.sciencedirect.com/science/article/pii/0584853980801280

[76] R. Meinke, R. Richter, T. Möller, B. A. Tkachenko, P. R. Schreiner, C. Thomsen, and J. Maultzsch, "Experimental and theoretical Raman analysis of functionalized diamantane," *J. Phys. B At. Mol. Opt. Phys.*, vol. 46, no. 2, p. 025101, 2013. [Online]. Available: http://stacks.iop.org/0953-4075/46/i=2/a=025101

[77] C. V. Raman and K. S. Krishnan, "A new type of secondary radiation," *Nature*, vol. 121, no. 501, 1928.

[78] A. Smekal, "Zur Quantentheorie der Dispersion," *Naturwissenschaften*, vol. 11, no. 43, pp. 873–875, Oct 1923. [Online]. Available: https://doi.org/10.1007/BF01576902

[79] P. M. Morse, "Diatomic molecules according to the wave mechanics. II. Vibrational levels," *Phys. Rev.*, vol. 34, pp. 57–64, Jul 1929. [Online]. Available: https://link.aps.org/doi/10.1103/PhysRev.34.57

[80] T. Hertel and G. Moos, "Electron-phonon interaction in single-wall carbon nanotubes: A time-domain study," *Phys. Rev. Lett.*, vol. 84, pp. 5002–5005, May 2000. [Online]. Available: https://link.aps.org/doi/10.1103/PhysRevLett.84.5002

[81] C. Tyborski, R. Meinke, R. Gillen, T. Bischoff, A. Knecht, R. Richter, A. Merli, A. A. Fokin, T. V. Koso, V. N. Rodionov, P. R. Schreiner, T. Möller, T. Rander, C. Thomsen, and J. Maultzsch, "From isolated diamondoids to a van-der-waals crystal: A theoretical and experimental analysis of a trishomocubane and a diamantane dimer in the gas and solid phase," *The Journal of Chemical Physics*, vol. 147, no. 4, p. 044303, 2017. [Online]. Available: http://aip.scitation.org/doi/abs/10.1063/1.4994898

[82] F. Tuinstra and J. L. Koenig, "Raman spectrum of graphite," *The Journal of Chemical Physics*, vol. 53, no. 3, pp. 1126–1130, 1970. [Online]. Available: https://doi.org/10.1063/1.1674108

[83] M. J. Matthews, M. A. Pimenta, G. Dresselhaus, M. S. Dresselhaus, and M. Endo, "Origin of dispersive effects of the Raman D band in carbon materials," *Phys. Rev. B*, vol. 59, pp. R6585–R6588, Mar 1999. [Online]. Available: https://link.aps.org/doi/10.1103/PhysRevB.59.R6585

[84] R. Narula, N. Bonini, N. Marzari, and S. Reich, "Dominant phonon wave vectors and strain-induced splitting of the 2D Raman mode of graphene," *Phys. Rev. B*, vol. 85, p. 115451, Mar 2012. [Online]. Available: https://link.aps.org/doi/10.1103/PhysRevB.85.115451

[85] A. C. Ferrari and J. Robertson, "Interpretation of Raman spectra of disordered and amorphous carbon," *Phys. Rev. B*, vol. 61, pp. 14 095–14 107, May 2000. [Online]. Available: https://link.aps.org/doi/10.1103/PhysRevB.61.14095

[86] D. Meschede, *Optik, Licht und Laser*. Vieweg+Teubner, 2008.

[87] P. A. Franken, A. E. Hill, C. W. Peters, and G. Weinreich, "Generation of optical harmonics," *Phys. Rev. Lett.*, vol. 7, pp. 118–119, Aug 1961. [Online]. Available: https://link.aps.org/doi/10.1103/PhysRevLett.7.118

[88] A. D. Buckingham and J. A. Pople, "A theory of magnetic double refraction," *Proceedings of the Physical Society. Section B*, vol. 69, no. 11, p. 1133, 1956. [Online]. Available: http://stacks.iop.org/0370-1301/69/i=11/a=311

[89] D. Eimerl, L. Davis, S. Velsko, E. K. Graham, and A. Zalkin, "Optical, mechanical, and thermal properties of barium borate," *Journal of Applied Physics*, vol. 62, no. 5, pp. 1968–1983, 1987. [Online]. Available: https://doi.org/10.1063/1.339536

[90] G. J. Kent, S. A. Godleski, E. Osawa, and P. v. R. Schleyer, "Syntheses and relative stability of (D3)-trishomocubane (pentacyclo[6.3.0.02,6.03,10.05,9]undecane), the pentacycloundecane stabilomer," *The Journal of Organic Chemistry*, vol. 42, no. 24, pp. 3852–3859, 1977. [Online]. Available: http://dx.doi.org/10.1021/jo00444a012

[91] T. Koso, "Unsaturated nanodiamonds: Synthesis and functionalization of coupled diamondoids as a direct route to nanometer-sized building blocks," doctoral thesis, Justus-Liebig University, Giessen, 2013, http://geb.uni-giessen.de/geb/volltexte/2013/9874/.

[92] R. Meinke, "Resonante Raman-Spektroskopie an modifizierten diamantoiden und $sp^2 - sp^3$ - Kohlenstoff-Nanostrukturen - vibronische, elektronische und geometrische Eigenschaften," doctoral thesis, Technische Universität, Berlin, 2015, http://dx.doi.org/10.14279/depositonce-4609.

[93] V. N. Popov and P. Lambin, "Radius and chirality dependence of the radial breathing mode and the G-band phonon modes of single-walled carbon nanotubes," *Phys. Rev. B*, vol. 73, p. 085407, Feb 2006. [Online]. Available: https://link.aps.org/doi/10.1103/PhysRevB.73.085407

[94] V. Schettino, M. Pagliai, L. Ciabini, and G. Cardini, "The vibrational spectrum of fullerene C60," *The Journal of Physical Chemistry A*, vol. 105, no. 50, pp. 11 192–11 196, 2001. [Online]. Available: http://dx.doi.org/10.1021/jp012874t

[95] I. C. Walker, A. Stamatovic, and S. F. Wong, "Vibrational excitation of ethylene by electron impact: 1-11 eV," *The Journal of Chemical Physics*, vol. 69, no. 12, pp. 5532–5537, 1978. [Online]. Available: https://doi.org/10.1063/1.436547

[96] R. Gillen, department für Physik, Friedrich-Alexander Universität Erlangen-Nürnberg, Department für Physik, AG Maultzsch, Staudtstraße 7, 91058 Erlangen, Germany.

[97] M. Tsuboi and A. Y. Hirakawa, "A correlation between vibronic coupling, adiabatic potential, and Raman scattering: A theoretical background of a proposed rule," *J. Raman Spectrosc.*, vol. 5, no. 1, pp. 75–86, 1976. [Online]. Available: http://dx.doi.org/10.1002/jrs.1250050109

[98] T. Zimmermann, R. Richter, A. Knecht, A. A. Fokin, T. V. Koso, L. V. Chernish, P. A. Gunchenko, P. R. Schreiner, T. Möller, and T. Rander, "Exploring covalently bonded diamondoid particles with valence photoelectron spectroscopy," *J. Chem. Phys.*, vol. 139, no. 8, 2013. [Online]. Available: http://scitation.aip.org/content/aip/journal/jcp/139/8/10.1063/1.4818994

[99] J. P. Perdew, K. Burke, and M. Ernzerhof, "Generalized gradient approximation made simple," *Phys. Rev. Lett.*, vol. 77, pp. 3865–3868, Oct 1996.

[100] G. Herzberg, "Electronic spectra and electronic structure of polyatomic molecules," Ph.D. dissertation, Van Nostrand, 1966.

[101] A. M. Mebel, Y.-T. Chen, and S.-H. Lin, "$\pi - \pi^*$ vibronic spectrum of ethylene from ab initio calculations of the Franck-Condon factors," *Chem. Phys. Let.*, vol. 258, no. 1-2, pp. 53–62, 1996. [Online]. Available: http://www.sciencedirect.com/science/article/pii/0009261496006276

[102] R. J. Buenker, V. Bonačić-Koutecký, and L. Pogliani, "Potential energy and dipole moment surfaces for simultaneous torsion and pyramidalization of ethylene in its lowest-lying singlet excited states: A CI study of the sudden polarization effect," *J. Chem. Phys.*, vol. 73, no. 4, pp. 1836–1849, 1980. [Online]. Available: http://scitation.aip.org/content/aip/journal/jcp/73/4/10.1063/1.440319

[103] R. J. Sension and B. S. Hudson, "Vacuum ultraviolet resonance Raman studies of the excited electronic states of ethylene," *J. Chem. Phys.*, vol. 90, no. 3, pp. 1377–1389, 1989. [Online]. Available: http://scitation.aip.org/content/aip/journal/jcp/90/3/10.1063/1.456080

[104] A. Y. Hirakawa and M. Tsuboi, "Molecular geometry in an excited electronic state and a preresonance Raman effect," *Science*, vol. 188, no. 4186, pp. 359–361, 1975. [Online]. Available: http://science.sciencemag.org/content/188/4186/359

[105] R. S. Mulliken, "The excited states of ethylene," *The Journal of Chemical Physics*, vol. 66, no. 6, pp. 2448–2451, 1977. [Online]. Available: http://dx.doi.org/10.1063/1.434239

[106] A. A. Fokin, L. V. Chernish, P. A. Gunchenko, E. Y. Tikhonchuk, H. Hausmann, M. Serafin, J. E. P. Dahl, R. M. K. Carlson, and P. R. Schreiner, "Stable alkanes containing very long carbon-carbon bonds," *Journal of the American Chemical Society*, vol. 134, no. 33, pp. 13 641–13 650, 2012. [Online]. Available: https://doi.org/10.1021/ja302258q

[107] F. H. Allen, O. Kennard, D. G. Watson, L. Brammer, A. G. Orpen, and R. Taylor, "Tables of bond lengths determined by X-ray and neutron diffraction. Part 1. Bond lengths in organic compounds," *J. Chem. Soc., Perkin Trans. 2*, pp. S1–S19, 1987. [Online]. Available: http://dx.doi.org/10.1039/P298700000S1

[108] K. Martin, M. Bernhard, and S. Hermann, "Breakdown of bond length-bond strength correlation: A case study," *Angewandte Chemie International Edition*, vol. 39, no. 24, pp. 4607–4609, 2000. [Online]. Available: https://onlinelibrary.wiley.com/doi/abs/10.1002/1521-3773%2820001215%2939%3A24%3C4607%3A%3AAID-ANIE4607%3E3.0.CO%3B2-L

[109] A. A. Zavitsas, "The relation between bond lengths and dissociation energies of carbon-carbon bonds," *The Journal of Physical Chemistry A*, vol. 107, no. 6, pp. 897–898, 2003. [Online]. Available: https://doi.org/10.1021/jp0269367

[110] B. Kahr, D. Van Engen, and K. Mislow, "Length of the ethane bond in hexaphenylethane and its derivatives," *Journal of the American Chemical Society*, vol. 108, no. 26, pp. 8305–8307, 1986. [Online]. Available: https://doi.org/10.1021/ja00286a053

[111] H. F. Bettinger, P. v. R. Schleyer, H. F. Bettinger, and H. F. Schaefer III, "Tetraphenyldihydrocyclobutaarenes-what causes the extremely long 1.72 Å C-C single bond?" *Chem. Commun.*, pp. 769–770, 1998. [Online]. Available: http://dx.doi.org/10.1039/A800741A

[112] E. I. Bagrii, R. E. Safir, and Y. A. Arinicheva, "Methods of the functionalization of hydrocarbons with a diamond-like structure," *Petroleum Chemistry*, vol. 50, no. 1, pp. 1–16, Jan 2010. [Online]. Available: https://doi.org/10.1134/S0965544110010019

[113] B. Delley, "From molecules to solids with the DMol3 approach," *The Journal of Chemical Physics*, vol. 113, no. 18, pp. 7756–7764, 2000. [Online]. Available: https://doi.org/10.1063/1.1316015

[114] J. P. Perdew and Y. Wang, "Accurate and simple analytic representation of the electron-gas correlation energy," *Phys. Rev. B*, vol. 45, pp. 13 244–13 249, Jun 1992. [Online]. Available: https://link.aps.org/doi/10.1103/PhysRevB.45.13244

[115] K.-T. Tang and J. P. Toennies, "Johannes diderik van der Waals: A pioneer in the molecular sciences and Nobel prize winner in 1910," *Angewandte Chemie International Edition*, vol. 49, no. 50, pp. 9574–9579, 2010. [Online]. Available: http://dx.doi.org/10.1002/anie.201002332

[116] H. Hamaker, "The London-van der Waals attraction between spherical particles," *Physica*, vol. 4, no. 10, pp. 1058 – 1072, 1937. [Online]. Available: http://www.sciencedirect.com/science/article/pii/S0031891437802037

[117] G. Reichardt, J. Bahrdt, J.-S. Schmidt, W. Gudat, A. Ehresmann, R. Müller-Albrecht, H. Molter, H. Schmoranzer, M. Martins, N. Schwentner, and S. Sasaki, "A 10 m-normal incidence monochromator at the quasi-periodic undulator U125-2 at BESSY II," *Nucl. Instrum. Methods Phys. Res., Sect. A*, vol. 467-468, no. 0, pp. 462–465, 2001.

[118] Helmholtz-Zentrum Berlin für Materialien und Energie. The U125-2 NIM beamline at BESSY II, "The U125-2 NIM beamline at BESSY II," *Journal of large-scale research facilities*, vol. 2, p. A53, 2016. [Online]. Available: http://dx.doi.org/10.17815/jlsrf-2-76

[119] T. E. Jenkins and A. R. Bates, "A Raman study of the three-solid-state phase transition in diamantane," *J. Phys. C*, vol. 12, no. 6, p. 1003, 1979. [Online]. Available: http://stacks.iop.org/0022-3719/12/i=6/a=013

[120] C. G. Windsor, D. H. Saunderson, J. N. Sherwood, D. Taylor, and G. S. Pawley, "Lattice dynamics of adamantane in the disordered phase," *Journal of Physics C: Solid State Physics*, vol. 11, no. 9, p. 1741, 1978. [Online]. Available: http://stacks.iop.org/0022-3719/11/i=9/a=013

[121] I. L. Karle and J. Karle, "The crystal and molecular structure of congressane, C14H20, by X-ray diffraction," *Journal of the American Chemical Society*, vol. 87, no. 4, pp. 918–920, 1965. [Online]. Available: https://doi.org/10.1021/ja01082a043

[122] R. Cernik, E. Evans, R. Hine, and J. Richards, "Phase transitions in triamantane," *Solid State Communications*, vol. 27, no. 10, pp. 1017 – 1019, 1978. [Online]. Available: http://www.sciencedirect.com/science/article/pii/0038109878910281

[123] F. Emmerling, federal Institute for Materials Research and Testint (BAM), Richard-Willstätter-Straße 11, 12489 Berlin, Germany.

[124] P. Kahl, J. P. Wagner, C. Balestrieri, J. Becker, H. Hausmann, G. J. Bodwell, and P. R. Schreiner, "[2](1,3)Adamantano[2](2,7)pyrenophane: A hydrocarbon with a large dipole moment," *Angew. Chem. Int. Ed.*, vol. 55, no. 32, pp. 9277–9281, 2016. [Online]. Available: http://dx.doi.org/10.1002/anie.201602201

[125] J. C. Randel, F. C. Niestemski, A. R. Botello-Mendez, W. Mar, G. Ndabashimiye, S. Melinte, J. E. P. Dahl, R. M. K. Carlson, E. D. Butova, A. A. Fokin, P. R. Schreiner, J.-C. Charlier, and H. C. Manoharan, "Unconventional molecule-resolved current rectification in diamondoid-fullerene hybrids," *Nat. Comm.*, vol. 5, 2014. [Online]. Available: http://dx.doi.org/10.1038/ncomms5877

[126] L. Ralf, N. Martin, and V. Fritz, "Darstellung, Struktur und konformatives Verhalten gespannter Adamantanophane," *Chemische Berichte*, vol. 127, no. 6, pp. 1147–1156, 1994. [Online]. Available: https://onlinelibrary.wiley.com/doi/abs/10.1002/cber.19941270628

[127] M. Kim, J. N. Hohman, E. I. Morin, T. A. Daniel, and P. S. Weiss, "Self-assembled monolayers of 2-adamantanethiol on Au111: Control of structure and displacement," *The Journal of Physical Chemistry A*, vol. 113, no. 16, pp. 3895–3903, 2009. [Online]. Available: https://doi.org/10.1021/jp810048n

[128] W. L. Yang, J. D. Fabbri, T. M. Willey, J. R. I. Lee, J. E. Dahl, R. M. K. Carlson, P. R. Schreiner, A. A. Fokin, B. A. Tkachenko, N. A. Fokina, W. Meevasana, N. Mannella, K. Tanaka, X. J. Zhou, T. van Buuren, M. A. Kelly, Z. Hussain, N. A.

Melosh, and Z.-X. Shen, "Monochromatic electron photoemission from diamondoid monolayers," *Science*, vol. 316, no. 5830, pp. 1460–1462, 2007. [Online]. Available: http://science.sciencemag.org/content/316/5830/1460

[129] T. Xiong, "Vibrationally resolved absorption, emission, resonance Raman and photoelectron spectra of selected organic molecules, associated radicals and cations: A time-dependent approach," doctoral thesis, University of Potsdam, Potsdam, 2018.

[130] C. M. Jones and S. A. Asher, "Ultraviolet resonance Raman study of the pyrene S4, S3, and S2 excited electronic states," *The Journal of Chemical Physics*, vol. 89, no. 5, pp. 2649–2661, 1988. [Online]. Available: https://doi.org/10.1063/1.455015

[131] T. Xiong, institut für Chemie, Universität Potsdam, AK Peter Saalfrank, Karl-Liebknecht-Straße, 14476 Potsdam-Golm, Germany.

[132] M. Kasha, "Characterization of electronic transitions in complex molecules," *Discuss. Faraday Soc.*, vol. 9, pp. 14–19, 1950. [Online]. Available: http://dx.doi.org/10.1039/DF9500900014

[133] J. Ferguson, "Absorption and fluorescence spectra of crystalline pyrene," *The Journal of Chemical Physics*, vol. 28, no. 5, pp. 765–768, 1958. [Online]. Available: https://doi.org/10.1063/1.1744267

[134] C. Thomsen and S. Reich, "Raman scattering in carbon nanotubes," in *Light Scattering in Solids IX*, ser. 108. Springer-Verlag, 2007, ch. 3, pp. 115–232.

[135] M. Dresselhaus, G. Dresselhaus, R. Saito, and A. Jorio, "Raman spectroscopy of carbon nanotubes," *Physics Reports*, vol. 409, no. 2, pp. 47 – 99, 2005. [Online]. Available: http://www.sciencedirect.com/science/article/pii/S0370157304004570

[136] K. F. Mak, M. Y. Sfeir, Y. Wu, C. H. Lui, J. A. Misewich, and T. F. Heinz, "Measurement of the optical conductivity of graphene," *Phys. Rev. Lett.*, vol. 101, p. 196405, Nov 2008. [Online]. Available: https://link.aps.org/doi/10.1103/PhysRevLett.101.196405

[137] T. Stauber, N. M. R. Peres, and A. K. Geim, "Optical conductivity of graphene in the visible region of the spectrum," *Phys. Rev. B*, vol. 78, p. 085432, Aug 2008. [Online]. Available: https://link.aps.org/doi/10.1103/PhysRevB.78.085432

[138] K. F. Mak, L. Ju, F. Wang, and T. F. Heinz, "Optical spectroscopy of graphene: From the far infrared to the ultraviolet," *Solid State Communications*, vol. 152, no. 15, pp. 1341 – 1349, 2012, exploring Graphene, Recent Research Advances. [Online]. Available: http://www.sciencedirect.com/science/article/pii/S0038109812002700

[139] K. F. Mak, J. Shan, and T. F. Heinz, "Seeing many-body effects in single- and few-layer graphene: Observation of two-dimensional saddle-point excitons," *Phys. Rev. Lett.*, vol. 106, p. 046401, Jan 2011. [Online]. Available: https://link.aps.org/doi/10.1103/PhysRevLett.106.046401

[140] S. Piscanec, M. Lazzeri, F. Mauri, A. C. Ferrari, and J. Robertson, "Kohn anomalies and electron-phonon interactions in graphite," *Phys. Rev. Lett.*, vol. 93, p. 185503, Oct 2004. [Online]. Available: https://link.aps.org/doi/10.1103/PhysRevLett.93.185503

[141] M. Lazzeri and F. Mauri, "Nonadiabatic Kohn anomaly in a doped graphene monolayer," *Phys. Rev. Lett.*, vol. 97, p. 266407, Dec 2006. [Online]. Available: https://link.aps.org/doi/10.1103/PhysRevLett.97.266407

[142] E. H. Hwang and S. Das Sarma, "Screening, Kohn anomaly, Friedel oscillation, and RKKY interaction in bilayer graphene," *Phys. Rev. Lett.*, vol. 101, p. 156802, Oct 2008. [Online]. Available: https://link.aps.org/doi/10.1103/PhysRevLett.101.156802

[143] W. Kohn, "Image of the Fermi surface in the vibration spectrum of a metal," *Phys. Rev. Lett.*, vol. 2, pp. 393–394, May 1959. [Online]. Available: https://link.aps.org/doi/10.1103/PhysRevLett.2.393

[144] F. Herziger, M. Calandra, P. Gava, P. May, M. Lazzeri, F. Mauri, and J. Maultzsch, "Two-dimensional analysis of the double-resonant 2D Raman mode in bilayer graphene," *Phys. Rev. Lett.*, vol. 113, p. 187401, Oct 2014. [Online]. Available: https://link.aps.org/doi/10.1103/PhysRevLett.113.187401

[145] J. Maultzsch, S. Reich, and C. Thomsen, "Double-resonant Raman scattering in graphite: Interference effects, selection rules, and phonon dispersion," *Phys. Rev. B*, vol. 70, p. 155403, Oct 2004. [Online]. Available: https://link.aps.org/doi/10.1103/PhysRevB.70.155403

[146] A. C. Ferrari, "Raman spectroscopy of graphene and graphite: Disorder, electron-phonon coupling, doping and nonadiabatic effects," *Solid State Communications*, vol. 143, no. 1, pp. 47 – 57, 2007, exploring graphene. [Online]. Available: http://www.sciencedirect.com/science/article/pii/S0038109807002967

[147] M. A. Pimenta, G. Dresselhaus, M. S. Dresselhaus, L. G. Cancado, A. Jorio, and R. Saito, "Studying disorder in graphite-based systems by Raman spectroscopy," *Phys. Chem. Chem. Phys.*, vol. 9, pp. 1276–1290, 2007. [Online]. Available: http://dx.doi.org/10.1039/B613962K

[148] X. Wan, A. M. Turner, A. Vishwanath, and S. Y. Savrasov, "Topological semimetal and Fermi-arc surface states in the electronic structure of pyrochlore iridates," *Phys. Rev. B*, vol. 83, p. 205101, May 2011. [Online]. Available: https://link.aps.org/doi/10.1103/PhysRevB.83.205101

[149] P. May, M. Lazzeri, P. Venezuela, F. Herziger, G. Callsen, J. S. Reparaz, A. Hoffmann, F. Mauri, and J. Maultzsch, "Signature of the two-dimensional phonon dispersion in graphene probed by double-resonant Raman scattering," *Phys. Rev. B*, vol. 87, p. 075402, Feb 2013. [Online]. Available: http://link.aps.org/doi/10.1103/PhysRevB.87.075402

[150] O. Frank, M. Mohr, J. Maultzsch, C. Thomsen, I. Riaz, R. Jalil, K. S. Novoselov, G. Tsoukleri, J. Parthenios, K. Papagelis, L. Kavan, and C. Galiotis, "Raman 2D-band splitting in graphene: Theory and experiment," *ACS Nano*, vol. 5, no. 3, pp. 2231–2239, 2011. [Online]. Available: https://doi.org/10.1021/nn103493g

[151] H. Lipson and A. R. Stokes, "The structure of graphite," *Proceedings of the Royal Society of London A: Mathematical, Physical and Engineering Sciences*, vol. 181, no. 984, pp. 101–105, 1942. [Online]. Available: http://rspa.royalsocietypublishing.org/content/181/984/101

[152] J. Maultzsch, S. Reich, C. Thomsen, H. Requardt, and P. Ordejón, "Phonon dispersion in graphite," *Phys. Rev. Lett.*, vol. 92, p. 075501, Feb 2004. [Online]. Available: https://link.aps.org/doi/10.1103/PhysRevLett.92.075501

[153] N. Scheuschner, R. Gillen, M. Staiger, and J. Maultzsch, "Interlayer resonant Raman modes in few-layer MoS_2," *Phys. Rev. B*, vol. 91, p. 235409, Jun 2015. [Online]. Available: https://link.aps.org/doi/10.1103/PhysRevB.91.235409

[154] S. Reich and C. Thomsen, "Raman spectroscopy of graphite," *Philosophical Transactions of the Royal Society of London A: Mathematical, Physical and Engineering Sciences*, vol. 362, no. 1824, pp. 2271–2288, 2004. [Online]. Available: http://rsta.royalsocietypublishing.org/content/362/1824/2271

[155] P. H. Tan, W. P. Han, W. J. Zhao, Z. H. Wu, K. Chang, H. Wang, Y. F. Wang, N. Bonini, N. Marzari, N. Pugno, G. Savini, A. Lombardo, and A. C. Ferrari, "The shear mode of multilayer graphene," *Nature Materials*, vol. 11, no. 294, 2012.

[156] N. Mounet and N. Marzari, "First-principles determination of the structural, vibrational and thermodynamic properties of diamond, graphite, and derivatives," *Phys. Rev. B*, vol. 71, p. 205214, May 2005. [Online]. Available: https://link.aps.org/doi/10.1103/PhysRevB.71.205214

[157] R. Nicklow, N. Wakabayashi, and H. G. Smith, "Lattice dynamics of pyrolytic graphite," *Phys. Rev. B*, vol. 5, pp. 4951–4962, Jun 1972. [Online]. Available: https://link.aps.org/doi/10.1103/PhysRevB.5.4951

[158] C. Oshima, T. Aizawa, R. Souda, Y. Ishizawa, and Y. Sumiyoshi, "Surface phonon dispersion curves of graphite (0001) over the entire energy region," *Solid State Communications*, vol. 65, no. 12, pp. 1601 – 1604, 1988. [Online]. Available: http://www.sciencedirect.com/science/article/pii/0038109888906606

[159] S. Siebentritt, R. Pues, K.-H. Rieder, and A. M. Shikin, "Surface phonon dispersion in graphite and in a lanthanum graphite intercalation compound," *Phys. Rev. B*, vol. 55, pp. 7927–7934, Mar 1997. [Online]. Available: https://link.aps.org/doi/10.1103/PhysRevB.55.7927

[160] H. Yanagisawa, T. Tanaka, Y. Ishida, M. Matsue, E. Rokuta, S. Otani, and C. Oshima, "Analysis of phonons in graphene sheets by means of HREELS measurement and ab initio calculation," *Surface and Interface Analysis*, vol. 37,

no. 2, pp. 133–136, 2005. [Online]. Available: https://onlinelibrary.wiley.com/doi/abs/10.1002/sia.1948

[161] M. Mohr, J. Maultzsch, E. Dobardžić, S. Reich, I. Milošević, M. Damnjanović, A. Bosak, M. Krisch, and C. Thomsen, "Phonon dispersion of graphite by inelastic X-ray scattering," *Phys. Rev. B*, vol. 76, p. 035439, Jul 2007. [Online]. Available: https://link.aps.org/doi/10.1103/PhysRevB.76.035439

[162] I. Calizo, I. Bejenari, M. Rahman, G. Liu, and A. A. Balandin, "Ultraviolet Raman microscopy of single and multilayer graphene," *Journal of Applied Physics*, vol. 106, no. 4, p. 043509, 2009. [Online]. Available: https://doi.org/10.1063/1.3197065

[163] W. Zhou, J. Zeng, X. Li, J. Xu, Y. Shi, W. Ren, F. Miao, B. Wang, and D. Xing, "Ultraviolet Raman spectra of double-resonant modes of graphene," *Carbon*, vol. 101, pp. 235 – 238, 2016. [Online]. Available: http://www.sciencedirect.com/science/article/pii/S0008622316300902

[164] A. C. Ferrari, J. C. Meyer, V. Scardaci, C. Casiraghi, M. Lazzeri, F. Mauri, S. Piscanec, D. Jiang, K. S. Novoselov, S. Roth, and A. K. Geim, "Raman spectrum of graphene and graphene layers," *Phys. Rev. Lett.*, vol. 97, p. 187401, Oct 2006. [Online]. Available: https://link.aps.org/doi/10.1103/PhysRevLett.97.187401

[165] D. L. Mafra, G. Samsonidze, L. M. Malard, D. C. Elias, J. C. Brant, F. Plentz, E. S. Alves, and M. A. Pimenta, "Determination of LA and TO phonon dispersion relations of graphene near the Dirac point by double resonance Raman scattering," *Phys. Rev. B*, vol. 76, p. 233407, Dec 2007. [Online]. Available: https://link.aps.org/doi/10.1103/PhysRevB.76.233407

[166] P. T. Araujo, D. L. Mafra, K. Sato, R. Saito, J. Kong, and M. S. Dresselhaus, "Phonon self-energy corrections to nonzero wave-vector phonon modes in single-layer graphene," *Phys. Rev. Lett.*, vol. 109, p. 046801, Jul 2012. [Online]. Available: https://link.aps.org/doi/10.1103/PhysRevLett.109.046801

[167] T. Shimada, T. Sugai, C. Fantini, M. Souza, L. G. Cançado, A. Jorio, M. A. Pimenta, R. Saito, A. Grüneis, G. Dresselhaus, M. S. Dresselhaus, Y. Ohno, T. Mizutani, and H. Shinohara, "Origin of the 2450 cm^{-1} Raman bands in HOPG, single-wall and double-wall carbon nanotubes," *Carbon*, vol. 43, pp. 1049–1054, 2005.

[168] F. Herziger, C. Tyborski, O. Ochedowski, M. Schleberger, and J. Maultzsch, "Double-resonant la phonon scattering in defective graphene and carbon nanotubes," *Phys. Rev. B*, vol. 90, p. 245431, Dec 2014. [Online]. Available: https://link.aps.org/doi/10.1103/PhysRevB.90.245431

[169] L. Malard, M. Pimenta, G. Dresselhaus, and M. Dresselhaus, "Raman spectroscopy in graphene," *Physics Reports*, vol. 473, no. 5, pp. 51 – 87, 2009. [Online]. Available: http://www.sciencedirect.com/science/article/pii/S0370157309000520

[170] Y. Kawashima and G. Katagiri, "Fundamentals, overtones, and combinations in the Raman spectrum of graphite," *Phys. Rev. B*, vol. 52, pp. 10 053–10 059, Oct 1995. [Online]. Available: https://link.aps.org/doi/10.1103/PhysRevB.52.10053

[171] F. Herziger, "Double-resonant Raman scattering in graphene, few-layer graphene, and carbon nanotubes," doctoral thesis, Technische Universität, Berlin, 2015, https://depositonce.tu-berlin.de/handle/11303/5205.

[172] J. Kürti, V. Zólyomi, A. Grüneis, and H. Kuzmany, "Double resonant Raman phenomena enhanced by van Hove singularities in single-wall carbon nanotubes," *Phys. Rev. B*, vol. 65, p. 165433, Apr 2002. [Online]. Available: https://link.aps.org/doi/10.1103/PhysRevB.65.165433

[173] M. Mohr, K. Papagelis, J. Maultzsch, and C. Thomsen, "Two-dimensional electronic and vibrational band structure of uniaxially strained graphene from ab initio calculations," *Phys. Rev. B*, vol. 80, p. 205410, Nov 2009. [Online]. Available: https://link.aps.org/doi/10.1103/PhysRevB.80.205410

[174] D. Yoon, Y.-W. Son, and H. Cheong, "Strain-dependent splitting of the double-resonance Raman scattering band in graphene," *Phys. Rev. Lett.*, vol. 106, p. 155502, Apr 2011. [Online]. Available: https://link.aps.org/doi/10.1103/PhysRevLett.106.155502

[175] D. M. Basko, "Theory of resonant multiphonon Raman scattering in graphene," *Phys. Rev. B*, vol. 78, p. 125418, Sep 2008. [Online]. Available: https://link.aps.org/doi/10.1103/PhysRevB.78.125418

[176] J. Bendtsen, "The rotational and rotation-vibrational Raman spectra of $14N_2$, 14N15N and $15N_2$," *Journal of Raman Spectroscopy*, vol. 2, no. 2, pp. 133–145, 1974. [Online]. Available: http://dx.doi.org/10.1002/jrs.1250020204

[177] P. Giura, N. Bonini, G. Creff, J. B. Brubach, P. Roy, and M. Lazzeri, "Temperature evolution of infrared- and Raman-active phonons in graphite," *Phys. Rev. B*, vol. 86, p. 121404, Sep 2012. [Online]. Available: https://link.aps.org/doi/10.1103/PhysRevB.86.121404

[178] M. S. Dresselhaus, G. Dresselhaus, and A. Jorio, *Applications of Group Theory to the Physics of Solids*. Springer, 2002.

[179] N. P. Valentin, "Two-phonon Raman scattering in graphene for laser excitation beyond the π-plasmon energy," *Journal of Physics: Conference Series*, vol. 764, no. 1, p. 012008, 2016. [Online]. Available: http://stacks.iop.org/1742-6596/764/i=1/a=012008

[180] F. Herziger, C. Tyborski, O. Ochedowski, M. Schleberger, and J. Maultzsch, "Tunable quantum interference in bilayer graphene in double-resonant Raman scattering," *Carbon*, vol. 133, pp. 254 – 259, 2018. [Online]. Available: http://www.sciencedirect.com/science/article/pii/S0008622318302690

[181] D. L. Rousseau, R. P. Bauman, and S. P. S. Porto, "Normal mode determination in crystals," *Journal of Raman Spectroscopy*, vol. 10, no. 1, pp. 253–290, 1981. [Online]. Available: https://onlinelibrary.wiley.com/doi/abs/10.1002/jrs.1250100152

[182] M. Damnjanović, I. Milošević, E. Dobardžić, T. Vuković, and B. Nikolić, in *Applied Physics of Nanotubes: Fundamentals of Theory, Optics and Transport Devices*. Springer-Verlag, 2005, ch. 2.

[183] V. N. Popov and P. Lambin, "Comparative study of the two-phonon Raman bands of silicene and graphene," *2D Materials*, vol. 3, no. 2, p. 025014, 2016. [Online]. Available: http://stacks.iop.org/2053-1583/3/i=2/a=025014

[184] C. Cong, T. Yu, K. Sato, J. Shang, R. Saito, G. F. Dresselhaus, and M. S. Dresselhaus, "Raman characterization of ABA- and ABC-stacked trilayer graphene," *ACS Nano*, vol. 5, no. 11, pp. 8760–8768, 2011. [Online]. Available: https://doi.org/10.1021/nn203472f

[185] E. H. Martins Ferreira, M. V. O. Moutinho, F. Stavale, M. M. Lucchese, R. B. Capaz, C. A. Achete, and A. Jorio, "Evolution of the Raman spectra from single-, few-, and many-layer graphene with increasing disorder," *Phys. Rev. B*, vol. 82, p. 125429, Sep 2010. [Online]. Available: https://link.aps.org/doi/10.1103/PhysRevB.82.125429

[186] Y. Hao, Y. Wang, L. Wang, Z. Ni, Z. Wang, R. Wang, C. K. Koo, Z. Shen, and J. T. L. Thong, "Probing layer number and stacking order of few-layer graphene by Raman spectroscopy," *Small*, vol. 6, no. 2, pp. 195–200, 1 2010. [Online]. Available: http:https://doi.org/10.1002/smll.200901173

[187] F. Herziger, P. May, and J. Maultzsch, "Layer-number determination in graphene by out-of-plane phonons," *Phys. Rev. B*, vol. 85, p. 235447, Jun 2012. [Online]. Available: https://link.aps.org/doi/10.1103/PhysRevB.85.235447

[188] M. Bruna and S. Borini, "Observation of Raman G-band splitting in top-doped few-layer graphene," *Phys. Rev. B*, vol. 81, p. 125421, Mar 2010. [Online]. Available: https://link.aps.org/doi/10.1103/PhysRevB.81.125421

[189] J.-B. Wu, X. Zhang, M. Ijäs, W.-P. Han, X.-F. Qiao, X.-L. Li, D.-S. Jiang, A. C. Ferrari, and P.-H. Tan, "Resonant Raman spectroscopy of twisted multilayer graphene," *Nature Comm.*, vol. 5, no. 5309, 11 2014. [Online]. Available: http://dx.doi.org/10.1038/ncomms6309

[190] G. Tsoukleri, J. Parthenios, C. Galiotis, and K. Papagelis, "Embedded trilayer graphene flakes under tensile and compressive loading," *2D Materials*, vol. 2, no. 2, p. 024009, 2015. [Online]. Available: http://stacks.iop.org/2053-1583/2/i=2/a=024009

[191] J.-A. Yan, W. Y. Ruan, and M. Y. Chou, "Phonon dispersions and vibrational properties of monolayer, bilayer, and trilayer graphene: Density-functional perturbation theory," *Phys. Rev. B*, vol. 77, p. 125401, Mar 2008. [Online]. Available: https://link.aps.org/doi/10.1103/PhysRevB.77.125401

[192] S. K. Saha, U. V. Waghmare, H. R. Krishnamurthy, and A. K. Sood, "Phonons in few-layer graphene and interplanar interaction: A first-principles study," *Phys. Rev. B*, vol. 78, p. 165421, Oct 2008. [Online]. Available: https://link.aps.org/doi/10.1103/PhysRevB.78.165421

[193] D. Graf, F. Molitor, K. Ensslin, C. Stampfer, A. Jungen, C. Hierold, and L. Wirtz, "Spatially resolved Raman spectroscopy of single- and few-layer graphene," *Nano Letters*, vol. 7, no. 2, pp. 238–242, 2007. [Online]. Available: https://doi.org/10.1021/nl061702a

[194] D. Yoon, H. Moon, Y.-W. Son, J. S. Choi, B. H. Park, Y. H. Cha, Y. D. Kim, and H. Cheong, "Interference effect on Raman spectrum of graphene on SiO_2/Si," *Phys. Rev. B*, vol. 80, p. 125422, Sep 2009. [Online]. Available: https://link.aps.org/doi/10.1103/PhysRevB.80.125422

[195] P. Blake, E. W. Hill, A. H. C. Neto, K. S. Novoselov, D. Jiang, R. Yang, T. J. Booth, and A. K. Geim, "Making graphene visible," *Applied Physics Letters*, vol. 91, no. 6, p. 063124, 2007. [Online]. Available: https://doi.org/10.1063/1.2768624

[196] R. J. Nemanich and S. A. Solin, "First- and second-order Raman scattering from finite-size crystals of graphite," *Phys. Rev. B*, vol. 20, pp. 392–401, Jul 1979. [Online]. Available: https://link.aps.org/doi/10.1103/PhysRevB.20.392

[197] A. Grüneis, R. Saito, G. G. Samsonidze, T. Kimura, M. A. Pimenta, A. Jorio, A. G. S. Filho, G. Dresselhaus, and M. S. Dresselhaus, "Inhomogeneous optical absorption around the K point in graphite and carbon nanotubes," *Phys. Rev. B*, vol. 67, p. 165402, Apr 2003. [Online]. Available: https://link.aps.org/doi/10.1103/PhysRevB.67.165402

[198] Y.-J. Lin and J.-J. Zeng, "Tuning the work function of graphene by ultraviolet irradiation," *Applied Physics Letters*, vol. 102, no. 18, p. 183120, 2013. [Online]. Available: https://doi.org/10.1063/1.4804289

[199] M.-L. Sham and J.-K. Kim, "Surface functionalities of multi-wall carbon nanotubes after UV/ozone and TETA treatments," *Carbon*, vol. 44, no. 4, pp. 768 – 777, 2006. [Online]. Available: http://www.sciencedirect.com/science/article/pii/S0008622305005476

[200] M. Grujicic, G. Cao, A. Rao, T. Tritt, and S. Nayak, "UV-light enhanced oxidation of carbon nanotubes," *Applied Surface Science*, vol. 214, no. 1, pp. 289 – 303, 2003. [Online]. Available: http://www.sciencedirect.com/science/article/pii/S0169433203003611

[201] E. Najafi, J.-Y. Kim, S.-H. Han, and K. Shin, "UV-ozone treatment of multi-walled carbon nanotubes for enhanced organic solvent dispersion," *Colloids and Surfaces A: Physicochemical and Engineering Aspects*, vol. 284-285, pp. 373 – 378, 2006, a selection of papers from the 11th International Conference on Organized Molecular Films (LB11), June 26-30, 2005, Sapporo. [Online]. Available: http://www.sciencedirect.com/science/article/pii/S0927775705009222

[202] S. Mathew, T. Chan, D. Zhan, K. Gopinadhan, A.-R. Barman, M. Breese, S. Dhar, Z. Shen, T. Venkatesan, and J. T. Thong, "The effect of layer number and substrate on the stability of graphene under MeV proton beam irradiation," *Carbon*, vol. 49, no. 5, pp. 1720 – 1726, 2011. [Online]. Available: http://www.sciencedirect.com/science/article/pii/S000862231000936X

[203] G. Compagnini, F. Giannazzo, S. Sonde, V. Raineri, and E. Rimini, "Ion irradiation and defect formation in single layer graphene," *Carbon*, vol. 47, no. 14, pp. 3201 – 3207, 2009. [Online]. Available: http://www.sciencedirect.com/science/article/pii/S0008622309004564

[204] R. Krupke, technische Universität Darmstadt, Institut für Materialwissenschaft, Building L1/08, office 401, Petersenstraße 23, 64287 Darmstadt, Germany.

[205] L. Song, W. Ma, Y. Ren, W. Zhou, S. Xie, P. Tan, and L. Sun, "Temperature dependence of Raman spectra in single-walled carbon nanotube rings," *Appl. Phys. Lett.*, vol. 92, no. 12, p. 121905, 2008. [Online]. Available: http://dx.doi.org/10.1063/1.2891870

[206] Z. Zhou, X. Dou, L. Ci, L. Song, D. Liu, Y. Gao, J. Wang, L. Liu, W. Zhou, S. Xie, and D. Wan, "Temperature dependence of the Raman spectra of individual carbon nanotubes," *J. Phys. Chem. B*, vol. 110, no. 3, pp. 1206–1209, 2006. [Online]. Available: http://dx.doi.org/10.1021/jp053268r

[207] I. Calizo, A. A. Balandin, W. Bao, F. Miao, and C. N. Lau, "Temperature dependence of the Raman spectra of graphene and graphene multilayers," *Nano Letters*, vol. 7, no. 9, pp. 2645–2649, 2007. [Online]. Available: http://dx.doi.org/10.1021/nl071033g

[208] A. Bassil, P. Puech, L. Tubery, W. Bacsa, and E. Flahaut, "Controlled laser heating of carbon nanotubes," *Applied Physics Letters*, vol. 88, no. 17, p. 173113, 2006. [Online]. Available: https://doi.org/10.1063/1.2199467

[209] P. Tan, Y. Deng, Q. Zhao, and W. Cheng, "The intrinsic temperature effect of the Raman spectra of graphite," *Applied Physics Letters*, vol. 74, no. 13, pp. 1818–1820, 1999. [Online]. Available: https://doi.org/10.1063/1.123096

[210] H. D. Li, K. T. Yue, Z. L. Lian, Y. Zhan, L. X. Zhou, S. L. Zhang, Z. J. Shi, Z. N. Gu, B. B. Liu, R. S. Yang, H. B. Yang, G. T. Zou, Y. Zhang, and S. Iijima, "Temperature dependence of the Raman spectra of single-wall carbon nanotubes," *Applied Physics Letters*, vol. 76, no. 15, pp. 2053–2055, 2000. [Online]. Available: https://doi.org/10.1063/1.126252

[211] J. Menéndez and M. Cardona, "Temperature dependence of the first-order Raman scattering by phonons in Si, Ge, and $\alpha - \mathrm{Sn}$: Anharmonic effects," *Phys. Rev. B*, vol. 29, pp. 2051–2059, Feb 1984. [Online]. Available: https://link.aps.org/doi/10.1103/PhysRevB.29.2051

[212] E. Ganz, A. B. Ganz, L.-M. Yang, and M. Dornfeld, "The initial stages of melting of graphene between 4000 K and 6000 K," *Phys. Chem. Chem. Phys.*, vol. 19, pp. 3756–3762, 2017. [Online]. Available: http://dx.doi.org/10.1039/C6CP06940A

[213] J. H. Los, K. V. Zakharchenko, M. I. Katsnelson, and A. Fasolino, "Melting temperature of graphene," *Phys. Rev. B*, vol. 91, p. 045415, Jan 2015. [Online]. Available: https://link.aps.org/doi/10.1103/PhysRevB.91.045415

[214] C. Tyborski, A. Vierck, R. Narula, V. N. Popov, and J. Maultzsch, "Double-resonant Raman scattering with optical and acoustic phonons in carbon nanotubes," *Phys. Rev. B*, vol. 97, p. 214306, Jun 2018. [Online]. Available: https://link.aps.org/doi/10.1103/PhysRevB.97.214306

[215] A. Jorio, A. G. Souza Filho, G. Dresselhaus, M. S. Dresselhaus, A. K. Swan, M. S. Ünlü, B. B. Goldberg, M. A. Pimenta, J. H. Hafner, C. M. Lieber, and R. Saito, "G-band resonant Raman study of 62 isolated single-wall carbon nanotubes," *Phys. Rev. B*, vol. 65, p. 155412, Mar 2002. [Online]. Available: https://link.aps.org/doi/10.1103/PhysRevB.65.155412

[216] M. Dresselhaus, A. Jorio, A. S. Filho, G. Dresselhaus, and R. Saito, "Raman spectroscopy on one isolated carbon nanotube," *Physica B: Condensed Matter*, vol. 323, no. 1, pp. 15 – 20, 2002, proceedings of the Tsukuba Symposium on Carbon Nanotube in Commemoration of the 10th Anniversary of its Discovery. [Online]. Available: http://www.sciencedirect.com/science/article/pii/S0921452602008736

[217] M. Dresselhaus, G. Dresselhaus, A. Jorio, A. S. Filho, and R. Saito, "Raman spectroscopy on isolated single wall carbon nanotubes," *Carbon*, vol. 40, no. 12, pp. 2043 – 2061, 2002. [Online]. Available: http://www.sciencedirect.com/science/article/pii/S0008622302000660

[218] J. Laudenbach, F. Hennrich, H. Telg, M. Kappes, and J. Maultzsch, "Resonance behavior of the defect-induced Raman mode of single-chirality enriched carbon nanotubes," *Phys. Rev. B*, vol. 87, p. 165423, Apr 2013. [Online]. Available: https://link.aps.org/doi/10.1103/PhysRevB.87.165423

[219] G. S. Duesberg, I. Loa, M. Burghard, K. Syassen, and S. Roth, "Polarized Raman spectroscopy on isolated single-wall carbon nanotubes," *Phys. Rev. Lett.*, vol. 85, pp. 5436–5439, Dec 2000. [Online]. Available: https://link.aps.org/doi/10.1103/PhysRevLett.85.5436

[220] H. Telg, J. Maultzsch, S. Reich, F. Hennrich, and C. Thomsen, "Chirality distribution and transition energies of carbon nanotubes," *Phys. Rev. Lett.*, vol. 93, p. 177401, Oct 2004. [Online]. Available: https://link.aps.org/doi/10.1103/PhysRevLett.93.177401

[221] J. Maultzsch, S. Reich, and C. Thomsen, "Chirality-selective Raman scattering of the 2D mode in carbon nanotubes," *Phys. Rev. B*, vol. 64, p. 121407, Sep 2001. [Online]. Available: https://link.aps.org/doi/10.1103/PhysRevB.64.121407

[222] L. G. Moura, M. V. Moutinho, P. Venezuela, F. Mauri, A. Righi, M. S. Strano, C. Fantini, and M. A. Pimenta, "The double-resonance Raman spectra in single-chirality (n, m) carbon nanotubes," *Carbon*, vol. 117, no. Supplement C, pp. 41 – 45, 2017. [Online]. Available: http://www.sciencedirect.com/science/article/pii/S000862231730177X

[223] C. Fantini, A. Jorio, M. Souza, M. S. Strano, M. S. Dresselhaus, and M. A. Pimenta, "Optical transition energies for carbon nanotubes from

resonant Raman spectroscopy: Environment and temperature effects," *Phys. Rev. Lett.*, vol. 93, p. 147406, Sep 2004. [Online]. Available: https://link.aps.org/doi/10.1103/PhysRevLett.93.147406

[224] S. Reich, C. Thomsen, and P. Ordejón, "Electronic band structure of isolated and bundled carbon nanotubes," *Phys. Rev. B*, vol. 65, p. 155411, Mar 2002. [Online]. Available: https://link.aps.org/doi/10.1103/PhysRevB.65.155411

[225] M. Zheng and E. D. Semke, "Enrichment of single chirality carbon nanotubes," *Journal of the American Chemical Society*, vol. 129, no. 19, pp. 6084–6085, 2007. [Online]. Available: http://dx.doi.org/10.1021/ja071577k

[226] M. S. Arnold, S. I. Stupp, and M. C. Hersam, "Enrichment of single-walled carbon nanotubes by diameter in density gradients," *Nano Letters*, vol. 5, no. 4, pp. 713–718, 2005. [Online]. Available: http://dx.doi.org/10.1021/nl050133o

[227] J. Laudenbach, F. Hennrich, M. Kappes, and J. Maultzsch, "Resonance behavior of defect-induced modes in metallic and semiconducting single-walled carbon nanotubes," *physica status solidi (b)*, vol. 249, no. 12, pp. 2460–2464, 2012. [Online]. Available: http://dx.doi.org/10.1002/pssb.201200175

[228] M. A. Pimenta, A. Marucci, S. A. Empedocles, M. G. Bawendi, E. B. Hanlon, A. M. Rao, P. C. Eklund, R. E. Smalley, G. Dresselhaus, and M. S. Dresselhaus, "Raman modes of metallic carbon nanotubes," *Phys. Rev. B*, vol. 58, pp. R16 016–R16 019, Dec 1998. [Online]. Available: https://link.aps.org/doi/10.1103/PhysRevB.58.R16016

[229] S. D. M. Brown, A. Jorio, P. Corio, M. S. Dresselhaus, G. Dresselhaus, R. Saito, and K. Kneipp, "Origin of the Breit-Wigner-Fano lineshape of the tangential G-band feature of metallic carbon nanotubes," *Phys. Rev. B*, vol. 63, p. 155414, Mar 2001. [Online]. Available: https://link.aps.org/doi/10.1103/PhysRevB.63.155414

[230] R. Krupke, F. Hennrich, H. v. Löhneysen, and M. M. Kappes, "Separation of metallic from semiconducting single-walled carbon nanotubes," *Science*, vol. 301, no. 5631, pp. 344–347, 2003. [Online]. Available: http://science.sciencemag.org/content/301/5631/344

[231] J. Jiang, R. Saito, A. Grüneis, G. Dresselhaus, and M. Dresselhaus, "Optical absorption matrix elements in single-wall carbon nanotubes," *Carbon*, vol. 42, no. 15, pp. 3169 – 3176, 2004. [Online]. Available: http://www.sciencedirect.com/science/article/pii/S0008622304004919

[232] V. N. Popov, "Curvature effects on the structural, electronic and optical properties of isolated single-walled carbon nanotubes within a symmetry-adapted non-orthogonal tight-binding model," *New Journal of Physics*, vol. 6, no. 1, p. 17, 2004. [Online]. Available: http://stacks.iop.org/1367-2630/6/i=1/a=017

[233] J. Jiang, R. Saito, G. G. Samsonidze, A. Jorio, S. G. Chou, G. Dresselhaus, and M. S. Dresselhaus, "Chirality dependence of exciton effects in single-wall carbon

nanotubes: Tight-binding model," *Phys. Rev. B*, vol. 75, p. 035407, Jan 2007. [Online]. Available: https://link.aps.org/doi/10.1103/PhysRevB.75.035407

[234] V. N. Popov and L. Henrard, "Comparative study of the optical properties of single-walled carbon nanotubes within orthogonal and nonorthogonal tight-binding models," *Phys. Rev. B*, vol. 70, p. 115407, Sep 2004. [Online]. Available: https://link.aps.org/doi/10.1103/PhysRevB.70.115407

[235] M. Machón, S. Reich, C. Thomsen, D. Sánchez-Portal, and P. Ordejón, "Ab initio calculations of the optical properties of 4-Å-diameter single-walled nanotubes," *Phys. Rev. B*, vol. 66, p. 155410, Oct 2002. [Online]. Available: https://link.aps.org/doi/10.1103/PhysRevB.66.155410

[236] O. Dubay and G. Kresse, "Accurate density functional calculations for the phonon dispersion relations of graphite layer and carbon nanotubes," *Phys. Rev. B*, vol. 67, p. 035401, Jan 2003. [Online]. Available: https://link.aps.org/doi/10.1103/PhysRevB.67.035401

[237] J. Jiang, R. Saito, G. G. Samsonidze, S. G. Chou, A. Jorio, G. Dresselhaus, and M. S. Dresselhaus, "Electron-phonon matrix elements in single-wall carbon nanotubes," *Phys. Rev. B*, vol. 72, p. 235408, Dec 2005. [Online]. Available: https://link.aps.org/doi/10.1103/PhysRevB.72.235408

[238] M. Machón, S. Reich, H. Telg, J. Maultzsch, P. Ordejón, and C. Thomsen, "Strength of radial breathing mode in single-walled carbon nanotubes," *Phys. Rev. B*, vol. 71, p. 035416, Jan 2005. [Online]. Available: https://link.aps.org/doi/10.1103/PhysRevB.71.035416

[239] J. Maultzsch, S. Reich, and C. Thomsen, "Chirality-selective Raman scattering of the D mode in carbon nanotubes," *Phys. Rev. B*, vol. 64, p. 121407, Sep 2001. [Online]. Available: https://link.aps.org/doi/10.1103/PhysRevB.64.121407

[240] ——, "Raman scattering in carbon nanotubes revisited," *Phys. Rev. B*, vol. 65, p. 233402, May 2002. [Online]. Available: https://link.aps.org/doi/10.1103/PhysRevB.65.233402

[241] P. Eklund, J. Holden, and R. Jishi, "Vibrational modes of carbon nanotubes; spectroscopy and theory," *Carbon*, vol. 33, no. 7, pp. 959 – 972, 1995, nanotubes. [Online]. Available: http://www.sciencedirect.com/science/article/pii/000862239500035C

[242] C. Fantini, A. Jorio, M. Souza, R. Saito, G. G. Samsonidze, M. S. Dresselhaus, and M. A. Pimenta, "Steplike dispersion of the intermediate-frequency Raman modes in semiconducting and metallic carbon nanotubes," *Phys. Rev. B*, vol. 72, p. 085446, Aug 2005. [Online]. Available: https://link.aps.org/doi/10.1103/PhysRevB.72.085446

[243] M. Kalbac, L. Kavan, M. Zukalová, and L. Dunsch, "The intermediate frequency modes of single- and double-walled carbon nanotubes: A Raman

spectroscopic and in situ Raman spectroelectrochemical study," *Chemistry - A European Journal*, vol. 12, no. 16, pp. 4451–4457, 2006. [Online]. Available: http://dx.doi.org/10.1002/chem.200501364

[244] A. Vierck, F. Gannott, M. Schweiger, J. Zaumseil, and J. Maultzsch, "ZA-derived phonons in the Raman spectra of single-walled carbon nanotubes," *Carbon*, vol. 117, no. Supplement C, pp. 360 – 366, 2017. [Online]. Available: http://www.sciencedirect.com/science/article/pii/S0008622317302300

[245] C. Tyborski, F. Herziger, and J. Maultzsch, "Raman spectroscopy of nondispersive intermediate frequency modes and their overtones in carbon nanotubes," *physica status solidi (b)*, vol. 252, no. 11, pp. 2551–2557, 2015. [Online]. Available: http://dx.doi.org/10.1002/pssb.201552513

[246] C. Fantini, M. A. Pimenta, and M. S. Strano, "Two-phonon combination Raman modes in covalently functionalized single-wall carbon nanotubes," *J. Phys. Chem. C*, vol. 112, pp. 13 150–13 155, 2008.

[247] V. W. Brar, G. G. Samsonidze, M. S. Dresselhaus, G. Dresselhaus, R. Saito, A. K. Swan, M. S. Ünlü, B. B. Goldberg, A. G. Souza Filho, and A. Jorio, "Second-order harmonic and combination modes in graphite, single-wall carbon nanotube bundles, and isolated single-wall carbon nanotubes," *Phys. Rev. B*, vol. 66, p. 155418, Oct 2002. [Online]. Available: http://link.aps.org/doi/10.1103/PhysRevB.66.155418

[248] A. V. Ellis, "Second-order overtone and combination modes in the LOLA region of acid treated double-walled carbon nanotubes," *Journal of Chemical Physics*, vol. 125, p. 121103, 2006.

[249] V. N. Popov, "Two-phonon Raman bands of bilayer graphene: Revisited," *Carbon*, vol. 91, no. Supplement C, pp. 436 – 444, 2015. [Online]. Available: http://www.sciencedirect.com/science/article/pii/S0008622315004170

[250] R. Narula, department of Physics, Indian Institute of Technology Delhi, Haus Khas, New Delhi-110016, India.

[251] V. N. Popov, "Origin of the complex lineshape of the Raman 2D band of single-walled carbon nanotubes," *ArXiv e-prints*, Apr. 2018.

[252] S. Piscanec, M. Lazzeri, J. Robertson, A. C. Ferrari, and F. Mauri, "Optical phonons in carbon nanotubes: Kohn anomalies, Peierls distortions, and dynamic effects," *Phys. Rev. B*, vol. 75, p. 035427, Jan 2007. [Online]. Available: https://link.aps.org/doi/10.1103/PhysRevB.75.035427

[253] O. Dubay, G. Kresse, and H. Kuzmany, "Phonon softening in metallic nanotubes by a Peierls-like mechanism," *Phys. Rev. Lett.*, vol. 88, p. 235506, May 2002. [Online]. Available: https://link.aps.org/doi/10.1103/PhysRevLett.88.235506

[254] J. Maultzsch, S. Reich, U. Schlecht, and C. Thomsen, "High-energy phonon branches of an individual metallic carbon nanotube," *Phys. Rev. Lett.*, vol. 91, p. 087402, Aug 2003. [Online]. Available: https://link.aps.org/doi/10.1103/PhysRevLett.91.087402

[255] M. Oron-Carl, F. Hennrich, M. M. Kappes, H. v. Löhneysen, and R. Krupke, "On the electron-phonon coupling of individual single-walled carbon nanotubes," *Nano Letters*, vol. 5, no. 9, pp. 1761–1767, 2005. [Online]. Available: https://doi.org/10.1021/nl051107t

[256] H. Telg, J. G. Duque, M. Staiger, X. Tu, F. Hennrich, M. M. Kappes, M. Zheng, J. Maultzsch, C. Thomsen, and S. K. Doorn, "Chiral index dependence of the G+ and G- Raman modes in semiconducting carbon nanotubes," *ACS Nano*, vol. 6, no. 1, pp. 904–911, 2012. [Online]. Available: https://doi.org/10.1021/nn2044356

[257] V. N. Popov and P. Lambin, "Non-adiabatic phonon dispersion of metallic single-walled carbon nanotubes," *Nano Research*, vol. 3, no. 11, pp. 822–829, Nov 2010. [Online]. Available: https://doi.org/10.1007/s12274-010-0052-2

[258] V. N. Popov, faculty of Physics, University of Sofia, BG-1164, Bulgaria.

[259] F. Herziger, A. Vierck, J. Laudenbach, and J. Maultzsch, "Understanding double-resonant Raman scattering in chiral carbon nanotubes: Diameter and energy dependence of the D mode," *Phys. Rev. B*, vol. 92, p. 235409, Dec 2015. [Online]. Available: https://link.aps.org/doi/10.1103/PhysRevB.92.235409

[260] V. N. Popov, "Two-phonon Raman bands of single-walled carbon nanotubes: A case study," *Phys. Rev. B*, vol. 98, p. 085413, Aug 2018. [Online]. Available: https://link.aps.org/doi/10.1103/PhysRevB.98.085413

[261] J. Laudenbach, D. Schmid, F. Herziger, F. Hennrich, M. Kappes, M. Muoth, M. Haluska, F. Hof, C. Backes, F. Hauke, A. Hirsch, and J. Maultzsch, "Diameter dependence of the defect-induced Raman modes in functionalized carbon nanotubes," *Carbon*, vol. 112, no. Supplement C, pp. 1 – 7, 2017. [Online]. Available: http://www.sciencedirect.com/science/article/pii/S0008622316309277

[262] R. B. Weisman and S. M. Bachilo, "Dependence of optical transition energies on structure for single-walled carbon nanotubes in aqueos suspension: An empirical Kataura plot," *Nano Letters*, vol. 3, no. 9, pp. 1235–1238, 2003. [Online]. Available: https://doi.org/10.1021/nl034428i

[263] S. E., "Quantisierung als Eigenwertproblem," *Annalen der Physik*, vol. 385, no. 13, pp. 437–490, 1926. [Online]. Available: https://onlinelibrary.wiley.com/doi/abs/10.1002/andp.19263851302

[264] P. Kim, T. W. Odom, J.-L. Huang, and C. M. Lieber, "Electronic density of states of atomically resolved single-walled carbon nanotubes: Van Hove singularities and end states," *Phys. Rev. Lett.*, vol. 82, pp. 1225–1228, Feb 1999. [Online]. Available: https://link.aps.org/doi/10.1103/PhysRevLett.82.1225

[265] J. W. G. Wilder, L. C. Venema, A. G. Rinzler, R. E. Smalley, and C. Dekker, "Electronic structure of atomically resolved carbon nanotubes," *Nature*, vol. 391, jan 1998. [Online]. Available: http://dx.doi.org/10.1038/34139

[266] F. Wang, G. Dukovic, L. E. Brus, and T. F. Heinz, "The optical resonances in carbon nanotubes arise from excitons," *Science*, vol. 308, no. 5723, pp. 838–841, 2005. [Online]. Available: http://science.sciencemag.org/content/308/5723/838

[267] C. D. Spataru, S. Ismail-Beigi, L. X. Benedict, and S. G. Louie, "Excitonic effects and optical spectra of single-walled carbon nanotubes," *Phys. Rev. Lett.*, vol. 92, p. 077402, Feb 2004. [Online]. Available: https://link.aps.org/doi/10.1103/PhysRevLett.92.077402

[268] J. Maultzsch, R. Pomraenke, S. Reich, E. Chang, D. Prezzi, A. Ruini, E. Molinari, M. S. Strano, C. Thomsen, and C. Lienau, "Exciton binding energies in carbon nanotubes from two-photon photoluminescence," *Phys. Rev. B*, vol. 72, p. 241402, Dec 2005. [Online]. Available: https://link.aps.org/doi/10.1103/PhysRevB.72.241402

[269] A. Jorio, C. Fantini, M. S. S. Dantas, M. A. Pimenta, A. G. Souza Filho, G. G. Samsonidze, V. W. Brar, G. Dresselhaus, M. S. Dresselhaus, A. K. Swan, M. S. Ünlü, B. B. Goldberg, and R. Saito, "Linewidth of the Raman features of individual single-wall carbon nanotubes," *Phys. Rev. B*, vol. 66, p. 115411, Sep 2002. [Online]. Available: https://link.aps.org/doi/10.1103/PhysRevB.66.115411

[270] J. C. Meyer, M. Paillet, T. Michel, A. Moréac, A. Neumann, G. S. Duesberg, S. Roth, and J.-L. Sauvajol, "Raman modes of index-identified freestanding single-walled carbon nanotubes," *Phys. Rev. Lett.*, vol. 95, p. 217401, Nov 2005. [Online]. Available: https://link.aps.org/doi/10.1103/PhysRevLett.95.217401

[271] A. Hirsch, "Functionalization of single-walled carbon nanotubes," *Angewandte Chemie International Edition*, vol. 41, no. 11, pp. 1853–1859, 2002. [Online]. Available: http://dx.doi.org/10.1002/1521-3773(20020603)41:11<1853::AID-ANIE1853>3.0.CO;2-N

[272] M. S. Strano, C. A. Dyke, M. L. Usrey, P. W. Barone, M. J. Allen, H. Shan, C. Kittrell, R. H. Hauge, J. M. Tour, and R. E. Smalley, "Electronic structure control of single-walled carbon nanotube functionalization," *Science*, vol. 301, no. 5639, pp. 1519–1522, 2003. [Online]. Available: http://science.sciencemag.org/content/301/5639/1519

[273] Y.-P. Sun, K. Fu, Y. Lin, and W. Huang, "Functionalized carbon nantubes: Properties and applications," *Accounts of Chemical Research*, vol. 35, no. 12, pp. 1096–1104, 2002. [Online]. Available: http://dx.doi.org/10.1021/ar010160v

[274] K. Balasubramanian and M. Burghard, "Chemically functionalized carbon nanotubes," *Small*, vol. 1, no. 2, pp. 180–192, 2005. [Online]. Available: https://onlinelibrary.wiley.com/doi/abs/10.1002/smll.200400118

[275] B. Gebhardt, F. Hof, C. Backes, M. Müller, T. Plocke, J. Maultzsch, C. Thomsen, F. Hauke, and A. Hirsch, "Selective polycarboxylation of semiconducting single-walled carbon nanotubes by reductive sidewall functionalization," *Journal of the American Chemical Society*, vol. 133, no. 48, pp. 19 459–19 473, 2011. [Online]. Available: http://dx.doi.org/10.1021/ja206818n

[276] Z. Liu, X. Sun, N. Nakayama-Ratchford, and H. Dai, "Supramolecular chemistry on water-soluble carbon nanotubes for drug loading and delivery," *ACS Nano*, vol. 1, no. 1, pp. 50–56, 2007. [Online]. Available: http://dx.doi.org/10.1021/nn700040t

[277] D. Chattopadhyay, I. Galeska, and F. Papadimitrakopoulos, "A route for bulk separation of semiconducting from metallic single-wall carbon nanotubes," *Journal of the American Chemical Society*, vol. 125, no. 11, pp. 3370–3375, 2003. [Online]. Available: http://dx.doi.org/10.1021/ja028599l

[278] J. Chen, C. Klinke, A. Afzali, and P. Avouris, "Self-aligned carbon nanotube transistors with charge transfer doping," *Applied Physics Letters*, vol. 86, no. 12, p. 123108, 2005. [Online]. Available: https://doi.org/10.1063/1.1888054

[279] M. Prato, K. Kostarelos, and A. Bianco, "Functionalized carbon nanotubes in drug design and discovery," *Accounts of Chemical Research*, vol. 41, no. 1, pp. 60–68, 2008. [Online]. Available: http://dx.doi.org/10.1021/ar700089b

[280] M. P. Mattson, R. C. Haddon, and A. M. Rao, "Molecular functionalization of carbon nanotubes and use as substrates for neuronal growth," *Journal of Molecular Neuroscience*, vol. 14, no. 3, pp. 175–182, Jun 2000. [Online]. Available: https://doi.org/10.1385/JMN:14:3:175

[281] S. H. Hoke, J. Molstad, D. Dilettato, M. J. Jay, D. Carlson, B. Kahr, and R. G. Cooks, "Reaction of fullerenes and benzyne," *The Journal of Organic Chemistry*, vol. 57, no. 19, pp. 5069–5071, 1992. [Online]. Available: http://dx.doi.org/10.1021/jo00045a012

[282] A. Hirsch, *Fullerens and Related Structures*. Springer, 1999.

[283] E. Mickelson, C. Huffman, A. Rinzler, R. Smalley, R. Hauge, and J. Margrave, "Fluorination of single-wall carbon nanotubes," *Chemical Physics Letters*, vol. 296, no. 1, pp. 188 – 194, 1998. [Online]. Available: http://www.sciencedirect.com/science/article/pii/S0009261498010264

[284] F. Liang, A. K. Sadana, A. Peera, J. Chattopadhyay, Z. Gu, R. H. Hauge, and W. E. Billups, "A convenient route to functionalized carbon nanotubes," *Nano Letters*, vol. 4, no. 7, pp. 1257–1260, 2004. [Online]. Available: http://dx.doi.org/10.1021/nl049428c

[285] F. Herziger, R. Mirzayev, E. Poliani, and J. Maultzsch, "In-situ Raman study of laser-induced graphene oxidation," *physica status solidi (b)*, vol. 252, no. 11, pp. 2451–2455, 2015. [Online]. Available: http://dx.doi.org/10.1002/pssb.201552411

[286] S. Ryu, L. Liu, S. Berciaud, Y.-J. Yu, H. Liu, P. Kim, G. W. Flynn, and L. E. Brus, "Atmospheric oxygen binding and hole doping in deformed graphene on a SiO_2 substrate," *Nano Letters*, vol. 10, no. 12, pp. 4944–4951, 2010. [Online]. Available: https://doi.org/10.1021/nl1029607

[287] J. E. Lee, G. Ahn, J. Shim, Y. S. Lee, and S. Ryu, "Optical separation of mechanical strain from charge doping in graphene," *Nature Communications*, vol. 3, no. 1024, 2012. [Online]. Available: http://dx.doi.org/10.1038/ncomms2022

[288] R. Sen, A. Govindaraj, and C. Rao, "Carbon nanotubes by the metallocene route," *Chemical Physics Letters*, vol. 267, no. 3, pp. 276 – 280, 1997. [Online]. Available: http://www.sciencedirect.com/science/article/pii/S0009261497000808

[289] T. Takahashi, H. Tokailin, and T. Sagawa, "Angle-resolved ultraviolet photoelectron spectroscopy of the unoccupied band structure of graphite," *Phys. Rev. B*, vol. 32, pp. 8317–8324, Dec 1985. [Online]. Available: https://link.aps.org/doi/10.1103/PhysRevB.32.8317

[290] Y.-J. Yu, Y. Zhao, S. Ryu, L. E. Brus, K. S. Kim, and P. Kim, "Tuning the graphene work function by electric field effect," *Nano Letters*, vol. 9, no. 10, pp. 3430–3434, 2009. [Online]. Available: https://doi.org/10.1021/nl901572a

[291] P. Liu, Q. Sun, F. Zhu, K. Liu, K. Jiang, L. Liu, Q. Li, and S. Fan, "Measuring the work function of carbon nanotubes with thermionic method," *Nano Letters*, vol. 8, no. 2, pp. 647–651, 2008. [Online]. Available: https://doi.org/10.1021/nl0730817

[292] D. Langille and D. O'Shea, "Raman spectroscopy studies of antiferromagnetic feco3 and related carbonates," *Journal of Physics and Chemistry of Solids*, vol. 38, no. 10, pp. 1161 – 1171, 1977. [Online]. Available: http://www.sciencedirect.com/science/article/pii/0022369777900440

[293] N. Buzgar and A. Apopei, "The Raman study of certain Raman modes," *Analele Stiintifice de Universitatii A.I. Cusa din lasi. Sect. 2, Geologie*, vol. 55, no. 2, pp. 97–112, 2009. [Online]. Available: http://geology.uaic.ro/auig/articole/2009%20no2/1_L10-Buzgar%20-%20pag%2097-112.pdf

[294] H. N. Rutt and J. H. Nicola, "Raman spectra of carbonates of calcite structure," *Journal of Physics C: Solid State Physics*, vol. 7, no. 24, p. 4522, 1974. [Online]. Available: http://stacks.iop.org/0022-3719/7/i=24/a=015

[295] C. Klein and C. H. Jr., *Manual of Mineralogy.* John Wiley and Sons, Inc., 1985.

[296] A. P. Trushina, V. G. Goldort, S. A. Kochubei, and A. V. Baklanov, "Quantum yield and mechanism of singlet oxygen generation via UV photoexcitation of O_2-O_2 and N_2-O_2 encounter complexes," *The Journal of Physical Chemistry A*, vol. 116, no. 25, pp. 6621–6629, 2012. [Online]. Available: https://doi.org/10.1021/jp301471e

Acknowledgment

I would like to thank many kind people who helped me on the way to finish my thesis. In particular

my supervisor Prof. Dr. Janina Maultzsch with her great foresight ordering an UV Raman laboratory. This, in particular, has given me the possibility to work on new topics in the field of carbon materials. Also, for her constant and always very kind support in various matters. I have enjoyed being in the AG Maultzsch.

Prof. Dr. Michael Lehmann for being the chairman of the thesis committee.

Prof. Dr. Ralph Krupke for reviewing this thesis.

Prof. Dr. Axel Hoffmann for reviewing this thesis.

Felix Herziger who constantly came up with clever and stimulating ideas and, in his inimitable way, brought even the most complicated things to the point.

Roland Gillen for so many nice moments in New York, Boston, Athens, and of course for so many deep, interesting, and inspiring physical discussions. Also, for the vast theoretical support concluding with several joint articles.

Harald Scheel for his analytic expertise and the non-stopping support in my sometimes stubborn laboratory.

René Meinke for building up the UV laboratory and supporting me in my first months.

Rohit Narula for many animated discussions concerning double-resonant Raman scattering in graphene and carbon nanotubes, and of course for his support for our joint article.

Valentin N. Popov for many stimulating discussions concerning double-resonant Raman scattering in bilayer graphene, graphite, carbon nanotubes, and of course for his kind support for our joint article.

The whole AK Peter Schreiner and in particular Andrey A. Fokin, Tetyana V. Koso, Vladimir N. Rodionov, Natalie A. Fokina, Heike Hausmann, Paul Kahl, Philipp Wagner, Ciro Balestrieri, Jonathan Becker, Graham J. Bodwell for the kind providing of the manifold diamondoid samples. Further, Peter Schreiner for the very critical proof reading of our joint articles.

The whole AG Möller and in particular Robert Richter, Tobias Bischoff, André Knecht, Andrea Merli, Torbjörn Rander for the beam line measurements at BESSY II. Further, Tobias Bischoff and André Knecht for many fruitful discussion on diamondoids.

Prof. Dr. Peter Saalfrank and Tao Xiong for a theoretical introduction to the electronic structure of diamondoid derivatives.

Stefan Kalinowski for the support of several measurements in the "Gelbes Labor".

The very well organized and supportive Anja Sandersfeld to manage all the bureaucracy.

Our daily, very early (11:15) lunch group with many amusing and refreshing moments.

The office colleagues, Stefan Westerkamp, Felix Kampmann, and Stefan Kalinowski for so many rememberable moments, deep and interesting physical, political and humorous discussions.

My Bachelor and Master student Tobias Hückstaedt always coming up with well-reasoned and interesting ideas.

The whole groups AG Maultzsch and AG Hoffmann for the nice atmosphere during the last years, especially Dirk Heinrich, Harald Scheel, Sevak Kachadorian, Thomas Kure, Felix Nippert, Ludwig Greif, Stefan Jagsch, Alexander Mittelstädt, Stefan Kalinowski, Andrei Schliwa, Felix Kampmann, Markus Wagner, Narine Ghazaryan and Michael Mayer.